SISSA
Scuola
Internazionale
Superiore di
Studi Avanzati

Physics Area – PhD course in

THEORY and NUMERICAL SIMULATIONS of CONDENSED MATTER

Entanglement dynamics and chaos in long-range quantum systems

CANDIDATE:

Silvia Pappalardi

ADVISORS:

Prof. Rosario Fazio

Prof. Alessandro Silva

Trieste, Academic Year 2019 - 2020

"Sosteneva, fra l'altro, che le inopinate catastrofi non sono mai la conseguenza o l'effetto che dir si voglia d'un unico motivo, d'una causa al singolare: ma sono come un vortice, un punto di depressione ciclonica nella coscienza del mondo, verso cui hanno cospirato tutta una molteplicità di causali convergenti. Diceva anche nodo o groviglio, o garbuglio, o gnommero, che alla romana vuol dire gomitolo."

— C. E. Gadda, Quer pasticciaccio brutto de via Merulana

Invitation

One of the most challenging questions of modern physics concerns how to reconcile macroscopic irreversibility with the microscopic – hence quantum – description of nature. This requires a deep understanding of the *approach to thermal equilibrium*, as much as to unveil the principles that describe its *dynamics*. This problem, that already challenged standard classical statistical mechanics, is made even more difficult in condensed matter due to the presence of complex quantum interactions. In this realm, nature coexists with fundamentally new concepts, such as the superposition principle or *quantum entanglement*. Understanding the role of these quantum correlations in the emergence of our stationary classical world has been under intense debate since the early days of quantum mechanics. Nevertheless, due to the inadequacy of the theoretical equilibrium notions in this domain, the field of quantum out-of-equilibrium dynamics is still being largely explored and many basic questions currently remain unanswered. Far from being only academic issues, these intricate questions have become particularly relevant in the past twenty years, due to the recent exciting *experimental and technological progress* in the field of quantum simulation and computation. These allow for exploring the unitary quantum dynamics in isolation from the environment at unprecedented time-scales in many-body physics. Following these renewed motivations, the contemporary non-equilibrium statistical mechanics community has started answering these problems, leading to a relatively well-established paradigm. The present framework is identified, among others, by three primary pillars: the solvability of integrable systems, the local thermalization of generic Hamiltonians and the failure of equilibration due to various mechanisms. The first more refined concept concerns the dynamics of integrable systems, that can now be exactly described through analytical and algebraic descriptions[1]. On the second place, quantum thermalization of generic local non-integrable models is nowadays understood in terms of local physical observables, via the celebrated eigenstate thermalization hypothesis[2]. At the same time, it is now also acknowledged that the approach to equilibrium can be strongly hindered by different instances of ergodicity breaking, that can induce localized dynamical phases.

In all these developments, *quantum information theoretical tools* (one for all the entanglement entropy) have been essential in providing a deeper understanding of quantum dynamics, chaos, and its violations. For example, the emergence of classicality from quantum mechanics can be understood in terms of *decoherence* between

[1] Sutherland, World scientific (2004).

[2] D'Alessio, Kafri, Polkovnikov, and Rigol, Advances in Physics 65, 239 (2016)

the system and the environment[3]. Moreover, the time-dependent growth of the entanglement entropy allows one to distinguish between different phases of matter. Thermalization itself can be identified with the accumulation in time of quantum entanglement between a subsystem and the rest of the system.
Beyond these notable results, there are many fundamental questions waiting for a complete answer. For instance, is there a general definition, or possible classification, of many-body quantum chaos? What is the key mechanism for ergodicity breaking in the quantum domain? How can these concepts be exploited to encode and transfer information? Correspondingly, the non-equilibrium community is continuously developing new tools and ideas willing to answer these questions.

The present thesis aims addressing mainly the following problem: How does the above paradigm changes in the presence of *long-range interactions*?
Because of screening, condensed matter systems are usually described by short-range local interactions. For this reason, classical statistical mechanics, as well as the quantum version above, are formulated for locally interacting systems. However, long-range interactions are very often present in nature. Fascinating examples in classical physics include plasmas, galaxies, ionic crystals, etc.. In the quantum domain, atomic-molecular-optical systems can be often described in terms of effective Hamiltonians with long-range interactions. Their study is recently becoming a more established topic that has already led to a plethora of exceptional experiments, as well as numerous original theoretical ideas for problems that do not have a short-range counterpart. Despite the progress, the general principles and theorems of non-equilibrium dynamics, discussed above, cease to be valid. Hence, it would be highly desirable to have a deeper general understanding of the effect of long-range interactions (clean or disordered) to many-body physics and the coherent non-equilibrium dynamics[4].

We further consider a different, connected question. After generic unitary quantum dynamics, stationary local observables are described by standard (classical) statistical mechanics. Hence one cannot prescind from asking: Is there something fully non-classical of quantum thermalization? And, if so, how to quantify it?

We approach these questions employing the quantum information tools that have already proved insightful for the study of out-of-equilibrium dynamics of short-range systems. In particular, we concentrate on the bipartite and multipartite entanglement spreading and information scrambling. As mentioned above, *bipartite entanglement entropy* (EE) has rapidly become a fundamental paradigm of our understanding of in and out-of-equilibrium many-body physics. Another notable concept is multipartite entanglement, as witnessed by the *quantum Fisher information* (QFI), that further quantifies the usefulness of a quantum state for metrological

[3] Zurek, Rev. Mod. Phys. 75, 715 (2003).

[4] The same question has been addressed also in classical statistical mechanics, whose standard formulation also relies on the presence of local interactions. It is now well appreciated that classical long-range interactions give rise to remarkable static and dynamical properties that do not possess a short-range counterpart, such as non-additivity of energy, ergodicity breaking, slow relaxations, etc. For a beautiful book on the topic, we refer to "Campa, Dauxois, Fanelli, and Ruffo, OUP Oxford (2014)".

purposes. Besides, recently *scrambling* has been proposed as a relatively new notion to characterize many-body dynamics. Generically identified as the delocalization of quantum information, scrambling is commonly quantified by the dynamics of out-of-time ordered correlators (OTOC).

The thesis is organized as follows. We start with Chapter 1 by providing an overview of the general setting of non-equilibrium many-body entanglement dynamics, as introduced above. The goal is two-fold: on one side we give the general background on the topic, on the other we introduce the definitions of the entanglement and scrambling quantifiers that will be used across the thesis.
The hearth of the discussion is devoted to entanglement and its evolution in spin systems with long-range couplings, characterized by interactions that decay algebraically with the distance. Finally, we study the multipartite entanglement of chaotic eigenstates, addressing the issue of the quantum nature of thermalization.

The first question requires a strong shift in the paradigm (and techniques) usually employed to solve standard short-range quantum dynamics. Whenever the interaction between the elementary constituents is sufficiently long-range, one expects mean-field approximation to be valid. Dynamically, this implies that the observable equations of motion are typically well approximated by the classical ones at relatively short times, before the so-called Ehrenfest time. For instance, it is well-known that systems with clean all-to-all interactions are so cooperative that they behave as a single, collective, and classical object. Hence, it is natural to ask whether the semiclassical description may survive when interactions have a long but finite range or when they are disordered.

For this reason, the bulk of the analysis contained in this thesis is performed using *semiclassical tools*, which allow recognizing the different contributions in the dynamics, especially in connection with the buildup of quantum correlations. Therefore, the second Chapter 2 is devoted to a review of the broad field of semiclassical dynamics and to the introduction of the techniques that have been applied and extended in the rest of the thesis.

On this basis, we first develop a generic approach to the study of quantum entanglement in generic semiclassical systems, where the extent of the initial quantum fluctuations is given by a vanishing Plank constant. This problem was already largely studied in the '90s and early 2000 when it was recognized that entanglement generation and dynamical chaos are related by the process of decoherence. In those years, the interest was on the understanding of quantum irreversibility and decoherence through the dynamics of the purity and the Loschmidt echo. In Chapter 3, we propose a unifying framework that directly connects "contemporary" entanglement quantities (EE and QFI) to the quantifiers of classical (Lyapunov spectrum) and quantum chaos (scrambling). In the semiclassical regime, we derive a complete theory, model-independent, which allows making general predictions of the entanglement dynamics depending on the underlying classical phase-space of the model. For instance, in the absence of semiclassical chaos, the EE grows logarithmically in time, while whenever chaos or instabilities are present, its growth is linear. We then apply this theory to textbook infinite-range models, well known for the study of collective dynamics or quantum chaos.

The real challenge is to understand how these collective entanglement dynamics are modified by long but finite range interactions, beyond the semiclassical collective limit. Chapter 4 is dedicated to a collection of numerical results on a specific spin-chain, describing quantum correlation dynamics aside from the classical limit. Firstly, we introduce clean long-range systems and their salient features. Then, we explore the important differences between entanglement and scrambling for infinite-range spin systems beyond the Ehrenfest time. We conclude by discussing the numerical results for the different entanglement quantifiers upon changing the range of interaction between the spin. A clear semiclassical entanglement behavior emerges, whenever the range of the interaction is smaller than the dimensionality. Indeed, the same "counterintuitive"[5] slow entanglement entropy growth was reported by several numerical simulations also in the past.

The goal of Chapter 5 is to tackle this issue more rigorously. We discuss the qualitative change in the underlying mechanism to the EE dynamics. Whenever interactions are sufficiently long-range, the so-called "quasi-particle picture" of local interacting integrable systems gets suppressed. This follows from the quasi-conservations of spin-waves excitations on top of the collective zero-mode dynamics. Therefore, the dominant contribution is given by the semiclassical collective entanglement, introduced in the previous chapter, that predicts generally a slow logarithmic growth.

In the following Chapter 6, we turn to disordered long-range interactions and we explore irreversibility and scrambling. We consider the Sherrington-Kirkpatrick model, which shares many characteristics with a different notorious model, namely the Sachedev-Ye-Kitaev model[6]. Due to disorder, the vicinity to the classical limit is less obvious in this case, yet we show that the semiclassical analysis remains valid, with $1/N$ serving as an effective Planck's constant, where N is the system size. The presence of a classical chaotic limit ensures that the scrambling quantifiers are characterized by a semiclassical exponential growth in the intermediate time regime. We also discuss a short-range version of the SK model, where the OTOC increases only polynomially in time.

In the last two chapters, we study entanglement beyond the semiclassical description, with the same goal of a better understanding of long-range interactions and quantumness in thermalization.

In Chapter 7, we perform an equilibrium analysis and study the ground state entanglement entropy of the long-range *Dyson hierarchical model*, a toy system devised by Dyson in 1969. Via a real-space renormalization group solution, we derive the analytical EE of the critical ground state. Our main and surprising result is that at criticality, although the correlation functions decay algebraically, the entanglement entropy obeys an area law. Unusual scalings of the entanglement in critical ground states have been already observed in long-range models. In the present case, this

[5] Whenever long-range interactions are present, correlations between distant degrees of freedom can buildup very fast in time. On the other hand, the entanglement entropy features slow entanglement dynamics (logarithmic growth in time), significantly slower in comparison to the linear increase of short-range systems.

[6] This model is a strongly correlated, chaotic many-body system, that is also conformally invariant, and exactly solvable. For these reasons, it is currently believed to potentially bring crucial insights into the understanding of strongly correlated materials and high energy physics.

is due to the hierarchical structure of the renormalized ground state which can be written as a tree tensor network with a finite bond dimension.

We conclude with Chapter 8, where we consider the issue of the quantum properties of generic chaotic eigenstates. One of the main results of quantum thermalization is that all thermal states with the same energy density (eigenstates, Gibbs states, microcanonical ensembles) are indistinguishable using local probes or fluctuation-dissipation relations. In this chapter, we show instead that a quantum information perspective can shed new light on this issue. By deriving the QFI for different thermal states, we show that their multipartite entanglement content is in stark contrast, with difference amplified in the presence of thermal phase-transitions.

The specific perspectives stemming from the work of the earlier chapters are outlined at the end of each of them. Still, this PhD work leaves room for many questions and opened problems. The last Chapter 9 contains some thoughts regarding promising directions for future research.

List of publications

The content of this thesis is based on the following publications:

[1] **S. Pappalardi**, A. Russomanno, A. Silvia, and R. Fazio,
Multipartite entanglement after a quantum quench,
Journal of Statistical Mechanics, 053104 (2017).

Chapter 8.

[2] **S. Pappalardi**, A. Russomanno, B. Žunkovič, F. Iemini, A. Silvia, and R. Fazio,
Scrambling and entanglement spreading in long-range spin chains,
Physical Review B **98**, 134303 (2018).

Chapter 4.

[3] **S. Pappalardi**, P. Calabrese, and G. Parisi,
Entanglement entropy of the long-range Dyson hierarchical model,
Journal of Statistical Mechanics 073102 (2019).

Chapter 7.

[4] A. Lerose and **S. Pappalardi**,
Origin of the slow growth of entanglement entropy in long-range interacting spin systems,
Physical Review Research **2**, (2020).

Chapters 3 and 5.

[5] M. Brenes, **S. Pappalardi**, J. Goold, and A. Silva,
Multipartite entanglement structure in the Eigenstate Thermalization Hypothesis,
Physical Review Letter **124**, 040605 (2020).

Chapter 8.

[6] **S. Pappalardi**, A. Polkovnikov, and A. Silva,
Quantum echo dynamics in the Sherrington-Kirkpatrick model,
SciPost Physics, 9, 021 (2020).

Chapter 6.

[7] A. Lerose and **S. Pappalardi**,
Bridging entanglement dynamics and chaos in semiclassical systems,
Physical Review A **102**, 032404, (2020).

Chapter 3.

The forthcoming publications are based on research involved in this thesis:

[8] **S. Pappalardi**, T. Parolini, A. Lerose, and R. Fazio
Athermal scarred eigenstates in long-range spin chains.

[9] M. Brenes, **S. Pappalardi**, J. Goold, and A. Silva,
Gaussianity of the eigenstate thermalization hypothesis and out-of-time oredered correlators.

Contents

Chapter 1

Non-equilibrium many-body systems and their entanglement

This chapter aims at illustrating the profound and rich connections between quantum entanglement and the study of out-of-equilibrium dynamics. First, we recall the standard paradigm of quantum dynamics, thermalization, and its violations in isolated quantum systems. Then, after introducing the main quantifiers of entanglement and scrambling, we review the relevant results concerning out-of-equilibrium entanglement.

In this chapter, we aim at giving an overview of the general setting and state-of-the-art of the topics addressed in this thesis. Specifically, we introduce the standard framework of quantum many-body dynamics and we attempt to illustrate why entanglement is such an insightful quantity to characterize it. The chapter has two main objectives. On one side it provides the general background on quantum statistical mechanics out-of-equilibrium. On the other, it introduces the definitions for the entanglement and scrambling quantifiers that will be used in the thesis. The last section intends to review the profound and rich connections between these two, namely the standard paradigm for the entanglement dynamics and scrambling for out-of-equilibrium systems out-of-equilibrium. The broad goal of the thesis is to extend it to long-range interacting systems, where the present framework ceases to be valid.

1.1 Quantum statistical mechanics out-of-equilibrium

The study of non-equilibrium dynamics has emerged since the foundations of statistical mechanics as an essential tool to properly reconcile microscopic determinism with a statistical description of many-particle systems [8, 9]. Questions as irreversibility, relaxation to thermal equilibrium, the emergence of statistical ensembles, etc., have been addressed several times since the early days of quantum mechanics.

Undoubtedly, the last wave of interest over the past twenty years has been driven by the extraordinary experimental progress in the field of ultra-cold matter and synthetic materials. Laboratories worldwide are now able to trap, cool, and manipulate atoms, ions, and molecules at extremely low temperatures and in isolations from the environment. Such technological advancements have allowed for probing quantum time-evolution on unprecedented timescales in many-body systems [10–12].

This novel access to real-time dynamics has reinvigorated the interest for the foundations of the statistical mechanics of out-of-equilibrium of systems in their full quantum regime, i.e. $\hbar = 1$. This has led to the systematic study of many-body-dynamics of quantum systems in isolation, characterized by unitary evolution [13–17].

The approach of pure quantum states to thermal equilibrium is now understood in terms of the evolution in time of local observables [17, 18]. Typically, after an initial time transient, the relevant observables attain their thermal equilibrium values described by conventional statistical mechanics. A widely accepted framework for understanding thermalization from quantum dynamics is known as the eigenstate thermalization hypothesis [17]. It can be seen as a condition on matrix elements of generic operators in the energy eigenbasis.

Thermalization can be violated for a long (or infinite) time as a result of different instances of ergodicity breaking, such as integrability, many-body-localization, prethermalization, etc.. This issue has been the focus of growing attention in the past few years. Surprisingly, the generic approach to thermal equilibrium predicted by the eigenstate thermalization hypothesis (at least in its strong sense) seems to be much less general than expected.

These two different scenarios (approach to thermal equilibrium or its failure) are illustrated pictorially in Figure 1.1. Different initial pure states with the same energy density are represented by blue dots. Their complex dynamical evolution is given by the arrows. After the transient out-of-equilibrium regime, pure quantum states might eventually attain stationary states, represented by a smooth manifold in the space of reduced density matrices. The rest of this section is devoted to an overview of the intriguing phenomena underlying this picture.

The well-understood paradigm for quantum non-equilibrium dynamics holds for generic *local* Hamiltonians, characterized by short-range interactions. Conversely, as we will see across the thesis, in the case of long-range interacting systems, much less is known.

1.1.1 Non-equilibrium unitary evolution of quantum systems

Consider a quantum system described by a generic local Hamiltonian $\hat{H}$, which we assume to be bounded and isolated, with N degrees of freedom with $N \gg 1$. Since the system is bounded, the energy eigenvalues are discrete. Let E_n denote the energy eigenvalue corresponding to the energy eigenstate $|E_n\rangle$. To study out-of-equilibrium dynamics, the system is initialized at time $t = 0$ in a pure initial state $|\psi_0\rangle$, which could be prepared for example as the ground state of a different Hamiltonian $\hat{H}_0$. Since the system is isolated, its time evolution is governed by the Schrödinger equation. Namely, the initial state will evolve unitarily in time as

$$|\psi(t)\rangle = e^{-i\hat{H}t/\hbar}\,|\psi_0\rangle = \sum_n c_n\, e^{-iE_nt/\hbar}\,|E_n\rangle\ , \tag{1.1}$$

where on the right-hand side $c_n = \langle E_n|\psi_0\rangle$ is the overlap between the initial state and a single energy eigenstate. Unless $\hat{H}$ commutes with $\hat{H}_0$, the resulting evolution is generally nontrivial, with local observables and their quantum correlations

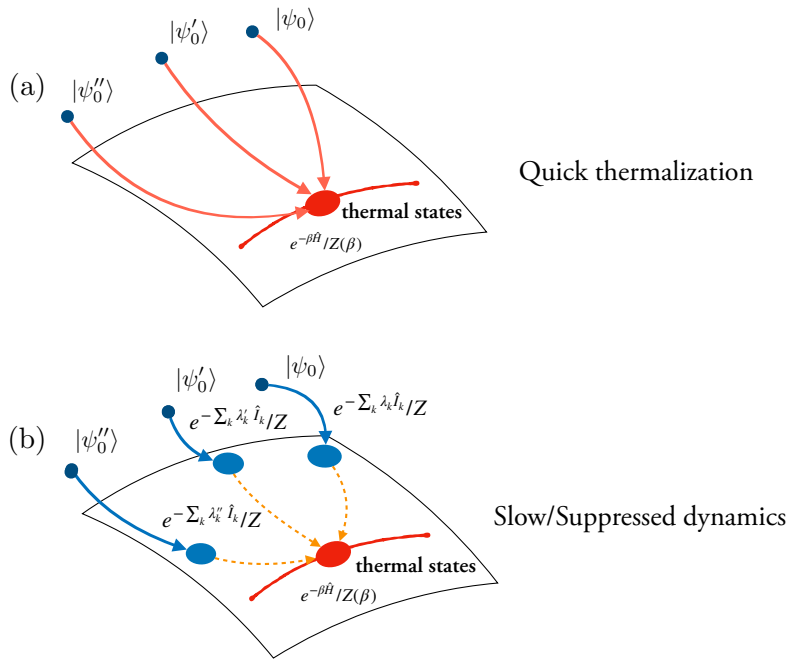

Figure 1.1: Pictorial representation of the local equilibration dynamics after a sudden quench: (a) thermalization (b) instances of ergodicity breaking. The cartoon shows the evolution from three possible initial states (blu small dots) with the same energy density. The white surface indicates the manifold of the reduced density matrices of finite subsystems and the arrows represent the complex many-body dynamics. The two different scenarios are accompanied by a variety of interesting dynamical phenomena. (a) Quick thermalization discussed in Section 1.1.2. All the initial states thermalize to the same reduced density matrix, identified by only one parameter — the temperature $1/\beta_E$ — uniquely fixed by the initial energy [cf. Eq.(1.2)]. (b) Slow relaxation in the presence of ergodicity breaking discussed Section 1.1.3. For integrable or MBL systems, the initial states equilibrate to asymptotic density matrices determined by their initial conditions, i.e. the GGE [cf. Eq.(1.17)], represented by the big blue dots. In the presence of small integrability breaking term (as in Eq.(1.20)) or in the presence of non-exact quantum scars, these states are expected to slowly drift towards the asymptotic thermal state. Image inspired from Ref.[19].

changing in time as the state of the system evolves. This protocol goes under the name of *quantum quench* and represents the simplest example to drive the system out-of-equilibrium. Typically, *global* and *sudden* quenches refer to protocols where one parameter h_0 of the pre-quench Hamiltonian $\hat{H}_0 = \hat{H}(h_0)$ is changed uniformly and instantaneously to h of the final one $\hat{H} = \hat{H}(h)$. One can also consider inhomogeneous or local quenches, where $\hat{H}_0$ differs from $\hat{H}$ only by a local impurity. In a global quench, a finite amount of energy $E = \langle\psi_0|\hat{H}|\psi_0\rangle$ is introduced into the system, which corresponds, in jargon, to an increase in temperature $1/\beta_E$, usually identified by the following relation between the energies

$$\langle\psi_0|\hat{H}|\psi_0\rangle = E = \mathrm{Tr}\left(\hat{H}\,\frac{e^{-\beta_E\hat{H}}}{Z}\right) . \tag{1.2}$$

Even if the dynamics are entirely unitary, after the transient non-equilibrium evolution, many-body systems are expected to eventually equilibrate either to a thermal state or otherwise failing thermalization. This is intimately linked to the presence or absence of quantum chaos and the emergence of irreversibility in the quantum realm [17], as elaborated upon in the next two sections.

However, in the past twenty years, a great focus of attention has been devoted to the study of the transient non-equilibrium properties. The recent experimental advances in the field of ultra-cold atoms allow for studying dynamics of quantum systems in isolation from the environment and the absence of dissipation. Quantum non-equilibrium dynamics has become a vast field of research and a plethora of exotic phenomena have been explored: From the fate of phase-transitions and universality, as explained e.g. by the Kibble-Zurek mechanism [20, 21], to exotic effects due to periodic driving [22–24], from the existence of new dynamical phases such as time crystals [25], to the understanding of electronic transport [26] and the spreading of magnetized domains [27, 28]. Much attention has also been given to the different dynamical regimes, from the analysis of early time behavior to the different ways equilibrium can be approached.
An interesting question concerns the nature of *dynamical criticality* or the so-called *dynamical phase-transitions* (DPT) which have been associated with several different concepts [29–35]. A possible class of DPT is related to the singular behavior in the transient real-time evolution of Loschmidt echoes [34, 35]. On the other hand, dynamical criticality can be defined from the existence of long-range order for stationary states and it is characterized by a non-equilibrium order parameter [29, 32]. This second type of DPT arises in long-range spin systems and it will be analyzed concerning entanglement in Sections 3.2 and 5.2.

Another important topic in the field of non-equilibrium dynamics is the study of *quantum correlation spreading* after a quench. Whenever systems are characterized by local Hamiltonians, out-of-equilibrium quantum correlations are known to spread with a light cone structure. In fact, the propagation of information in non-relativistic quantum lattice systems obeys a speed limit given by the *Lieb Robinson theorem* [36]. This states that the support of an operator $\hat{O}_{\mathbf{x}_0}$, initially localized in a finite region around site $\mathbf{x}_0$, which time-evolves in the Heisenberg representation with a local Hamiltonian $\hat{H}$, spreads in space with a maximum velocity $v_{\rm LR}$. Formally, for any locally interacting lattice system there exist positive constants ξ, μ and $v_{\rm LR}$ such that

$$||\hat{O}_{\mathbf{x}}(t) - \hat{O}_{\mathbf{x}_0}(0)|| \leq \xi ||\hat{O}_{\mathbf{x}}||\, ||\hat{O}_{\mathbf{x}_0}||\, e^{-\mu\, \max(0, |\mathbf{x}-\mathbf{x}_0| - v_{\rm LR} t)}\,, \tag{1.3}$$

where $||\cdot||$ is the operator norm. Namely, the weight of the time-evolved operator outside the region $|\mathbf{x}-\mathbf{x}_0| \leq v_{\rm LR} t$ is exponentially suppressed as $|\mathbf{x}-\mathbf{x}_0| - v_{\rm LR} t \to \infty$. The light-cone propagation of information has important implications for entanglement dynamics, as reviewed in Section 1.3.3.

1.1.2 Equilibration and the eigenstate thermalization hypothesis

We begin the discussion of quantum equilibration by restricting to generic non-integrable Hamiltonians without global symmetries [17]. Generalizations and violations of this assumption are discussed in the next section. For generic Hamiltonians,

the energy eigenvalues typically have the same statistical properties as the eigenvalues of gaussian random matrices [37, 38]. This characteristic property has been (and still is) intensively analyzed [39–42]. In this the thesis, we shall focus instead on dynamical evolution and the approach to equilibrium.

In the spirit of the von Neumann's theorem [43], quantum equilibration refers to the dynamics of observables. In particular, the primary quantities are *local* observables $\hat{O}^A$, with support in a finite region A of the physical space. The time evolution can be expressed in terms of the matrix element of the operator in the energy eigenbasis as

$$\langle \hat{O}^A(t) \rangle \equiv \langle \psi(t) | \hat{O}^A | \psi(t) \rangle = \sum_n |c_n|^2 \, O^A_{nn} + \sum_{n \neq m} c_n \, c^*_m e^{-i(E_n - E_m)t/\hbar} \, O^A_{nm} \, , \tag{1.4}$$

with $O^A_{mn} = \langle E_m | \hat{O}^A | E_n \rangle$. A system is said to *equilibrate* if the expectation value of all local observables converge to a finite value at infinite times, i.e.,

$$\lim_{t \to \infty} \langle \hat{O}^A(t) \rangle = O^A_{\text{eq}} \, . \tag{1.5}$$

This is formally studied via the *infinite-time average* of $\langle \hat{O}^A(t) \rangle$, defined as

$$\overline{O^A} \equiv \lim_{T \to \infty} \int_0^T dt \, \langle \hat{O}^A(t) \rangle \, . \tag{1.6}$$

Notice that the infinite-time average must be regarded as a purely mathematical tool [1] [44]. In the absence of degeneracies in the spectrum, a mild assumption for non-integrable systems without global symmetries, one obtains

$$\overline{O^A} = \sum_n |c_n|^2 \, O^A_{nn} = \text{Tr} \left(\hat{\rho}_{\text{DE}} \, \hat{O}^A \right) \equiv \langle \hat{O}^A \rangle_{\text{DE}} \, , \tag{1.7}$$

where $\hat{\rho}_{\text{DE}}$ is the density matrix of the so-called *diagonal ensemble* defined by

$$\hat{\rho}_{\text{DE}} = \sum_n |c_n|^2 \, |E_n\rangle\langle E_n| \, , \tag{1.8}$$

which, in principle, contains all the information about the initial state $|\psi_0\rangle$. Notice, however, that typical initial states have an extensive energy and sub-extensive energy fluctuations, i.e.,

$$E \propto N \qquad \delta E^2 / E^2 \propto \frac{1}{N} \, , \tag{1.9}$$

with $\delta E^2 = \langle \psi_0 | \hat{H}^2 | \psi_0 \rangle - \langle \psi_0 | \hat{H} | \psi_0 \rangle^2$. Hence the overlaps $|c_n|^2$ in the diagonal ensemble can be taken generally as a smooth distribution peaked around energy E with small variance.

A system is said to *thermalize* if it equilibrates to the value predicted by statistical mechanics and it remains close to it at most later times. In other words, a quantum

[1] In fact, the averaging time T has to be larger than all the relevant time-scales and in particular then the Heisenberg time $T_{\text{Heis}} = 2\pi\hbar/\delta \sim e^N$, with δ the mean spacing between energy eigenvalues. Hence, this time scale is too large to be physically relevant.

system thermalizes if the equilibrium value in Eq.(1.5) corresponds to the microcanonical prediction at energy E or, in the presence of equivalence of ensembles[2], to the thermal expectation value at temperature $1/\beta_E$ (1.2), i.e.[3] ,

$$\lim_{t\to\infty}\lim_{N\to\infty}\langle\hat{O}^A(t)\rangle = \mathrm{Tr}\left(\hat{O}^A\,\frac{e^{-\beta_E\hat{H}}}{Z}\right) . \tag{1.10}$$

Let us conclude this section by adopting a "local" perspective. In general, the expectation values $\langle\psi|\hat{O}^A|\psi\rangle$ of local observables $\hat{O}^A$ are encoded in the *reduced density matrix* $\hat{\rho}_A = \mathrm{Tr}_{\overline{A}}|\psi\rangle\langle\psi|$, where $\mathrm{Tr}_{\overline{A}}$ indicates the partial trace performed over $\overline{A}$, the complement of A. This follows from $\langle\psi|\hat{O}^A|\psi\rangle = \mathrm{Tr}\left(\hat{O}^A\hat{\rho}_A\right)$. Therefore, thermalization on observables [cf. Eq.(1.10)] implies that the stationary state of the system will be locally equivalent to a thermal state

$$\lim_{t\to\infty}\lim_{N\to\infty}\hat{\rho}^A(t) = \mathrm{Tr}_{\overline{A}}\left(\frac{e^{-\beta_E\hat{H}}}{Z}\right) , \tag{1.11}$$

with the temperature fixed by the energy (1.2), see e.g. Ref.[48] for a detailed definition of local relaxation. So, despite the global evolution is unitary (the total information is conserved), thermalization implies a local loss of information: Independently of the initial states, all the stationary density matrices locally "look" thermal [cf. Eq.(1.11)]. It is now well known that this apparent paradox is explained by the non-local growth in time of quantum correlations, i.e. entanglement dynamics, that will be discussed in detail in what follows. This first observation already shows how a quantum information perspective can be very insightful for the understanding of the thermalization of quantum systems.

Eigenstate thermalization hypothesis (ETH)

A predictive framework for understanding thermalization goes under the name of *eigenstate thermalization hypothesis*. Inspired by early works by Berry [49, 50], later formulated by Deutsch [51], the ETH was fully established by Srednicki in a series of papers in the early 1990's [44, 52, 53]. He was able to complement random matrix theory with the structure given by the energy dependence, in such a way for all statistical mechanics to naturally follow. The ETH solves the issue of the relaxation of observables to the microcanonical predictions and it explains why they remain close to it almost all large times. In Appendix A we provide a pedagogical review of the topic.

[2] Equivalence of ensemble holds when observables take practically the same value for the greatest part of the microscopic states accessible in each ensemble, namely the relevant fluctuations are negligible in the thermodynamic limit. Mathematically this is associated with the extensivity, additivity, and concavity of the thermodynamic functions, such as the energy, the entropy, or the free energy [45]. This is well established for standard statistical mechanics of short-range interacting Hamiltonians, see e.g. Ref.[46]. Notable exemptions include long-range interacting systems [47].

[3] Notice the order of the limits in Eq.(1.10): The thermodynamic limit $N\to\infty$ has to be taken first because, for finite size systems, recurrences occur at exponentially large times in N. Alternatively, one resorts to the infinite time-average in Eq.(1.6).

The ETH is usually formulated as an ansatz for the matrix elements of observables in the eigenstates of a Hamiltonian $\hat{H}$ ($\hat{H}|E_n\rangle = E_n|E_n\rangle$). For a generic operator $\hat{O}$, it reads [44]

$$O_{nm} \equiv \langle E_n|\hat{O}|E_m\rangle = \mathcal{O}(\bar{E})\,\delta_{nm} + e^{-S(\bar{E})/2}\, f_{\hat{O}}(\bar{E},\omega)\, R_{nm}\ , \tag{1.12}$$

where $\bar{E} = (E_n + E_m)/2$ is the average energy of the two eigenstates, $\omega = E_n - E_m$ is the energy difference, $\mathcal{O}(\bar{E})$ is the micro-canonical value at energy $\bar{E}$, $S(\bar{E})$ is the thermodynamic entropy (logarithm of the density of states) and $f_{\hat{O}}(\bar{E},\omega) = f_{\hat{O}}(\bar{E},-\omega)$ is a real smooth functions of its two arguments. The numbers R_{nm} are erratically fluctuating variables, that can be seen as are random real or complex numbers with zero mean and unit variance ($\overline{R_{nm}^2} = 1$ or $\overline{|R_{nm}|^2} = 1$ respectively) [4].

The validity of ETH is restricted to states which have a finite energy density, away from the edges of the spectrum. ETH is said to hold in a *strong* (weak) sense, if all (almost all) the eigenstates at the center of the spectrum obey Eq.(1.12) [57]. Understanding the range of applicability of ETH in physical Hamiltonians has motivated a considerable body of numerical work over the past decade [17, 40, 58]. Recent numerical and analytical studies have demonstrated a violation of strong ETH in several classes of spin chains, due to the existence of athermal eigenstates in the center of the spectrum [59–65]. This will be discussed in the context of ergodicity breaking in Section 1.1.3.

The ETH ansatz (1.12) is enough to deduce thermalization in isolated quantum systems. It can be shown that the stationary values of *local observables* after a quenched dynamics, i.e. $\overline{O}$ [cf. Eq.(1.5)], correspond to their thermal expectation values $\langle\hat{O}\rangle_{\text{Gibbs}} = \text{Tr}(e^{-\beta\hat{H}}\hat{O})/Z$. The latter, in turn, can be calculated on single eigenstates corresponding to the average energy, namely [44]

$$\overline{O} \simeq \langle\hat{O}\rangle_{\text{Gibbs}} \simeq \mathcal{O}(E) \simeq \langle E|\hat{O}|E\rangle\ . \tag{1.13}$$

where $\simeq$ stands for an equality at the leading order in N and temperature is fixed by the initial energy via Eq.(1.2). A simple derivation of this equality [44] can be found e.g. in Appendix A.1. Eq.(1.13) describes the relaxation of local observables to the microcanonical prediction and it constitutes the essence of the eigenstate thermalization hypothesis. The latter also explains why instantaneous observables remain close to the microcanonical value at most later times. In fact, one can compute the time fluctuations of the expectation values of the observable $\hat{O}$ as

$$\sigma^2_{\hat{O}} \equiv \overline{O^2} - \overline{O}^2 = \sum_{mn,m\neq n} |c_n|^2|c_m|^2\,|O_{nm}|^2 \leq \max|O_{nm}|^2 \propto e^{-S(\bar{E})}\ , \tag{1.14}$$

where one first inserts the energy eigenbasis in the definition (1.6), then one computes the infinite-time average and lastly one estimates the maximum with the ETH ansatz in Eq.(1.12).

[4] At this level, no assumption is made on the distribution of the R_{nm} (besides its mean and variance). However, focusing on a small energy window where $f_{\hat{O}}(\bar{E},\omega) \sim$ const., one should retrieve the random matrix theory prediction in which non-diagonal elements are Gaussian random variables. More generally, the Gaussian nature of the R_{nm} has been questioned, see e.g. Ref.[54, 55], and this has brought to generalized versions of ETH in Ref.[56].

The smooth function $f_{\hat{O}}(\bar{E},\omega)$ in the ETH ansatz completely determines also *two-point correlation functions* and, through that, it allows derive the *fluctuation dissipation theorem* [17, 66]. The response function and the symmetrized noise are defined respectively as $\chi_{\hat{O}}(t_1,t_2) \coloneqq -i\theta(t_1-t_2)\langle[\hat{O}(t_1),\hat{O}(t_2)]\rangle$ and $S_{\hat{O}}(t_1,t_2) \coloneqq \langle\{\hat{O}(t_1),\hat{O}(t_2)\}\rangle - 2\langle\hat{O}(t_1)\rangle\langle\hat{O}(t_2)\rangle$. When the expectation value is taken to respect to a single energy eigenstate $\hat{H}|E_n\rangle = E_n|E_n\rangle$, the Fourier transform can be performed over the time difference $\tau = t_1 - t_2$. For local operators or sums of local operators, the spectral function $\mathrm{Im}[\chi_{\hat{O}}(E_n,\omega)] = -\chi''_{\hat{O}}(E_n,\omega)$ and $S_{\hat{O}}(E_n,\omega)$ can be approximated imposing the ETH [17, 44]. In the thermodynamic limit they read

$$\chi''_{\hat{O}}(E_n,\omega) \simeq 2\pi \sinh\left(\frac{\beta\omega}{2}\right) |f_{\hat{O}}(E_n,\omega)|^2 \,, \tag{1.15a}$$

$$S_{\hat{O}}(E_n,\omega) \simeq 4\pi \cosh\left(\frac{\beta\omega}{2}\right) |f_{\hat{O}}(E_n,\omega)|^2 \,. \tag{1.15b}$$

These relations satisfy the fluctuation dissipation theorem (FDT)

$$\chi''_{\hat{O}}(E_n,\omega) = \frac{1}{2}\tanh(\beta\omega/2)\, S_{\hat{O}}(E_n,\omega) \,. \tag{1.16}$$

It can be shown that the latter holds both for single energy eigenstates or for asymptotic states of a quenched dynamics. For a detailed review on two point functions within ETH see, e.g., Appendix A.2.

As one of the main outcomes, we have shown that pure energy eigenstates are indistinguishable from thermal states using local probes, fluctuation dissipation relations, or for their entropic content (see Section 1.3.2). At the end of this thesis, in Chapter 8, we will illustrate how a quantum information perspective can be very insightful in discriminating between these different thermal states.

1.1.3 Instances of ergodicity breaking

As discussed above, thermalization is well understood as the out-of-equilibrium relaxation to a state determined completely by its initial energy $E = \langle\psi_0|\hat{H}|\psi_0\rangle$. This is reminiscent of the ergodic hypothesis in statistical mechanics [46]: At equilibrium observables only depend on few macroscopic properties (like energy) and the equilibrium state is equally likely to be any of those satisfying macroscopic conditions. Equivalently, one can describe equilibrium via the Gibbs density matrix $\hat{\rho}_{\text{Gibbs}} = e^{-\beta\hat{H}}/Z$ that can be found as the state that maximizes the entropy at fixed energy density $e(\beta) \equiv E(\beta)/N$.

Generic thermalization, however, can be strongly modified by different forms of ergodicity breaking.

The first class of systems is determined by models that have several local or quasi-local conserved quantities. Let $\hat{I}_1, \hat{I}_2, \ldots$ be the additional conserved quantities. The equilibrium state, defined via Eq.(1.5), will now retain the memory of their initial values, hence of the initial state. The maximum entropy principle then suggests that the stationary state density matrix should be given by a *generalized Gibbs ensemble* (GGE) [67]

$$\hat{\rho}_{\text{GGE}} = \exp\left(-\sum_k \lambda_k \hat{I}_k\right)/Z \,, \tag{1.17}$$

where Z is the normalization and λ_k are the Lagrange multipliers. They are uniquely fixed by the expectation values of the conserved quantities on the initial state $\langle\psi_0|\hat{I}_k|\psi_0\rangle = \mathrm{Tr}\left(\hat{I}_k\,\hat{\rho}_{\mathrm{GGE}}\right)$. Usually one fixes $\hat{I}_0 = \hat{H}$ with $\lambda_0 = \beta$.
One possibility is that the local conservation laws are associated with global symmetries of the Hamiltonian. In this case, Eq.(1.17) corresponds to the grand-canonical state in standard thermodynamics. A second alternative is represented by systems possessing an extensive number of non-trivial local conserved quantities. These are called (in analogy with classical mechanics) *integrable systems* [68]. The easiest case is given by quadratic models of bosons or fermions or by non-interacting systems which can be mapped onto them. The textbook example is illustrated by the one dimensional transverse-field-Ising model [69]

$$\hat{H} = -J\sum_{i=1}^{L}\hat{\sigma}_i^x\hat{\sigma}_{i+1}^x - h\sum_{i=1}^{L}\hat{\sigma}_i^z\ . \tag{1.18}$$

This system can be mapped to a set of non-interacting fermionic *quasiparticles*

$$\hat{H} = E_0 + \sum_k \epsilon_k\,\hat{\gamma}_k^\dagger\hat{\gamma}_k\ ,$$

where E_0 is the ground state energy, $\hat{\gamma}_k/\hat{\gamma}_k^\dagger$ are the Bogoliubov quasiparticles at momentum $k = 2\pi n/L$ with $n = 0, 1, L-1$ and quasienergy $\epsilon_k = 2\sqrt{J^2+h^2-2hJ\cos k}$. The operators $\hat{\gamma}_k$ satisfy the canonical commutation relations and the number of excitations $\hat{n}_k = \hat{\gamma}_k^\dagger\hat{\gamma}_k$ is a constant of motion. While Fourier modes are individually nonlocal, it can be shown that suitable linear combinations of such modes yields a set of local conserved quantities, see, e.g. Ref.[48]. Beyond free quasiparticles systems, there is a class of *interacting integrable* one-dimensional quantum systems, which can be treated via analytical (Bethe-ansatz solution) and algebraic (Yang-Baxter theory) descriptions [70]. Integrable systems relax to the generalized Gibbs ensemble of Eq.(1.17), which retains the memory of the initial condition $|\psi_0\rangle$ via the conserved quantities. For an illustration see Figure 1.1 (b). This approach to equilibrium is dubbed *generalized thermalization*, as it can still be described in the same way as outlined in Section 1.1.1. Moreover, it still represents a dramatic erasure of local information, in fact, despite the extensive number of conservation laws, the complexity of the full Hilbert space is exponential in the number of degrees of freedom. Thermalization and generalized thermalization are believed to be generical "fast", i.e., to take place over a time scale given by the inverse of the typical energy scale of the system.

Another paradigmatic example of the failure of thermalization is given by strongly disordered interacting systems, via the so-called *many-body localization* (MBL) [71]. In the case of non-interacting particles, the presence of a disordered potential changes the nature of the single-particle wave function, which becomes localized in space, giving rise to an insulating phase known as Anderson localization [72]. Yet, this phenomenon survives in the presence of short-range interactions resulting, at large disorder, in the many-body localized phase. This is characterized by localized energy eigenstates at finite energy densities, hence at finite temperature. Theoretically, MBL systems can be explained by the emergence of an extensive set of quasi-local

integrals of motion $\hat{\tau}_i^z$, which provide an intuitive explanation of the breakdown of thermalization [73]. The quasi-local operators $\hat{\tau}_i^{x,y,z} = \hat{U}\,\hat{\sigma}_i^{x,y,z}\,\hat{U}^\dagger$ are single-site Pauli operators dressed by the quasi-local transformation $\hat{U}$. All the MBL phenomenology and dynamics can be understood assuming that the generic Hamiltonian has the following general form [74]

$$\begin{aligned} \hat{H}_{\mathrm{MBL}} &= \sum_i \tilde{h}_i \hat{\tau}_i^z + \sum_{ij} \tilde{J}_{ij}\,\hat{\tau}_i^z\,\hat{\tau}_j^z + \sum_{ijk} \tilde{J}_{ijk}\,\hat{\tau}_i^z\,\hat{\tau}_j^z\,\hat{\tau}_k^z + \dots \\ &\text{with} \quad \tilde{J}_{ij} \propto J_0 e^{-|i-j|/\tilde{\xi}}\,, \quad \tilde{J}_{ijk} \propto J_0 e^{-|i-k|/\tilde{\xi}}\,, \quad \dots \end{aligned} \tag{1.19}$$

where J_0 is proportional to the interactions strength and $\tilde{\xi}$ defines an interactions length scale. By construction $\hat{H}_{\mathrm{MBL}}$ conserves the local integrals of motions, i.e. $[\hat{H}_{\mathrm{MBL}}, \hat{\tau}_i^z] = 0$. The emergent integrability strongly constrains the system dynamics leading to characteristic dynamical properties, such as the equilibration to highly non-thermal values (determined by the initial conditions) or the logarithmic growth of entanglement entropy in time. The latter will be the subject of Section 1.3.3.
Notice that besides phenomenological approaches and effective renormalization group studies [75, 76], numerical techniques remain the main tools to access the MBL properties, mostly exact diagonalization [77–79]. This approach is restricted to small system sizes, making difficult to predict the thermodynamic limit behavior. In this sense, there remain several controversies. For example, the transition between the thermal phase (at small disorder strength) to the localized one (at large disorder) is still the focus of great debate. Likewise, the possible persistence of MBL in the presence of long-range interactions or in dimension greater than one is still largely discussed.
Notably, these localization phenomena — both Anderson and MBL — have been explored experimentally over several synthetic quantum systems, over which different signatures of many-body localization have been observed [80–82].

These two examples (integrability and MBL) have been considered for a long-time to be the primary sources of ergodicity breaking in quantum systems. Much less was known about the possibility of more subtle intermediate behaviors. Nowadays, growing attention is given to other interesting mechanisms that yield a different phenomenology. Relevant examples include confinement [83, 84], constraint dynamics [85, 86], Hilbert-space fragmentation [87], prethermalization, the so-called quantum scars, and many others.

Let us briefly describe, for example, *prethermalization*. This involves a first relaxation to some athermal state (that could be a GGE), followed at very long-times by a thermalization to the expected Gibbs value. Such a scenario is induced by the presence of two competing energy scales and it occurs in weakly perturbed Hamiltonians of the form

$$\hat{H} = \hat{H}_0 + \epsilon \hat{V}\,, \tag{1.20}$$

where $\hat{H}_0$ is the integrable Hamiltonian (with extensive conservation laws), $\hat{V}$ is the integrability breaking term, and $\epsilon \gg 1$ is the strength of the perturbation. The quenched time-evolution of a different ground state will feel the effect of the perturbation $\hat{V}$ only over a parametrically long time scale in $1/\epsilon$. This may be much

larger than the generalized thermalization time of that initial state and producing this "two-steps" relaxation. This phenomenon has been studied with methods of field and quantum many-body theory [88–92], but it is not fully understood to present date [93, 94]. It can be represented pictorially in the space of the reduced density matrices as a shift of the Lagrange multipliers toward the thermal state, see Figure1.1 (b) .

More recently, a similar phenomenology has been found in non-integrable Hamiltonians without a small parameter, yet characterized (for certain initial states) by slow non-thermal dynamics. This phenomenon, discovered experimentally in a platform of Rydberg atoms [59], has been linked to the existence of an extensive number of athermal eigenstates [60], dubbed *many-body quantum scars*[5]. These states occur at finite energy density, are usually equidistant in energy, and are characterized by a small entanglement entropy as opposed to the thermal case (this will be described more in detail in Section 1.3). Surprisingly enough, these towers of states can be written exactly in different non-integrable spin chains [61–64], without any explicit relation induced by trivial or non-trivial symmetries. Unifying these results, the authors of Ref.[65] have illustrated the general mechanism to embed subspaces of equally spaced athermal eigenstates in otherwise non-integrable Hamiltonians. See also Ref.[97].

These special eigenstates are found to have a surprisingly high overlap with "easy" initial states[6], hence resulting in slow dynamics. In particular, systems with an exact tower of states yield perfect revivals of time-dependent observables or fidelity. Conversely, in more complicated systems, the slow fluctuations are only a transient effect, and observables are supposed to thermalize at infinite times, see e.g. Refs.[60].

1.2 Entanglement and scrambling

Entanglement as "*the* characteristic trait of quantum mechanics" is arguably one of the most puzzling properties of composite quantum systems, "the one that enforces its entire departure from classical lines of thought" [98]. Nevertheless, for about 40 years its physical relevance remained elusive until the groundbreaking experiments of Aspect and collaborators in 1981 [99]. They demonstrated experimentally the violation of the Bell inequalities [100], hence the quantumness of our physical world.

Since then, a new and exciting branch of quantum theory started rapidly developing with a highly interdisciplinary character. Key concepts such as superposition and entanglement, initially explored mostly within quantum information and quantum optics [101], are now intensively studied over several fields and they are believed to be at the heart of the new revolutionary technologies of quantum computation. More recently, the interest in entanglement properties of many-particle systems has spread to several theoretical research communities, ranging from statistical physics

[5]The name has been given in analogy to the quantum scars studied in single-particle billiards. Anyhow, while the latter is related to the existence of unstable semiclassical trajectories, the former is rather related to regular motion [95, 96]

[6]For example, product states or known exact ground states. This is the case of the Rydberg experiment, where the slow oscillations were observed when initializing the state in a charge-density-wave [59].

[102] and condensed matter theory [103] to quantum information [104, 105] and high-energy physics [106, 107].

In particular, a large body of information concerning complex quantum many-body systems can be extracted from the study of their entanglement properties [104, 108–110]. At present, there are many examples of this connection spanning a wide spectrum of phenomena, including the characterization of in and out-of-equilibrium properties of quantum statistical mechanics and condensed matter systems. Section 1.3 will be devoted to a discussion of the main results for the entanglement growth in out-of-equilibrium systems.

As already discussed in Section 1.1.1, an insightful example of this cross-fertilization is represented by the non-local growth of quantum correlations in a quench protocol. While the global evolution is unitary and the total information is conserved, in thermalizing systems initially localized information spreads in time becoming completely non-local. The concept of information spreading goes now under the name of *scrambling* and it is currently the focus of great attention.

In this section, we will first provide the definitions for the bipartite and multipartite entanglement quantifiers studied throughout the thesis. Secondly, we will introduce the echo and the square-commutator used in the characterization of scrambling. We will conclude by briefly discussing the difference between entanglement and operator scrambling.

1.2.1 Entanglement entropy

We wish to define the bipartite entanglement of a pure quantum state $|\psi\rangle \in \mathcal{H}$, belonging to the Hilbert space $\mathcal{H}$. In the case of an extended quantum many-body system of N constituents, $\mathcal{H} = \bigotimes_{i=1}^{N} \mathcal{H}_i$ is the tensor product of the N local Hilbert spaces $\mathcal{H}_i$ associated with local degrees of freedom. Consider a bipartition between two complementary regions A and B, which can be, for example, a finite region in space and its complement, see, i.e. Figure 1.2 (a). Hence, the global Hilbert space can be written as a tensor product of the two subsystems $\mathcal{H} = \mathcal{H}_A \otimes \mathcal{H}_B$. The bipartition between A and B identifies the *Schmidt decomposition*

$$|\psi_{AB}\rangle = \sum_{i=1}^{m} \sqrt{\lambda_i} |i_A\rangle \otimes |i_B\rangle \ , \tag{1.21}$$

where $\{|i_A\rangle\}$ e $\{|i_B\rangle\}$ are orthonormal basis respectively belonging to $\mathcal{H}_A$ e $\mathcal{H}_B$, and $m \leq \min\{\dim \mathcal{H}_A, \dim \mathcal{H}_B\}$ are real positive numbers λ_i, with $0 < \lambda_i \leq 1$. This decomposition is unique if the eigenvalues are non-degenerate. The coefficients λ_i define the *bipartite entanglement spectrum* and are also called *Schmidt coefficients*. From the normalization condition, they have the following properties: $\lambda_i \geq 0$ and $\sum_{i=1}^{m} \lambda_i = 1$. The reduced states of the systems A and B are defined by the partial traces

$$\hat{\rho}_A = \mathrm{Tr}_B \, |\psi\rangle\langle\psi| \ , \qquad \hat{\rho}_B = \mathrm{Tr}_A \, |\psi\rangle\langle\psi| \ . \tag{1.22}$$

By virtue of Eq.(1.21), the *reduced density matrices* $\hat{\rho}_A$ and $\hat{\rho}_B$ have the same spectrum and the particular basis coincide with the eigenbasis of the corresponding reduced density operators $\hat{\rho}_{B/A} = \sum_i \lambda_i |i_{B/A}\rangle\langle i_{B/A}|$. The number of non-zero eigenvalues

λ_i coincides with the rank of both the matrix that represents the reduced density operators.

The state $|\psi\rangle$ is separable concerning the bipartition (A, B) if and only if there is only one non-zero Schmidt coefficient. Entanglement is defined as the absence of this separability. Therefore, it is connected to the distribution of the entanglement spectrum. The amount of bipartite entanglement can be quantified by the *Renyi entropies*

$$S_A^\alpha = -\frac{1}{1-\alpha} \ln \mathrm{Tr}\, \hat{\rho}_A^\alpha \,, \tag{1.23}$$

parameterized by $\alpha > 1$. The *entanglement entropy* is defined as the von Neumann entropy of the reduced density matrix of a subsystem

$$S_A = -\mathrm{Tr}\big(\hat{\rho}_A \ln \hat{\rho}_A\big) \tag{1.24}$$

and it is obtained as the limit for $\alpha \to 1$ of the Renyi entropies (1.23). Notice that $S_A = S_B$, since $\hat{\rho}_A$ and $\hat{\rho}_B$ share the same spectrum, hence S_A is a property of the only bipartition. The entanglement entropy vanishes on separable states and it possesses several mathematic properties such as convexity, continuity, monotonicity under local operations and classical communication, etc.. As such, it constitutes a *measure of entanglement* according to the axioms of quantum information theory (see, e.g., Ref.[111]).

In spatially extended systems with interactions depending on the distance between particles, it is natural to consider bipartitions where subsystem A is constituted by degrees of freedom within a connected region of space, and B its complement. In particular, for one dimensional systems of L sites, A is usually an interval of length ℓ of neighboring degrees of freedom, while B is the complement of length $L - \ell$. See Figure 1.2 (a). On the other hand, in fully-connected N-particle systems, such as the ones analyzed in this thesis, the permutational symmetry makes spatial bipartitions meaningless. Hence, we will consider bipartitions specified by the number $N_A = f_A\, N$ of particles in subsystem A (with $N_B = N - N_A = f_B\, N$).

1.2.2 (Tripartite) mutual information

It is possible to analyze the structure of bipartite correlations also via the *quantum mutual information* between two subsystems A and B

$$I(A:B) = S_A + S_B - S_{AB} \,, \tag{1.25}$$

where S_A is the entanglement entropy of a subsystem A (1.24). This quantity vanishes on uncorrelated or separable states and reaches its maximum for entangled states. As such, it quantifies the amount of information one can access about the system B by measuring A and vice versa. Notice that $I(A:B)$, defined also for mixed states, takes into account classical correlations as well [7]. In this sense, it can be interpreted as the work necessary to erase the total correlations existing in a bipartite system [112]. In the case of pure states, for a bipartition between A and its

[7] Consider, for example, the mixed state $\hat{\rho} = (|0\rangle\langle 0|_A \otimes |0\rangle\langle 0|_B + |1\rangle\langle 1|_A \otimes |1\rangle\langle 1|_B$. This is unentangled but classically correlated. A simple calculation yields $S_A = S_B = S_{AB} = \ln 2$ resulting in $I(A:B) = \ln 2$.

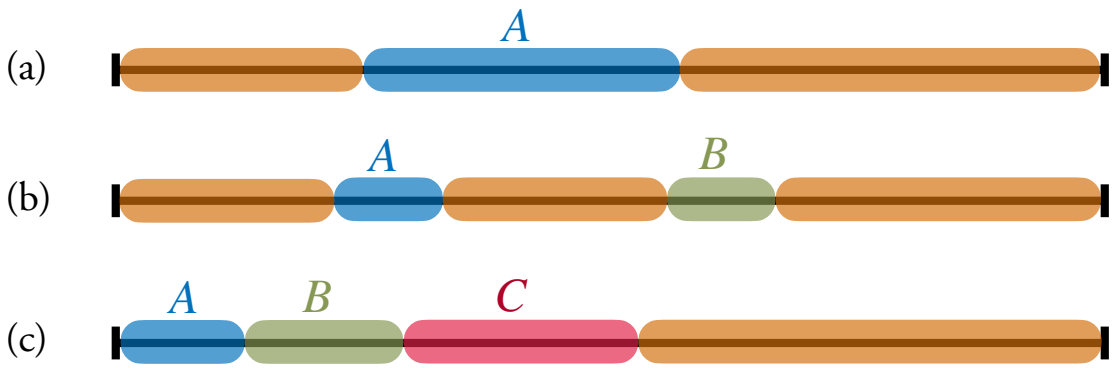

Figure 1.2: Pictorial representation the possible partitions in space in one dimensional systems. (a) Bipartition in reference to the Renyi and entanglement entropies (1.23)-(1.24). The full region is bipartite between an interval A and the complement B. (b) Tripartition in reference to the mutual information (1.25). The full space contains two disjoint intervals A and B separated by a region C. (c) Four-partition in reference to the tripartite mutual information (1.26).

complement (see Figure 1.2 (a)) the mutual information coincides with twice the entanglement entropy, since $S_{AB} = 0$. So, typically, one studies the mutual information between two distant intervals A and B as in Figure 1.2 (b). This kind of tripartition has been considered to study entanglement spreading in integrable systems, see i.e. Refs.[113, 114]. For mixed states or for partitions as in Figure 1.2 (b), another standard quantifier of entanglement is given by the *entanglement negativity*, see e.g. Ref.[115].

Let us now discuss the *tripartite mutual information* (TMI), as a complementary quantity that accounts for the delocalization of information. Consider a system of size N and divide it into four subsystems A, B, C, D as in Figure 1.2 (c). The information is spread over all the degrees of freedom of the system if one can not reconstruct A by local measures of B and C separately. Therefore, a natural measure of delocalization of information is the TMI defined as

$$I_3(A:B:C) = I(A:B) + I(A:C) - I(A:BC)\ , \tag{1.26}$$

where $I(A:B)$ is the mutual informations in Eq.(1.25) [8]. From its definition (1.26), we can appreciate that $-I_3(A:B:C)$ quantifies the amount of information on the region A that can be recovered by global measurements in $B \cup C$, but can not be obtained by probing B and C individually. Thus, if $-I_3(A:B:C)$ is large the information localized in a subsystem A of the state can be recovered only by global measurements, signalling efficient scrambling of quantum information. Note that

[8] The TMI (1.26) is defined in terms of mutual informations, anyhow it can be then rewritten as a combination of entropies

$$I_3(A:B:C) = S_A + S_B + S_C + S_{ABC} - S_{AB} - S_{AC} - S_{BC}\ . \tag{1.27}$$

In this way, the knowledge about the different entanglement entropies gives access to I_3. Notice, however, that in this expression appears also S_{AC}, i.e. the entanglement entropy between disjoint intervals. The latter is usually more difficult to access, both numerically and analytically.

the negativity of I_3 signals the super-extensivity of the mutual information.

The choice of the partition depends on the physical system under analysis and the same considerations of the end of Section 1.2.1 hold.
Usually, I_3 is associated with the delocalization of quantum information in the context of unitary quantum channels [116–118]. In this thesis, more appropriately, we study the delocalization of the initial state information under the dynamics, which is a complementary measure of entanglement.

1.2.3 Quantum Fisher information

A different approach is to characterize the system via the multipartite entanglement properties of the quantum state, as given by the quantum Fisher information (QFI) $\mathcal{F}(\hat{O}, \hat{\rho})$ [119–122]. This quantity was introduced in metrology for phase-estimation purposes and it plays a central role in quantum information theory [122–126] together with spin squeezing [127–130]. More recently, it has attracted a lot of interest also in condensed matter and quantum statistical physics, mostly because of its connection to thermal susceptibilities and its experimental accessibility [131–133].

The QFI is defined operationally in quantum metrology, in a very different setting to respect to the typical condensed matter approach to the study of many-body entanglement. Hence, we will first recall the operational definition and later describe its properties as a multipartite entanglement witness.

Operational definition

When estimating an unknown parameter ϕ in a quantum system, one prepares a probe state $\hat{\rho}$ and let it interact with the system. This occurs through the generic transformation $\hat{\mathcal{T}}(\phi)$ which depends on the real parameter ϕ. The parameter is then inferred by measuring the probe state after it has interacted $\hat{\mathcal{T}}(\phi) : \hat{\rho} \to \hat{\rho}_\phi$. The measurement can be performed by choosing some observables $\hat{E}_\mu$ with eigenvalues μ [9]. The conditional probability of finding the outcome μ for a given value of ϕ is given by the likelihood $P(\mu|\phi) = \mathrm{Tr}\left(\hat{E}_\mu\, \hat{\rho}_\phi\right)$. The measurements are then repeated M times, obtaining $\vec{\mu} = (\mu_1, \mu_2, \dots \mu_M)$. From each of them, one obtains for an estimator $\phi_{\text{est}}(\vec{\mu})$, with average $\langle \phi_{\text{est}} \rangle$ and variance $(\Delta\phi_{\text{est}})^2 = \langle \phi^2_{\text{est}} \rangle - \langle \phi_{\text{est}} \rangle^2$, evaluated of all possible sets of measurements. If we consider unbiased measurement $\langle \phi_{\text{est}} \rangle = \phi$, by evaluating the variance from the measurements conditioned probability it can be shown that [134]

$$\Delta\phi_{\text{est}} \geq \frac{1}{\sqrt{M F(\hat{\rho}_\phi)}}\,, \tag{1.28}$$

[9] More rigorously, the results are given by *generalized quantum measurements*, described by a set of positive observables $\hat{E}(\mu)$ parametrized by μ, the "positive operator-valued measurements". These have the only constraint that $\sum_\mu \hat{E}_\mu = \mathbb{1}$. For details see [101], Section 2.2.6.

where M is the number of measurements and $F(\rho,\phi)$ is the (classical) Fisher information, defined as

$$F(\hat{\rho}_\phi) = \sum_\mu \frac{1}{P(\mu|\phi)} \left(\frac{\partial P(\mu|\phi)}{\partial \phi}\right)^2 . \tag{1.29}$$

Eq.(1.28) is also known as the classical Cramer-Rao bound, in which F encodes the amount of information about the parameter ϕ contained in the measurements $\vec{\mu}$, see e.g. Ref.[134]. Notice that F in Eq.(1.29) not only depends on the initial state $\hat{\rho}$ and on the phase ϕ via the transformation $\hat{\mathcal{T}}$, but also on the observables $\hat{E}_\mu$.

Physically, the Fisher information is related to the degree of *statistical distinguishability* between the states $\hat{\rho}$ and $\hat{\rho}_\phi$, whenever ϕ is small. To appreciate it, let us consider the distance between the probabilities $P(\mu|0)$ and $P(\mu|\phi)$ of measuring μ via $\hat{\rho}$ and $\hat{\rho}_\phi$ respectively. This can be quantified, for instance, by the Hellinger distance $d^2_{\rm H}(P_0,P_\phi) = 1 - \sum_\mu \sqrt{P(\mu|0)P(\mu|\phi)}$. This distance is non-negative and its Taylor expansion reads

$$d^2_{\rm H}(P_0,P_\phi) = \frac{1}{8} F(\hat{\rho}_\phi)\,\phi^2 + O(\phi^3) . \tag{1.30}$$

Therefore the Fisher information $F(\hat{\rho}_\phi) = 8(\partial d_{\rm H}/\partial\phi)^2$ can be understood as the square of the statistical speed of variation of the distribution probability when tuning the parameter ϕ [122]. This interpretation allows also to extract the QFI from experimental data [131].

The *quantum Fisher information* is then derived from Eq.(1.29), by maximizing over all the possible measurements

$$F(\hat{\rho}_\phi) \leq \max_{\hat{E}} F(\hat{\rho}_\phi) \equiv \mathcal{F}(\hat{\rho}_\phi) . \tag{1.31}$$

This modifies the bound in Eq.(1.28) into the *quantum Cramer-Rao bound*

$$\Delta\phi_{\rm est} \geq \frac{1}{\sqrt{M\mathcal{F}(\hat{\rho}_\phi)}} . \tag{1.32}$$

Let us now restrict to *unitary transformations*

$$\hat{\mathcal{T}}(\phi) = e^{-i\phi\hat{O}} \tag{1.33}$$

generated by the observable $\hat{O}$. This is the standard operation for interferometric measurements [135]. In this case, the QFI can also be related to a state distance in the Hilbert space, namely the *Bures distance* [136] and operationally interpreted as the maximal degree of distinguishability of the two states $\hat{\rho}$ and $\hat{\rho}_\phi$. It was shown by Braunstein and Caves [123] that the QFI can be written explicitly in terms of the spectral decomposition of the initial quantum state $\hat{\rho} = \sum_n p_n |n\rangle\langle n|$ as

$$\mathcal{F}(\hat{O},\hat{\rho}) = 2\sum_{n,m} \frac{(p_n - p_m)^2}{p_n + p_m} |\langle n|\hat{O}|m\rangle|^2 \leq 4\,\langle \Delta\hat{O}^2\rangle , \tag{1.34}$$

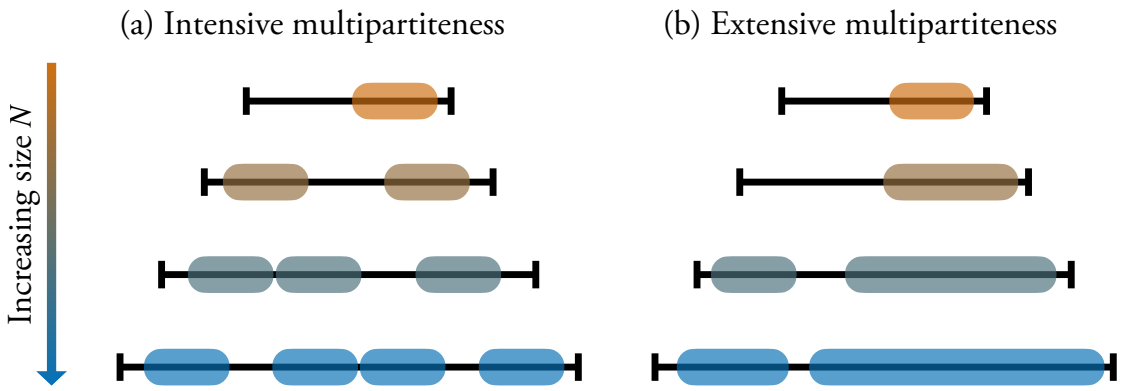

Figure 1.3: Pictorial representation of the different scenarios for the scaling of quantum Fisher information density f_Q (1.37) as the total number of parties N increases. (a) In the case of intensive multipartiteness $f_Q = O(1)$, the entanglement depth is finite even in an infinite system. (b) For the extensive multipartite entanglement, the size of the biggest entangled block scales with the system size $f_Q = O(N)$ and the state is genuinely multipartite.

with $\langle \Delta \hat{O}^2 \rangle = \mathrm{Tr}(\hat{\rho}\,\hat{O}^2) - \mathrm{Tr}(\hat{\rho}\,\hat{O})^2$. Notice that now the QFI (1.31) does not depend on the phase ϕ, but only on the initial state and the generator of the transformation. The equality in Eq.(1.34) holds for pure states $\hat{\rho} = |\psi\rangle\langle\psi|$, namely

$$\mathcal{F}(\hat{O}, |\psi\rangle) = 4\langle \Delta \hat{O}^2 \rangle = 4 \left(\langle \hat{O}^2 \rangle - \langle \hat{O} \rangle^2 \right) . \tag{1.35}$$

Throughout the thesis, we will take Eq.(1.34) as the definition of the quantum Fisher information.

Connection to multipartite entanglement

The QFI has key mathematical properties [120, 122–124], such as convexity, additivity, monotonicity that can be used to probe the multipartite entanglement structure of a quantum state [125, 126]. Several relations have been established between the QFI and the criteria for recognizing multipartite entanglement [126, 137].

The first connection was discussed in the context of interferometry, when focusing on ensemble of N qubits with the generator of the transformation in (1.33) consisting in a linear collective spin operator $\hat{O}_{lin} = \hat{J}_{\mathbf{n}}$ in some direction $\mathbf{n}$. It was shown that QFI satisfies two different bounds depending if the state is separable or entangled, see e.g. Refs.[138, 139]. Namely,

$$\text{separable states :} \qquad \mathcal{F}(\hat{O}_{lin}, \hat{\rho}_{sep}) \leq N \, , \tag{1.36a}$$

$$\text{entangled states :} \qquad \mathcal{F}(\hat{O}_{lin}, \hat{\rho}_{ent}) \leq N^2 \, . \tag{1.36b}$$

These relations immediately demonstrate another fundamental aspect identified by the QFI: the *usefulness of entanglement* for metrological purposes. While for separable states the phase uncertainty is limited by $\Delta\phi \geq 1/\sqrt{MN}$ — the so-called shot noise limit —, entangled states allow to reach a fundamental metrological bound: the Heisenberg limit $\Delta\phi \geq 1/\sqrt{M}N$.

Let us now present a practical yet general criterion linking the QFI to the multipartite entanglement structure of a state $\hat{\rho}$ [126, 137]. Consider a quantum system composed of N distinguishable parties and living on a finite-dimensional Hilbert space ($\mathcal{H} = \bigotimes_{i=1}^{N} \mathcal{H}_i$ with $\mathcal{H}_i$ the local Hilbert space that we assume to be the same for all the parties). If, for a certain $\hat{O}$, the QFI density of the state $\hat{\rho}$ satisfies the inequality

$$f_Q(\hat{O}) = \frac{\mathcal{F}(\hat{O}, \hat{\rho})}{N} > m \ , \tag{1.37}$$

then, at least $(m+1)$ parties in the system are entangled (with $1 \leq m \leq N-1$ a divisor of N). In particular, if $N - 1 \leq f_Q(\hat{O}) \leq N$, then the state is called *genuinely N-partite entangled*. See Figure 1.3 for a pictorial illustration of the different scenarios. For example, in the case of N qubits, the Greenberger-Horne-Zeilinger (GHZ) [161] or "Schrödinger cat" state $|GHZ\rangle = (|0\rangle^{\otimes N} + |1\rangle^{\otimes N})/\sqrt{2}$ saturates the bound in Eq.(1.37) $f_Q(\hat{J}_z) = N$ to respect to the collective magnetization in the z direction $\hat{O} = \hat{J}_z$.

The other rigorous criteria — based on the notion of k-particle entanglement [140] — are derived for local operators in Refs. [125, 126] or quasi-local operators in Ref.[141]. This choice, for instance, allows to characterize the multipartite entangled structure of topological phases [142]. In fact, generally different operators $\hat{O}$ lead to different bounds and there is no systematic method (without some knowledge on the physical system [132, 143]) to choose the optimal one. The QFI is only a *witness* and not an entanglement measure, since it does not fulfill all the axiomatic criteria of Ref.[111] [10].

We remark that the QFI answers to a complementary question to respect to the bipartite entanglement entropy. On one side S_A quantifies the amount of quantum correlations given a bipartition A/B, conversely, f_Q identifies the size of the largest entangled block, see Figure 1.3. If a state is genuinely multipartite than it is also bipartite entangled to respect all the bipartitions.

Multipartite entanglement in spin systems

In the case of spin systems, a standard choice is to consider collective spin projections $\hat{O} = \hat{S}_{\mathbf{n}} = \sum_{i=1}^{N} \mathbf{n} \cdot \hat{\mathbf{s}}_i$ in the direction of the $3d$ unit vector $\mathbf{n}$[11]. The optimal QFI is then given by the maximal fluctuation of the total spin as

$$f_Q(t) = 4 \max_{\mathbf{n}} \frac{\langle \Delta \hat{S}^2_{\mathbf{n}}(t) \rangle}{N} \ . \tag{1.38}$$

A related experimentally relevant indicator of multipartite entanglement in spin systems is given by *spin squeezing*, a concept first introduced in Ref.[145]. This

[10] In particular, it does not "vanish on separable states". The $f_Q(\hat{O})$ is only a lower bound on the amount of entanglement in the state $\hat{\rho}$. As such, it can result in $f_Q \simeq 1$ also for entangled states. For instance, the same $|GHZ\rangle$, which is genuinely multipartite to respect to $\hat{J}_z$ (see main text), leads to $f_Q(\hat{J}_x) = f_Q(\hat{J}_y) = 1$ for the collective operators in the transverse directions.

[11] In the case a composite system of multiple degrees of freedom, one typically considers $\hat{O} = \mathbb{1}_{\overline{S}} \otimes \hat{S}_{\mathbf{n}}$, where $\overline{S}$ is the complement of the spin subsystem. Note that in this case, the QFI detects not only the correlations between the individual spins, but also the entanglement between the collective spin and the other degrees of freedom (see e.g., Ref.[144])

observable is associated with the reduction of collective spin quantum fluctuations along one direction at the expense of enhancement of orthogonal fluctuations, due to the Heisenberg principle. Spin squeezing is usually quantified by the minimal transverse variance of collective spin fluctuations [127–130] as

$$\xi^2 \equiv \min_{|\mathbf{u}|=1,\mathbf{u}\perp\mathbf{Z}} \frac{\left\langle \left(\mathbf{u}\cdot\hat{\mathbf{S}}\right)^2 \right\rangle}{N/4}. \tag{1.39}$$

The squeezing parameter ξ^2 is equal to 1 for coherent states, and smaller for squeezed states (see, e.g., Refs. [130, 145]). It has long been known [129, 139, 146] that collective spin squeezing is a witness of many-body quantum entanglement. It is possible to demonstrate that [139]

$$\xi^2 \geq \frac{1}{f_Q}\,, \tag{1.40}$$

namely there exists a class of states which are not spin-squeezed but can be maximally entangled. In this thesis, we will show that a simple relation exists between the QFI and spin squeezing in the semiclassical regime.

1.2.4 OTOC's: the echo and the square-commutator

Very recently, the notion of scrambling — as the study of quantum information spreading — has become an increasingly growing focus of the scientific interest. This has been mostly motivated by Kitaev in 2015 [147]. He proposed to quantify chaos in many-body systems in terms of the growth in time of the square of the non-equal time commutator of two initially commuting observables $\hat{A}$ and $\hat{B}$, i.e.

$$c(t) = -\langle [\hat{B}(t), \hat{A}]^2 \rangle\,, \tag{1.41}$$

or of the closely connected out of time order correlators (OTOC) $\langle \hat{A}\hat{B}(t)\hat{A}\hat{B}(t)\rangle$. These objects are characterized by an unusual time-ordering which does not assume any casual time-evolution [12]. Correspondently, they can not be computed via standard theoretical techniques. The study of scrambling has spread rapidly over different communities: from quantum information [116, 149], to high energy physics [150, 151], from quantum-thermodynamics [152, 153] to condensed matter theory [148, 154–156]. These concepts have also been explored experimentally over various atomic platforms [157–159]. In general, the growth of the square commutator indicates the non-commutativity of two observables induced by the dynamics, the so-called *operator spreading*. For example, in the case of locally interacting systems, it describes the non-local growth in time of the support of an initially local operator, as discussed below.

At the same time, such considerations contributed to reviving the topic of *quantum chaos and irreversibility* [116, 147, 150, 160–163]. As elaborated above, these concepts have been of pivotal importance since the foundations of statistical mechanics [164–166] and have been intensively addressed during the '90s and early

[12] More precisely, OTOC are defined as multi-point and multi-time correlation functions (more or equal than three body) which cannot be represented on a single Keldysh contour [148].

2000 [167–171]. One of the first and most widely used ways to characterize quantum chaotic dynamics is the study of imperfect time-reversal evolution of the wave function $|\psi_0\rangle$, in particular, the *Loschmidt echo*. Conceived by Peres in Ref.[167], this concept has been introduced systematically by the group of Levstein, Jalabert, Patawski, and collaborators in a series of papers during the 2000 see e.g. Ref.[170, 171]. The Loschmidt echo is defined as the overlap between two states evolving under the action of two slightly perturbed Hamiltonians, i.e.

$$\mathcal{L}(t) = \langle\psi_0|e^{i(\hat{H}+\epsilon\hat{B})t/\hbar}\, e^{-i\hat{H}t/\hbar}|\psi_0\rangle \ , \tag{1.42}$$

where $\hat{H}$ is the bare Hamiltonian, $\hat{B}$ represents the perturbation, and ϵ its strength. Under classical chaotic dynamics, as a result of the exponential sensitivity of trajectories to small perturbations, any imperfection in a time-reversed protocol hinders a full recovery of the initial information, making time-reversal impossible in practice. This approach has been explored successfully in few-body quantum systems [170–173] and scrutinized in many-body ones [174–176]. For instance, whenever a semi-classical limit is well defined, $\mathcal{L}(t)$ display a dynamical regime characterized by an exponential decay in time, with a rate that (in certain limits) coincides with the classical Lyapunov exponents [168], see also the reviews [170, 171].

As the concept of scrambling was introduced resonating with these ideas, in what follows we will define the square-commutator and OTOC via an imperfect-time reversal protocol on operators. Let us mention that the square commutator encodes information beyond the one contained in the Loschmidt echo. It represents a phenomenon occurring in the *operator space*, while the Loschmidt echo is a characterization of the wave-function. The difference between the operator spreading and entanglement dynamics is briefly discussed at the end of this section.

Let us start with the definition of an interesting protocol: an imperfect time-reversal of an observable, in a spirit similar to Loschmidt echo experiments and to nuclear magnetic resonance (NMR) magic echoes (see Refs. [177–180] and [181–183]). In this setting, the system is prepared in the eigenstate of some observable $\hat{A}$, such as a polarized state of the magnetization, and it is then allowed to evolve under the action of the Hamiltonian $-\hat{H}$ for a certain time t. It is then subject to a rapid rotation generated by the unitary operator $e^{i\epsilon\hat{B}}$ and it then evolves back under the reversed Hamiltonian $+\hat{H}$ for an identical time interval t. Afterward, the observable $\hat{A}$ is measured. The corresponding time-evolved operator $\hat{A}$ reads

$$\begin{aligned}\hat{A}_\epsilon(t) &= e^{i\hat{H}t/\hbar}e^{-i\epsilon\hat{B}}e^{-i\hat{H}t/\hbar}\,\hat{A}\,e^{i\hat{H}t/\hbar}e^{i\epsilon\hat{B}}e^{-i\hat{H}t/\hbar} = e^{-i\epsilon\hat{B}(t)}\,\hat{A}\,e^{i\epsilon\hat{B}(t)} \\ &= \hat{A} - i\epsilon\,[\hat{B}(t),\hat{A}] - \frac{\epsilon^2}{2}\,[\hat{B}(t),[\hat{B}(t),\hat{A}]] + \mathcal{O}(\epsilon^3)\ ,\end{aligned} \tag{1.43}$$

where $\hat{B}(t) = e^{i\hat{H}t/\hbar}\hat{B}\,e^{-i\hat{H}t/\hbar}$ is the perturbing operator in the Heisenberg representation.

The difference $\hat{A}_\epsilon(t) - \hat{A}$ is associated to the echo response of the observable $\hat{A}$. One can study its full distribution by taking the expectation value on a generic quantum state $\hat{\rho}$, which could be either pure or mixed. The first and second moments

read

$$\mu(t) = \lim_{\epsilon\to 0} \frac{1}{\epsilon^2} \langle \hat{A}_\epsilon(t) - \hat{A}\rangle = -\frac{1}{2} \langle [\hat{B}(t), [\hat{B}(t), \hat{A}]]\rangle \ , \tag{1.44}$$

$$c(t) = \lim_{\epsilon\to 0} \frac{1}{\epsilon^2} \langle \Big(\hat{A}_\epsilon(t) - \hat{A}\Big)^2 \rangle = - \langle [\hat{B}(t), \hat{A}]^2\rangle \ . \tag{1.45}$$

where $\langle \dots \rangle = \mathrm{Tr}\,(\hat{\rho}\dots)$ stands for the average with respect to the initial state, which can also be pure.

The first moment $\mu(t)$ is the so-called *echo-response observable* which has been studied in Refs.[181, 183]. In principle, in $\hat{A}_\epsilon(t) - \hat{A}$ there is a further term proportional to ϵ, i.e. $-i\epsilon\langle[\hat{B}(t), \hat{A}]\rangle$. It corresponds to a standard Kubo-type linear response susceptibility, which does not contain information about unusual time-ordering and therefore it should be subtracted from the echo. Furthermore, if the initial state $\hat{\rho} = |\psi_0\rangle\langle\psi_0|$ is an eigenstate of $\hat{A}$, then $\langle[\hat{B}(t), \hat{A}]\rangle$ vanishes and the result is simply (1.44). The function $\mu(t)$ contains the out-of-time correlators as, in particular, it contains $\langle\hat{B}(t)\hat{A}\hat{B}(t)\rangle$.

The second moment in Eq.(1.45) is the *square commutator* (1.41) [160–162, 184–186]. This object was originally introduced in 1969 by Larkin and Ovchinnikov in Ref.[160] to describe semiclassically the exponential sensitivity to initial conditions and the associated Lyapunov exponent. In fact, in the classical limit, $c(t)$ encodes the square of the derivatives of the classical trajectory to respect to the initial conditions [161]. Thus, whenever the classical limit is chaotic, $c(t)$ is expected to grow exponentially in time, with a rate set by twice the classical Lyapunov exponent [162, 183–187, 187–190, 190–192]. It is conjectured that this Lyapunov exponent is bounded by quantum effects as $\lambda \leq 2\pi T/\hbar$ [151], and that this bound is saturated in certain large-N strongly interacting models with a classical gravity dual, such as the Sachdev-Ye-Kitaev (SYK) model [147, 193]. Anyhow, the square-commutator (or different OTOCs) does not necessarily exhibit an exponential growth away semiclassical or large-N limits, making the definition of the exponent ill-defined for generic nonintegrable Hamiltonians. In particular, in the case of local lattice systems, it has been proved that $c(t)$ grows at most polynomially in time [194].

Notice that $c(t)$ is generally different from $\mu(t)$, as it contains a different OTOC, namely $\langle\hat{B}(t)\hat{A}^2\hat{B}(t)\rangle$. Anyhow, in the semiclassical limit, both expressions have a similar structure containing the square of the derivatives of trajectories with respect to the initial conditions, which grow exponentially in time in the presence of the semiclassical chaos (c.f. Refs. [172, 181, 183]). We derive this result formally in Appendix B, by computing the semiclassical limits of the echo observable and the square commutator using the Bopp representation of the operators [195].

Finally, OTOC can be seen as a further contribution of the quantum information community to the study of chaos and irreversibility in quantum systems.

Entanglement spreading vs operator scrambling

Let us briefly comment on the different meanings associated with "entanglement spreading" versus "operator scrambling". On the whole, these two concepts

characterize two different phenomena: While entanglement (and its dynamics) is a property of the many-body wave-function, operator scrambling concerns growth of complexity in the operator space upon time evolution. As a simple illustration of such a different behavior, consider a system initialized in an infinite temperature density matrix, i.e. the identity. During the unitary time-evolution, the state will remain unchanged — and unentangled —, whereas the support of an initially local operator will, in general, grow nontrivially in the Heisenberg representation. This could be witnessed, for instance, via the growth of square commutator in time (1.45).

Beyond its semiclassical limit, the operator scrambling is unquestionably a novel concept[13] and, correspondingly, it has attracted a lot of attention in the past five years. For example, rigorous studies of the operator spreading with the square commutator have been obtained in random unitary models of quantum dynamics [196, 197] and extended to increasingly realistic systems [198, 199]. Besides, several interesting approaches have been introduced to characterize the operator growth in physical Hamiltonians. For instance, operator complexity can be studied with the operator entanglement entropy of the time evolution operator [200–204] or closely related entanglement of unitary quantum channels [116–118]. In this context, the second Renyi entropy [cf. Eq.(1.23) with $\alpha = 2$] of the channel has been related to an average of OTOC over the complete basis of the operators, see e.g. Ref.[116]. Another insightful proposal is to measure the operator spreading via the operator complexity growth rate, obtained from Lanczos coefficients in the operator space [205].

Summarizing, entanglement dynamics and operator scrambling are generally two distinct phenomena occurring in out-of-equilibrium many-body systems. Operator scrambling displays a plethora of novel phenomena that still need to be understood in their generality. For the rest of the thesis, we will focus on a specific limit of scrambling: the classical one, which is slightly better understood. In this limit, however, we will be able to find an analytical relation between entanglement dynamics (bipartite and multipartite) and the square-commutator.

1.3 Entanglement in and out-of-equilibrium

As we will elaborate in this section, entanglement has become a fundamental tool in the classification of quantum phases of matter, as well as in the characterization of their transient and stationary dynamical regimes.

A very important aspect concerns the efficiency of novel numerical methods for many-body physics, such as techniques based on matrix product states (MPS) or density matrix renormalization group (DMRG) [206–209]. Such tools intrinsically rely on the scaling of bipartite entanglement. In fact, these algorithms approximate quantum many-body wave-functions with matrices of finite dimension D, that can efficiently simulate only low entangled states, whose entropy can be estimated as $S_{\max} \sim \ln D$. In the non-equilibrium setting, the same reasoning applies. By now,

[13] Notice that the operator growth occurs when the evolution is governed both by integrable and nonintegrable Hamiltonians. Thus, it goes even beyond the broad notion of "quantum chaos".

time-dependent generalizations of MPS algorithms, such as tDMRG [210, 211] or the time dependent variational principle (TDVP) [212, 213], are considered among the most successful techniques in addressing many-body dynamics. For example, in this thesis we employ TDVP simulations for the study long-range dynamics in Chapters 3 and 4. Summarizing, both in and out-of-equilibrium, the amount of entanglement of the state governs the effectiveness of MPS numerical methods, limiting our ability to simulate quantum systems on classical devices.

1.3.1 Entanglement of equilibrium states

Let us first recall some relevant results in equilibrium. For a general survey, we refer the readers to the abundant literature on the topic, see e.g. Refs.[104, 108–110]. It is now well known that entanglement plays a fundamental role in classifying phases of matter. The Von Neumann entanglement entropy S_A, for example, is tightly connected to the topological properties of many-body systems [110] and to the emergence of quantum phase transitions [104]. One of the most important results concerning the equilibrium properties of the S_A in many-body systems goes under the name of *area law*. In the ground state of gapped local hamiltonians, the entanglement entropy (1.24) is known to scale with the area of its boundary, i.e.

$$S_A \propto \ell^{d-1} , \tag{1.46}$$

where d is the dimension and ℓ denotes the typical length of the subsystem A. Even if a rigorous proof exists only in one dimension [214], there is a unanimous consensus for its validity in arbitrary d [109]. Eq.(1.46) has tremendous consequences for the numerical simulability of quantum states on classical computers. It underlies the great success of MPS and DMRG techniques in describing the properties of one-dimensional models. However, there exist well-known violations to area law in Eq.(1.46), as for the case of *logaritmic correction* for gapless systems, as critical one-dimensional models [215, 216]. Notably, the logarithmic correction turns out to be universal, as it is proportional to the central charge of the conformal field theories describing the low energy properties at criticality [217].

Multipartite entanglement as well possesses universal properties close to quantum phase transitions [132, 218]. In fact, the QFI (1.34) of a thermal equilibrium states $\hat{\rho}_{\text{Gibbs}} = e^{-\beta \hat{H}}/Z$ can be written explicitly as a function of the thermal susceptibility [132], via

$$\mathcal{F}(\hat{O}, \hat{\rho}_{\text{Gibbs}}) = \frac{2}{\pi} \int_{-\infty}^{\infty} d\omega \tanh(\beta\omega/2)\ \chi''_{\hat{O}}(\omega) . \tag{1.47}$$

Hence, the multipartite structure of the state inherits all the universal properties of $\chi''_{\hat{O}}(\omega)$. In particular, at quantum criticality, the QFI of the ground state $|\psi_0\rangle$, for the order parameter $\hat{O}_{\text{op}}$, obeys the universal scaling

$$\mathcal{F}(\hat{O}_{\text{op}}, |\psi_0\rangle) \sim N^{1+\Delta_Q/d} , \tag{1.48}$$

where Δ_Q is the critical exponent of the correlation function [14]. Notice, nonetheless,

[14] Via the hyperscaling relations it is related to the other critical exponents via $\Delta_Q = \gamma/\nu - z$, where γ , ν and z are susceptibility, correlation length and dynamical critical exponents respectively [219].

that the QFI does not witness extensive multipartiteness close to thermal phase-transitions [132, 220], even if it reproduces the landscape of its phase-diagram [220].

1.3.2 Entanglement entropy of chaotic eigenstates

As opposed to the low-energy states described before, the entanglement entropy of chaotic eigenstates $S_A(|E\rangle)$ obeys volume law, i.e. it scales with the volume of the subregion A. More importantly, $S_A(|E\rangle)$ is equal to the thermodynamic entropy $S(E)$ at the same energy, at the leading order in the system size [221–223]. Denoting by N_A and N the size of the region A and of the whole system, one has

$$\lim_{N\to\infty} \frac{S_A(|E\rangle)}{N_A} \simeq \frac{S(E)}{N} \equiv s(E) \,, \tag{1.49}$$

where $|E\rangle$ is an eigenstate satisfying ETH (1.12) and s is the entropy density. The same applies also to Renyi entropies (1.23). The leading correction to Eq.(1.49) is universal and proportional to the square root of the system's heat capacity [223]. Eq.(1.49) can be seen analogously within the thermalization framework. In fact, the long-time saturation value of the entanglement entropy is expected to correspond to the value in the thermal ensemble. Using the convergence of the reduced density matrix in Eq.(1.11), one has

$$\lim_{t\to\infty}\lim_{N\to\infty} \frac{S_A(t)}{N_A} \simeq s(\beta_E) \,, \tag{1.50}$$

where the inverse temperature β_E is fixed by the initial energy via Eqs.(1.2) . These observations provide a profound bridge between quantum entanglement and standard thermodynamics: The thermalization of a subsystem is identified as the accumulation in time of quantum entanglement between the subsystem and the rest. In integrable systems the same considerations apply, with the only difference that $s(E)$ (or equivalently $s(\beta_E)$) corresponds to the thermodynamic GGE entropy [102, 224, 225].

The maximum value of the entanglement entropy in Eq.(1.49) is attained at "infinite temperature", i.e. for eigenstates at the center of the spectrum. These states are expected to match, at the leading order in N, the result of random pure states [222]. This goes under the name of *Page value* [226] and it reads

$$S_{\text{Page}} = \ln \dim \mathcal{H}_A - \frac{1}{2}\frac{(\dim \mathcal{H}_A)^2}{\dim \mathcal{H}} + O\left(\frac{1}{\dim \mathcal{H}}\right) \,, \tag{1.51}$$

with $\mathcal{H}_A$ and $\mathcal{H}$ are the Hilbert spaces of the subsystem A and of the whole system respectively. For example, in the case of random states of N qubits with a partition $N_A = N/2$, one has $\dim \mathcal{H}_A = \dim \mathcal{H}_B = 2^{N/2}$ and $S_{\text{Page}} = N/2 \ln 2 - 1/2$. In this view, the extensivity of the entanglement entropy follows from the logarithm of an exponentially large Hilbert space.

Yet, this behavior is often violated. This is the case not only for the low-energy states discussed above, but also for MBL eigenstates [227, 228] – which obey area

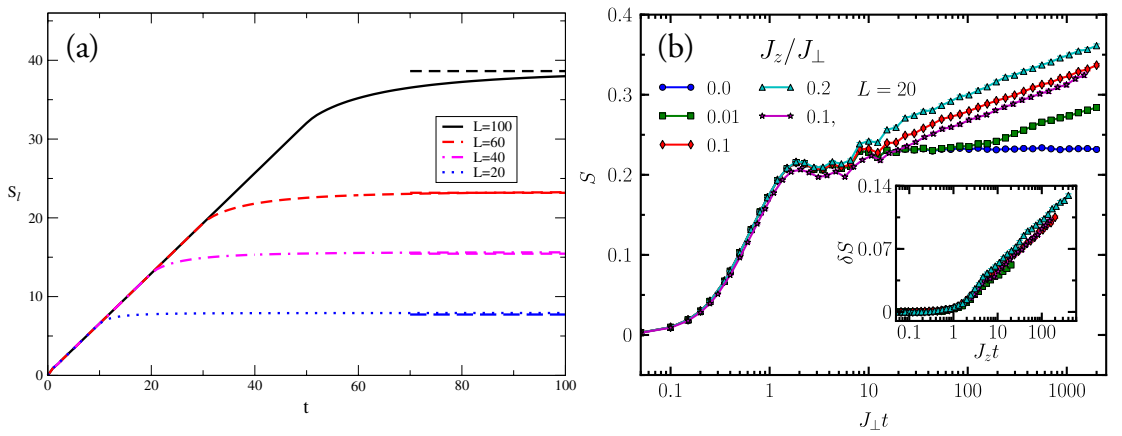

Figure 1.4: Paradigm for the entanglement entropy growth of a pure state out-of-equilibrium. (a) Linear growth of $S_A(t)$ for integrable systems (from Ref.[114]). (b) Logarithmic growth of the entanglement entropy in a MBL system (from Ref.[229]). In the noninteracting limit ($J_z = 0$), the entanglement saturates and obeys area law. The two scenarios can be understood from the spreading (or quasi-localization) of the elementary excitations, see the discussion in the text.

law – or for scarred eigenstates for which $S_A \sim \ln \ell$ [61–65]. Indeed, the scaling of the eigenstate entanglement with ℓ is commonly used to distinguish between different many-body phases in realistic models.

1.3.3 Entanglement entropy out-of-equilibrium

As far as out-of-equilibrium systems are concerned, it is by now well established that a large body of information about the many-body dynamics, their thermalization properties, and the complexity of their numerical simulations, can be inferred from the evolution of their entanglement.

As far as local Hamiltonians are concerned, there is a well-acknowledged paradigm for the entanglement entropy growth of pure states out-of-equilibrium. As a broad consequence of the Lieb-Robinson bound [cf. Eq.(1.3)], in thermalizing local systems the entanglement entropy $S_A(t)$ grows linearly in time before saturating to a value proportional to its volume [230–232]. An analytical understanding of this behavior has come only recently from the study of random unitary circuits [233]. In this framework, the entanglement entropy corresponds to the surface of the minimal space-time membrane separating the two subsystems. The linear spreading of $S_A(t)$ before a volume law saturation is well-established for integrable systems, where this behavior has been explained via a semiclassical picture based on quasi-particle propagation [102, 225, 234, 235]. For an example, see Figure 1.4 (a). On the other hand, the presence of an extensive number of local conserved quantities (exact or approximate) causes a dramatic slow down of the entanglement growth, with a distinguished logarithmic increase for MBL systems [229, 236–238], see Figure 1.4 (b).

Before going into further details, let us remark that the study entanglement entropy dynamics is still the focus of ongoing research and new developments. For

instance, it has been discussed recently that the interplay between unitary dynamics and local projective measurements gives rise to a new universality class [239–241]. This describes a measurement-induced transition between two distinct dynamical phases, one characterized by a volume-law scaling of entanglement entropy, the other by an area-law. The full characterization of such transition is now the subject of intense study, see e.g. [242–245].

Quasiparticle picture for bipartite entanglement

In the case of integrable systems discussed in Section 1.1.3, the entanglement entropy grows linearly in time, as in Figure 1.4. The underlying mechanism, now known as *quasiparticle picture*, is built on the ballistic traveling of infinitely long-lived quasiparticles [102].

Let us describe the salient features in the case of only one type of elementary excitation (quasiparticle). For the quantitative and general treatment, we refer the reader to Refs.[102, 225, 234], for a recent review [235].

Consider the same quench protocol as outlined in Section 1.1.1. The initial state $|\psi_0\rangle$ has typically very high energy relative to the ground state of the Hamiltonian $\hat{H}$ and therefore can be considered as a source of quasiparticle excitations. These spread ballistically in the system and are identified by their quasi-momentum k and group velocity $v(k)$. The main assumption is that excitations emitted far apart in space are uncorrelated. Conversely, the only coherent contribution comes from entangled quasiparticles emitted at the same point in space [15] with opposite momentum $\pm k$ to the right and the left. As they propagate, larger regions of the system get entangled. The entanglement entropy of a subsystem A will be proportional to the total number of quasiparticles that, after being emitted from the same point, lie simultaneously in the subsystem A and its complement. Therefore, the amount of entanglement at time t can evaluated by a quasiparticle counting. In one dimension, for a subsystem A of ℓ sites, one has

$$S_A(t) \sim 2t \int_{2|v|t<\ell} dk\, v(k)\, f(k) + \ell \int_{2|v|t>\ell} dk\, f(k)\,, \tag{1.52}$$

where $f(k)$ is related to the quasiparticles production rate and in principle is calculable. This relation holds for $t, \ell \to \infty$ at t/ℓ fixed. If the maximum of the quasiparticle velocity v_M exists, then for $t \leq \ell/2v_M$, S_A grows linearly in time, whereas for $t \gg \ell/2v_M$, the entanglement is volume law, i.e. $S_A \propto \ell$. In fact, unless $|v| = 1$[16], S_A is not strictly proportional to ℓ for $t \geq \ell/2$, but the asymptotic limit is always approached from below.

The quasiparticle picture has been verified analytically in free [224, 246] and interacting models [225, 234] and it was confirmed numerically in several studies, e.g. [236, 247]. The same approach has been recently exploited to understand entanglement spreading via the mutual information (1.25) in integrable systems [114].

Slow growth of bipartite entanglement for MBL systems

One of the distinctive signatures of many-body localization (see Section 1.1.3) is

[15] More precisely, quasi-particles emitted within the initial correlation length.

[16] This is the case of conformal field theories.

the logarithmic growth of $S_A(t)$. In the absence of interactions, out-of-equilibrium states maintain a low degree of entanglement upon evolution and S_A obeys an area law. On the other hand, as soon as the interaction is turned on, the entanglement entropy shows slow logarithmic growth in time, as shown in Figure 1.4 (b). This was initially demonstrated numerically [229, 236, 237] and then explained as a result of dephasing between different eigenstates in Ref.[238], see also Refs.[71] . For weak interactions, this mechanism predicts

$$S_A(t) \sim \xi \ln (J_0\, t) \ , \tag{1.53}$$

where ξ is the single particle localization length and J_0 is proportional to the interaction strength.

Let us briefly sketch the heuristic argument, while for all the details we refer to Refs.[71, 238]. Consider a system of N spins and an initial state which is taken to be a product state of the physical spins. Let $\tilde{h}_{i,i+x}$ be the effective field acting on the site i because of the spin at distance x [17]. Accordingly, the i-th spin will acquire a phase of order one at a time scale $t(x)$, set by the condition $\tilde{h}_{i,i+x}\, t(x) \simeq 1$. Using the exponential decay of the couplings in the MBL effective Hamiltonian (1.19), one can show that also the effective field is suppressed exponentially $\tilde{h}_{i,i+x} \sim J_0\, e^{-x/\xi'}$, where ξ' is proportional to the correlation length. This decay, together with the condition $\tilde{h}_{i,i+1}\, t(x) \simeq 1$ yields a logarithmic "light cone" of entanglement, i.e. $x_{\text{ent}}(t) \sim \xi \ln (J_0 t)$. With a counting argument similar to the quasiparticle picture, $S_A(t)$ is proportional to the length of spins which posses phases dependent on the states of the other spins $x_{\text{ent}}(t)$. This leads to Eq.(1.53).
After this dynamical regime, the entanglement entropy approaches a value proportional to the so-called diagonal entropy [248, 249]. The latter, even if it obeys volume law, it keeps memory about the initial conditions. This shows that entanglement growth is not necessarily associated with the transport of energy and matter, which is completely suppressed in localized systems.

This behavior has been confirmed numerically in several MBL models and in systems that exhibit the same phenomenology [250–254].

[17] This effective field can be written from the MBL Hamiltonian (1.19) as $\tilde{h}_{i,i+x} = \tilde{J}_{i,i+x}\hat{\tau}^z_{i+x} + \tilde{J}_{i,i+1,i+x}\hat{\tau}^z_{i+1}\hat{\tau}^z_{i+x} + \dots$.

Chapter 2

Semiclassical dynamics

> *"This lovely theory, though it has been available for nearly half a century, remains – except to specialists in quantum optics and a few other fields – much less well known than it deserves to be. "*
>
> — N. Wheeler, Remarks concerning the status and some ramifications of Ehrenfest's theorem

The goal of this chapter is to review the standard approach to semiclassical dynamics, understood as classical equations of motion equipped with quantum fluctuations. We will start by introducing the classical limit and its validity for fully connected systems. Then, we summarize the salient features of numerical truncated Wigner approximations of phase-space methods and complement them with the description of a semi-analytical technique.

In the previous chapter, we discussed the general framework for entanglement and thermalization in local many-body systems, in their fully quantum regime occurring at $\hbar = 1$. Nevertheless, the hearth of this thesis is devoted to the understanding of entanglement and its evolution in spin systems with long-range interactions. Addressing this problem requires a strong shift in the paradigm and techniques usually employed to solve standard short-range quantum dynamics.
Whenever the interaction between the elementary constituents is sufficiently long-range, one expects mean-field approximation to be valid. Dynamically, this implies that such systems can often exhibit a semiclassical behavior with some effective Planck constant $\hbar_{\text{eff}} \to 0$: When a system is initialized in a localized wave-packet, quantum observables obey the classical equation of motion at short times, in the spirit of the Ehrenfest theorem [255].

Accordingly, the bulk of the analysis contained in this thesis is performed using semiclassical tools, which allow recognizing the different contributions in the dynamics, especially in connection with the buildup of quantum correlations. Hence, the purpose of this chapter is to provide a (partial) review of the broad field of semiclassical dynamics and to introduce the techniques applied and extended in the rest of the thesis.

There are many successful approaches to semiclassical physics, from Wentzel–Kramers–Brillouin (WKB) method [256] to the Gurzwiller propagator [257]. In this thesis, we will study semiclassical dynamics as referred to *classical mean-field equations of motion supplemented with quantum fluctuations*, whose strength is controlled by $\hbar$. Such a semiclassical description holds every time it is possible to define an effective Plank constant that vanishes in the appropriate limit of $\hbar_{\text{eff}} \to 0$. Examples include bosonic systems with large occupation numbers, large s spin systems or models characterized by permutational symmetry.

The latter is particularly relevant for our discussion since mean-field large-N models can be considered the starting point for the analysis of the long-range clean interactions. For this reason, we introduce the classical limit and its applicability to fully-connected systems in the first section Section 2.1. Furthermore, many atomic, molecular and optical quantum systems, such as Bose-Einstein condensates [131, 258], cavity-QED setups [259, 260] and trapped ions [158, 261], can be described by collective uniform interactions between their N elementary degrees of freedom. As such, these many-body systems exhibit a *permutational invariance* which, as we will show in Section 2.1.1, give rise to a controlled emergence of *semiclassical dynamical behavior in the limit of large* N [262]. Such systems thereby offer a natural playground for experimental efforts toward a deeper understanding of the entanglement growth in the semiclassical regime and beyond.

The above definition of semiclassics (classical trajectories with quantum fluctuations) is the cornerstone of phase-space methods, an alternative formulation of quantum mechanics, that we review in Section 2.2. In the limit $\hbar \to 0$, phase-space techniques result in the class of *truncated Wigner approximations*. These account for quantum fluctuations in the Wigner function describing the initial state, while keeping the equation of motion of the phase-space variables at the classical level. As such, these methods have proved to be extraordinarily accurate in describing the dynamics in the above limits and beyond. As the first application, in Appendix B we derive the semiclassical expression for the echo observable and the square-commutator [cf. Section 1.2.4] using Bopp formalism, introduced below. Secondly, in Chapters 4 and 6 we employ the numerical TWA and its extensions to study the scrambling dynamics of clean and disordered all-to-all interacting spin systems.

These numerical techniques can be complemented by semi-analytical approaches. In this thesis, we consider a *time-dependent* version of the standard *Holstein Primakoff* transformations, that we introduce in detail in Section 2.3. Within this method, one can access two types of fluctuations: the collective (semiclassical) ones and the finite wave-length (quantum) fluctuations. The latter arises when permutational symmetry is broken. This approach, together with the classical limit of Section 2.1, will be heavily employed in the next Chapter 3 in the study of semiclassical entanglement and in Chapter 5 for the analysis of long-range models. As we will illustrate, all these techniques rely on closing the equation of motion at the Gaussian level, while keeping into account the initial quantum fluctuations.

2.1 The classical limit

We focus on quantum systems characterized by a small parameter $\hbar_{\rm eff}$, which controls the impact of the quantum fluctuations. A system in this class is described by n degrees of freedom, identifyed by $2n$ operators $\hat{\boldsymbol{\xi}} = (\hat{q}_1, \dots, \hat{q}_n, \hat{p}_1, \dots, \hat{p}_n)$. These satisfy the standard canonical commutation relations $[\hat{q}_i, \hat{p}_j] = i\hbar_{\rm eff}\,\delta_{ij}$, o more compactly $[\hat{\boldsymbol{\xi}}, \hat{\boldsymbol{\xi}}] = i\hbar_{\rm eff}\mathbb{J}$, where $\mathbb{J}$ is the symplectic unit[1]. The system is such that allows a re-scaling of the Hamiltonian

$$\hat{H} = \hbar_{\rm eff}^{-1}\,\mathcal{H}_{\rm cl}(\hat{\boldsymbol{\xi}})\;, \tag{2.1}$$

that leads to the following the Heisenberg equation of motion[2]

$$\dot{\hat{\boldsymbol{\xi}}} = \mathbb{J}\,\partial\mathcal{H}_{\rm cl}(\hat{\boldsymbol{\xi}})\;. \tag{2.2}$$

One could equivalently define a classical system described by $2n$ classical phase-space variables $\boldsymbol{\xi}_{\rm cl} = (q_1, \dots, q_n, p_1, \dots, p_n)$, obeying the canonical Poisson brackets $\{q_i, p_j\} = \delta_{ij}$ and whose dynamics is given by the Hamilton-Jacobi equation of motion $\dot{\boldsymbol{\xi}}_{\rm cl} = \{\boldsymbol{\xi}_{\rm cl}, \mathcal{H}_{\rm cl}\} = \mathbb{J}\,\partial\mathcal{H}_{\rm cl}(\boldsymbol{\xi}_{\rm cl})$.

The full quantum evolution for the expectation value of the operator $\hat{\boldsymbol{\xi}}(t)$ evaluated on a the generic quantum state $|\psi_0\rangle$ reads

$$\frac{d}{dt}\langle\hat{\boldsymbol{\xi}}(t)\rangle = \mathbb{J}\,\langle\partial\mathcal{H}_{\rm cl}(\hat{\boldsymbol{\xi}}(t))\,\rangle\;. \tag{2.3}$$

This is exactly what stated by the Ehrenfest theorem [255], which describes the exact quantum evolutions of operators at time t, without approximations. Even if this relation is reminiscent of the Hamilton's equations for the classical variable $\boldsymbol{\xi}_{\rm cl}$, in principle one has $\langle\partial\mathcal{H}_{\rm cl}(\hat{\boldsymbol{\xi}})\rangle \neq \partial\mathcal{H}_{\rm cl}(\langle\hat{\boldsymbol{\xi}}\rangle)$. However, whenever quantum fluctuations are small one can look at the replacements[3]

$$\langle\partial\mathcal{H}_{\rm cl}(\hat{\boldsymbol{\xi}})\rangle \to \partial\mathcal{H}_{\rm cl}(\langle\hat{\boldsymbol{\xi}}\rangle)\;. \tag{2.4}$$

This substitution is equivalent closing the cumulants at second order, namely to take $\langle\hat{\xi}\;\hat{\xi}'\rangle = \langle\hat{\xi}\rangle\langle\hat{\xi}'\rangle$. We consider the case in which the initial state $|\psi_0\rangle$ corresponds to a narrow Gaussian wave-packet, centered around a point with a *small variance* Δ^2 of quantum fluctuations of order $\Delta^2 \sim \mathcal{O}(\hbar_{\rm eff})$. A large number of relevant initial states lie in this class. For instance, consider coherent states or pure nonentangled ones, such as uncorrelated product states, routinely prepared in cold-atom experiments via standard techniques. Weakly entangled initial states may be treated on equal footing.

Therefore, by virtue of Eq.(2.4), the average $\langle\hat{\boldsymbol{\xi}}(t)\rangle$ moves along the classical trajectory to the leading order in $\hbar_{\rm eff}$,

$$\frac{d}{dt}\langle\hat{\boldsymbol{\xi}}(t)\rangle = \mathbb{J}\,\partial\mathcal{H}_{\rm cl}\left(\langle\hat{\boldsymbol{\xi}}(t)\rangle\right) + \mathcal{O}(\hbar_{\rm eff})\;, \tag{2.5}$$

[1] The symplectic matrix $\mathbb{J}$ is given by the $2n \times 2n$ antisymmetric matrix $\mathbb{J} = \begin{pmatrix} \mathbb{0}_n & \mathbb{1}_n \\ -\mathbb{1}_n & \mathbb{0}_n \end{pmatrix}$, which satisfies $\mathbb{J}^2 = -\mathbb{1}_{2n}$.

[2] Subtleties related to the ordering of the operators are not relevant in the following discussion.

[3] Notice that this is always exact the case of quadratic Hamiltonians.

that is

$$\langle \hat{\boldsymbol{\xi}}(t) \rangle = \boldsymbol{\xi}_{\rm cl}(t) + O(\hbar_{\rm eff}) \ . \tag{2.6}$$

According to the standard semiclassical theory [263–265], quantum fluctuations around the classical trajectory $\boldsymbol{\xi}_{\rm cl}(t)$ will remain approximately Gaussian for a diverging time scale as $\hbar_{\rm eff} \to 0$ during the evolution, the so-called *Ehrenfest time* scale $T_{\rm Ehr} = T_{\rm Ehr}(\hbar_{\rm eff})$. At $T_{\rm Ehr}$ quantum interference effects become dominant and the semiclassical description breaks down. The Ehrenfest time can be defined as the time scale for which the gaussian approximation breaks down and quantum fluctuations become of the order of one, i.e. $\Delta^2(T_{\rm Ehr}) = O(1)$. This depends on how quantum fluctuations evolve in time that, in turn, is determined by the regularity properties of the classical trajectories. As such, it will be discussed in detail in Section 3.1.2. In general one has

$$T_{\rm Ehr} \propto \begin{cases} \hbar_{\rm eff}^{-1/2} & \text{regular trajectory} \\ \ln \ \hbar_{\rm eff}^{-1} & \text{chaotic/unstable trajectory} \end{cases} . \tag{2.7}$$

This semiclassical description is not restricted to phase-space or coherent variables, but it describes the dynamics of several interesting models. In particular, Sciolla and Biroli [262] formulated a general theory for systems with full permutational invariance in states belonging to the totally-symmetric sector.

2.1.1 Classical limit of permutationally invariant systems

We recall how the permutational symmetries allow for exactly mapping collective quantum models to systems of few degrees of freedom characterized by a vanishingly small effective Planck constant in the thermodynamic limit [262].

We consider a Hamiltonian $\hat{H}$ characterizing a uniform all-to-all interaction of N elementary constituents, such as spins or particles. The symmetry under permutations of the degrees of freedom makes the mean-field treatment of the quantum dynamics exact for large N. To show how the semiclassical description emerges, we consider an ensemble of N identical q-level quantum systems. A basis of the many-body Hilbert space can be constructed as the tensor product of identical single-unit bases $\{|\alpha\rangle\}$ with $\alpha = 1, \dots, q$. Binary permutation operators are unitary transformations that exchange a pair of units in the system. Their action is defined by

$$\hat{P}_{ij} |\alpha_1, \dots, \alpha_i, \dots \alpha_j, \dots, \alpha_N\rangle = |\alpha_1, \dots, \alpha_j, \dots \alpha_i, \dots, \alpha_N\rangle \ , \tag{2.8}$$

for all pairs $i > j$. A system has full permutational invariance if its Hamiltonian $\hat{H}$ commutes with all permutation operators. The totally-symmetric subspace (TSS) of the many-body Hilbert space is simultaneously invariant under all permutations [4]. A basis of the TSS can be obtained by symmetrizing the many-body configurations $|\alpha_1, \dots, \alpha_N\rangle$ with respect to all permutations. It can be labelled by the numbers $N_1, \dots, N_q$ of units occupying each level with $\sum_{\alpha=1}^{q} N_\alpha = N$. The dimension of the TSS,

$$\dim \text{TSS} \ = \binom{N+q-1}{q-1} \underset{N\to\infty}{\sim} \frac{N^{q-1}}{(q-1)!} \ , \tag{2.9}$$

[4] Unless permutational symmetry is spontaneously broken or fragmentation phenomena take place [266].

is only polynomially large in N, which allows for the exact numerical analysis of large systems. Due to the symmetry of $\hat{H}$, the time-evolution of totally symmetric initial states never leaves the TSS. Typically, such initial states may be simple products of identical single-body states, or ground states, like the ones prepared in experiments.

It was shown by Sciolla and Biroli in Ref.[262] that the dynamics of symmetric observables within the TSS is classical in the thermodynamic limit. To show this, observe that possible off-diagonal transitions governed by $\hat{H}$ are uniquely identified by a set of integers $m_1, \ldots, m_q$

$$|N_1, \ldots, N_q\rangle \to |N_1 + m_1, \ldots, N_q + m_q\rangle. \tag{2.10}$$

For convenience, we turn the occupation numbers N_α into fractions $x_\alpha \equiv N_\alpha/N$, with $0 \leq x_\alpha \leq 1$ and $\sum_{\alpha=1}^{q} x_\alpha = 1$, and denote basis states by $|\mathbf{x}\rangle$, where $\mathbf{x} = (x_1, \ldots, x_q)$. Hence, we write the matrix elements of $\hat{H}$ as [5]

$$H_{\mathbf{x},\mathbf{x}'} \equiv \langle \mathbf{x}|\hat{H}|\mathbf{x}'\rangle = V(\mathbf{x})\,\delta_{\mathbf{x},\mathbf{x}'} - \sum_{\mathbf{m}\neq\mathbf{0}} T_{\mathbf{m}}(\mathbf{x})\delta_{\mathbf{x},\mathbf{x}'+\mathbf{m}/N}, \tag{2.11}$$

with $\mathbf{m} = (m_1, \ldots, m_q) \in \mathbb{Z}^q$. Terms in the Hamiltonian $\hat{H}$ involving up to k bodies yield "local" transitions in the TSS basis, characterized by $|\mathbf{m}| \equiv \sum_\alpha |m_\alpha| \leq 2k$. By the extensivity of the Hamiltonian $\hat{H}$, both $V(\mathbf{x})$ and $T_{\mathbf{m}}(\mathbf{x})$ are extensive,

$$V(\mathbf{x}) \sim N\, v(\mathbf{x}), \qquad T_{\mathbf{m}}(\mathbf{x}) \sim N\, t_{\mathbf{m}}(\mathbf{x}). \tag{2.12}$$

Crucially, the densities v and t are smooth functions of $\mathbf{x}$, as they generally result from combinatoric factors of the occupation numbers which are insensitive to small changes $N_\alpha \mapsto N_\alpha \pm 1, 2, \ldots$ to leading order in the thermodynamic limit [262]. This result is based on the smoothness of the matrix elements of $\hat{H}$ between two TSS states concerning small changes in the occupation numbers $N_\alpha \to N_\alpha \pm 1, \pm 2, \ldots$. These properties allow to rewrite the Schrödinger equation in the TSS as

$$\frac{1}{N}\frac{\partial}{\partial t}\psi(\mathbf{x},t) = \left[v(\mathbf{x}) - \sum_{0\leq|\mathbf{m}|\leq 2k} t_{\mathbf{m}}(\mathbf{x})\, \cosh\left(\frac{\mathbf{m}}{N}\frac{\partial}{\partial \mathbf{x}}\right) \right] \psi(\mathbf{x},t)\ . \tag{2.13}$$

Equation (2.13) shows that the dynamics of wave-functions in the TTS is governed by the effective Hamiltonian

$$\mathcal{H}_{\rm cl}(\hat{\mathbf{q}},\hat{\mathbf{p}}) \equiv v(\hat{\mathbf{q}}) - \sum_{\mathbf{m}} t_{\mathbf{m}}(\hat{\mathbf{x}})\, \cosh\left(\mathbf{m}\cdot\hat{\mathbf{p}}\right)\ , \tag{2.14}$$

expressed in terms of the conjugated canonical operators $\hat{\boldsymbol{\xi}} = (\hat{\mathbf{q}}, \hat{\mathbf{p}})$

$$\frac{N_\alpha}{N} \mapsto \hat{q}_\alpha, \qquad -i\frac{\partial}{\partial N_\alpha} \mapsto \hat{p}_\alpha\ , \tag{2.15}$$

[5] For simplicity, we assume time-reversal invariance, which results in real matrix elements $T_{\mathbf{m}}(\mathbf{x}) \in \mathbb{R}$.

with an effective Planck constant

$$\hbar_{\text{eff}} \equiv \frac{1}{N} \qquad (\hbar = 1 \text{ in our units}) \,, \tag{2.16}$$

that approaches zero in the thermodynamic limit. Thus, the quantum system of the original system of all-to-all interacting q-level units is mapped to $n = q - 1$ [6] collective degrees of freedom. As outlined in the previous section, its quantum dynamics is equivalent, in the thermodynamic limit, to the one governed by the Hamilton equations generated by $\mathcal{H}_{\text{cl}}$.

2.1.2 Fully connected spin systems

In the specific case a system of N interacting spins-s, the limiting semiclassical description can be formulated more directly and intuitively, by considering that the TSS coincides with the Dicke manifold of maximal collective spin $S = Ns$, whereby the behavior of collective spin operators approaches the classical limit. In fact, consider general spin models with arbitrary all-to-all multi-body interactions, described by a Hamiltonian of the form

$$\hat{H} = -\sum_{p=1,2,\dots} \left\{ \sum_{\mu_1,\dots,\mu_p=x,y,z} \frac{J_{\mu_1\dots\mu_p}}{N^{p-1}} \sum_{i_1\neq\dots\neq i_p}^{N} \hat{s}_{i_1}^{\mu_1} \dots \hat{s}_{i_p}^{\mu_p} \right\} \tag{2.17}$$

where $\hat{\mathbf{s}}_i$, $i = 1, 2, \dots, N$ are quantum spins-s. The rescaling factor $1/N^{p-1}$ is such that the energy contribution of all p-body interactions is extensive. These Hamiltonians can be written in terms of the collective spin of the system

$$\hat{\mathbf{S}} = \sum_{i=1}^{N} \hat{\mathbf{s}}_i \,, \tag{2.18}$$

as [7]

$$\frac{\hat{H}}{N} = -\sum_{p\geq 1} \left\{ \frac{1}{N^p} \sum_{\mu_1,\dots,\mu_p=x,y,z} J_{\mu_1\dots\mu_p}\, \hat{S}^{\mu_1} \dots \hat{S}^{\mu_p} \right\} . \tag{2.19}$$

The collective spin magnitude $|\hat{\mathbf{S}}| = \sqrt{S(S+1)}$ with $S = Ns, Ns-1, Ns-2, \dots$ is extensive and conserved,

$$\left[\hat{\mathbf{S}}^2, \hat{H}\right] = 0 \,. \tag{2.20}$$

The Hamiltonian $\hat{H}$ is thus diagonalizable in each total spin sector S. Each subspace is spanned by $|S, m\rangle$, with $m = -S, -S+1, \dots, S$ and has therefore dimension $\dim \mathcal{H}(S) = 2S + 1$. Notice that each sector is degenerate, with degeneracy

$$g_N(S) = \frac{2S+1}{N/2+S+1} \binom{N}{N/2-S} \,, \tag{2.21}$$

[6] Notice that the exact constraint $\sum_\alpha x_\alpha = 1$ can be solved explicitly, eliminating one degree of freedom.

[7] In going from Eq. (2.17) to Eq. (2.19), one needs to add terms with equal indices in the sums. Such terms are immaterial for $s = 1/2$, while they provide corrections to the coefficients of order $1/N$ in higher-spin systems. This small modification does not alter the subsequent analysis and, accordingly, we will simply ignore it.

such that $\sum_{S=0}^{Ns} g_N(S) \dim \mathcal{H}(S) = (2s+1)^N$ coincides with the full many-body Hilbert space. In the case of ferromagnetic interaction, the ground state belongs to the maximal total spin sector, characterized by the maximal spin projection $S = Ns$ (see, e.g., Ref.[266]). In what follows, whenever we refer to ground states, we will always imply ferromagnetic couplings.

For such states with maximal spin, the thermodynamic limit $N \to \infty$ is equivalent to the semiclassical limit of a single degree of freedom $n = 1$, or, in loose terms, to a classical continuous spin

$$\vec{\mathcal{S}} = \frac{\langle \hat{\mathbf{S}} \rangle}{N} \tag{2.22}$$

of (conserved) length s. In fact, these reduced spin variables satisfy a commutation relation of the form

$$\left[\frac{\hat{S}^\mu}{N}, \frac{\hat{S}^\nu}{N} \right] = \frac{i}{N} \, \epsilon_{\mu\nu\rho} \, \frac{\hat{S}^\rho}{N} \, , \tag{2.23}$$

whence one sees that Eq.(2.19) defines a semiclassical system with an effective Planck constant $\hbar_{\text{eff}} \equiv 1/N$ which vanishes in the thermodynamic limit $N \to \infty$. The limiting classical Hamiltonian $\hat{H}/N \to \mathcal{H}_{\text{cl}}$ thus reads

$$\mathcal{H}_{\text{cl}}(\vec{\mathcal{S}}) = -\sum_{\mu_1} J_{\mu_1} \, \mathcal{S}^{\mu_1} - \sum_{\mu_1,\mu_2} J_{\mu_1\mu_2} \, \mathcal{S}^{\mu_1} \mathcal{S}^{\mu_2} - \dots \, , \tag{2.24}$$

where now $\hat{\mathbf{S}}/N \to \vec{\mathcal{S}}$ represents a classical spin on the sphere of radius s which can be parametrized by spherical coordinates: choosing the z direction as the polar axis, $\vec{\mathcal{S}} = s\hat{\mathbf{Z}}$ with

$$\hat{\mathbf{Z}} = \begin{pmatrix} \sin\theta\cos\phi \\ \sin\theta\sin\phi \\ \cos\theta \end{pmatrix} \, . \tag{2.25}$$

The rigorous meaning of the classical limit is that, as $N \to \infty$, the ground state expectation values $\langle \hat{\mathbf{S}} \rangle_{\text{GS}}/N$ of the spin components converge to the minimum point $\vec{\mathcal{S}}^*$ of the classical Hamiltonian $\mathcal{H}_{\text{cl}}$ on the sphere, with vanishingly small quantum fluctuations. Hence, ground states lie in the TTS and their dynamics can be described semiclassically. One can consider as well fully polarized states, in which all spins point along a common direction on the sphere. Such initial states have a semiclassical nature, as their classical phase-space representations via the Wigner function [263, 265] (see Section 2.2) correspond to narrow Gaussian distributions centered around a point with quantum fluctuations of order $\mathcal{O}(1/N)$. For example, a system of N spins fully polarized in the z direction has

$$\left\langle \frac{\hat{\mathbf{S}}}{N} \right\rangle = s \begin{pmatrix} 0 \\ 0 \\ 1 \end{pmatrix} \, , \quad \left\langle \frac{\delta\hat{\mathbf{S}}^2}{N^2} \right\rangle = \frac{1}{2} s \begin{pmatrix} \hbar_{\text{eff}} \\ \hbar_{\text{eff}} \\ 0 \end{pmatrix} \, , \tag{2.26}$$

(with $\delta\hat{\mathbf{S}} = \hat{\mathbf{S}} - \langle \hat{\mathbf{S}} \rangle$), i.e., the collective spin fluctuations in the transverse directions are vanishingly small. Their nonequilibrium evolution $\langle \hat{\mathbf{S}}(t) \rangle/N$ upon varying in

time some parameter $J = J(t)$ in the Hamiltonian is described by the classical trajectory $\vec{\mathcal{S}}(t)$ on the sphere governed by $\mathcal{H}_{\rm cl}$, i.e.,

$$\dot{\vec{\mathcal{S}}} = \left\{\vec{\mathcal{S}}, \mathcal{H}_{\rm cl}\right\} , \tag{2.27}$$

with the Poisson brackets $\{\mathcal{S}^\mu, \mathcal{S}^\nu\} = \epsilon_{\mu\nu\rho}\mathcal{S}^\rho$. This time-evolution can be recast in terms of the spherical angles $\theta(t)$, $\phi(t)$ defined in Eq.(2.73).

If $s > 1/2$, a permutationally invariant Hamiltonian may feature additional "self-interaction" terms with $j_1 = j_2$ in Eq.(2.17), e.g., energy contributions proportional to $\sum_{j=1}^N (\hat{s}_j^z)^2$. Such terms break the conservation of the collective spin magnitude. In this case, the dynamics take place in the full TSS, which is strictly larger than the Dicke manifold, in agreement with the general mapping of Ref.[262] reviewed above.

2.1.3 Beyond global permutational symmetry

The semiclassical approach reviewed in the previous Sections 2.1.1 and 2.1.2 applies to a much wider class of states and models than discussed therein.

One natural extension consists of a *composite system of M collective subsystems*, possibly composed of different kinds of degrees of freedom. This is possible if interactions couple the various subsystems uniformly in their elementary units, i.e., via collective operators only. Thus, the global system has a semiclassical description. When each subsystem is large, the global system will be described by $\sum_{m=1}^M (q_m - 1)$ semiclassical collective degrees of freedom, where q_m is the number of levels for the m-th degree of freedom. For example, the Dicke model, where N spins interact collectively with a cavity mode (see also Section 3.4 below), can be viewed as an example of two classical degrees of freedom, one for the collective spin and one for the cavity mode. The same holds for the two-species kicked top [267].

A second, closely related generalization, is represented by *non-symmetric states which partially break the full permutational symmetry*. Such states may be obtained by bringing together a number $M \ll N$ of initially separated subsystems. In this case, the full permutational symmetry breaks down into the product of smaller permutational symmetries acting separately on each subsystem. While the full system evolves outside of its totally symmetric subspace (TSS), the restricted symmetry allows a description of the dynamics within the product of the TSSs of the M individual subsystems. The semiclassical theory can thereby be applied in the thermodynamic limit, and one ends up with a few-body semiclassical system described by $M \times (q-1)$ collective degrees of freedom. In this case, the Hamiltonian depends on these variables only via the $q-1$ global collective combinations, leaving all the $(M-1) \times (q-1)$ remaining coordinates frozen in their initial values. A simple example is given by a permutationally invariant system of N spins-1/2 initially in a random product state $|\cdots \nearrow\nearrow\nearrow\swarrow\nearrow\swarrow\swarrow\nearrow \ldots\rangle$ of spins pointing up or down along a given axis. Such a state is far away from the Dicke manifold of maximal total spin length $N/2$. Grouping together the spins pointing in the same direction into two subsystems A and B, with N_A and N_B spins respectively, the global system may be viewed as two interacting collective spins $\hat{\mathbf{S}}_A$, $\hat{\mathbf{S}}_B$, of length $N_A/2$ and $N_B/2$ respectively, initially pointing in opposite directions. In agreement with the

above observation, the motion of the two spins is not independent: the Hamiltonian generates a nonlinear collective precession, and the angle between $\hat{\mathbf{S}}_A$ and $\hat{\mathbf{S}}_B$ is a constant of motion.

2.2 Phase-space methods

Let us now introduce a general framework to study quantum mechanics, which allows us to include quantum fluctuations on top of the classical description outlined in the previous section.

Today is universally recognized that there are three alternative and equivalent approaches to formulate quantum mechanics: the usual Hilbert space framework, the Feynman path integral formalism, and eventually, the *phase space representation*. The third provides a characterization of quantum systems with c-numbers position and momentum variables, simultaneously defined in a way to respect the Heisenberg uncertainty principle. Even if usually dismissed in standard courses of quantum mechanics, the phase-space representation represents the most natural and smooth connection to the classical limit, since it works consistently in phase space with the same language of classical mechanics. In this picture, the non-commutativity of the operators is substituted by a special binary operation (the Moyal product) between phase-space variables. Quantum fluctuations are in turn captured — at least in part — by statistical fluctuations, encoded in a quasi-probability density[8] in phase space (the Wigner function), which is essentially the density matrix in this picture. As all quantum mechanics, also its phase-space formulation was reached via a tortuous path of numerous voices during the '30s and 40's [270–273]. For an interesting and stimulating historical survey, we recommend Ref.[268].
Phase space representation has found many applications in quantum optics [274, 275] and, more recently, in atomic systems [276] and in the field of cold atoms [277]. In the last years, these methods have been developed to access many-body dynamics, also in models which are not directly expressible as the one described in the previous Section 2.1.

The Wigner formalism is based on a mapping between the Hilbert space of a quantum system to its corresponding phase space, known as the Wigner-Weyl transform [270, 271]. This can be achieved, for example, through the so-called *phase-point operator* $\hat{A}(\mathbf{q},\mathbf{p})$ [9], where $\{\mathbf{q},\mathbf{p}\}$ are the $2n$ classical phase-space variables. Operators $\hat{O}$ are mapped to functions on phase-space, known as their *Weyl symbols*,

[8] Unlike the Liouville probability density of statistical mechanics, the Wigner function can assume negative "provocative" values [268]. These are the manifestation of the uncertainty principle and have been remarkably reconstructed in experiments [269].

[9] This object has been defined in Ref.[278] in order to be consistent with the standard formulations. It can be written in the position or momentum basis as

$$\langle \mathbf{q}'|\hat{A}(\mathbf{q},\mathbf{p})|\mathbf{q}''\rangle = \delta\left(\mathbf{q}-\frac{\mathbf{q}'+\mathbf{q}''}{2}\right) e^{i\mathbf{p}\cdot(\mathbf{q}'-\mathbf{q}'')/\hbar}\,, \tag{2.28a}$$

$$\langle \mathbf{p}'|\hat{A}(\mathbf{q},\mathbf{p})|\mathbf{p}''\rangle = \delta\left(\mathbf{p}-\frac{\mathbf{p}'+\mathbf{p}''}{2}\right) e^{-i\mathbf{q}\cdot(\mathbf{p}'-\mathbf{p}'')/\hbar}\,. \tag{2.28b}$$

i.e.

$$\hat{O}(\hat{\mathbf{q}},\hat{\mathbf{p}}) \to O^{\mathrm{w}}(\mathbf{q},\mathbf{p}) = \mathrm{tr}[\hat{O}\,\hat{A}(\mathbf{q},\mathbf{p})] = \int d\boldsymbol{\xi}\,\langle \mathbf{q}-\boldsymbol{\xi}/2|\hat{O}(\hat{\mathbf{q}},\hat{\mathbf{p}})|\mathbf{q}+\boldsymbol{\xi}/2\rangle e^{i\mathbf{p}\cdot\boldsymbol{\xi}/\hbar}\,. \tag{2.29}$$

The Weyl symbol of the density matrix $\hat{\rho}$ is called *Wigner function*

$$\hat{\rho} \to W(\mathbf{q},\mathbf{p}) = \frac{1}{(2\pi\hbar)^n}\,\mathrm{tr}[\hat{\rho}\,\hat{A}(\mathbf{q},\mathbf{p})] = \frac{1}{(2\pi\hbar)^n}\int d\boldsymbol{\xi}\,\langle \mathbf{q}-\boldsymbol{\xi}/2|\,\hat{\rho}\,|\mathbf{q}+\boldsymbol{\xi}/2\rangle e^{i\mathbf{p}\cdot\boldsymbol{\xi}/\hbar}\,. \tag{2.30}$$

The $W(\mathbf{q},\mathbf{p})$ inherits the density matrix hermiticity and normalization

$$\int d\mathbf{q}\,d\mathbf{p}\,W(\mathbf{q},\mathbf{p}) = 1\,, \tag{2.31}$$

being a quasi-probability distribution, in general non-positive, see Note 8. The Wigner function together with Weyl symbols yields a complete description of a given quantum system. In particular, the expectation value of any operator $\hat{O}(\hat{\mathbf{q}},\hat{\mathbf{p}})$ is computed by averaging the Weyl symbol of the operator with the Wigner function in phase-space, as

$$\langle \hat{O}(\hat{\mathbf{q}},\hat{\mathbf{p}})\rangle = \int d\mathbf{q}d\mathbf{p}\,W(\mathbf{q},\mathbf{p})\,O_{\mathrm{w}}(\mathbf{q},\mathbf{p})\,. \tag{2.32}$$

The Weyl symbol of the product of two operators $\hat{O}_1$ and $\hat{O}_2$ is the so-called *Moyal product* [273], also known as star-product [279], i.e.

$$\left(\hat{O}_1\,\hat{O}_2\right)^{\mathrm{w}}(\mathbf{q},\mathbf{p}) = O_1^{\mathrm{w}}(\mathbf{q},\mathbf{p})\,\exp\left[-i\hbar\,\{\cdot,\cdot\}/2\right]\,O_2^{\mathrm{w}}(\mathbf{q},\mathbf{p})\,, \tag{2.33}$$

where $\{\cdot,\cdot\}$ are the symplectic the Poisson brackets

$$\{\cdot,\cdot\} = \frac{\overrightarrow{\partial}}{\partial\mathbf{p}}\cdot\frac{\overleftarrow{\partial}}{\partial\mathbf{q}} - \frac{\overrightarrow{\partial}}{\partial\mathbf{q}}\cdot\frac{\overleftarrow{\partial}}{\partial\mathbf{p}}\,, \tag{2.34}$$

and $\overrightarrow{\partial}/\partial\mathbf{q}$ acts on the operator on the right, while $\overleftarrow{\partial}/\partial\mathbf{q}$ on the operator on the left. Eq.(2.33) leads to the famous *Moyal brackets*, namely the Weyl symbol of the commutator

$$\left([\hat{O}^1,\hat{O}^2]\right)^{\mathrm{w}} \equiv i\hbar\{O_1^{\mathrm{w}},O_2^{\mathrm{w}}\}_{\mathrm{MB}}\,, \tag{2.35}$$

which gives

$$\{\cdot,\cdot\}_{\mathrm{MB}} = \frac{2}{\hbar}\,\sin\left(\frac{\hbar}{2}\,\{\cdot,\cdot\}\right)\,, \tag{2.36}$$

with the Poisson brackets $\{\cdot,\cdot\}$ defined in Eq.(2.34). From this expression is already clear that the Moyal bracket corresponds to the Poisson bracket at the leading order in $\hbar$. With this definition, also *quantum dynamical evolution* naturally follows. The Weyl product of the standard Heisenberg evolution $i\hbar\dot{\hat{O}} = [\hat{O},\hat{H}]$ reads

$$\frac{\partial}{\partial t}O^{\mathrm{w}} = \{O^{\mathrm{w}},H^{\mathrm{w}}\}_{\mathrm{MB}}\,, \tag{2.37}$$

where $H^{\rm w}$ is the Weyl symbol of the Hamiltonian. This equation completely specifies the full quantum evolution of observables in the phase-space representation, except that $O^{\rm w}(\mathbf{q}(t),\mathbf{p}(t))$ and $H^{\rm w}(\mathbf{q}(t),\mathbf{p}(t))$ are now classical functions in phase-space, and the non-commutativity is ensured by the Moyal brackets. Evidently, this language makes the link between quantum commutators and Poisson brackets more transparent[10]. Within this frame, time-dependent expectation values naturally arise as weighted averages over phase space of the Weyl symbols (2.32), as

$$\langle \hat{O}(t)\rangle = \mathrm{tr}[\hat{\rho}_0\,\hat{O}(t)] = \int d\mathbf{q}_0\,d\mathbf{p}_0\,W(\mathbf{q}_0,\mathbf{p}_0)\,O^{\rm w}(\mathbf{q}(t),\mathbf{p}(t)) \equiv \overline{\overline{O^{\rm w}(\mathbf{q}(t),\mathbf{p}(t))}}\,, \tag{2.38}$$

where $\hat{\rho}_0 = |\psi_0\rangle\langle\psi_0|$ is the initial state and the double overline is defined as the average weighted with the initial Wigner function $W(\mathbf{q}_0,\mathbf{p}_0)$. This equation can also be derived via a path-integral formulation [195, 280], see Appendix D for the main steps of the derivation

All the results listed above generalize to the *coherent state representation* of the phase space, see, e.g., Ref.[195]. Exactly the same formalism applies: The bosonic fields $\hat{\mathbf{a}}^\dagger$ and $\hat{\mathbf{a}}$ map to complex phase space variables $\boldsymbol{\alpha}^*$ and $\boldsymbol{\alpha}$, which have the conventional Poisson bracket relations: $\{\boldsymbol{\alpha},\boldsymbol{\alpha}^*\}_{\rm c} = 1$. Under this mapping, any operator maps to a function of these variables

$$\hat{O}(\hat{\mathbf{a}},\hat{\mathbf{a}}^\dagger) \to O^{\rm w}(\boldsymbol{\alpha},\boldsymbol{\alpha}^*), \quad \hat{\rho}(\hat{\mathbf{a}},\hat{\mathbf{a}}^\dagger) \to W(\boldsymbol{\alpha},\boldsymbol{\alpha}^*)\,, \tag{2.39}$$

and the coherent Moyal brackets (2.36) read

$$\{\cdot,\cdot\}_{\rm MBc} = 2\,\sinh\left(\frac{1}{2}\{\cdot,\cdot\}_{\rm c}\right)\,, \quad \text{with} \quad \{\cdot,\cdot\}_{\rm c} \equiv \frac{\overrightarrow{\partial}}{\partial\boldsymbol{\alpha}}\cdot\frac{\overleftarrow{\partial}}{\partial\boldsymbol{\alpha}^*} - \frac{\overrightarrow{\partial}}{\partial\boldsymbol{\alpha}^*}\cdot\frac{\overleftarrow{\partial}}{\partial\boldsymbol{\alpha}}\,. \tag{2.40}$$

In this case, the classical limit is achieved for large occupation numbers, namely $\left([\hat{O}_1(\hat{\mathbf{a}},\hat{\mathbf{a}}^\dagger),\hat{O}_2(\hat{\mathbf{a}},\hat{\mathbf{a}}^\dagger)]\right)^{\rm w} = \{O_1^{\rm w},O_2^{\rm w}\}_{\rm MBc} \sim \{O_1^{\rm w},O_2^{\rm w}\}_{\rm c}$. Notice also that the coherent state Moyal bracket (2.40) directly match to the commutator without need to multiply by $i\hbar$. This follows from the fact that the wave limit of the classical Hamilton equation of motion reads $i\hbar\partial_t\boldsymbol{\alpha} = \{\mathcal{H},\boldsymbol{\alpha}\}_{\rm c}$.
This representation is particularly useful since it allows us to retrieve the results for the conjugate variables and to further derive phase-space representation for spin variables. As it is well known, conjugate position and momentum can be written as

$$\hat{\mathbf{q}} = \sqrt{\frac{\hbar}{2}}\,\left(\hat{\mathbf{a}}^\dagger + \hat{\mathbf{a}}\right)\,, \quad \hat{\mathbf{p}} = i\,\sqrt{\frac{\hbar}{2}}\,\left(\hat{\mathbf{a}}^\dagger - \hat{\mathbf{a}}\right)\,. \tag{2.41}$$

On the other hand, the easiest way to derive semiclassics for a spin system is to use the *Schwinger boson representation* [281]. Any spin-s operator, which satisfies the

[10] For example, at the leading order in $\hbar$, Eq.(2.37) yields exactly the Hamilton equations of motion for the conjugate variables $\mathbf{q},\mathbf{p}$, i.e. $\dot{\mathbf{q}} = \partial H^{\rm w}/\partial\mathbf{p}$, $\dot{\mathbf{p}} = -\partial H^{\rm w}/\partial\mathbf{q}$.

canonical commutation relations $[\hat{s}^x, \hat{s}^y] = i\hbar\hat{s}^z$, can be represented by two bosonic operators $\hat{a}$ and $\hat{b}$, as

$$\hat{s}^z = \hbar\,\frac{1}{2}(\hat{a}^\dagger\hat{a} - \hat{b}^\dagger\hat{b}) \qquad \hat{s}^+ = \hbar\,\hat{a}^\dagger\hat{b}\,, \qquad \hat{s}^- = \hbar\,\hat{b}^\dagger\hat{a}\,, \tag{2.42}$$

with the additional constraint that $\hat{\mathbf{a}}^\dagger\hat{\mathbf{a}} + \hat{b}^\dagger\hat{b} = 2s$. In the case of systems of N spins, this representation can be applied on the individual spins and chatacterize the system in terms of the $2N$ bosonic variables $\hat{\mathbf{a}}$ and $\hat{\mathbf{b}}$.

We would like to remark that the phase-space formalism discussed so far constitutes an exact representation of quantum mechanics, exactly as the standard representation in the Hilbert space. Accordingly, in the case of many-body systems, the quantum evolution in Eq.(2.38) is as involved as the complex dynamics occurring in the exponentially large Hilbert space discussed in the previous Chapter 1.
However, in the limit of small $\hbar$ (or equivalently small $\hbar_{\text{eff}}$, e.g. see the previous Section 2.1), great simplifications occur. In the purely classical limit $\hbar = 0$, the Wigner function coincides with the classical probability distribution and Eq.(2.37) reduces to the classical Liouville evolution. Meanwhile for small but finite $\hbar$ and for a large class of initial states[11], one can approximate the quantum evolution of the Weyl symbols (2.37) by the classical equation of motion and keep exact the impact of the quantum fluctuations. This approximation is known as *truncated Wigner approximation*. Its main formulation and generalizations are the subject of the next sections. As we will see, also the validity of this method is restricted to "short-times", before the Ehrenfest one T_{Ehr}.

2.2.1 Truncated Wigner approximation (TWA)

The truncated Wigner approximation (TWA) is known as one of the most successful approaches to investigate numerically non-equilibrium problems close to their classical limit [195, 277, 278, 282–284]. For a cohesive review of the topic, we refer the reader to Ref.[195].

The truncated Wigner approximation incorporates quantum fluctuation at the leading order to the classical dynamics. It amounts in expanding the Moyal brackets in Eq.(2.37) in powers of $\hbar$ and in keeping only the first order, namely the classical equation of motion given by the Poisson brackets. Since the number of classical equations of motion scales linearly with the number of degrees of freedom, it is usually possible to simulate efficiently the classical dynamics of relatively large systems. Hence, time-dependent observables (2.38) read

$$\langle\hat{O}(t)\rangle \simeq \int d\mathbf{q}_0\, d\mathbf{p}_0\, W(\mathbf{q}_0,\mathbf{p}_0)\, O^{\text{w}}(\mathbf{q}_{\text{cl}}(t),\mathbf{p}_{\text{cl}}(t)) = \overline{\overline{O^{\text{w}}(\mathbf{q}_{\text{cl}}(t),\mathbf{p}_{\text{cl}}(t))}}\,, \tag{2.43}$$

where the double overline is the weighted average with the Wigner function [cf. Eq.(2.38)] and $\mathbf{q}_{\text{cl}}(t)$ and $\mathbf{p}_{\text{cl}}(t)$ represent the classical trajectory which evolve ac-

[11] One considers initial states characterized by a positive definite Wigner function, which can, therefore, be interpreted as a probability distribution in phase-space. Product states or semiclassical ground states, like the one introduced discussed next chapter lie in this class

cording to the Hamilton equations

$$\dot{\mathbf{q}}_{\rm cl} = \frac{\partial H^{\rm w}\left(\mathbf{q}_{\rm cl}, \mathbf{p}_{\rm cl}\right)}{\partial \mathbf{p}_{\rm cl}} \,, \qquad \dot{\mathbf{p}}_{\rm cl} = -\frac{\partial H^{\rm w}\left(\mathbf{q}_{\rm cl}, \mathbf{p}_{\rm cl}\right)}{\partial \mathbf{q}_{\rm cl}} \,.$$

Eq.(2.43) *is* the truncated Wigner approximation. As discussed for the classical limit in Eq.(3.8), also at this level, the equation of motion is approximated via a cumulant closure at second order. However, this method keeps into account quantum fluctuations and their nonlinearities, via the interference arising from the average of the different classical trajectories. In Refs.[195, 280] it was shown that TWA naturally arises as a saddle point approximation to the path integral representation of the time evolution of a generic observable on a Keldysh contour. We report the main steps of the derivation in the Appendix D.1.
When the $W(\mathbf{q}_0, \mathbf{p}_0)$ is positive, it can be interpreted as a probability distribution and, from a numerical point of view, it is possible to consider a Montecarlo sampling

$$\langle \hat{O}(t) \rangle = \lim_{N_{\rm sim}\to\infty} \frac{1}{N_{\rm sim}} \sum_{k=1}^{N_{\rm sim}} O^{\rm w}\left(\mathbf{q}_{\rm cl}^{(k)}(t), \mathbf{p}_{\rm cl}^{(k)}(t)\right) \,, \tag{2.44}$$

where $\mathbf{q}_{cl}^{(k)}(t)$ and $\mathbf{p}_{cl}^{(k)}(t)$ are the classical trajectories corresponding to the $k-$th initial condition randomly distributed according to the initial Wigner function.

The same considerations can be applied to the coherent representation (2.39) and therefore, via Eq.(2.42), to spin operators. For instance, the classical equation of motion for the bosonic variables read

$$i\dot{\boldsymbol{\alpha}} = \frac{\partial H^{\rm w}(\boldsymbol{\alpha}, \boldsymbol{\alpha}^*)}{\partial \boldsymbol{\alpha}^*} \,. \tag{2.45}$$

Going back from Schwinger bosons (2.42) to classical angular momentum variables one recovers standard classical Hamiltonian equations for spin (angular momentum) variables

$$\dot{s}^\alpha = \{s^\alpha, H^{\rm w}(\vec{s})\} = \epsilon_{\alpha\beta\gamma} \frac{\partial H^{\rm w}(\vec{s})}{\partial s^\beta} s^\gamma, \quad \leftrightarrow \quad \frac{d\vec{s}}{dt} = \frac{\partial H^{\rm w}}{\partial \vec{s}} \times \vec{s} \,, \tag{2.46}$$

where α, β, γ stand for x, y, z spin components, and $\epsilon_{\alpha\beta\gamma}$ is the fully anti-symmetric Levi-Civita symbol.

While formally the equations of motion for the Schwinger bosons coincide with the equations obtained using the Dirac's variational principle [285], TWA goes well beyond these approximations as it includes quantum fluctuations encoded in the Wigner function, which, in many cases, are essential for correctly describing the dynamics of the system. Only in the limit of an infinitesimally narrow Wigner function describing the initial state, TWA reduces to the so-called Dirac time-dependent variational principle [286]. Also, generally, the variational principle completely fails in describing non-equal time correlation functions and can not be used, for example, to compute the echo of observables and the OTOC. On the other hand, unlike the conventional Keldysh diagrammatic technique, the derivation of TWA is not tied to the exponential Gibbs form of the initial density matrix nor it relies on assumptions of small nonlinearities [287].

Wigner functions

Let us briefly comment upon the Wigner function representing the initial states. As we already mentioned, the analysis with TWA is restricted to positive definite Wigner functions, that represent general separable or low-entangled states [195].

Given an initial state $\hat{\rho}$, the *exact* Wigner function can always be computed via the integral in Eq.(2.30) and, in some special cases, it is known exactly. For instance, consider a coherent state $|\beta\rangle = e^{\beta\hat{a}^\dagger - \beta^*\hat{a}}|0\rangle$, where $|0\rangle$ is the bosonic vacuum. The corresponding Wigner function

$$W_\beta(\alpha,\alpha^*) = \frac{2}{\pi} e^{-|\beta-\alpha|^2} \ ,$$

is a Gaussian, with width $1/\sqrt{2}$, centered on the classical amplitude β, where it takes its maximum value $2/\pi$. See, e.g. Ref.[275]. The known result for Fock states can be used to derive the exact Wigner function for polarized spin states pointing in some directions, see e.g. Ref.[274]. Notice that in the case of small $\hbar$ (or $\hbar_{\rm eff}$) further simplifications occur. For example, consider the fully connected spin systems of Section 2.1.2, characterized by $\hbar_{\rm eff} = 1/N$. In this case, the TWA can be written in terms of the collective spins $\vec{\mathcal{S}} = \frac{1}{N}\sum_{i=1}^N \vec{s}_i$, which collectively obey the classical equation of motion in Eq.(2.46). At large N (small $\hbar_{\rm eff}$), the Wigner function of a fully polarized state along the z axis reads [195]

$$W(\vec{\mathcal{S}}) = \frac{1}{\pi s/N}\, e^{-\frac{\mathcal{S}_x^2+\mathcal{S}_y^2}{s/N}} \delta(\mathcal{S}_z - \sqrt{s^2-\mathcal{S}_x^2+\mathcal{S}_y^2}) \ . \tag{2.47}$$

It is easy to check that $W(\vec{\mathcal{S}})$ reproduces the average and fluctuations of the quantum state, see also Eq.(2.1.2).

On the other hand, instead of the exact Wigner function, one can choose equivalently its *Gaussian approximation*, where its first and the second moments are fixed by the mean and the variance of the corresponding quantum spin operators in the initial state $|\psi_0\rangle$. This has been discussed in Ref.[285] and is particularly useful in systems where the Weyl symbol of the Hamiltonian can not be written in terms of collective variables. For a system of N spins one fixes

$$\langle\psi_0|\hat{s}_i^\alpha|\psi_0\rangle = \overline{\overline{s_i^\alpha(0)}} \ , \quad \frac{1}{2}\langle\psi_0|\hat{s}_i^\alpha\hat{s}_i^\beta + \hat{s}_i^\beta\hat{s}_i^\alpha|\psi_0\rangle = \overline{\overline{s_i^\alpha(0)s_i^\beta(0)}} \ , \tag{2.48}$$

for $i,j = 1,\dots N$ and $\alpha,\beta = x,y,z$. In the case of $s = 1/2$, the initial state $|\psi_0\rangle = |\downarrow\downarrow\dots\downarrow\rangle$ corresponds to

$$\overline{\overline{s_i^z(0)}} = -1/2 \ , \ \overline{\overline{s_i^{x,y}(0)}} = 0 \ , \ \overline{\overline{s_i^\alpha(0)s_i^\beta(0)}} = \frac{1}{4}\delta_{\alpha\beta} \ . \tag{2.49}$$

One can show that this matching can be achieved for any product initial state [285]. The Gaussian Wigner function has the advantage that it is positive definite and easy to sample. Also, the accuracy of the TWA is set by the second power of the effective Planck's constant, which is the same as the accuracy of the Gaussian approximation of the Wigner function [285].

Multi-time correlation functions and Bopp representation

Interestingly, the TWA allows one to compute multi-time correlation functions via the use of *Bopp operators*, which involves evaluating non-equal time response functions on classical trajectories, see e.g. Ref. [195].

Symmetric Bopp representation of quantum operators is intrinsically connected to the Wigner-Weyl quantization. These allow to map operators to functions of phase space variables without any need of performing tedious partial Fourier transforms (2.29). In particular, the position and momentum operators, or bosonic creation and annihilation operators, in the Bopp representation read

$$\hat{q} \to q + \frac{i\hbar}{2}\frac{\partial}{\partial p}\,, \quad \hat{p} \to p - \frac{i\hbar}{2}\frac{\partial}{\partial q}\,, \tag{2.50a}$$

$$\hat{a}^\dagger \to \alpha^* - \frac{1}{2}\frac{\partial}{\partial \alpha}, \quad \hat{a} \to \alpha + \frac{1}{2}\frac{\partial}{\partial \alpha^*}. \tag{2.50b}$$

Then, the Weyl symbol of, for instance, the operator $\hat{q}\hat{p}$ or the number operator, is obtained by simply writing it in Bopp representation

$$(\hat{q}\hat{p})^{\mathrm{w}} = \left(q + \frac{i\hbar}{2}\frac{\partial}{\partial p}\right) p = q\,p + \frac{i\hbar}{2}\,, \tag{2.51a}$$

$$n^{\mathrm{w}} = (\hat{a}^\dagger \hat{a})^{\mathrm{w}} = \left(\alpha^* - \frac{1}{2}\frac{\partial}{\partial \alpha}\right)\alpha = \alpha^*\alpha - \frac{1}{2}\,. \tag{2.51b}$$

Interestingly, Bopp formalism immediately allows to compute *non-equal correlation functions* e.g.

$$\left(\hat{p}(t_1)\hat{q}(t_2)\right)_{\mathrm{w}} = p(t_1)\,q(t_2) - \frac{i\hbar}{2}\frac{\partial q(t_2)}{\partial q(t_1)}\,, \tag{2.52a}$$

$$\left(\hat{a}^\dagger(t_1)\hat{a}(t_2)\right)_{\mathrm{w}} = \alpha^*(t_1)\alpha(t_2) - \frac{1}{2}\frac{\partial \alpha(t_2)}{\partial \alpha(t_1)}\,, \tag{2.52b}$$

where the derivative to respect to $q(t_1)$ or $\alpha(t_1)$ represents the non-equal time response. One can show that time ordered correlation functions always allow for a casual representation in the language of Bopp operators, while OTOC do not allow for such a representation [195, 288]. Bopp operators can also be written in a more compact form

$$\hat{q}(t) \to q(t) + \frac{i\hbar}{2}\{q(t), \cdot\}\,, \quad \hat{p}(t) \to p(t) + \frac{i\hbar}{2}\{p(t)\,, \cdot\}\,, \tag{2.53a}$$

$$\hat{a}^\dagger(t) \to \alpha^*(t) + \frac{}{2}\{\alpha^*(t), \cdot\}\,, \quad \hat{a}(t) \to \alpha(t) + \frac{1}{2}\{\alpha(t), \cdot\}\,, \tag{2.53b}$$

where $\{\cdot, \cdot\}$ stands for the classical Poisson bracket. In Bopp representation the momentum and the coordinate operators (and similarly the creation and annihilation operators) map to the corresponding phase space variables plus half of the Poisson bracket.

For more complicated operators, like non-linear bosonic variables or spin operators, this simple interpretation is lost as generally higher-order derivatives emerge.

In particular, for a generic time-dependent operator $\hat{B}(t)$, Bopp representation can be written as a Taylor expansion in $\hbar$ as

$$\hat{B}(t) \to B_t + \hbar D^{(1)}_{B_t} + \hbar^2 D^{(2)}_{B_t} + O(\hbar^3) \,, \tag{2.54}$$

where B_t is the Weyl symbol of the operator $\hat{B}$ evaluated at time t, the linear order is given by half of the Poisson brackets $D^{(1)}_{B_t} = i/2\{B_t, \cdot\}$, and $D^{(2)}_{B_t}$ contains the second-order derivatives and its explicit form depends on the operator $\hat{B}(t)$. For example, for spin operators as $\hat{B}(t) = \hat{\mathbf{S}}(t)$ the second order expansion is exact and one has

$$B_t = \mathbf{S}_t \,, \quad D^{(1)}_{\mathbf{S}_t} = \frac{i}{2}\{\mathbf{S}_t \,, \cdot\} = -\frac{i}{2}\,\mathbf{S}_t \times \boldsymbol{\nabla} \,, \quad D^{(2)}_{\mathbf{S}_t} = -\frac{1}{8}\left[\boldsymbol{\nabla}_t + (\mathbf{S}_t \cdot \boldsymbol{\nabla}_t)\,\boldsymbol{\nabla}_t - \frac{1}{2}\mathbf{S}_t\,\boldsymbol{\nabla}_t^2\right] \,, \tag{2.55}$$

where $\boldsymbol{\nabla}_t = \partial/\partial \mathbf{S}_t$, i.e. see Ref.[195]. The second order contribution can be re-written in a more compact way as

$$D^{(2)}_{\mathbf{S}_t} = -\frac{1}{8}\frac{\partial}{\partial \mathbf{S}_t} + A^{\mathbf{S}}_{\alpha\beta\gamma}\, S^\alpha_t \frac{\partial^2}{\partial S^\beta_t \partial S^\gamma_t} \,, \tag{2.56}$$

where one has to sum over $\alpha, \beta, \gamma = x, y, z$ and the coefficients of $A^{\mathbf{S}}_{\alpha\beta\gamma}$ are determined explicitly from Eq.(2.55), e.g. $A^{S^z}_{xxx} = 0$, $A^{S^z}_{zzz} = 1/16$ or $A^{S^z}_{zxx} = -1/16$, etc.. In the case of operators which are linear in the creation and annihilation operators (or in the position and momentum operators) the second-order term vanishes $D^{(2)} = 0$ and one gets Eqs.(2.50b-2.53b).

In Appendix B, we apply the Bopp representation to compute also OTOC as the square commutator (1.45) or the echo-observable (1.44). We show that both the quantities contain in the classical limit the square of the derivatives to respect to the initial condition, encoding the classical Lyapunov exponent.

2.2.2 Discrete TWA (DTWA)

It is also possible to characterize the initial Wigner function on a discrete phase-space [278]. This yields an exact description of quantum mechanical systems that have a finite number of orthogonal states, such as spin models with local Hamiltonians. Just as the continuous phase-space, also in this framework one can approximate the quantum dynamics at the classical level and account for the quantum uncertainty through the fluctuations of the discrete initial conditions. This yields a discrete version of the truncated Wigner approximation of the previous section, also known as discrete TWA, or DTWA [284]. As discussed in what follows, it differs from the standard TWA only via the different sampling of the initial conditions. While in this method the initial Wigner function is exact, in TWA the initial conditions are approximated at the Gaussian level [cf. Eq.(2.48)].

As shown in Section 2.2.4, the biggest quality of DTWA it that it captures finite time revivals, as a consequence of its discrete structure. For these reasons, this technique has been widely used to access the quantum dynamics of several spin chains in the proximity of their classical limit or not [284, 289, 290].

We now generalize the previous mapping (2.30)-(2.29) to systems with n discrete degrees of freedom, where the continuous phase space is replaced with a discrete one [278]. Consider as example for $n = 2$ one spin-$1/2$. It can be described in a discrete phase space made of $n^2 = 4$ points, each of them associated with coordinates

$$\alpha = (a_1, a_2) \in \{(0,0), (0,1), (1,0), (1,1)\} \, . \tag{2.57}$$

This can be generalized to $n > 2$, with n prime. Let $\hat{A}_\alpha$ be the discrete phase point operator associated to the point α. As in the continuous case, each operator implements the mapping between the Hilbert space of the quantum system and this discrete phase space. One can show that, by choosing $\hat{A}_\alpha$ in an appropriate way, all the properties of the phase space operator that hold in the continuum case (as the normalization or the orthonormality) still hold. Such a choice can be achieved by

$$\hat{A}_\alpha = \frac{1}{2}\left[(-1)^{a_1}\hat{\sigma}_z + (-1)^{a_2}\hat{\sigma}_x + (-1)^{a_1+a_2}\hat{\sigma}_y + \mathbb{I}\right] = \frac{1}{2}\left(\mathbb{I} + \mathbf{r}_\alpha \cdot \hat{\boldsymbol{\sigma}}\right) \, , \tag{2.58}$$

with $\mathbf{r}_\alpha = ((-1)^{a_2}, (-1)^{a_1+a_2}, (-1)^{a_1})$ and $\hat{\boldsymbol{\sigma}} = (\hat{\sigma}_x, \hat{\sigma}_y, \hat{\sigma}_z)$ are the Pauli matrices. Then, one can construct the Weyl symbol of a generic operator as before: $O^w_\alpha = \mathrm{tr}(\hat{O}\hat{A}_\alpha)/2$. The discrete Wigner function $w_\alpha = \mathrm{tr}(\hat{\rho}\hat{A}_\alpha)/2$ can be pictured as a 2×2 matrix, see Eq.(2.59), and it gives the probability that a state is in the point α. Moreover, following the construction of $\hat{A}_\alpha$ from [278], the sum over the horizontal lines of w_α gives the probabilities for the z component of the spin, the sum over the vertical lines gives the probabilities for the x components and the sum on the diagonal ones gives the y component probabilities. As example, consider a spin pointing along the $z-$direction: $\hat{\rho} = |\uparrow\rangle\langle\uparrow|$. Its description in the discrete phase space will be

$$w_\alpha = \begin{array}{|c|c|}\hline w_{00} & w_{01} \\ \hline w_{10} & w_{11} \\ \hline \end{array} = \begin{array}{|c|c|}\hline 1/2 & 1/2 \\ \hline 0 & 0 \\ \hline \end{array} \, , \tag{2.59}$$

therefore the state will point along z with probability one, while the probability of being along $+x$ or $-x$ (or along $+y$ or $-y$) will be $1/2$.

If now we consider a composite system made of N spins $1/2$, the previous description can be immediately generalized. In this case, the space is represented by 4^N configurations: $\boldsymbol{\alpha} = \{\alpha_1, \alpha_2, \ldots, \alpha_N\}$. The phase-point operator is given by the tensor product of the single-sites one, as:

$$\hat{A}_{\boldsymbol{\alpha}} = \hat{A}_{\alpha_1} \otimes \hat{A}_{\alpha_2} \otimes \cdots \otimes \hat{A}_{\alpha_N} \, . \tag{2.60}$$

The expectation values of operators are written as

$$\langle \hat{O} \rangle = \sum_{\boldsymbol{\alpha}} w_{\boldsymbol{\alpha}} \, O^w_{\boldsymbol{\alpha}} \, , \tag{2.61}$$

with the discrete Wigner-function $w_{\boldsymbol{\alpha}} \equiv \frac{1}{2}\mathrm{Tr}[\hat{A}_{\boldsymbol{\alpha}}\hat{\rho}]$, where now $\hat{\rho}$ is the many-body density matrix and the Weyl transform of the operator: $O^w_{\boldsymbol{\alpha}} \equiv \mathrm{Tr}[\hat{O}\,\hat{A}_{\boldsymbol{\alpha}}]$. Notice that for pure states $\hat{\rho}$ is a sum of projectors, hence $w_{\boldsymbol{\alpha}}$ factorizes too. In particular for initially separable states, $w_{\boldsymbol{\alpha}}$ factorizes in the product of N independent spin-$1/2$

w_{α_j} with $j = 1, \ldots, N$. Indeed, the initial state $|\psi_0\rangle = |\uparrow\uparrow \ldots \uparrow\rangle$ will be mapped into $w_{\boldsymbol{\alpha}}(0) = \prod_{i=1}^{N} w_{\alpha_i}^{[i]}$ with $w_{\alpha_i}^{[i]}$ equal to Eq.(2.59) $\forall i$.

The *discrete* Truncated Wigner Approximation (DTWA) is equivalent to the TWA, but on this discrete phase space representation [284]. Hence, starting from Eq.(2.61), one evolves classically the Weyl symbol of the operator and averages over the initial Wigner function as

$$\langle \hat{O}(t) \rangle = \sum_{\boldsymbol{\alpha}} w_{\boldsymbol{\alpha}}(0)\, O_{\boldsymbol{\alpha}}^{\mathrm{w}}(t) \simeq \sum_{\boldsymbol{\alpha}} w_{\boldsymbol{\alpha}}(0)\, O_{\boldsymbol{\alpha}}^{\mathrm{w,cl}}(t) = \lim_{N_{\mathrm{sim}}\to\infty} \frac{1}{N_{\mathrm{sim}}} \sum_{m}^{N_{\mathrm{sim}}} O_{\boldsymbol{\alpha}_m}^{\mathrm{w,cl}}(t)\ , \quad (2.62)$$

where one extracts N_{sim} initial spin configurations according to the initial Wigner transform. The usual TWA integrates classical trajectories on continuous phase space and then averages over initial conditions, similarly, DTWA discretizes the initial conditions and then evolves them classically. This approximation is the same as shifting the time dependence on the phase-space operator and then to approximate it as factorized at every time t, as done in [284]

$$\hat{A}_{\boldsymbol{\alpha}}(t) \simeq \hat{A}_{\alpha_1}(t) \otimes \hat{A}_{\alpha_2}(t) \otimes \cdots \otimes \hat{A}_{\alpha_N}(t)\ . \quad (2.63)$$

This yields the classical equation of motion for the Weyl symbols. It corresponds, again, in assuming a second order cumulant closure on each trajectory.

2.2.3 Clustered TWA (CTWA)

The range of validity of the two previous methods is limited to quantum systems close to some classical limit [12]. On the other hand, these techniques are well known to fail in purely quantum many-body systems described by local Hamiltonians. In these cases, $\hbar_{\mathrm{eff}} = \hbar = 1$ making the Ehrenfest time (2.7) order one and correspondently the quantum dynamics occur onto an exponentially large Hilbert space. The numerical techniques to study such complex dynamics are restricted to very small systems sizes (exact diagonalization) or very small entanglement (MPS based algorithms).

Hence it is natural to wonder whether it is possible to extend phase-space methods to interpolate between the classical and the quantum dynamics. With this aim, Wurtz, Polkovnikov, and Sels introduced in Ref.[285] a cluster version of the truncated Wigner approximation, or CTWA. The idea consists in generalizing TWA to higher dimensional phase spaces, where phase space variables are associated with a complete set of quantum operators spanning finite-size clusters. Within the cluster, the quantum evolution is treated exactly, while different clusters interact at the mean-field level. Also in this case, the fluctuations are approximated to be Gaussians. This method reduces to the standard TWA for clusters of size one, while it becomes exact for a single cluster with the same size of the system. Crucially, the presence of the fluctuating initial conditions allows reproducing also quantum hydrodynamics of locally interacting systems [291]. Hence, CTWA can be seen as well as a powerful version of cluster mean-field equipped with the proper initial fluctuations

[12] Formally, it is restricted to systems characterized by a small parameter $\hbar$ or $\hbar_{\mathrm{eff}}$ which allows approximating the quantum Moyal brackets with the classical Poisson ones [cf. Eq.(2.36)]

CTWA improves standard phase-space approaches in mainly in two directions. First of all, this method becomes exact for a single cluster, namely when its size coincides with the system's one. Therefore, one can simulate models without a classical limit and study the convergence of the method upon increasing the cluster size. Secondly, CTWA allows studying operator scrambling by keeping exact the quantum dynamics on the cluster size. Notice that in the other approaches the support of the operator is always approximated as local, see e.g. Eq.(2.63).

This technique can be formulated equivalently using operators or wave-functions. In what follows we recall the main ideas of the operator approach in one dimension, while we refer the reader to Ref.[285] for all the details.

Consider a one-dimensional system of length L, which is split in N_{clust} clusters of length $L_{\text{clust}} = L/N_{\text{clust}}$. On each of them, one defines *a complete set of operators* $\{\hat{x}^{\alpha}_{i'}\}$, where $i' = 1, \dots, N_{\text{clust}}$, while $\alpha = 0, \dots D^2 - 1$ spans the Hilbert space of each cluster i' and D is its dimension. In the case of $1/2$-spins one has $D = 2^{L_{\text{clust}}}$. In the case of $N_{\text{clust}} = L$ one retrieves the TWA of Section 2.2.1 where the basis is spanned by the 2×2 Pauli matrices plus the identity. Conversely for a single cluster $N_{\text{clust}} = 1$ of L spins $1/2$ one retrieves the full Hilbert space dimensionality $D = 2^L$. The operator basis identifies the *structure constant* $f_{\alpha\beta\gamma}$ defined by the following commutator

$$[\hat{x}^{\alpha}_{i'}, \hat{x}^{\beta}_{j'}] = i\hbar \, f_{\alpha\beta\gamma} \, \delta_{i'j'} \, \hat{x}^{\gamma}_{i'} \, . \tag{2.64}$$

In the case of single spin variables $f_{\alpha\beta\gamma}$ coincides with the Levi-Civita symbol. This allows to re-write every generic Hamiltonian $\hat{H} = \hat{H}(\hat{\mathbf{x}})$ as a function of the operators $\{\hat{x}^{\alpha}_{i'}\}$. Notice that the terms of $\hat{H}$ defined within a single cluster are linear in $\hat{x}^{\alpha}_{i'}$, while terms connecting different clusters are signalled by an interaction term, e.g. $\hat{x}^{\alpha}_{i'}\hat{x}^{\beta}_{j'}$.

At this point, one proceeds with the *identification between the quantum operators* $\hat{x}^{\beta}_{j'}$ *and the classical variables* $x^{\alpha}_{i'}$. This is done with the same spirit of the Bopp transformations of Eq.(2.53) by the following transformation

$$\hat{x}^{\alpha}_{i'} \to x^{\alpha}_{i'} + \frac{i\hbar}{2} \, x^{i'}_{\beta} \, f_{\alpha\beta\gamma} \, \frac{\partial}{\partial x^{i'}_{\gamma}} \, , \quad \text{such that} \quad \{x^{\alpha}_{i'}, x^{j'}_{\beta}\} = \delta_{i'j'} \, f_{\alpha\beta\gamma} \, x^{i'}_{\gamma} \, , \tag{2.65}$$

where now $\{\cdot, \cdot\}$ represent Poisson brackets on this enlarged classical phase-space. Using this mapping, one can re-write the *Weyl symbols* of the Hamiltonian $\hat{H} \to H^{\text{w}} = H^{\text{w}}(\mathbf{x})$ and of the relevant observables $\hat{O} \to O^{\text{w}} = O^{\text{w}}(\mathbf{x})$. Therefore, as with the standard phase-space methods, also these generalized variables obey classical equations of motion

$$\dot{x}^{\alpha}_{i'} = \{x^{\alpha}_{i'}, H^{\text{w}}(\mathbf{x})\} = f_{\alpha\beta\gamma} \frac{\partial H^{\text{w}}(\mathbf{x})}{\partial x^{\beta}_{i'}} x^{\gamma}_{i'} \, . \tag{2.66}$$

These correspond to $N_{\text{clust}} \times (D^2 - 1)$ equations. By keeping fixed the cluster length L_{clust} (hence D), this number scales only linearly with the system size L and one can efficiently simulate the quantum dynamics of large systems. In the case of clusters of length one, this equation coincides with the classical spin precession in Eq.(2.46).

So far, we have only introduced a cluster mean-field. We now need to define the Wigner function of the initial state $|\psi_0\rangle$. For convenience, one starts from a pure separable state, whose Wigner function factorizes among the clusters, i.e. $W(\mathbf{x}(t=0)) = \prod_{i'=1}^{N_{\text{clust}}} W_{i'}(\{x_{i'}^{\alpha}(0)\})$. As for the TWA [cf. Eq.(2.48)], one considers a Gaussian approximation, by fixing the average values and variances of the of the basis operators

$$\langle\psi_0|\hat{x}_{i'}^{\alpha}|\psi_0\rangle = \overline{\overline{x_{i'}^{\alpha}(0)}} \ , \quad \frac{1}{2}\langle\psi_0|\hat{x}_{i'}^{\alpha}\hat{x}_{j'}^{\beta} + \hat{x}_{j'}^{\beta}\hat{x}_{i'}^{\alpha}|\psi_0\rangle = \overline{\overline{x_{i'}^{\alpha}(0)x_{j'}^{\beta}(0)}} \ , \tag{2.67}$$

where the double line represents the average over the initial Wigner function.

Finally, the initial conditions $\{x_{i'}^{\alpha}(0)\}$ sampled according to the Eq.(2.67), are evolved independently via the classical equation of motion (2.66). Through $\{x_{i'}^{\alpha}(t)\}$, CTWA allows to compute the time-dependent expectation values via the standard Montecarlo sampling

$$\langle\hat{O}(t)\rangle \simeq \overline{\overline{O^{\text{w}}(\mathbf{x}(t))}} = \lim_{N_{\text{sim}}\to\infty} \frac{1}{N_{\text{sim}}} \sum_{k=1}^{N_{\text{sim}}} O^{\text{w}}\left(\{\mathbf{x}_{i'}^{\alpha\,(k)}(t)\}\right) \ . \tag{2.68}$$

The above discussion fully captures the conceptual ideas beyond CTWA. As far as the numerical implementation is concerned, a further simplification occurs, namely a dimensional reduction from $N_{\text{clust}} \times (D^2-1)$ to $N_{\text{clust}} \times 2D$ equations. For the details of the numerical implementation used in the rest of the thesis, we follow Appendix D of Ref.[285].

2.2.4 Comparison between different semiclassical methods

In this section, we briefly show the salient features of the different TWA methods introduced above, in a regime when the validity of the semiclassical description is well justified. With this aim, we consider as an illustrative example the infinite-range Ising model with a transverse field for N spins $1/2$, i.e.,

$$\hat{H} = -\frac{J}{N}\,(\hat{S}^x)^2 - h_z\,\hat{S}^z \ . \tag{2.69}$$

This model is also known as the Lipkin-Meshkov-Glick (LMG) model [292], originally introduced in nuclear physics. Its entanglement properties will be intensively discussed in Section 3.2 before T_{Ehr} and in Section 4.2 beyond that. This system belongs to the class of fully-connected spin Hamiltonians (2.17) discussed in Section 2.1.2. Hence, ground states and out-of-equilibrium ones posses a maximum global spin $S = N/2$. Furthermore, the model is characterized by an effective Plank constant $\hbar_{\text{eff}} = 1/N$, and quantum observables are expected to obey the classical equations of motion before the Ehrenfest time (2.7), which in this case for generic trajectories reads $T_{\text{Ehr}} = \sqrt{N}$.

We consider the following protocol: The system is initialized in $|\psi_0\rangle = |\uparrow\uparrow\ldots\uparrow\rangle$ and evolved with the Hamiltonian (2.69), fixing $h_z/J = 2$. We inspect the time-evolution of the collective magnetization and of the variance along the z direction

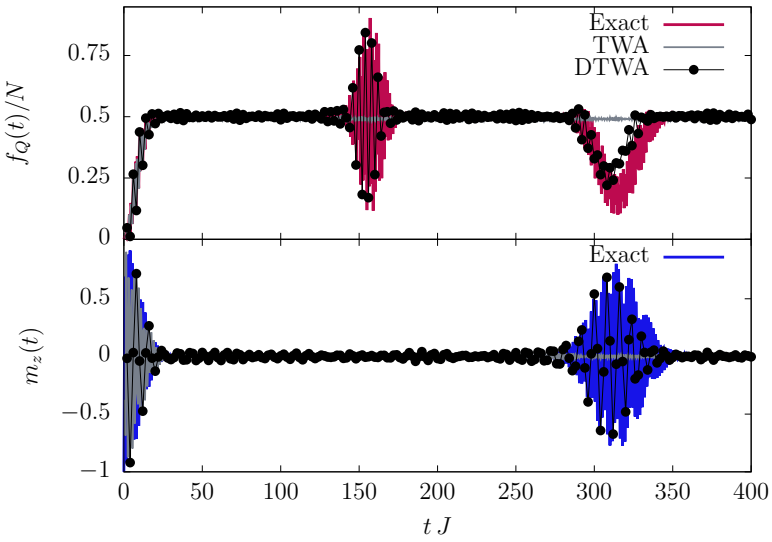

Figure 2.1: Comparison between the exact results obtained with ED and the different semiclassical approaches to the dynamics of collective observable $m_z(t)$ (bottom) and the collective variance (top). For $N = 100$ and $h_z/J = 2$. TWA and DTWA obtained with $N_{\text{sim}} = 5 \cdot 10^3$ samplings. In contrast with the other methods, DTWA is able to reproduce up to the recurrence time and beyond.

(which corresponds to the QFI (1.35) introduced in the previous Chapter), i.e.

$$m_z(t) = \frac{\langle \hat{S}^z(t) \rangle}{N/2} , \quad f_Q(t) = \frac{\langle \left(\hat{S}^z(t) \right)^2 \rangle - \langle \hat{S}^z(t) \rangle^2}{N} , \tag{2.70}$$

where $\hat{S}^z = \sum_{i=1} \hat{s}_i^z$ is the collective spin operator. We also study the operator scrambling via the square commutator in Eq.(1.45) fixing $\hat{B} = \hat{A} = \hat{S}^z$. We postpone the detailed discussion of the physical properties of these quantities to Section 3.2 and Section 4.2. Here, we aim at describing the methodological differences between the three phase-space approaches.

We compare the exact numerical results obtained with exact diagonalization (ED) with the semiclassical TWA [cf. Section 2.2.1], DTWA [cf. Section 2.2.2] and CTWA [cf. Section 2.2.3]. The Wigner functions corresponding to the intial state $|\psi_0\rangle$ are given in Eq.(2.47) Eq.(2.59) Eq.(2.67) respectively.

First of all, all the approaches reproduce the dynamics of collective observables and their variance up to the Ehrenfest time, where the exact quantum results saturate as a consequence of quantum interference. All the three methods replicate this saturation at T_{Ehr}, as a result of the classical interference between the various classical trajectories. See Figure 2.1 and Figure 2.2 on the left. The TWA treats the quantum degrees of freedom collectively and on a continuum phase-space. For this reason, this method does not capture long-time dynamics and, in particular, the revivals that occur in the exact quantum system as a consequence of the discreteness of the spectrum. On the other hand, the DTWA is well known to work incredibly well for both $m_z(t)$ and $f_Q(t)$ [284], as it reproduces the long-time behavior and the quantum recurrences. This is shown in Figure 2.1, where the DTWA prediction (black dots) is compared with the TWA ones (grey curve). We verified the long-

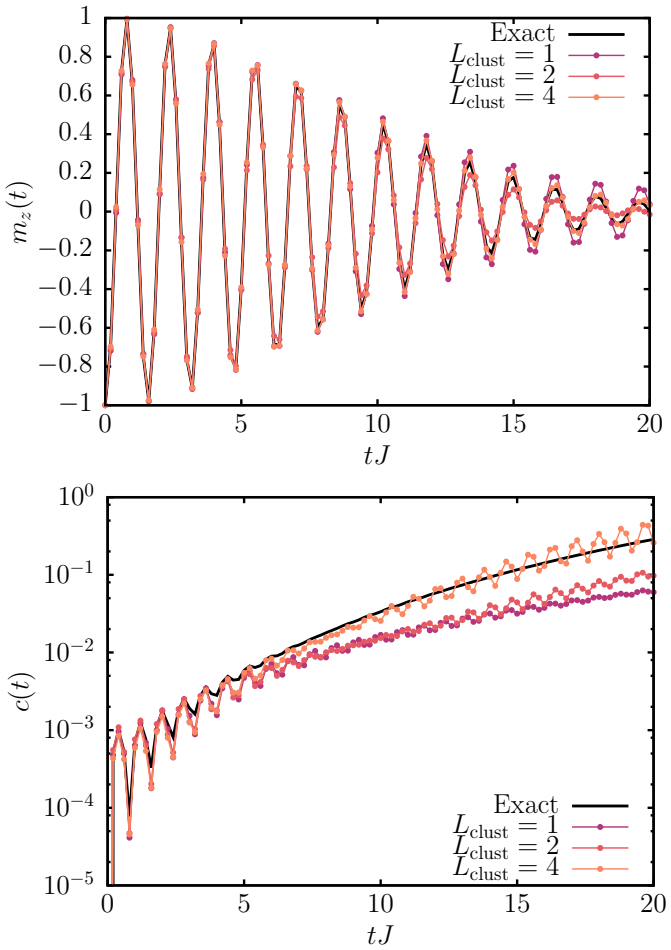

Figure 2.2: Comparison between the exact results obtained with ED and the CTWA simulations for fixed system size $N = 16$ and increasing cluster length $L_{\text{clust}} = 1, 2, 4$. (Top) Dynamics of the collective observable $m_z(t)$. (Bottom) Dynamics of the square commutator $c(t) = -\langle[\hat{S}_z(t), \hat{S}_z]^2\rangle$. By increasing cluster size L_{clust}, the CTWA reproduces the quantum dyanamics also beyond the Ehrenfest timescale, in the fully quantum regime. CTWA obtained with $N_{\text{sim}} = 5 \cdot 10^3$ samplings

time validity also for correlators at different times, like $\langle \hat{m}_x(0)\hat{m}_z(t)\rangle$. Note that even CTWA does not reproduce the recurrences. Even if in this case the degrees of freedom are treated individually, this method relies on a phase-space representation in a continuum phase-space. Hence, it can not capture the discrete properties of the quantum system.

As a second remark, we show the usefulness of the CTWA for studying the dynamics beyond T_{Ehr}. While collective observables and their variances saturate after the Ehrenfest time, the square commutator $c(t)$ describes the non-local growth of the operator support. As we will discuss in detail in Section 4.2, for generic quenches after T_{Ehr}, the square commutator displays a fully quantum dynamics signaling this operator growth. Such a regime can not be reproduced by the "local" semiclassical approaches, i.e. TWA or DTWA, which all assume that the operators are factorized on each site at all times [cf. Eq.(2.63)]. On the other hand, by increasing the clus-

ter size L_{cluster} in CTWA, one can retrieve the non-local growth of $\hat{S}^z(t)$ witnessed by $c(t)$. This is illustrated in the bottom of Figure 2.2, where the exact results are compared with the CTWA for different L_{cluster}.
An open question concerns the definition of a $L_{\text{clust}}(N)$ such that, for each system size N, the CTWA can reproduce the non-local growth of the operators. We leave this interesting problem for future work.

2.3 Time-dependent Holstein-Primakoff transformation

In this section, we describe a semi-analytical approach that complements the previous numerical phase-space techniques for the study of semiclassical dynamics. We shall limit the discussion to spin models, on which we mostly concentrate on the rest of the thesis. The method corresponds to a time-dependent expansion in quantum fluctuations around the classical solution [19, 293, 294]. Also in this case, the validity of the approximation is restricted before the Ehrenfest time [cf. Eq.(2.7)].

Time-dependent Holstein-Primakoff transformations aim at understanding the impact of quantum uncertainty on top of the classical physics of fully connected models, discussed in Section 2.1.2.
Quantum fluctuations naturally arise in two ways, very different in nature. The first concerns the quantum fluctuations of the collective degree of freedom controlled by $\hbar_{\text{eff}} = 1/N$. These are associated with the Heisenberg uncertainty and are the ones encoded in the initial Wigner function, see e.g. Section 2.2.1. These *collective fluctuations* (at zero momentum) do not break permutational symmetry, leaving the dynamics in the symmetric subspace, whose dimension scales only linearly with the system size. On the other hand, whenever permutational symmetry is broken, the second type of *quantum fluctuations* arises and participates in the dynamics *at all possible length scales*. As a result, the system is expected to eventually thermalize. It is natural to investigate the possible persistence of instances of semiclassical dynamics whenever permutational symmetry is broken. We here focus on small perturbations given by interactions depending on the spatial position of the spins.

In what follows, we will first describe this approach for the infinite range case (where only collective fluctuations are present) and we will then discuss its generalization in the presence of finite range of interactions. This method has been introduced and developed by Lerose and collaborators in Refs.[19, 293, 294], whose references we follow.

2.3.1 Infinite range systems

We start by analyzing fully connected spin Hamiltonians as given by Eq.(2.17) in Section 2.1.2. As an illustrative example, we examine again the fully connected LMG Hamiltonian (2.69). For generic spin s, the Hamiltonian reads

$$\hat{H} = -\frac{J}{2sN}\,(\hat{S}^x)^2 - h_z\,\hat{S}^z\,. \tag{2.71}$$

Consider typical states in and out of equilibrium characterized by a maximal collective spin magnitude. As discussed in Section 2.1.2, in the limit $N \to \infty$ they

can be pictured as point on a Bloch sphere of radius s, parametrized by the polar coordinates (θ, ϕ), possibly depending on time.

We will now illustrate how the following technique allows us to study equilibrium properties, such as ground state and the elementary excitations, as well as the out-of-equilibrium dynamics. Let us first introduce a rotated reference frame $\mathcal{R} = (\mathbf{X}, \mathbf{Y}, \mathbf{Z})$, such that the $\hat{Z}$ axis is aligned with the spin expectation value $\langle \vec{S} \rangle = Ns\mathbf{Z}$. In the time-dependent setup, this holds time by time, i.e. $\langle \vec{S}(t) \rangle = Ns\mathbf{Z}(t)$. This is achieved via rotation

$$\hat{V} = \hat{V}(\,\theta, \phi\,) = e^{-i\phi \hat{S}^z} e^{-i\theta \hat{S}^y} \,. \tag{2.72}$$

where the angles possibly depend on time $(\theta, \phi) = (\theta(t), \phi(t))$ in the out-of-equilibrium scenario. With this choice, the rotating frame $\mathcal{R}$ is parametrized by the Euler angles as

$$\mathbf{X} = \begin{pmatrix} \cos\theta\cos\phi \\ \cos\theta\sin\phi \\ -\sin\theta \end{pmatrix} , \quad \mathbf{Y} = \begin{pmatrix} -\sin\phi \\ \cos\phi \\ 0 \end{pmatrix} , \quad \mathbf{Z} = \begin{pmatrix} \sin\theta\cos\phi \\ \sin\theta\sin\phi \\ \cos\theta \end{pmatrix} . \tag{2.73}$$

The spins can be decomposed on the rotating basis and conversely. For example, the spin along the $\mathbf{Z}$ axis of the rotating frame reads

$$\hat{V}\, \hat{S}^z\, \hat{V}^\dagger \equiv \hat{S}^Z = \mathbf{Z} \cdot \hat{\mathbf{S}} = (\mathbf{Z} \cdot \mathbf{x})\, \hat{S}^x + (\mathbf{Z} \cdot \mathbf{y})\, \hat{S}^y + (\mathbf{Z} \cdot \mathbf{z})\, \hat{S}^z \,, \tag{2.74}$$

where the components are given by Eq.(2.73), for instance $\mathbf{Z} \cdot \mathbf{z} = \cos\theta$, $\mathbf{Z} \cdot \mathbf{x} = \sin\theta\cos\phi$ and $\mathbf{Z} \cdot \mathbf{y} = \sin\theta\sin\phi$.

In the new frame, one can safely bosonize the collective spin fluctuations via the Holstein-Primakoff transformations [295], expanding to the lowest order in $1/\sqrt{Ns}$. The collective spin reads

$$\begin{cases} \hat{S}^X &= \sqrt{N\,s}\,\hat{Q} \;+ \mathcal{O}\Big(1/\sqrt{sN}\Big) \\ \hat{S}^Y &= \sqrt{N\,s}\,\hat{P} \;+ \mathcal{O}\Big(1/\sqrt{sN}\Big) \\ \hat{S}^Z &= N\,s - \dfrac{\hat{Q}^2 + \hat{P}^2 - 1}{2} - \dfrac{\hat{q}^2 + \hat{p}^2 - 1}{2} = N\,s - \hat{n}_{\text{exc}} - \hat{n}_{\text{sw}} \end{cases} , \tag{2.75}$$

where we have defined

$$\hat{n}_{\text{exc}} \equiv \frac{\hat{Q}^2 + \hat{P}^2 - 1}{2} \,, \tag{2.76a}$$

$$\hat{n}_{\text{sw}} \equiv \frac{\hat{q}^2 + \hat{p}^2 - 1}{2} \,, \tag{2.76b}$$

the number of collective and spin-waves excitations respectively. In fact, the $(\hat{Q}, \hat{P})$ mode represents uniform collective spin excitations in the entire system, and, accordingly, does not affect the collective spin magnitude $\hat{\mathbf{S}}^2$. On the other hand, the $(\hat{q}, \hat{p})$ mode represents out-of-phase excitations of spins, or "spin waves"[13], which decrease the collective spin magnitude

$$\hat{\mathbf{S}}^2 = (Ns - \hat{n}_{\text{sw}})\,(Ns - \hat{n}_{\text{sw}} + 1) \,. \tag{2.77}$$

[13] The reason why we refer to them as spin waves will be caryfied in next section.

Using Eqs. (2.75), the expansion of the Hamiltonian has the form

$$\begin{aligned}\hat{H} = Ns\,\mathcal{H}_{\rm cl}(\theta,\phi) + \sqrt{Ns}\Big[h^{(1)}_Q\,\hat{Q} + h^{(1)}_P\,\hat{P}\Big] \\ + h^{(2)}_{QQ}\,\frac{\hat{Q}^2}{2} + h^{(2)}_{PP}\,\frac{\hat{P}^2}{2} + h^{(2)}_{QP}\,\frac{\hat{Q}\hat{P}+\hat{P}\hat{Q}}{2} + h^{(2)}_{\rm sw}\,\hat{n}_{\rm sw} + O\Big(1/\sqrt{sN}\Big)\,,\end{aligned} \tag{2.78}$$

where the explicit expression of the time-dependent coefficients $\mathcal{H}_{\rm cl}(\theta,\phi)$, $h^{(1)} = h^{(1)}(\theta,\phi)$, $h^{(2)}(t) = h^{(2)}(\theta,\phi)$ is given by the couplings J of the specific Hamiltonian (2.17). The example in Eq.(2.71) reads

$$\begin{aligned}\hat{H} =& Ns\left(-\frac{J}{2}\sin^2\theta\cos^2\phi - h_z\cos\theta\right) \\ &+ \sqrt{Ns}\left[\hat{Q}\left(h_z\sin\theta - J\cos\theta\sin\theta\cos^2\phi\right) + \hat{P}\left(J\sin\theta\cos\phi\sin\phi\right)\right] \\ &+ \frac{\hat{Q}^2}{2}\left(h_z\cos\theta + J\sin^2\theta\cos^2\phi - J\cos\theta^2\cos\phi^2\right) + \frac{\hat{P}^2}{2}\left(h_z\cos\theta + J\sin^2\theta\cos^2\phi - J\sin^2\phi\right) \\ &+ \frac{\hat{Q}\hat{P}+\hat{P}\hat{Q}}{2}\left(J\cos\theta\cos\phi\sin\phi\right) + \hat{n}_{\rm sw}\left(h_z\cos\theta + J\sin^2\theta\cos^2\phi\right) + O\Big(1/\sqrt{sN}\Big)\end{aligned} \tag{2.79}$$

At equilibrium, the angles (θ,ϕ) are fixed in such a way that the linear terms $h^{(1)}$ vanish, and, to leading order in $1/N$, this yields the minimum point of the classical Hamiltonian $\mathcal{H}_{\rm cl}$. The mode $(\hat{q},\hat{p})$ enters Eq. (2.78) only through the number of bosons $\hat{n}_{\rm sw}$ (2.76b), and, accordingly, these spin waves cannot be excited in the ground state nor dynamically in infinite-range systems, i.e.,

$$\langle \hat{n}_{\rm sw}\rangle \equiv 0\,. \tag{2.80}$$

For the same reason one also has vanishing mixed correlations

$$\langle \hat{q}\hat{Q}\rangle = \langle \hat{p}\hat{P}\rangle = \langle \hat{q}\hat{P}\rangle = \langle \hat{p}\hat{Q}\rangle \equiv 0\,. \tag{2.81}$$

On the other hand, the number of collective excitations $\hat{n}_{\rm exc}$ (2.76a) is not conserved. In the ground state, correlations of $\hat{Q}$ and $\hat{P}$ are non-trivially related to the coefficients of the quadratic part of the Hamiltonian, and can be obtained by diagonalizing $\hat{H}$ with a generalized Bogoliubov transformation [14].

Let us now discuss the out-of-equilibrium scenario. When the system is driven out of equilibrium, the direction of the collective spin configuration $\theta(t)$, $\phi(t)$ moves along the corresponding classical trajectory on the sphere. Following Refs. [293, 294], the motion of the angles $\theta(t)$, $\phi(t)$ can be accounted for by letting the rotated

[14] These can be achieved for example as

$$\begin{cases}\hat{Q} = e^{\gamma}\cos\eta\,\hat{Q}' - e^{\gamma}\sin\eta\,\hat{P}' \\ \hat{P} = e^{-\gamma}\sin\eta\,\hat{Q}' + e^{-\gamma}\cos\eta\,\hat{P}'\end{cases} \quad \text{with} \quad \tan(2\eta) \equiv \frac{h^{(2)}_{QP}}{h^{(2)}_{QQ}+h^{(2)}_{PP}}\,, \quad e^{2\gamma} \equiv \frac{h^{(2)}_{QQ}+h^{(2)}_{PP}-\Delta}{h^{(2)}_{QQ}+h^{(2)}_{PP}+\Delta}, \tag{2.82}$$

and with $\Delta \equiv (h^{(2)}_{QQ} - h^{(2)}_{PP})\cos(2\eta) + 2h^{(2)}_{QP}\sin(2\eta)$.

frame $(\mathbf{X}, \mathbf{Y}, \mathbf{Z})$ in Eq. (2.73) change in time in such a way that the $\mathbf{Z}$-axis self-consistently follows the evolution of $\langle \hat{\mathbf{S}}(t) \rangle = Ns\hat{Z}(t)$. The Heisenberg equations for $\hat{S}^\alpha$ with $\alpha \in \mathcal{R}$ on the mobile frame will then read

$$\frac{d}{dt}\,\hat{S}^\alpha = \frac{d}{dt}\,V\hat{S}^a V^\dagger = \frac{1}{i}[\hat{S}^\alpha, \tilde{H}]\;, \tag{2.83}$$

with the time-dependent Hamiltonian

$$\tilde{\hat{H}}(t) \equiv \hat{V}\,\hat{H}\,\hat{V}^\dagger + i\hat{V}\dot{\hat{V}}^\dagger\;, \tag{2.84}$$

which includes a $\hat{V}$-dependent term in analogy with the emergence of apparent forces in classical mechanics in a rotating frame. A simple calculation shows

$$i\hat{V}\dot{\hat{V}}^\dagger = -\,\boldsymbol{\omega}(t)\cdot\hat{\mathbf{S}}\;, \qquad \text{with} \quad \boldsymbol{\omega}(t) = \begin{pmatrix} -\sin\theta\,\dot{\phi} \\ \dot{\theta} \\ \cos\theta\,\dot{\phi} \end{pmatrix}\;. \tag{2.85}$$

The resulting time-dependent Hamiltonian $\tilde{\hat{H}}(t)$ is then computed from Eq.(2.17) via Eq.(2.84). The linear terms in the new frame, denoted $\tilde{h}^{(1)}$, change as

$$\tilde{h}^{(1)}_Q(t) \equiv h^{(1)}_Q(\theta(t),\phi(t)) + \sin\theta(t)\;\dot{\phi}\;, \tag{2.86a}$$

$$\tilde{h}^{(1)}_P(t) \equiv h^{(1)}_P(\theta(t),\phi(t)) - \dot{\theta}\;, \tag{2.86b}$$

while quadratic ones, denoted $\tilde{h}^{(2)}(t)$ are given by

$$\tilde{h}^{(2)}_{QQ,PP,\mathrm{sw}}(t) \equiv h^{(2)}_{QQ,PP,\mathrm{sw}}\big(\theta(t),\phi(t)\big) - \cos\theta(t)\;\dot{\phi}, \tag{2.87a}$$

$$\tilde{h}^{(2)}_{QP}(t) \equiv h^{(2)}_{QP}\big(\theta(t),\phi(t)\big). \tag{2.87b}$$

Hence, the evolution of $\theta(t)$ and $\phi(t)$ is determined by the vanishing of the linear terms $\tilde{h}^{(1)}(t)$, ensuring

$$\langle \hat{S}^X(t)\rangle = \langle \hat{S}^Y(t)\rangle = 0\;. \tag{2.88}$$

This yields the classical trajectory governed by the classical Hamiltonian $\mathcal{H}_{\mathrm{cl}}$. In the LMG example (2.71), the equations of motion read

$$\begin{cases} \dot{\theta} = J\sin\theta\cos\phi\sin\phi \\ \dot{\phi} = -h_z + J\cos\theta\cos^2\phi \end{cases}\;. \tag{2.89}$$

Note that the spin-wave mode $\hat{n}_{\mathrm{sw}}$ (2.76b) is still conserved [cf. Eq.(2.80)], since $[\tilde{\hat{H}}(t), \hat{n}_{\mathrm{sw}}] = 0$ at all orders in the Holstein-Primakoff expansion. On the other hand, the number of collective excitations $\hat{n}_{\mathrm{exc}}$ (2.76a) is not conserved and it evolves in time. Its dynamics is governed by the time-dependent quadratic part $\widetilde{h}^{(2)}(t)$ in Eq.(2.87a). These determine the dynamical generation of collective bosonic excitations $(\hat{Q}, \hat{P})$, which can be monitored thorugh the correlation functions $G^{QQ}(t)$, $G^{QP}(t)$, $G^{PP}(t)$. In order to evaluate them, one computes the Heisenberg equations of motion

$$\begin{cases} \dot{\hat{Q}} = +\widetilde{h}^{(2)}_{QP}(t)\;\hat{Q} + \widetilde{h}^{(2)}_{PP}(t)\;\hat{P} \\ \dot{\hat{P}} = -\widetilde{h}^{(2)}_{QQ}(t)\;\hat{Q} - \widetilde{h}^{(2)}_{QP}(t)\;\hat{P} \end{cases}\;, \tag{2.90}$$

that admit as formal solution $\begin{pmatrix}\hat{Q}(t)\\ \hat{P}(t)\end{pmatrix} = U(t)\begin{pmatrix}\hat{Q}(0)\\ \hat{P}(0)\end{pmatrix}$, with $U(t)$ the evolutor. One can collect the dynamical correlations

$$\begin{cases} G^{QQ}(t) \equiv \langle \hat{Q}^2(t)\rangle, \\ G^{PP}(t) \equiv \langle \hat{P}^2(t)\rangle, \\ G^{QP}(t) \equiv \dfrac{\langle \hat{Q}(t)\hat{P}(t) + \hat{P}(t)\hat{Q}(t)\rangle}{2}, \end{cases} \tag{2.91}$$

in the *correlation matrix*

$$G(t) = \begin{pmatrix} G^{QQ}(t) & G^{QP}(t) \\ G^{QP}(t) & G^{PP}(t)\end{pmatrix} = U(t)\, G(t=0)\, U^T(t), \tag{2.92}$$

and the number of dynamically generated excitations can be expressed as

$$\langle \hat{n}_{\rm exc}(t)\rangle = \frac{G^{QQ}(t) + G^{PP}(t) - 1}{2} = \frac{1}{2}\mathrm{Tr}\left[G(t) - \frac{\mathbb{1}}{2}\right]. \tag{2.93}$$

Note that $\det G(t) \equiv 1/4$, which is an exact property of *pure* Gaussian states preserved by the evolution Eq. (2.90). In the example under analysis(2.71), the equation of motion for the correlations (2.91) read

$$\begin{cases} \dot{G}^{QQ} = 2J\cos\theta\sin\phi\cos\phi\, G^{QQ} + 2J\left(\cos^2\phi - \sin^2\phi\right) G^{QP} \\ \dot{G}^{PP} = -2J\cos\theta\sin\phi\cos\phi\, G^{PP} - 2J\cos^2\phi\sin^2\theta\, G^{PQ} \\ \dot{G}^{PQ} = -J\cos^2\phi\sin^2\theta\, G^{QQ} + J\left(\cos^2\phi - \sin^2\phi\right) G^{PP} \end{cases}. \tag{2.94}$$

The formalism outlined in this section relies on the truncation of the Holstein-Primakoff transformation (2.75), which is accurate for Gaussian states with a small number of collective excitations $\langle \hat{n}_{\rm exc}\rangle \ll N$ compared to the system size. This assumption is generically valid for ground states, even at the quantum critical points [296, 297], as well as in the non-equilibrium setting before the Ehrenfest time (2.7). Within this language the latter is defined as well as the time for which fluctuations become of the order of the system size, i.e. $\langle \hat{n}_{\rm exc}(T_{\rm Ehr})\rangle \sim N$.

2.3.2 Systems with finite range of interactions

In order to study the impact of fluctuations on the physics of the fully-connected spin models (2.17), we resort to the method introduced and developed in Ref.[293, 294]. To be conceptually clear, it is convenient to consider a toy model with additional finite-range interactions, e.g.

$$\hat{H} = -\frac{J}{2sN}(\hat{S}^x)^2 - h_z\,\hat{S}^z - \sum_{\mathbf{r},\mathbf{r}'} J_{\mathbf{r},\mathbf{r}'}\hat{\sigma}^x_{\mathbf{r}}\hat{\sigma}^x_{\mathbf{r}'}\,, \tag{2.95}$$

where $\mathbf{r},\mathbf{r}'$ run over a d-dimensional lattice with N sites, and the coupling $J_{\mathbf{r},\mathbf{r}'} \equiv J_{\mathbf{r}}$ decays with the distance $\mathbf{r} = |\mathbf{r} - \mathbf{r}'|$. The distance $|\mathbf{r}_i - \mathbf{r}_j|$ between two sites

on the periodic lattice can be taken to be $\sqrt{\sum_{\mu=1}^{d}\left[\min(|r_i^\mu - r_j^\mu|, L - |r_i^\mu - r_j^\mu|)\right]^2}$. For illustration purposes we now focus on the one-dimensional $d = 1$ case, even if the results do not depend on this assumption, as we will see when we apply this technique to the long-range case in Section 5.1.

The formalism introduced in the previous section can be refined to make it suitable for many-body problems. The idea is to expand the individual spins around the instantaneous direction $\langle \mathbf{S}(t)\rangle = Ns\mathbf{Z}$ of the collective spin, via Holstein-Primakoff transformations

$$\hat{\mathbf{s}}_j \simeq \sqrt{s}\,\mathbf{X}\,\hat{q}_j + \sqrt{s}\,\mathbf{Y}\,\hat{p}_j + \mathbf{Z}\left(s - \frac{\hat{q}_j^2 + \hat{p}_j^2 - 1}{2}\right) \tag{2.96}$$

where the time-dependent rotated frame $(\mathbf{X}, \mathbf{Y}, \mathbf{Z})$ parameterized by spherical angles θ, ϕ was introduced in Eq. (2.73). Before, we consider the Fourier transform of the Hamiltonian (2.95) via $\tilde{\hat{\mathbf{a}}}_k = \sum_j e^{-ikj}\,\hat{\mathbf{s}}_j$, with $k = 2\pi n/N$ with $n = 0, \ldots, N-1$. This yields

$$\hat{H} = -\frac{J_0}{2Ns}\,(\tilde{\hat{s}}_0^x)^2 - h_z\,\tilde{\hat{s}}_0^z - \frac{1}{Ns}\sum_{k\neq 0}\tilde{J}_k\;\tilde{\hat{s}}_k^x\,\tilde{\hat{s}}_{-k}^x\;, \tag{2.97}$$

where $\tilde{J}_k = \tilde{J}_k = \sum_{r=0}^{N-1} e^{-ikr} J_r$ and $J_0 = J + \tilde{J}_0$. Evidently, the fully connected Hamiltonian (2.71) is function only of the zero mode $k = 0$, while the distance dependent perturbation involves all the modes at $k \neq 0$. When the perturbation is small, the degree of excitation of the modes with $k \neq 0$ is expected to be minor, at least in the dynamical transient.

One then performs the time-dependent transformation from $\hat{H}$ to $\tilde{\hat{H}}(t)$ and then apply the Holstein-Primakoff transformations (2.96). The transformed generic Hamiltonian reads

$$\tilde{\hat{H}}(t) = \tilde{\hat{H}}_0(t) + \hat{H}_{\rm sw}(t) + \frac{1}{\sqrt{Ns}}\hat{U}_3(t) + \frac{1}{Ns}\hat{U}_4(t) + O\left(\frac{1}{(Ns)^{3/2}}\right)\;. \tag{2.98}$$

Let us discuss one by one the terms appearing in Eq.(2.98). The element $\tilde{\hat{H}}_0(t)$ describes the collective spin and its excitations. It coincides with the infinite-range Hamiltonian (2.84) discussed above. It is now clear that the quantum fluctuations of the collective spin (2.76a) coincide with the zero-mode fluctuations

$$\hat{Q} \equiv \tilde{q}_{\mathbf{0}}\;, \quad \hat{P} \equiv \tilde{p}_{\mathbf{0}}\;, \quad \hat{n}_{\rm exc} \equiv \hat{n}_0\;, \tag{2.99}$$

while that the total number spin-wave excitations $\hat{n}_{\rm sw}$ (2.76b) is given by the sum of bosonic occupation numbers of all the other spin-wave modes at finite wavelength

$$\hat{n}_{\rm sw} = \sum_{k\neq 0}\hat{n}_k\;, \quad \text{with} \quad \hat{n}_k \equiv \frac{\tilde{q}_k\tilde{q}_{-k} + \tilde{p}_k\tilde{p}_{-k} - 1}{2}\;. \tag{2.100}$$

Notice that $\hat{n}_k$ are an exact conserved quantity of the collective-mode Hamiltonian $\widetilde{H}_0(t)$, as $\left[\hat{n}_{\mathbf{k}}, \widetilde{\hat{H}}_0\right] = 0$ for all $\mathbf{k} \neq 0$.

On the other hand, the other terms in Eq.(2.98) $\tilde{\hat{H}}_{\rm sw}(t)$, $\hat{U}_3(t)$, $\hat{U}_4(t)$ represent the quadratic, cubic and quartic contribution in the spin-waves respectively. They are proportional to $\widetilde{J}_{k\neq 0}$ and read

$$\hat{H}_{\rm sw}(t) = \sum_{k\neq 0} \widetilde{J}_k \left[h^{(2)}_{qq}(t)\, \frac{\tilde{q}_k \tilde{q}_{-k}}{2} + h^{(2)}_{pp}(t)\, \frac{\tilde{p}_k \tilde{p}_{-k}}{2} + h^{(2)}_{qp}(t)\, \frac{\tilde{q}_k \tilde{p}_{-k} + \tilde{p}_k \tilde{q}_{-k}}{2} \right] , \tag{2.101a}$$

$$\begin{aligned} \hat{U}_3(t) = \sum_{k\neq 0} \widetilde{J}_k \Bigg[& h^{(3)}_{q}(t)\, \tilde{q}_k \sum_{k'} \frac{\tilde{q}_{k'} \tilde{q}_{-k-k'} + \tilde{p}_k \tilde{p}_{-k-k'}}{2} + (k \leftrightarrow k') \\ & + h^{(3)}_{p}(t)\, \tilde{p}_k \sum_{k'} \frac{\tilde{q}_{k'} \tilde{q}_{-k-k'} + \tilde{p}_k \tilde{p}_{-k-k'}}{2} + (k \leftrightarrow k') \Bigg] , \end{aligned} \tag{2.101b}$$

$$\hat{U}_4(t) = \sum_{k\neq 0} \widetilde{J}_k\; h^{(4)}(t) \sum_{k'} \frac{\tilde{q}_{k'} \tilde{q}_{-k-k'} + \tilde{p}_k \tilde{p}_{-k-k'}}{2} \sum_{k''} \frac{\tilde{q}_{k''} \tilde{q}_{-k-k''} + \tilde{p}_k \tilde{p}_{-k-k''}}{2} , \tag{2.101c}$$

where the exact expression of $h^{(2)}(t)$, $h^{(3)}(t)$ and $h^{(4)}(t)$ depends on the specific couplings in the Hamiltonian under analysis. We postpone the calculations of the specific formulae of $h^{(2/3/4)}(t)$ for the relevant examples studied in this thesis, see e.g. Section 5.1.

We remark that this Gaussian approximation is accurate whenever $\widetilde{J}_{k\neq 0}$ induces only a small perturbation on top of the mean-field limit, such that when the spin waves *density* $\epsilon(t)$ generated by the dynamics remains small, i.e.

$$\epsilon(t) \equiv \frac{\langle \hat{n}_{\rm sw}(t) \rangle}{Ns} \ll 1 , \tag{2.102}$$

where $\hat{n}_{\rm sw}$ has been defined in Eq.(5.5). This corresponds to the requirement that the collective spin magnitude remains very close to the maximal value $S = Ns$. In fact, it is easy to show, see e.g. Eq.(2.77), that each spin wave with $k \neq 0$ decreases the collective spin magnitude by one unit, i.e.

$$|\hat{\mathbf{S}}|^2 = (Ns - \hat{n}_{\rm sw})\,(Ns - \hat{n}_{\rm sw} + 1) \ . \tag{2.103}$$

In this regime, the spin waves can be treated as weakly-interacting bosonic excitations. In principle, in Eq.(2.98) higher-order terms would arise, accounting for nonlinear scattering among the spin waves. In this treatment, they are expected to contribute to the dynamics only at times parametrically long in the spin-wave density.

Now, one would like to solve the dynamics governed by the Hamiltonian in Eq.(2.97), which describes the dynamics of the angles (θ, ϕ) and of the excitations $\tilde{q}_k$, $\tilde{p}_k$. Following Ref.[293, 294], one realizes that the only relevant interaction between the collective mode $\tilde{q}_0$, $\tilde{p}_0$ and the finite wave-length spin waves is encoded in terms of $\hat{U}_3(t)$ with $k' = 0, \pm k$ describing the scattering of a zero-momentum mode in a pairs of spin waves with opposite momenta or viceversa. By keeping into

account those terms[15], one can study how the dynamics of the of spin waves impact on the mean-field dynamics of the classical angles (θ, ϕ). Their equation of motion is again found by imposing the condition (2.88), namely by setting the coefficients of $\tilde{q}_0$ and $\tilde{p}_0$ in the Hamiltonian to zero. This yields a pairs of modified equations for the angles $\theta(t), \phi(t)$. In the example under analysis, Eqs.(2.89) become

$$\begin{cases} \dfrac{d}{dt}\theta = +J(1-\epsilon)\sin\theta\cos\phi\sin\phi \\ \qquad\qquad -\left(\dfrac{1}{Ns}\displaystyle\sum_{k\neq 0}\tilde{J}_k\ \langle\tilde{p}_k\tilde{p}_{-k}\rangle\right)\sin\theta\cos\phi\sin\phi \\ \qquad\qquad +\left(\dfrac{1}{Ns}\displaystyle\sum_{k\neq 0}\tilde{J}_k\dfrac{\langle\tilde{q}_k\tilde{p}_{-k}+\tilde{p}_k\tilde{q}_{-k}\rangle}{2}\right)\cos\theta\sin\theta\cos^2\phi, \\ \dfrac{d}{dt}\phi = -h+J(1-\epsilon)\cos\theta\cos^2\phi \\ \qquad\qquad -\left(\dfrac{1}{Ns}\displaystyle\sum_{k\neq 0}\tilde{J}_k\ \langle\tilde{q}_k\tilde{q}_{-k}\rangle\right)\cos\theta\cos^2\phi \\ \qquad\qquad +\left(\dfrac{1}{Ns}\displaystyle\sum_{k\neq 0}\tilde{J}_k\dfrac{\langle\tilde{q}_k\tilde{p}_{-k}+\tilde{p}_k\tilde{q}_{-k}\rangle}{2}\right)\sin\phi\cos\phi, \end{cases} \tag{2.104}$$

where ϵ is the spin-wave density of Eq.(2.102).

Let us now turn to spin-waves Hamiltonian $\hat{H}_{\rm sw}(t)$ which is equivalent to a set of *periodically driven quantum harmonic oscillators*, labeled by the quasimomentum $\mathbf{k}$. Their dynamics can be found by computing the commutator with the Hamiltonian (2.101a), that yields

$$\begin{cases} \dfrac{d}{dt}\tilde{q}_k = -h^{(2)}_{\rm sw}\ \tilde{p}_k + \tilde{J}_k\, h^{(2)}_{qp}(t)\ \tilde{q}_k + \tilde{J}_k\, h^{(2)}_{pp}(t)\tilde{p}_k \\ \dfrac{d}{dt}\tilde{p}_k = +h^{(2)}_{\rm sw}\ \tilde{q}_k - \tilde{J}_k\ h^{(2)}_{qq}(t)\ \tilde{q}_k - \tilde{J}_k\ h^{(2)}_{qp}(t)\ \tilde{p}_k \end{cases}, \tag{2.105}$$

where $h^{(2)}_{\rm sw}$ comes from the zero-mode Hamiltonian in Eq.(2.78). We further define the equal time correlation functions appearing in Eq.(2.104)

$$G^{qq}_k(t) \equiv \langle\, \tilde{q}_k(t)\tilde{q}_{-k}(t)\,\rangle \tag{2.106a}$$
$$G^{pp}_k(t) \equiv \langle\, \tilde{p}_k(t)\tilde{p}_{-k}(t)\,\rangle \tag{2.106b}$$
$$G^{qp}_k(t) \equiv \frac{1}{2}\langle\, \tilde{q}_k(t)\tilde{p}_{-k}(t) + \tilde{p}_k(t)\tilde{q}_{-k}(t)\rangle\ . \tag{2.106c}$$

Combining them with the equation for the spin waves coordinates (2.105) one obtains the evolution of the spin-waves fluctuations. In the case of the example (2.71),

[15] This corresponds to a Gaussian approximation which truncates at quadratic order both the collective mode at $k = 0$ and the spin waves and $k \neq 0$.

they read

$$\begin{cases} \dfrac{d}{dt}G_k^{qq} = 2\tilde{J}_k \cos\theta\cos\phi\sin\phi\, G_k^{qq} + 2\left(J\cos^2\phi - \tilde{J}_k \sin^2\phi\right) G_k^{qp}, \\ \dfrac{d}{dt}G_k^{pp} = -2\left(J\cos^2\phi - \tilde{J}_k \cos^2\theta\cos^2\phi\right) G_k^{qp} - 2\tilde{J}_k \cos\theta\cos\phi\sin\phi\,\Delta_k^{pp}, \\ \dfrac{d}{dt}G_k^{qp} = -\left(J\cos^2\phi - \tilde{J}_k \cos^2\theta\cos^2\phi\right) G_k^{qq} + \left(J\cos^2\phi - \tilde{J}_k \sin^2\phi\right) G_k^{pp} \end{cases} . \tag{2.107}$$

These equations of motion describe the dynamics of the Gaussian wavefunction of the spin waves. As for Eqs.(2.94), also these equations are not independent since the fluctuations are related by

$$4(G_k^{pq})^2 = 4\, G_k^{pp}\, G_k^{qq} - 1\ , \tag{2.108}$$

which is an exact property of Gaussian pure states (equivalent to having minimal quantum uncertainty), and which is then satisfied at all times and for all values of k.

The dynamical problem is now fully specified by the system of coupled evolution equations (2.104) and (5.20), together with suitable initial conditions, which may correspond to the ground state or a thermal state of the pre-quench Hamiltonian.

Chapter 3

Bridging entanglement dynamics and chaos in semiclassical models

In this chapter, we present a unifying framework that directly connects the bipartite and multipartite entanglement growth to the quantifiers of classical and quantum chaos in the semiclassical regime. Analytical predictions are confirmed by detailed numerical calculations for paradigmatic models, relevant in atomic and optical experiments: the fully connected Ising model, the quantum kicked top, and the Dicke model.

To isolate the contribution of collective degrees of freedom to entanglement dynamics of long-range systems, in this chapter we consider fully-connected models and, more generally, semiclassical evolution.

As argued in the first chapter, entanglement is arguably one of the most insightful properties of composite quantum systems. However, quantum dynamics can often exhibit a semiclassical behavior, as illustrated in the second chapter. Accordingly, understanding how to reconcile quantum entanglement with such semiclassical dynamics has been under debate since the early days of quantum mechanics.

An early insight was proposed by the seminal work of Zurek and Paz on decoherence in open systems [298, 299]. These authors conjectured that in a system coupled to an environment, the rate of entropy growth is equal to the sum of the positive Lyapunov exponents, the classical Kolmogorov-Sinai entropy rate [300–302]. A large body of numerical and analytical studies during early 2000 [267, 303–317] proved consistent with the Zurek-Paz surmise, establishing that the transient entanglement generation is associated with decoherence and suggesting further relationships between semiclassical entanglement dynamics and the chaoticity of the underlying trajectories. Related work focused on understanding the emergence of quantum irreversibility and decoherence through the dynamics of the purity and the Loschmidt echo [cf. Eq.(1.42)] [318, 319]. As discussed in Chapter 1, more recently the interest in entanglement properties of many-particle systems spread to several theoretical research communities, ranging from statistical physics [102] and condensed matter theory [103] to quantum information [104, 105] and high-energy physics [106, 107]. In this context, the Zurek-Paz conjecture has recently been laid on firm mathematical grounds by Bianchi *et al.* in Ref.[320], see also Refs.[321, 322].

In this chapter, we present a systematic and unifying picture connecting the bipartite and multipartite entanglement growth to the quantifiers of classical and

quantum chaos, which applies whenever a quantum system is characterized by an emergent semiclassical limit. We target many-particle systems with collective interactions initialized in quasiclassical states and let to evolve in isolation. The quantum fluctuations around the limiting classical trajectory remain under control until the so-called Ehrenfest time scale [cf. Eq.(2.7)], which diverges in the thermodynamic limit. By expanding the Hamiltonian in terms of the instantaneous quantum fluctuations, we show that their dynamics determine all the quantifiers of entanglement and chaos introduced above.

Following standard semiclassical arguments, the time-evolving correlation matrix of the quantum fluctuations, in turn, coincides with the classical Oseledets multiplicative matrix, which encodes the local divergence of nearby semiclassical trajectories via the finite-time Lyapunov spectrum. This allows us to write down an explicit analytical expression for the von Neumann entanglement entropy, the quantum Fisher information, the spin squeezing, and the square commutator in the semiclassical regime. Accordingly, the transient growth of these quantities before saturation is dictated by the nature of the underlying classical phase-space. In the absence of semiclassical chaos, the entanglement entropy grows logarithmically in time, while the multipartite and the square commutator grow quadratically. Contrarily, whenever chaos is present, the entanglement entropy grows linearly with a slope equal to the sum of the largest local Lyapunov exponents (in agreement with the Zurek-Paz conjecture), whereas the quantum Fisher information and the square commutator grow exponentially fast in time with a rate given by twice the local largest Lyapunov exponent. The same occurs for unstable trajectories in integrable systems.

The analysis is corroborated by detailed numerical computations in paradigmatic many-body collective quantum systems of current experimental relevance, namely the integrable Lipkin-Meshov-Glick model [292], and the quantum kicked top [323, 324], and the Dicke model [325, 326]. We find excellent agreement with the analytical predictions in all dynamical regimes. In particular, we observe and rationalize strong deviations from the asymptotic Lyapunov exponents, particularly apparent in regimes with mixed regular-chaotic phase space or with dynamical instabilities.

Semiclassical dynamics are studied with the same framework and notations as discussed in Section 2. The rest of the chapter is organized as follows. In Section 3.1, we present our analysis: We derive the general dynamics of quantum fluctuations around a semiclassical trajectory, and show how the entanglement measures can be explicitly related to that. In Sections 3.2-3.4, we introduce and study numerically the LMG model, quantum kicked top, and the Dicke model. We show the validity of the analytical predictions in all the different dynamical regimes. Finally, in Section 3.5 we present our conclusions and perspectives.

3.1 General theory

3.1.1 A classical interlude: the Lyapunov spectrum

Before describing the dynamics of quantum fluctuations around the classical solution, let us recall the definition and main properties of the Lyapunov spectrum. We refer the reader to the abundant literature on this topic, e.g., Ref. [327].

The notion of deterministic chaos is associated with the strong sensitivity of the evolved state of a system on its initial condition. Given a generic d-dimensional flow $\dot{\mathbf{x}} = \mathbf{f}(\mathbf{x})$ in phase space, the measure of the instability of a trajectory $\mathbf{x}(t)$ is provided by the *maximum Lyapunov exponent*. Consider an initial condition $\mathbf{x}(0)$ and a neighboring point $\tilde{\mathbf{x}}(0)$ displaced by an infinitesimal amount $\tilde{\mathbf{x}}(0) = \mathbf{x}(0) + \boldsymbol{\delta}(0)$. Chaos is defined by an exponential growth in time of the separation between the corresponding trajectories, $\delta(t) = |\tilde{\mathbf{x}}(t) - \mathbf{x}(t)| \sim \delta(0)\exp(\lambda t)$, with $\lambda > 0$. The rate λ generally depends on the initial state and on the observation time t. A non-ambiguous definition thus requires "time-averaging"

$$\lambda := \lim_{t\to\infty} \lim_{\delta(0)\to 0} \frac{1}{t} \ln \frac{\delta(t)}{\delta(0)} \,. \tag{3.1}$$

The inner limit $\delta(0) \to 0$ translates the (nonlinear) evolution of small displacements away from the initial condition into the (linear) tangential map of the flow along the given trajectory.

The number λ above does not exhaust all the possible information on the separation of nearby initial conditions. Consider an infinitesimal hypercube surrounding the initial condition $\mathbf{x}(0)$, identified by d independent infinitesimal displacements $\{\mathbf{w}^{(i)}\}_{i=1}^{d}$, which spans the tangent space at $\mathbf{x}(0)$. The evolution transports this hypercube along the trajectory $\mathbf{x}(t)$, and simultaneously deforms it. The tangent vectors $\{\mathbf{w}^{(i)}\}$ evolve according to the so-called variational equation

$$\dot{\mathbf{w}}(t) = A[\mathbf{x}(t)] \cdot \mathbf{w}(t) \,. \tag{3.2}$$

where $A[\mathbf{x}(t)] = \frac{\partial \mathbf{f}}{\partial \mathbf{x}}\big|_{\mathbf{x}(t)}$ is usually called the linear stability matrix. The formal solution to this linear equation is

$$\mathbf{w}(t) = U\big[\mathbf{x}(t)\big]\mathbf{w}(0) \,, \tag{3.3}$$

where $U\big[\mathbf{x}(t)\big] = \mathcal{T}\exp\int_0^t d\tau\, A[\mathbf{x}(\tau)]$ is the evolution operator, and $\mathcal{T}\exp$ denotes the time-ordered matrix exponential. The deformation of the hypercube in time is captured by inspecting the (positive) eigenvalues $\nu_1(t) \geq \nu_2(t) \geq \cdots \geq \nu_d(t) \geq 0$ of the symmetric matrix

$$G(t) = U(t)^T \cdot U(t) \,, \tag{3.4}$$

that we refer to as the Oseledets matrix [1]. The asymptotic *Lyapunov spectrum* is then defined as

$$\lambda_k = \lim_{t\to\infty} \frac{1}{t} \ln \sqrt{\nu_k(t)} \,. \tag{3.5}$$

[1] in the absence of a standard terminology.

The existence of this limit for almost all initial data is the content of the celebrated *Oseledets multiplicative theorem* [328]. In particular, one has $\lambda_1 \equiv \lambda$. In nonergodic dynamics, the numbers $\{\lambda_k\}$ may still depend on the particular trajectory.

We recall here some elementary but important properties of the Lyapunov spectrum concerning the K-dimensional ordiented volumes delimited by K tangent vectors, i.e. $\mathrm{Vol}_K(t) = \mathrm{Vol}[\mathbf{w}^{(1)}(t), \mathbf{w}^{(2)}(t), \dots \mathbf{w}^{(K)}(t)]$. An important consequence of the Oseledets theorem states that the expansion/contraction rate of $\mathrm{Vol}_K(t)$ is given by the sum of the first K exponents as

$$\Lambda_K = \sum_{k=1}^{K} \lambda_k = \lim_{t\to\infty} \frac{1}{t} \ln \left[\frac{\mathrm{Vol}_K(t)}{\mathrm{Vol}_K(0)} \right] . \tag{3.6}$$

This corresponds to the total expansion rate of a (generic) K-dimensional sub-manifold corresponding a subsystem of $K \leq d$ degrees of freedom. In particular, Λ_d is the total expansion rate of the flow, i.e., the average of $\mathrm{div}\, \mathbf{f}(\mathbf{x}(t))$ along the trajectory, which vanishes in conservative systems. For time-independent (autonomous) systems, one has $\lambda_k = 0$ for some k, because the direction of the trajectory is neither stretched nor shrunk. For Hamiltonian systems, which are the focus of this work, Lyapunov exponents come in conjugate pairs $\lambda_k = -\lambda_{2n-k}$ due to the symplectic nature of the phase space flow. In this case, Liouville-integrability of the dynamics is signaled by $\lambda_k \equiv 0$ for all k and in the whole phase space. By contrast, generic Hamiltonian systems do not possess analytic integrals of motion beyond their energy, and their constant-energy surfaces may present a complex structure with invariant submanifolds (Kolmogorov–Arnold–Moser – KAM– tori) intertwined by chaotic regions. In these cases, the Lyapunov spectrum presents strong phase-space and temporal fluctuations.

The Lyapunov spectrum allows one to access the *Kolmogorov-Sinai entropy* rate Λ_{KS}, a fundamental quantifier of irreversibility in dynamical systems. The latter is related to the asymptotic loss of information on the state of the system induced by an arbitrarily fine coarse-graining of the phase space [300, 301]. By Pesin's theorem [302], one has

$$\Lambda_{\mathrm{KS}} = \sum_{k\,:\,\lambda_k>0} \lambda_k \, . \tag{3.7}$$

It is important to stress that the characteristic Lyapunov exponents are defined by a long-time limit [see Eq.(3.5)]. Accessing the latter may be challenging in numerical simulations. The by-now standard algorithm for robust computation of the Lyapunov spectrum has been proposed by Benettin, Galgani, and Strelcyn in a series of papers around 1980 [329–331]. The convergence of the computations is typically quite slow in Hamiltonian systems. This is especially relevant in those undergoing an order/chaos transition, on which we will be concerned in the following. For finite observation-time windows, one naturally defines the *local* or *finite-time Lyapunov exponents* $\{\lambda_k(t)\}$ as in Eq.(3.5) without taking the long-time limit. This notion is particularly important in semiclassical dynamics due to the relatively short time window before saturation, as we will extensively discuss in Section 3.1.4.

In Appendix C.3 we briefly review the algorithm of Benettin *et al.* given its importance later on in this work.

3.1.2 Dynamics of quantum fluctuations

As reviewed in Section 2.1, collective interactions allow for a reformulation of the nonequilibrium dynamics as an effective few-body system in the semiclassical regime, where the impact of quantum fluctuations is controlled by the system size N via the relation $\hbar_{\text{eff}} = 1/N$. The generality of this approach has been discussed in Section 2.1.3.

A system in this class is thus described by n degrees of freedom, compactly denoted $\hat{\boldsymbol{\xi}} = (\hat{q}_1, \dots, \hat{q}_n, \hat{p}_1, \dots, \hat{p}_n)$, satisfying the canonical commutation relations $[\hat{q}_i, \hat{p}_j] = i\hbar_{\text{eff}}\delta_{ij}$, or $[\hat{\boldsymbol{\xi}}, \hat{\boldsymbol{\xi}}] = i\hbar_{\text{eff}}\mathbb{J}$. Here we have introduced the symplectic unit $\mathbb{J}$, given by the $2n \times 2n$ antisymmetric matrix $\mathbb{J} = \begin{pmatrix} \mathbb{0}_n & \mathbb{1}_n \\ -\mathbb{1}_n & \mathbb{0}_n \end{pmatrix}$, which satisfies $\mathbb{J}^2 = -\mathbb{1}_{2n}$. The evolution is governed by the Hamiltonian $\hat{H} = \hbar_{\text{eff}}^{-1}\, \mathcal{H}_{\text{cl}}(\hat{\boldsymbol{\xi}})$ and the Heisenberg equations read $\dot{\hat{\boldsymbol{\xi}}} = \mathbb{J}\, \partial\mathcal{H}_{\text{cl}}(\hat{\boldsymbol{\xi}})$ [2]. As discussed in Section 2.1, the relevant initial states $|\Psi_0\rangle$ in our study of entanglement dynamics are quasiclassical states, i.e., states which satisfy

$$\langle\Psi_0|\Big(\hat{\boldsymbol{\xi}} - \boldsymbol{\xi}(0)\Big)\Big(\hat{\boldsymbol{\xi}} - \boldsymbol{\xi}(0)\Big)|\Psi_0\rangle = \mathcal{O}(\hbar_{\text{eff}})\ , \tag{3.8}$$

with $\boldsymbol{\xi}(0) \equiv \langle\Psi_0|\hat{\boldsymbol{\xi}}|\Psi_0\rangle = \mathcal{O}(1)$. The meaning of this condition is that initial quantum fluctuations around the average are of the order of the minimal uncertainty allowed by the Heisenberg principle.

We now aim at describing the evolution of quantum fluctuations around the average. We observed that, by virtue of Eq.(3.8), the average $\langle\hat{\boldsymbol{\xi}}(t)\rangle$ moves along the classical trajectory to the leading order in $\hbar_{\text{eff}}$,

$$\frac{d}{dt}\langle\Psi(t)|\hat{\boldsymbol{\xi}}|\Psi(t)\rangle = \mathbb{J}\, \partial\mathcal{H}_{\text{cl}}\Big(\langle\Psi(t)|\hat{\boldsymbol{\xi}}|\Psi(t)\rangle\Big) + \mathcal{O}(\hbar_{\text{eff}})\ , \tag{3.9}$$

i.e., $\langle\Psi(t)|\hat{\boldsymbol{\xi}}|\Psi(t)\rangle = \boldsymbol{\xi}_{\text{cl}}(t) + \mathcal{O}(\hbar_{\text{eff}})$. Quantum fluctuations around the average are encoded in the dimensionless variables

$$\delta\hat{\boldsymbol{\xi}} \equiv \hbar_{\text{eff}}^{-1/2}\big(\hat{\boldsymbol{\xi}} - \boldsymbol{\xi}_{\text{cl}}(t)\big)\ , \tag{3.10}$$

which satisfy the commutation relations $[\delta\hat{\boldsymbol{\xi}}, \delta\hat{\boldsymbol{\xi}}] = i\mathbb{J}$, and, by construction, $\langle\delta\hat{\boldsymbol{\xi}}(t)\rangle = \mathcal{O}(\hbar_{\text{eff}}^{1/2})$ [332].

In systems of collectively interacting spins, the quantum fluctuations $\delta\hat{\boldsymbol{\xi}} = (\delta\hat{q}, \delta\hat{p})$ describe the collective spin fluctuations transverse to the instantaneous spin polarization direction, cf. Section 2.1.2. These spin fluctuations can be introduced in the formalism by performing the time-dependent Holstein-Primakoff transformation around the instantaneous average spin, as illustrated in Section 2.3 in the previous chapter. This amounts in mapping the transverse fluctuations of a quantum spin to a canonical bosonic mode, then approximated at the quadratic order. The transfor-

[2] Subtleties related to the ordering of the operators are not relevant in the following discussion

mations introduced in Section 2.3.1[3] can be summarized by

$$\frac{\hat{S}^\alpha}{Ns} = X_\alpha(t)\left(\frac{\hbar_{\text{eff}}}{s}\right)^{1/2}\delta\hat{q} + Y_\alpha(t)\left(\frac{\hbar_{\text{eff}}}{s}\right)^{1/2}\delta\hat{p} + Z_\alpha(t)\left(1-\left(\frac{\hbar_{\text{eff}}}{s}\right)\frac{\delta\hat{q}^2+\delta\hat{p}^2-1}{2}\right) + \mathcal{O}\left((\hbar_{\text{eff}}/s)^{3/2}\right) , \tag{3.11}$$

with $\alpha = x, y, z$. Here, the time-dependent unit vector $\mathbf{Z}(t)$ represents the classical dynamics of the collective spin polarization direction. It can be parameterized through the spherical angles $\phi(t)$ and $\theta(t)$ as in Eq.(2.73). The transverse directions identified by the unit vectors $\mathbf{X}(t)$, $\mathbf{Y}(t)$ that span the orthogonal space to $\mathbf{Z}(t)$ [cf. Eq.(2.73)]. The short-hand notation in Eq.(3.11) $X_\alpha(t)$, $Y_\alpha(t)$, $Z_\alpha(t)$ denotes the α-th components of the basis vectors $\mathbf{X}(t)$, $\mathbf{Y}(t)$, $\mathbf{Z}(t)$ in Eqs.(2.73) (i.e., $X_z = -\sin\theta$, $Y_z = 0$, $Z_z = \cos\theta$, ...). One can check that the bosonic operators $\delta\hat{q}, \delta\hat{p}$ introduced via the Holstein-Primakoff transformation (2.75), correspond to the rescaled fluctuations $\delta\hat{\boldsymbol{\xi}}$ introduced above for the collective spin when the Bloch sphere is parametrized through the canonical phase-space variables $q = \phi$ and $p = \cos\theta$. When the system comprises $M > 1$ collective spins, of magnitude $N_j s \gg 1$, $j = 1, \ldots, M$, one can perform the analogous transformation (3.11) on their components $\hat{S}_j^\alpha$ to obtain the joint semiclassical description.

The general transformation (3.10) is time-dependent. The exact evolution equations for the quantum fluctuations $\delta\hat{\boldsymbol{\xi}}$ are thus generated by the modified Hamiltonian

$$\hat{\tilde{H}}(t) = \hbar_{\text{eff}}^{-1}\,\mathcal{H}_{\text{cl}}\left(\boldsymbol{\xi}_{\text{cl}}(t) + \hbar_{\text{eff}}^{1/2}\delta\hat{\boldsymbol{\xi}}\right) - \hbar_{\text{eff}}^{-1/2}\,\dot{\boldsymbol{\xi}}_{\text{cl}}(t)\,\mathbb{J}\,\delta\hat{\boldsymbol{\xi}} . \tag{3.12}$$

We can now expand the Hamiltonian with respect to the small parameter $\hbar_{\text{eff}}$, obtaining the time-dependent Hamiltonian

$$\hat{\tilde{H}}(t) = \hbar_{\text{eff}}^{-1}\,\hat{H}_0(t) + \hbar_{\text{eff}}^{-1/2}\,\hat{H}_1(t) + \hat{H}_2(t) + \mathcal{O}(\hbar_{\text{eff}}^{1/2}) . \tag{3.13}$$

Here, $\hat{H}_0(t) = \mathcal{H}_{\text{cl}}\big(\boldsymbol{\xi}_{\text{cl}}(t)\big)$ is just a classical quantity (the classical energy along the classical trajectory), and the linear term $\hat{H}_1(t) = \Big[\partial\mathcal{H}_{\text{cl}}\big(\boldsymbol{\xi}_{\text{cl}}(t)\big) - \dot{\boldsymbol{\xi}}_{\text{cl}}(t)\mathbb{J}\Big]\delta\hat{\boldsymbol{\xi}}$ vanishes identically by construction, consistently with the vanishing of $\langle\delta\hat{\boldsymbol{\xi}}(t)\rangle$ to the leading order in $\hbar_{\text{eff}}$. Note that the expansion in Eq.(3.13) corresponds to the time-dependent Hamiltonian in Eq.(2.78), derived in the context of the time-dependent Holstein-Primakoff transformations.

The operator expansion thus starts from the (finite) quadratic order. Within the semiclassical regime, and for a time scale that diverges as $\hbar_{\text{eff}} \to 0$ (the Ehrenfest time scale, see e.g. Eq.(2.7)), we can neglect the remainder $\mathcal{O}(\hbar_{\text{eff}}^{1/2})$ in the expansion. The evolution of the quantum fluctuations in this regime is determined by a linear homogeneous differential equation,

$$\frac{d}{dt}\delta\hat{\boldsymbol{\xi}} = A(t)\,\delta\hat{\boldsymbol{\xi}} \equiv \mathbb{J}\,\partial^2\mathcal{H}_{\text{cl}}\big(\boldsymbol{\xi}_{\text{cl}}(t)\big)\,\delta\hat{\boldsymbol{\xi}} , \tag{3.14}$$

[3]The notation $(\hat{Q}, \hat{P})$ for the collective spin fluctuations of Section 2.1.2 is now substituted by $(\delta\hat{q}, \delta\hat{p})$.

identical with the classical variational equation for the evolution of infinitesimal displacements away from the classical trajectory [cf. Section 3.1.1 and Eq.(3.2)]. In fact, the classical and quantum evolutions generated by a quadratic Hamiltonian coincide, as is well known.

The solution to this equation is formally written as

$$\delta\hat{\boldsymbol{\xi}}(t) = U(t)\ \delta\hat{\boldsymbol{\xi}}(0)\ , \tag{3.15}$$

where $U(t) \equiv \mathcal{T} \exp \int_0^t d\tau\, A(\tau)$ is the tangential map, which encodes the evolution of infinitesimal classical displacements. Due to the asymptotic Gaussian description for small $\hbar_{\text{eff}}$, all the information on the quantum state is encoded in the *correlation matrix*

$$[G(t)]_{ij} = \frac{1}{2}\langle\Psi(t)|\delta\hat{\xi}_i\,\delta\hat{\xi}_j + \delta\hat{\xi}_j\,\delta\hat{\xi}_i|\Psi(t)\rangle\ , \tag{3.16}$$

with $i, j = 1, \ldots, 2n$. This matrix is symmetric and positive definite; the square root of its eigenvalues quantify the width of the quantum fluctuations around the classical average, and are constrained from below by the Heisenberg principle (see, e.g., Ref. [263]). Notice that the rescaling by $\hbar_{\text{eff}}^{1/2}$ in Eq.(3.8) is equivalent to the statement that $G(t) = \mathcal{O}(1)$. The evolution of the correlation matrix $G(t)$ can be directly expressed via Eq.(3.15) as

$$G(t) = U(t)^T\ G(0)\ U(t)\ . \tag{3.17}$$

3.1.3 Semiclassical entanglement and chaos

In this section, we will analytically derive the relation between the entanglement quantifiers of Section 1.2 and the chaos indicators in the semiclassical regime.

Entanglement entropies

We consider a quantum collective model and introduce a bipartition (A, B) of its degrees of freedom as discussed in Section 1.2.1. Within the semiclassical description, the bipartite system can be represented by two sets of semiclassical variables $\hat{\boldsymbol{\xi}} = (\hat{\boldsymbol{\xi}}_A, \hat{\boldsymbol{\xi}}_B)$, with n_A and n_B collective degrees of freedom, respectively $(n_A + n_B = n)$ [4]. In this regime, the entanglement between the two subsystems is encoded in the entanglement between their bosonic quantum fluctuations $\delta\hat{\boldsymbol{\xi}}_A$, $\delta\hat{\boldsymbol{\xi}}_B$. The extent of these quantum fluctuations is collected in their correlation matrix $G(t)$ in Eqs. (3.16)-(3.17). It is convenient to define the subsystem *reduced correlation matrix* $G_A(t)$ as the $2n_A \times 2n_A$ sub-matrix of $G(t)$ built out of the coordinates of subsystem A alone, i.e.,

$$[G_A(t)]_{ij} = \frac{1}{2}\langle\Psi(t)|\delta\hat{\xi}_i\,\delta\hat{\xi}_j + \delta\hat{\xi}_j\,\delta\hat{\xi}_i|\Psi(t)\rangle_{\substack{1\le i\le 2n_A \\ 1\le j\le 2n_A}}\ . \tag{3.18}$$

Due to the asymptotic Gaussian description for small $\hbar_{\text{eff}}$, the reduced density matrix $\hat{\rho}_A(t)$ is also Gaussian and fully determined by the matrix $G_A(t)$. The entanglement entropies can thus be computed via standard techniques [333].

[4] When bipartitions of a permutationally invariant system are considered, one has $n_A = n_B = n$, where $n = q - 1$ is the number of collective degrees of freedom [cf. Sections 2.1.2 and 2.1.3]

The dynamics of the entanglement entropies in bosonic systems governed by quadratic Hamiltonians have been derived and discussed in full generality in Refs. [320, 322]. It is shown therein, that the second Renyi entropy (1.23) can be expressed as the logarithm of the phase-space volume spanned by the time-evolving phase-space distribution associated with the reduced state of the subsystem, i.e.,

$$S_A^{(2)}(t) = \frac{1}{2} \ln \, \det \left(2G_A(t) \right) . \tag{3.19}$$

While the global evolution preserves the total volume, i.e., $\det \left(2G(t) \right) \equiv 1$, the information loss generated by projecting the collective quantum fluctuations onto a subsystem with $n_A < n$ yields an increase of entropy, whose origin is rooted in the development of quantum entanglement. By Eq.(3.19), this increase may be visualized as an enhancement of the projected volume spanned by the reduced quantum fluctuations within the subsystem phase space, due to the progressive stretching of the global phase-space volume spanned by the quantum fluctuations. Similarly, the von Neumann entanglement entropy (1.24) can be computed as

$$S_A(t) = \sum_{i=1}^{n_A} S(\nu_i(t)) \quad \text{with} \quad S(\nu) = \frac{\nu+1}{2} \ln \frac{\nu+1}{2} - \frac{\nu-1}{2} \ln \frac{\nu-1}{2} , \tag{3.20}$$

where $\pm\nu_i(t)$ ($\nu_i(t) \geq 1$) are the so-called symplectic eigenvalues of $2G_A(t)$ [5]. The entanglement entropy $S_A(t)$ is bounded above and below by the second Renyi entropy up to a constant, and hence their growths are superimposed after a finite transient, $S_A(t) \underset{t \gg 1}{\sim} S_A^{(2)}(t)$, see Ref.[320]. Their common asymptotic behavior generically depends on the subsystem only via its number n_A of degrees of freedom, and their evolution is completely determined by that of $G(t)$.

As discussed in Section 1.2.1, in many interesting semiclassical models, the relevant subsystem A is made of only one collective degree of freedom, i.e., $n_A = 1$. These include both the paradigmatic models discussed below, namely the LMG model, the quantum kicked top, and the Dicke model. In this case Eq.(3.20) simplifies and $S_A(t)$ can be expressed as a function of the determinant of $G_A(t)$, i.e.,

$$S_A(t) = 2\sqrt{\det G_A} \left(2\sqrt{\det G_A} \right) + \frac{1}{2} \ln \left(\det G_A - \frac{1}{4} \right) . \tag{3.21}$$

From this equation, the asymptotic result of Ref.[320] immediately follows, i.e., $S_A(t) \underset{t \gg 1}{\sim} \frac{1}{2} \ln \, \det G_A(t)$, since $\det G_A(t) \gg 1$, in agreement with the second Renyi entropy in Eq.(3.19).

In the case of collective spin systems of the form of Eq.(2.19), one considers bipartitions between two sets of $N_A = f_A N$ and $N_B = f_B N$ spins ($f_A + f_B = 1$), and a further simplification occurs. By performing a change of variables to the dynamical

[5] From the correlation matrix G, one defines $J = -2G\mathbb{J}$, where $\mathbb{J}$ is the $2n \times 2n$ symplectic unit. The matrix $[iJ]_A$ restricted to A can be shown to have pairs of opposite real eigenvalues $\pm\nu_i$ (with $\nu_i > 1$ as follows from the Heisenberg relations). The $\{\nu_i\}_{i=1,\dots n_A}$ are referred as the symplectic eigenvalues of G_A and determine the entanglement entropy via Eq.(3.20)

collective fluctuations and the frozen relative fluctuations of the two spins [6], it is easy to compute that

$$\det G_A = \frac{1}{4} + f_A\, f_B \langle \hat{n}_{\rm exc} \rangle \ , \tag{3.22}$$

where $\hat{n}_{\rm exc} = (\delta\hat{q}^2 + \delta\hat{p}^2 - 1)/2$ represents the number of bosonic excitations of the collective spin $\hat{\mathbf{S}}$. This allows computing $S_A(t)$ in a closed form, without the need to compute the reduced correlation matrix $G_A(t)$. It is then clear that S_A vanishes for $\langle \hat{n}_{\rm exc} \rangle \to 0$ and grows as $\frac{1}{2}\ln\langle \hat{n}_{\rm exc} \rangle$ for $\langle \hat{n}_{\rm exc} \rangle \gg 1$. Hence, Eqs.(3.21-3.22) clarify that the state of subsystem A (or B) is pure only if $\langle \hat{n}_{\rm exc} \rangle = 0$, i.e., if the spin system is fully polarized (coherent), as occurs in the absence of interactions. Conversely, the state is entangled in the presence of collective quantum excitations.
Besides the number of collective excitations $\langle \hat{n}_{\rm exc} \rangle$, it is also possible to characterize entanglement entropy via yet another significant quantity, i.e., the *effective temperature* of the two subsystems. In fact, the reduced density matrices may be written as $\hat{\rho}_{A,B} = Z_{A,B}^{-1} \exp(-\beta_{\rm eff} \hat{H}_{A,B})$, where the state-dependent quadratic operators $\hat{H}_{A,B}$ are usually termed *modular* or *entanglement Hamiltonian*. It is straightforward to derive a relation between the effective dimensionless inverse temperature and the other quantities, e.g.,

$$T_{\rm eff} = \frac{1}{2\,\mathrm{arctanh}\left(\frac{1}{\sqrt{1+4 f_A f_B \langle \hat{n}_{\rm exc} \rangle}} \right)} . \tag{3.23}$$

This equation makes it explicitly clear that the growth of $\langle \hat{n}_{\rm exc}(t) \rangle$ — which comes via collective spin squeezing — is responsible for "heating up" the two subsystems, i.e., for raising their effective temperature, thus continuously accumulating entanglement entropy in time.

As we will see in the next sections, the entanglement entropy of a collective spin system can be quantitatively related to the quantum Fisher information and the spin squeezing.

Quantum Fisher information and spin squeezing

The quantum Fisher information for collective spin systems is given by the maximal variance of the collective spin operators [cf. Eq.(1.38)]. This information is encoded in the correlation matrix $G(t)$ (3.16), which describes the dynamics of the fluctuations in the transverse direction. Therefore, the semiclassical QFI is given by the maximum eigenvalue of the correlation matrix $G(t)$

$$f_Q(t) = 4 \max\left[\mathrm{Eigvals}\, G(t) \right] \ . \tag{3.24}$$

In the case of a fully-connected spin system (Section 2.1.2), one can determine the QFI explicitly from Eq.(1.38), by computing the eigenvalue of the 2×2 spin

[6] Explicitly,

$$\begin{cases} \delta\hat{q} = +\sqrt{f_A}\, \hat{q}_A + \sqrt{f_B}\, \hat{q}_B \\ \delta\hat{q}_{\rm rel} = -\sqrt{f_B}\, \hat{q}_A + \sqrt{f_A}\, \hat{q}_B \end{cases} \begin{cases} \delta\hat{p} = +\sqrt{f_A}\, \hat{p}_A + \sqrt{f_B}\, \hat{p}_B \\ \delta\hat{p}_{\rm rel} = -\sqrt{f_B}\, \hat{p}_A + \sqrt{f_A}\, \hat{p}_B \end{cases} .$$

correlation matrix. This yields the equation

$$f_Q(t) = 1 + 2\langle \hat{n}_{\text{exc}}(t)\rangle + 2\sqrt{\langle \hat{n}_{\text{exc}}(t)\rangle(\langle \hat{n}_{\text{exc}}(t)\rangle + 1)}\,, \tag{3.25}$$

where $\langle \hat{n}_{\text{exc}}(t)\rangle$ is the number of bosonic excitations of the collective spin $\hat{\mathbf{S}}$ [cf. Eqs.(3.11) and (3.22)].

As discussed in Section 1.2.3, spin squeezing represents a convenient indicator of multipartite entanglement in spin systems. At the semiclassical level relevant here, quantum fluctuations are Gaussian, and from the definition (1.39) one derives

$$\xi^2(t) = 1 + 2\langle \hat{n}_{\text{exc}}(t)\rangle - 2\sqrt{\langle \hat{n}_{\text{exc}}(t)\rangle(\langle \hat{n}_{\text{exc}}(t)\rangle + 1)}\,. \tag{3.26}$$

Equations (3.21-3.22), (3.25) and (3.26) express the quantitative link — pictorially illustrated in Figure 3.9 — between the entanglement entropy S_A, the quantum Fisher information f_Q, and the spin squeezing parameter ξ, in collective spin models in the semiclassical regime in and out of equilibrium. In particular, in this regime the inequality discussed in Section 1.2.3 is saturated, i.e. $f_Q = 1/\xi^2$.

Semiclassical square commutator

Along similar lines, we can compute the semiclassical evolution of the out-of-time-order square commutator defined in Section 1.2.4 for a system initialized in a quasiclassical state. Starting from the definition in Eq.(1.41) and expanding the operators up to the quadratic order in the quantum fluctuations, one readily finds

$$c_{ij}(t) \equiv -\hbar_{\text{eff}}^{-2}\langle\Psi_0|\Big[\hat{\xi}_i(t), \hat{\xi}_j(0)\Big]^2|\Psi_0\rangle = \Big(U_{i\bar{j}}(t)\Big)^2 + \mathcal{O}(\hbar_{\text{eff}}), \tag{3.27}$$

where $\bar{j} \equiv (j+n) \mod 2n$. The semiclassical square commutator thus directly probes the sensitivity of the classical trajectories to infinitesimal perturbations.

In the case of fully-connected spin systems, the square commutator between two collective spin operators reads

$$c_{\alpha\beta}(t) = \Big[X_\alpha(t)\big(U_{qq}(t)\,Y_\beta(0) - U_{qp}(t)\,X_\beta(0)\big) + Y_\alpha(t)\,\big(U_{pq}(t)\,Y_\beta(0) - U_{pp}(t)\,X_\beta(0)\big)\Big]^2 + \mathcal{O}(\hbar_{\text{eff}})\,, \tag{3.28}$$

with the same notation as in Eq.(3.11). In order to get this result, one first plugs the expansion of the spin operators (3.11) into the definition (1.41). Then, after substituting the formal solution for the spin fluctuations at time t, i.e., $\delta\hat{q}(t) = U_{qq}(t)\,\delta\hat{q}(0) + U_{qp}(t)\,\delta\hat{p}(0)$ and $\delta\hat{p}(t) = U_{pq}(t)\,\delta\hat{q}(0) + U_{pp}(t)\,\delta\hat{p}(0)$ [cf. Eq.(3.15)], the equal-time commutators between the conjugate variables yield the above Eq.(3.28).

3.1.4 Entanglement growth and chaos

In the previous section, we have established how the semiclassical dynamics of quantum fluctuations determine the evolution of the entanglement quantifiers of interest, via the time-dependent correlation matrix $G(t)$. This connection highlights

Classical trajectory	Stable	Regular	Chaotic (Unstable)
entanglement entropy [298, 320]	oscillations	$\ln t$	$\Lambda_K\, t$
quantum Fisher information	oscillations	t^2	$e^{2\lambda t}$
square commutator	oscillations	t^2	$e^{2\lambda t}$
Ehrenfest time scale	$\mathcal{O}(\sqrt{N})$	$\mathcal{O}(\sqrt{N})$	$\mathcal{O}(\ln N)$

Table 3.1: Summary of the dynamical behavior of entanglement and chaos quantifiers of N-particle collective systems in the semiclassical regime. The growth of the entanglement quantifiers and the square commutator depends on the nature of the limiting classical trajectory in the $2n$-dimensional phase space (stable configuration, regular or chaotic), up to the Ehrenfest time. Here, $\lambda \equiv \lambda_1$ is the maximum Lyapunov exponent, and $\Lambda_K = \sum_{k=1}^{2K} \lambda_k$ is the sum of the $2K$ largest Lyapunov exponents, where K is the number of degrees of freedom associated with the considered subsystem. For K=$n/2$, one has the classical Kolmogorov-Sinai entropy rate $\Lambda_{\rm KS} = \sum_{k\,:\,\lambda_k>0} \lambda_k$.

that the entanglement growth is determined by the chaoticity properties of the semiclassical dynamics, in turn, dictated by the stability of the underlying phase-space trajectories, see Table 3.1 for a summary.

The correlation matrix $G(t)$ in Eq.(3.16) is equivalent to the Oseledets matrix that defines the Lyapunov spectrum in Eq.(3.5) [7], as the quantum fluctuations evolve in the same way as the linearized displacements. Hence, the spectrum of the growth rates of the quantum fluctuations encoded in $G(t)$ coincides with the *finite-time* Lyapunov spectrum $\{\lambda_k(t)\}$ of the underlying semiclassical trajectory within the Ehrenfest time scale $T_{\rm Eh}(N)$, and converges to the proper asymptotic Lyapunov spectrum $\{\lambda_k\}$ as $N \to \infty$.

When the classical dynamics is integrable, the collective motion of the system is orderly and takes place along regular trajectories in phase space, meaning that nearby initial conditions separate linearly in time (generically). This implies that all Lyapunov exponents vanish. This scenario largely persists under weak integrability-breaking Hamiltonian perturbations, as established by KAM theory [334], whereby regular trajectories gradually leave room to chaotic portions of the phase space arising from dynamical resonances. Thus, in integrable or near-integrable semiclassical systems, the temporal growth of the quantum correlations is at most polynomial, $G_{ij}(t) \sim t^2$, as can be shown explicitly by switching to action-angle variables. Conversely, in systems with far-from-integrable semiclassical dynamics featuring fully developed chaos in phase space, the Lyapunov spectrum is nonvanishing. This implies an asymptotic exponential growth of quantum fluctuations, generically given by $G_{ij}(t) \sim e^{2\lambda t}$, where λ is the maximal Lyapunov exponent. An immediate consequence of the above observations concerns the asymptotic growth rate of the square commutator. The latter results to be twice the maximum Lyapunov exponent of

[7] The presence of $G(0)$ instead of the identity matrix is immaterial for the definition of the Lyapunov exponents: these are intrinsic quantities associated with the flow that does not depend on the arbitrary choice of the phase-space metric.

the underlying semiclassical dynamics,

$$c(t) \sim e^{2\lambda t}. \tag{3.29}$$

Crucially, the chaoticity properties of the semiclassical dynamics determine the speed of the entanglement growth, as determined by Eqs.(3.20) and (3.24). In fact, by Eq.(3.24), we immediately derive that the QFI grows as

$$f_Q(t) \sim e^{2\lambda t}. \tag{3.30}$$

The determination of the bipartite entanglement entropy growth requires a more elaborate analysis. In Refs. [320, 322] Bianchi, Hackl, and collaborators discuss the bipartite entanglement dynamics generated by quadratic bosonic Hamiltonians. As thoroughly shown therein, the growth of $S_A(t)$ is generically linear in time with a rate set by the sum of the largest $2n_A$ Lyapunov exponents,

$$S_A(t) \underset{t\gg 1}{\sim} S_A^{(2)}(t) \sim \Lambda_A t = \left(\sum_{k=1}^{2n_A} \lambda_k\right) t. \tag{3.31}$$

For $n_A = n/2$, the rate coincides with the classical Kolmogorov-Sinai entropy rate $\Lambda_{KS} = \sum_{\lambda_k\,:\,\lambda_k>0} \lambda_k$ [300, 301, 327]. Analogous equations to the three above apply to the phase-space *separatrices* when the classical dynamics are integrable; in this case, the Lyapunov spectrum is given by the linearized dynamics around the unstable fixed point on which the trajectory terminates.

By contrast, for generic trajectories, integrable systems have $\Lambda_{KS} = 0$. In this case, one has

$$S_A(t) \underset{t\gg 1}{\sim} S_A^{(2)}(t) \sim c \ln t\,, \quad f_Q(t) \sim t^2\,, \quad c(t) \sim t^2\,, \tag{3.32}$$

with c an integer.

The classification is concluded by the case of stable equilibrium configurations, the linearized dynamics of which is equivalent to that of coupled harmonic oscillators. Accordingly, all the quantities of interest perform bounded (periodic or quasiperiodic) oscillations. (Note that the same applies to effective *linear* semiclassical dynamics with a suppressed anharmonic contribution, as in the recently discovered mechanism in Refs. [96, 335].) A summary of the above discussion is presented in Table 3.1.

Since quadratic Hamiltonians describe the dynamics of quantum fluctuations around the limiting classical trajectory in the limit $\hbar_{\text{eff}} \to 0$ to the leading order [cf. the discussion in Section3.1.2], Bianchi, Heykl, *et al.* conjecture that their analysis applies to generic quantum systems in the appropriate semiclassical regime. In particular, $S_A(t) \sim \Lambda_A t$, where Λ_A is the Kolmogorov-Sinai entropy rate determined by the Lyapunov spectrum as above. It is one of the main purposes of the present work to thoroughly assess this conjecture and firmly establish its range of validity in quantum many-body systems possessing a relevant and controlled semiclassical limit. The asymptotic results of Refs. [320, 322] ideally describe the *average* asymptotic growth at long times. However, typical semiclassical systems generally present strong additional finite-time fluctuations in the entanglement quantifiers.

For example, when the limiting classical trajectory is periodic with period $T_{\rm cl}$, for integrable (chaotic) dynamics one has $T_{\rm cl}$-periodic oscillations superimposed to the logarithmic (linear) growth of $S_A(t)$ and to the polynomial (exponential) growth of $f_Q(t)$ and $c(t)$. For general aperiodic classical trajectories, the time-dependence can be much more complicated. These effects can obscure the asymptotic growth until the saturation due to the finite $\hbar_{\rm eff}$. Accordingly, deviations from the asymptotic result of Refs. [320, 322] can be observed.

In Sections 3.2-3.4 below, we will concentrate on an integrable example and in systems exhibiting a progressive transition to chaos as a parameter is varied. In such systems, finite-time fluctuations play a major role, due to the complexity of the phase space, featuring a fractal structure of regular trajectories (KAM tori) and chaotic regions. For this reason, the correct semiclassical identification holds between the growth rate of quantum entanglement and the *finite-time* Lyapunov spectrum $\{\lambda_k(t)\}$, rather than the proper asymptotic one. The long-time convergence of the rate of growth of the relevant entanglement and chaos quantifiers to the asymptotic ones compatible with the Lyapunov spectrum compete with their saturation in a finite system at the Ehrenfest time scale $T_{\rm Eh}(N) \sim \ln N$. Hence, the theoretical long-time rates of growth will hardly be accessible in practice. In view of this discussion, it is evident that the transient growth of quantum fluctuations before saturation at the Ehrenfest time scale is not truly related to the Lyapunov spectrum, but rather to its finite-time version (see Section 3.1.1). This point is often overlooked in the recent literature on OTOC and its relation to chaos.

We conclude the discussion by commenting that not only the entanglement entropy $S_A(t)$ has a finite limit as $\hbar_{\rm eff} \to 0$, but this limiting quantity has a natural classical interpretation in terms of the loss of information under phase-space coarse-graining during the time-evolution [299, 315] — which is the meaning of the classical Kolmogorov-Sinai entropy in dynamical systems. It is also interesting to remark that the growth of entanglement entropy in the semiclassical regime is sensitive to the full Lyapunov spectrum, unlike the growth of the OTOCs, which is sensitive to the maximum Lyapunov exponent only.

3.1.5 Ehrenfest time and finite-size effects

At this stage, it is natural to comment on the time scale of the validity of the semiclassical description outlined above. The latter is the well known *Ehrenfest time scale* [cf. Eq.(3.1.1)], and it can be estimated as the time at which the size of quantum fluctuations becomes comparable with the typical length in phase space, i.e. $\mathcal{O}(G(t)) = \mathcal{O}(\hbar_{\rm eff}^{-1})$. For orderly, integrable-like motion, quantum fluctuations grow polynomially in time as $G(t) \sim t^2$, which yields $T_{\rm Eh} \sim \hbar_{\rm eff}^{-1/2} = \sqrt{N}$. In the presence of unstable, chaotic evolution, instead, one has $G(t) \sim e^{2\lambda t}$, where λ is the maximum Lyapunov exponent defined in Section 3.1.1. In this case, thus, $T_{\rm Eh} \sim (1/\lambda) \ln \hbar_{\rm eff}^{-1/2} = (1/2\lambda) \ln N$.

At this time scale, the semiclassical analysis described before breaks down, and a full quantum regime takes place, dominated by interference. From the numerical simulations for finite systems, we find that the entanglement descriptors saturate to values compatible with their statistical-mechanical predictions: in particular, we

find

$$S_A^\infty \propto \ln \hbar_{\text{eff}}^{-1} , \quad f_Q^\infty \propto \hbar_{\text{eff}}^{-1} , \tag{3.33}$$

which is also compatible with the results of Section 3.1.3-3.1.3 evaluated at T_{Eh}. In other words, the asymptotic state is genuinely multipartite entangled $f_Q^\infty \propto N$, while the bipartite entanglement entropy saturates to $S_A^\infty \propto \ln N_A$. This is related to the usual volume-law scaling of entanglement out of equilibrium [8]. For the chaotic driven dynamics, the value of the QFI is compatible with the values of the infinite temperature state: $f_Q^\infty = 1 + N/3 + \mathcal{O}(1/N)$. Likewise, the entanglement entropy saturates to the Page value (1.51) expected for a random state, wherein this case $\dim \mathcal{H}_A = N_A + 1$ is only linear with the size of the partition. On the other hand, in this regime, the square commutator (1.41) is characterized by a fully quantum nonperturbative growth which leads to saturation only in the case of a fully chaotic dynamics, while it grows polynomially in the case of integrable systems. This effect is discussed in Section 4.2.

3.2 The fully connected Ising model

We apply the general scheme and results of Section 3.1 to the fully connected transverse-field Ising ferromagnet of N interacting spins-1/2. It is described by the Hamiltonian

$$\hat{H}_{\text{LMG}} = -\frac{J}{N} (\hat{S}^x)^2 - h \hat{S}^z , \tag{3.34}$$

that lies in the class of fully-connected spin Hamiltonians (2.17) discussed in Section 2.1.2. The system is widely known as the Lipkin-Meshkov-Glick (LMG) model [292] and, because of its well-established classical limit, it has already considered as an illustrative example in Sections 2.2.4 and 2.3.1. The Hamiltonian (3.34) also describes a bosonic Josephson junction made of two weakly coupled and interacting Bose-Einstein condensates in the presence of an external field of strength [283, 336, 337].

For large values of the transverse field $|h| > J$ the system is paramagnetic, with a single equilibrium configuration of the spins aligned with the field direction, and the non-equilibrium dynamics consist in a precession around it, for an illustration see Figure 3.1 (c). A quantum phase transition at $h = \pm J$ separates this phase from a ferromagnetic one, with a pair of degenerate ground states with spin orientation in the x-z plane, symmetric with respect to flipping the x axis, for an illustration see Figure 3.1 (a-b).

The out-of-equilibrium behavior of this model has been widely studied [338–340], and, in the case of a quantum quench of the transverse field $h_0 \to h_f$, it is characterized by the phenomenon of *dynamical phase transitions* (DPTs) [262], introduced in Section 1.1.1. The non-equilibrium trajectories of the system may have paramagnetic or ferromagnetic character depending on the initial state and on the final

[8] In fact, the stationary states after a quantum quench explore all the allowed Hilbert space, and their entanglement is upper-bounded by $S_A \leq \dim(\mathcal{H}_A)$. In collective models under consideration here, however, the conservation of the collective spin magnitude $|\mathbf{S}|^2$ reduces the dimension of the allowed Hilbert space to $\dim(\mathcal{H}_A)$.

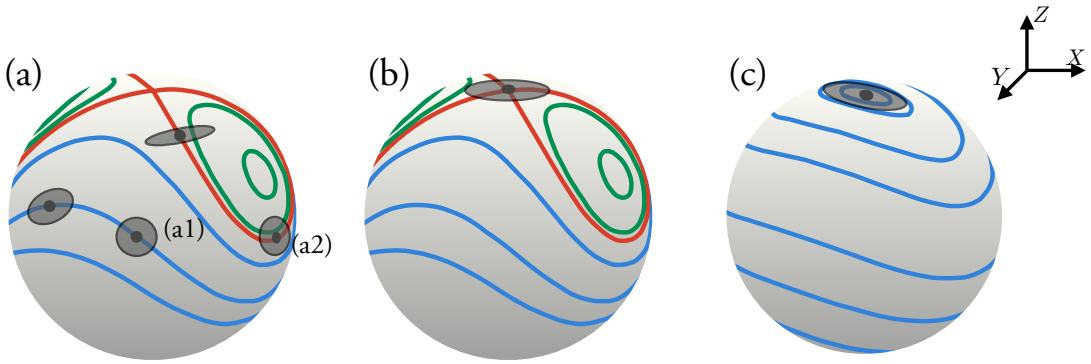

Figure 3.1: Illustration of the equilibrium configurations and of possible instances of non-equilibrium dynamics in the LMG model on the Bloch sphere of the collective spin. (a-b) For $h < |J|$, the energy possesses two minima characterized by non-vanishing, opposite magnetizations along x. (c) For $h > |J|$, the system is paramagnetic with a single equilibrium configuration in the direction of the field. In the out-of-equilibrium scenario, initial fully polarized states at $t = 0$ are pictured as a point on the Bloch sphere, surrounded by a small grey circle represented their transverse quantum fluctuations. (a) For initially ferromagnetic initial states $h_0 < |J|$, the time-evolution is characterized by ferromagnetic (green) or paramagnetic (blue) periodic trajectories, with $\overline{S_x(t)} \neq 0$ and $\overline{S_x(t)} = 0$, respectively, separated by the unstable trajectory occurring at h_c (red). Labels (a1) and (a2) refer to possible realizations of such states: (a1) a generic one, (a2) an initial state lying on the critical trajectory. Labels (b) and (c) refer to an initial paramagnetic state $h_0 = \infty$ evolved with two different Hamiltonians: (b) quench performed to a ferromagnetic Hamiltonian $h_f < |J|$, the initial state lies on the unstable trajectory, (c) quench performed to a different $h_f > |J|$ paramagnetic configuration.

transverse field h_f. The two families are distinguished by the time-averaged magnetization $\overline{S_x(t)}$ being vanishing or not, and are separated by a critical trajectory (*separatrix*) at $h_f = h_c = (h_0 + 1)/2$ with a diverging classical period, see Figure 3.1 for an illustration.

The ground state entanglement entropy of the LMG model has been studied in Refs. [103, 333], where it is found to be finite away from the quantum critical point and logarithmically divergent with the system size in correspondence of it. More recently, its growth in time after a quench of the transverse field has been numerically found to be consistent with a logarithmic behavior [341, 342].

In the limit of large N, the non-equilibrium evolution can be studied with the dynamical approach of Section.2.3, see e.g. Refs. [293, 294]. In this case, the equations of motion have been derived and illustrated in Section 2.3, which we refer to.

The mean-field trajectory, parametrized by $\theta(t), \phi(t)$ on the Bloch sphere evolves according to Eqs.(2.89)

$$\begin{cases} \dot{\theta} = J \sin\theta \cos\phi \sin\phi \\ \dot{\phi} = -h_z + J \cos\theta \cos^2\phi \end{cases} . \tag{3.35}$$

In turn, the evolution of collective quantum fluctuations $\delta\hat{q}, \delta\hat{p}$, encoded e.g. in $G^{qq}(t) = \langle \delta\hat{q}(t)^2 \rangle$, are governed by Eqs.(2.94), which read

$$\begin{cases} \dot{G}^{qq} = 2J\cos\theta\sin\phi\cos\phi\, G^{qq} + 2J\left(\cos^2\phi - \sin^2\phi\right) G^{qp} \\ \dot{G}^{pp} = -2J\cos\theta\sin\phi\cos\phi\, G^{pp} - 2J\cos^2\phi\sin^2\theta\, G^{pq} \\ \dot{G}^{qp} = -J\cos^2\phi\sin^2\theta\, G^{qq} + J\left(\cos^2\phi - \sin^2\phi\right) G^{pp} \end{cases} \tag{3.36}$$

These equations are exact for $N \to \infty$, while finite-size effects become manifest at the Ehrenfest time scale T_{Ehr}, which depends on the nature of the semiclassical trajectory. As previously discussed, for generic quenches $T_{\text{Ehr}} \sim \sqrt{N}$, while at the DPT, corresponding to the separatrix in the classical phase space, it becomes $T_{\text{Ehr}} \sim \ln N$. Equations (3.35)- (3.36) are a set of linear time-dependent differential equations and their numerical integration with the appropriate initial conditions, determines the time-evolution of the number of collective excitations $\langle \hat{n}_{\text{exc}}(t) \rangle$ in Eq. (2.93). This immediately leads to the semiclassical entanglement entropy, the QFI and the square-commutator via Eqs.(3.21, 3.22), (3.25) and (3.28) respectively.

3.2.1 Exact dynamics for finite systems

The analytical treatment is tested against exact-diagonalization (ED) numerical simulations. Due to the conservation of the collective spin $\hat{\mathbf{S}}^2$ in infinite-range systems, the time-evolving wavefunction is constrained within the maximal-spin Hilbert space sector $|\hat{\mathbf{S}}| = N/2$, whose dimension $N+1$ grows only linearly with the system size. As such, this allows us to easily simulate the dynamics of large systems. We compute entanglement following the decomposition in Ref. [103]. The numerical QFI is given by the maximal eigenvalue of the covariance matrix $\text{Cov}(\hat{A}, \hat{B}) = 4\langle \hat{A}\hat{B} \rangle - 4\langle \hat{A} \rangle \langle \hat{B} \rangle$ with $\hat{A}, \hat{B} = \hat{S}^{x,y,z}$ [343]. For the square commutator (1.45), we choose $\hat{A} = \hat{B} = \hat{S}^z/S$ for definiteness and we rescale its value by N^3 in order to study the semiclassical regime.

In what follows we will discuss the semiclassical regime of entanglement and scrambling, while we postpone a more detailed discussion of the dynamics beyond the Ehrenfest time to Section 4.2.

Quenches from the ferromagnetic ground state

We first focus on quantum quenches from a ferromagnetic ground state $h_0 < |J|$, see Panel (a) in Figure 3.1. For the sake of definiteness, we consider one of the two ground states of the LMG Hamiltonian (3.34) with $h_0 = 0$, e.g., the one fully polarized along the positive x-axis,

$$|\psi_0\rangle = |\rightarrow\rightarrow\cdots\rightarrow\rangle. \tag{3.37}$$

It corresponds to the initial conditions $\theta_0 = \pi/2$, $\phi_0 = 0$, $G^{pq}(t=0) = 0$ and $G^{qq}(t=0) = G^{pp}(t=0) = 1/2$ in Eqs. (3.35), (3.36). The initial state $|\psi_0\rangle$ is then evolved in the presence of a transverse field $h = h_f$, varying above, below and at the dynamical critical point $h_c = J/2$. As Figure 3.2 illustrates, in all the three cases the finite-size numerical result perfectly agree with the analytical result based on our

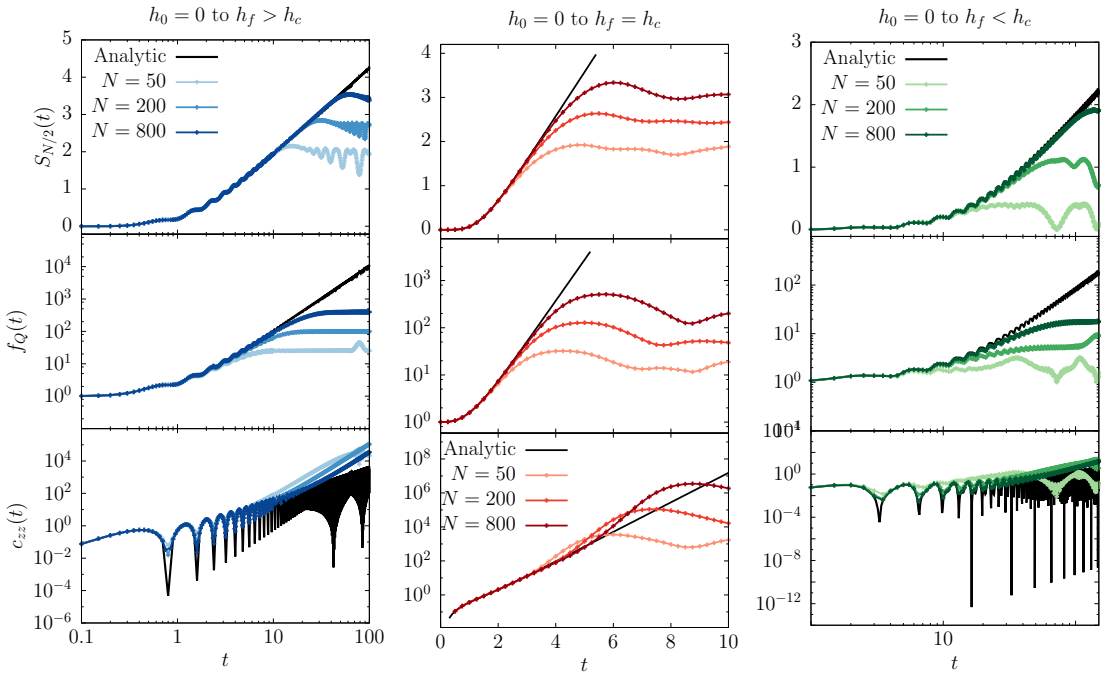

Figure 3.2: Entanglement and scrambling dynamics after a quench from the ferromagnetic ground state $|\psi_0\rangle$ to $h_f > 0$. The analytical prediction (black lines) is compared with exact numerical results (colours) at finite $N = 50, 200, 800$. We study the growth of the entanglement entropy (top), the quantum Fisher information (central), and the square commutator (bottom) quenching above, below, and at the dynamical phase-transition at $h_f = h_c$, as pictorially shown in Figure 3.1 (a). (Left) Quench above the DPT: $h_f = 2J > h_c$. (Right) Quench below the DPT: $h_f = 0.2J < h_c$. (Center) Quench at the DPT: $h_f = J/2$. See discussion in the text. Here we fixed $J = 1$.

general formulas for $t \lesssim T_{\text{Ehr}}$. For quenches above and below h_c, the entanglement entropy increases logarithmically after a transient, i.e., $S_A \sim \ln t$, while the QFI and semiclassical scrambling grow polynomially $f_Q \sim c_{zz}(t) \sim t^2$ before $t_{\text{Ehr}} \sim \sqrt{N}$, see Figure 3.2 and Figure 3.3 below. In turn, at the dynamical critical point, due to the exponential growth of the collective excitations, the entanglement entropy increases linearly in time, i.e., $S_A \sim \lambda_{h_c} t$, before saturation at $t_{\text{Ehr}} \sim \ln N$. The slope λ_{h_c} corresponds to the instability rate of the linearized flow, i.e., the imaginary eigenfrequency of the unstable fixed point. For this Hamiltonian and for the unstable point $\theta = 0$,

$$\lambda_h = \sqrt{h(J-h)}\,. \tag{3.38}$$

At finite size N, the entanglement (both bipartite and multipartite) is bounded and thus always saturates to a finite value, as in Eq. (3.33). For $N_A = N/2$ the entanglement entropy saturates to $\ln \sqrt{N}$, as shown in the inset of Figure 3.3 (top). Conversely, in Figure 3.3 (bottom), we plot the entanglement entropy dynamics for various possible bipartitions, i.e., various fractions f_A of spins in subsystem A, and we compare it with the numerically exact results at fixed N. The latter reproduces the former up to T_{Ehr}, when it saturates around the predicted value of $1/2 \ln N_A$.

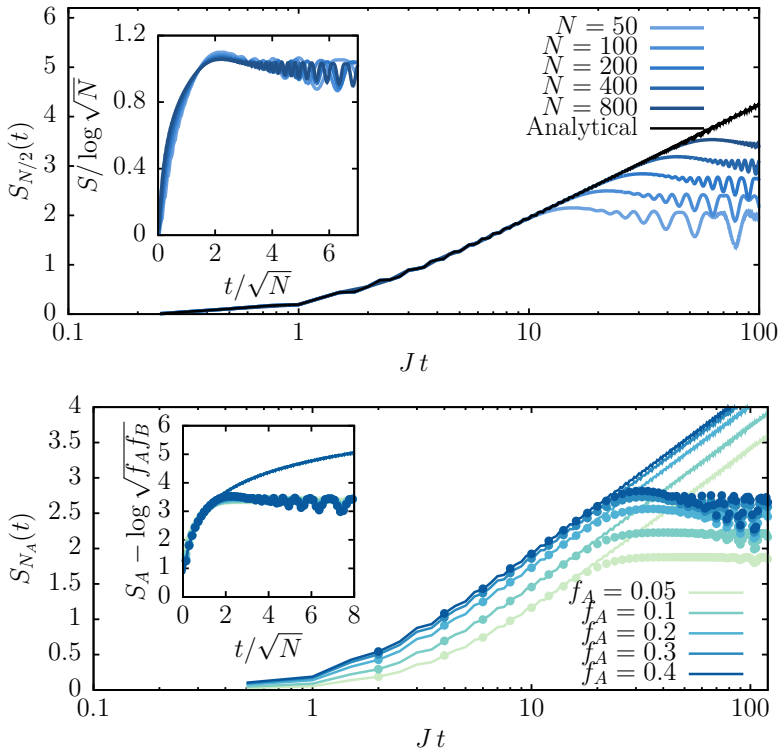

Figure 3.3: Entanglement entropy dynamics after a quench dynamics from $h_0 = 0$ to $h_f = 2J$. (Left) We compare our analytic formula (black line) for the half-system entanglement entropy $S_{N/2}$ with the ED data for increasing system sizes $N = 50 \div 800$. The exact diagonalization results follow the logarithmic growth up to $t_{\text{Ehr}} \sim \sqrt{N}$, where they saturate to $S_{N/2} \sim \ln N$. The inset shows the same data with $S_{N/2}$ rescaled by $\ln N$ and time by $\sqrt{N}$. (Right) $S_{N_A}(t)$ for various bipartitions with fractions of spins $f_A = N_A/N = 0.05 \div 0.4$ and fixed size $N = 200$. Analytical results from Eq. (3.21) (full lines) are compared with exact numerical results (dots). In the inset, $S_{N_A} - 1/2 \ln f_A f_B$ is plotted as a function of the rescaled time $t/\sqrt{N}$.

Quenches from the paramagnetic ground state

Let us now discuss the opposite case of a quantum quench from a paramagnetic initial state, see Panels(b-c) in Figure 3.1. We consider the ground state of Hamiltonian with from $h_0 = \infty$, i.e.

$$|\phi_0\rangle = |\uparrow\uparrow \ldots \uparrow\rangle, \tag{3.39}$$

which corresponds to the initial conditions $\theta_0 = 0$, $G^{qp}(t = 0) = 0$ and $G^{qq}(t = 0) = G^{pp}(t = 0) = 1/2$ in Eqs. (3.35), (3.36) (due to the singularity of spherical coordinates, the value of ϕ_0 is immaterial in this case). For $h_f > |J|$, the quantum fluctuations of the initial state undergo oscillations with the classical period T_{cl}, which leads to a periodic dynamics of entanglement entropy as in Figure 3.4 (left), with a simple semiclassical interpretation in terms of periodic squeezing of the collective spin. Conversely, for $h_f < |J|$, the initial state lies on top of the unstable trajectory at $\theta = 0$, hence the collective quantum fluctuations grow exponentially in time. The theory then predicts a linear increase $S_A \sim \lambda_{h_f} t$ of entanglement before

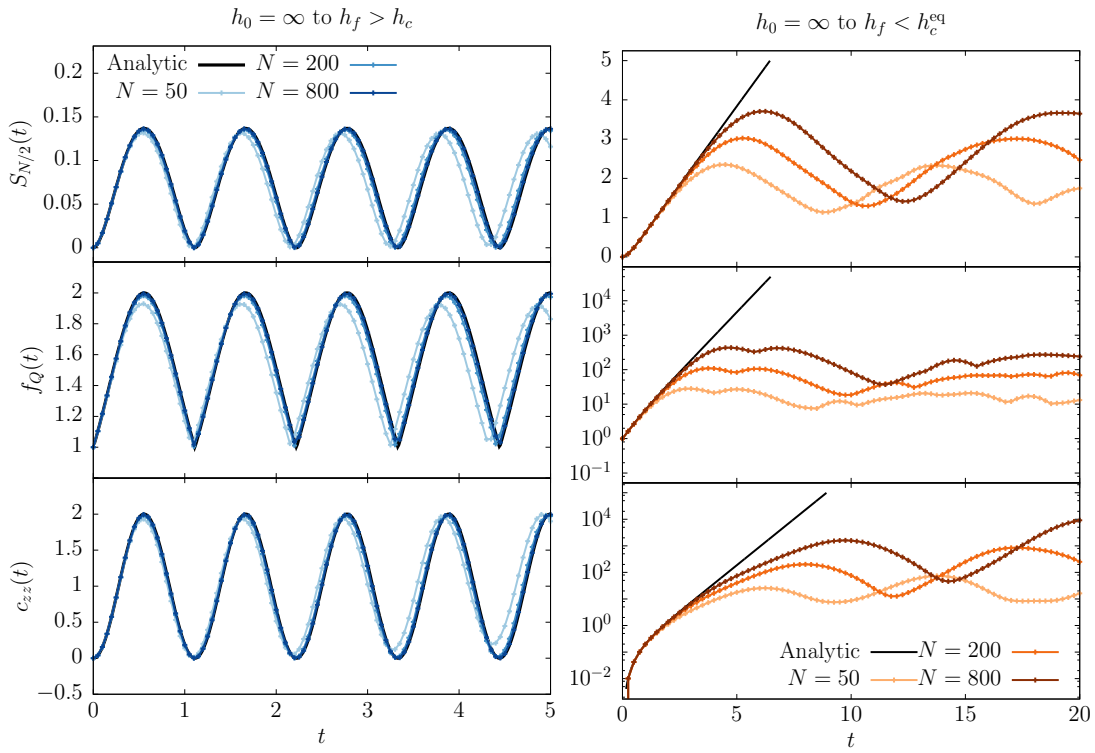

Figure 3.4: Half-system entanglement entropy dynamics after a quench from the paramagnetic ground state $|\phi_0\rangle$. Analytical results from Eq. (3.21) (black lines) are compared with exact numerical results (colours) at finite $N = 50 \div 800$. (Left) $h_f = 0.2J$ linear growth of $S_A \sim \lambda_{h_f} t$ with λ_{h_f} given in Eq. (3.38). (Right) $h_f = 2J$ periodic oscillations of $S_A(t)$ resulting from the periodic dynamics of the quantum collective fluctuations.

$T_{\rm Ehr}$, with λ_{h_f} given in Eq. (3.38), see Figure 3.4 (right).

3.2.2 Initial paramagnetic ground states

When the system is initialized in a paramagnetic ground state, one can derive analytically the time-evolution of $\langle \hat{n}_{\rm exc}(t) \rangle$ which enters in the entanglement quantifiers.
We use the Holstein-Primakoff transformation around the instantaneous average spin polarization (3.11), which in the present case lies on the z axis. Hence, the Holstein-Primakoff are performed by mapping the transverse (x and y) spin components to canonical bosonic variables

$$\begin{cases} S^y = \dfrac{N}{2} - \hat{n} = \dfrac{N}{2} - \dfrac{\delta\hat{q}^2 + \delta\hat{p}^2 - 1}{2}, \\ S^x \approx \sqrt{N/2}\, \delta\hat{q}, \\ S^y \approx \sqrt{N/2}\, \delta\hat{p}, \end{cases} \tag{3.40}$$

where the bosonic variables $\delta\hat{q}, \delta\hat{p}$ satisfy $[\delta\hat{q}, \delta\hat{p}] = i$; one can check that the spin commutation relations $[S^\alpha, S^\beta] = i\epsilon^{\alpha\beta\gamma} S^\gamma$ are satisfied to lowest order by the r.h.s.

of Eqs. (3.40). The quantum number $n = 0, 1, 2, \ldots$ labels the quantized spin projection along the direction x of the classical minimum.

Using Eqs. (3.40), the Hamiltonian (3.34) can be approximated by neglecting terms of order $1/N$,

$$\hat{H} = -\frac{N}{2}h + h\frac{\delta\hat{q}^2 + \delta\hat{p}^2 - 1}{2} - J\frac{\delta\hat{q}^2}{2} \,. \tag{3.41}$$

From this equation, one sees clearly that for $h \leq J$ the paramagnetic x polarization becomes unstable. The direction of the average spin polarization remains along z, by the symmetry of H.

We now want to determine the evolution of the quantum fluctuations, which is exact at the quadratic level and corresponds to the classical one. We start from initial coherent states, for which $G^{qq}(0) = G^{pp}(0) = 1/2$ and $G^{qp}(0) = 0$. Let us discuss the different situations separately.

One-axis twisting Let us start by discussing the distinctive case of the one-axis twisting with $h = 0$ [344]. From (3.41), one easily derives the equation of motion for the quantum fluctuations

$$\begin{cases} \dot{\delta\hat{q}} = 0 \\ \dot{\delta\hat{p}} = J\ \hat{q} \end{cases} , \tag{3.42}$$

which admits as solution

$$\begin{cases} \delta\hat{q}(t) = \delta\hat{q}(0) \\ \delta\hat{p}(t) = \delta\hat{p}(0) + J\hat{q}(0)\ t \end{cases} . \tag{3.43}$$

From this, one has

$$\langle \hat{n}_{\text{exc}} \rangle = \frac{J^2 t^2}{4} \,. \tag{3.44}$$

This expression, together with Eqs.(3.21, 3.22), (3.25) and (3.28), leads for $1 \ll t \leq T_{\text{Ehr}}$ to the expected logarithmic growth of the entanglement entropy and polynomial dynamics of the $f_Q(t)$ and of $c(t)$ for regular trajectories, see e.g. Table 3.1.

Let us now discuss the general case in which $h \neq 0$. The equations of motion read

$$\begin{cases} \dot{\delta\hat{q}} = h\ \delta\hat{p} \\ \dot{\delta\hat{p}} = (J - h)\ \delta\hat{q} \end{cases} . \tag{3.45}$$

Therefore, by defining $\lambda_h^2 \equiv h\ (h - J)$, as in Eq.(3.38), one can write explicitly the exact evolution for the quantum fluctuations.

Stable regime $h > J$ The solution of Eq.(3.45)

$$\begin{cases} \delta\hat{q}(t) = \delta\hat{q}(0)\ \cos(\lambda_h t) + \dfrac{h}{\lambda_h}\ \delta\hat{p}(0)\ \sin(\lambda_h t) \\ \delta\hat{p}(t) = -\dfrac{\lambda_h}{h}\ \delta\hat{p}(0)\ \sin(\lambda_h t) + \delta\hat{p}(0)\ \cos(\lambda_h t) \end{cases} . \tag{3.46}$$

yields

$$\langle \hat{n}_{\text{exc}} \rangle = \frac{1}{4} \left(\frac{h}{\lambda_h} - \frac{\lambda_h}{h} \right)^2 \sin^2(\lambda_h t) \, . \tag{3.47}$$

This expression, together with Eqs.(3.21, 3.22), (3.25) and (3.28), leads to the predicted entanglement oscillations, see e.g. Table 3.1 or Figure 3.4 (left).

Unstable regime $h < J$ In this case $\lambda_h^2 = h(J-h)$ and the solution of Eq.(3.45) is now

$$\begin{cases} \delta\hat{q}(t) = \delta\hat{q}(0) \, \cosh(\lambda_h t) + \dfrac{h}{\lambda_h} \, \delta\hat{p}(0) \, \sinh(\lambda_h t) \\ \delta\hat{p}(t) = -\dfrac{\lambda_h}{h} \, \delta\hat{p}(0) \, \sinh(\lambda_h t) + \delta\hat{p}(0) \, \cosh(\lambda_h t) \end{cases} . \tag{3.48}$$

yielding

$$\langle \hat{n}_{\text{exc}} \rangle = \frac{1}{4} \left(\frac{h}{\lambda_h} + \frac{\lambda_h}{h} \right)^2 \sinh^2(\lambda_h t) \, . \tag{3.49}$$

Hence, for large times (but before the Ehrenfest time) $\langle \hat{n}_{\text{exc}} \rangle \sim e^{2\lambda_h t}$ and the entanglement and scrambling are predicted by the semiclassical approach, see e.g. Table 3.1 and Figure 3.4 (right).

On the other hand, one could also analyze the early time expansions for $t \to 0$. The QFI and spin squeezing in this regime have been studied by Sorelli and collaborators in Ref.[345], where they performed a Taylor expansion at short times. In Appendix C.5, we compare the two approaches, showing that the general results of Eqs.(3.21, 3.22), (3.25) and (3.28) together with Eqs.(3.44,3.47,3.49) reduces to their expansion at early times.

3.3 The kicked top

In this section, we study a paradigmatic model of quantum chaos: the quantum kicked top. The latter can be defined as an ensemble of quantum spins in a magnetic field periodically kicked via collective interactions. The model is described by the Hamiltonian

$$\hat{H}(t) = \alpha \hat{S}_x + \frac{\beta}{2Ns} \hat{S}_z^2 \sum_{n=-\infty}^{\infty} \delta(t - n\tau) \, , \tag{3.50}$$

where $\hat{S}_{x,y,z}$ are the collective spin operators in Eq.(2.18) and τ the period of the periodic kicking. We fix $\tau = 1$. Depending on the value of the kicking strength β, this model is known to exhibit a transition between a regular regime and a chaotic one [323, 324]. Being a paradigmatic model for quantum chaotic behavior, its bipartite [267, 303, 346–354], multipartite entanglement [351, 355–357] and scrambling dynamics [357–359] have been intensively explored.

The stroboscopic time-evolution operator (namely, the time-evolution operator over one period) encodes the dynamical stability properties — regularity or chaos — of the system. It can be written as

$$\hat{U} = \hat{U}_\beta \hat{U}_\alpha \quad \text{with } \hat{U}_\alpha = e^{-i\alpha\hat{S}^x}, \; \hat{U}_\beta = e^{-i\frac{\beta}{2Ns}(\hat{S}^z)^2} \, . \tag{3.51}$$

This kicked evolution is fully equivalent to a periodically alternating evolution of period 1 in which the system is evolved from time $t = n$ to time $t = n + 1/2$ with the transverse field Hamiltonian $H_1 = 2\alpha S^x$ and then from time $t = n + 1/2$ to time $t = n + 1$ with the interaction Hamiltonian $\frac{\beta}{Ns}(S^z)^2$, with $n \in \mathbb{N}$. Due to the collective nature of the interactions, for large N the classical limit is approached. In this limit, the stroboscopic evolution from time $t = n$ to $t = n + 1$ can be expressed as a discrete map on the Bloch sphere. This is obtained as the composition of the two following transformations

$$\begin{cases} \phi' = \arctan\left[\tan\phi\cos\alpha - \dfrac{\sin\alpha}{\tan\theta\cos\phi}\right] + \pi\, H(-\cos\phi) \\ \cos\theta' = \cos\theta\cos\alpha + \sin\theta\sin\phi\sin\alpha\ , \end{cases} \tag{3.52a}$$

$$\begin{cases} \phi'' = \phi' + \beta\cos\theta' \\ \cos\theta'' = \cos\theta' \end{cases}, \tag{3.52b}$$

where $H(x)$ is the Heaviside step function. See Appendix C.1 for the derivation.

3.3.1 Evolution of the quantum fluctuations

We now derive the semiclassical evolution of the Gaussian spin fluctuations $\delta\hat{\boldsymbol{\xi}} = (\delta\hat{q}, \delta\hat{p})$ around the classical solution as a discrete map. We first perform the bosonization of spin fluctuations around the time-dependent polarization direction $\vec{\mathcal{S}}(t) \equiv \langle \mathbf{S}(t) \rangle \propto \mathbf{Z}$ via the Holstein-Primakoff transformation in Eqs.(3.11). The stroboscopic evolution from time $t = n$ to $t = n + 1$ of the 2×2 correlation matrix $G(n) = \langle \delta\boldsymbol{\xi}(n)\delta\boldsymbol{\xi}(n) \rangle$ is given by the composition of the following two maps

$$\begin{cases} G'_{qq} = \cos^2(\psi - \psi')\, G_{qq} + \sin[2(\psi - \psi')] G_{qp} \sin^2(\psi - \psi')\, G_{pp} \\ G'_{pp} = \sin^2(\psi - \psi')\, G_{qq} - \sin[2(\psi - \psi')] G_{qp} + \cos^2(\psi - \psi')\, G_{pp} \\ G'_{qp} = -\cos[2(\psi - \psi')]\, G_{qq} + \cos[2(\psi - \psi')] G_{qp} + \sin[2(\psi - \psi')]\, G_{pp} \end{cases} \tag{3.53a}$$

$$\begin{cases} G''_{qq} = G'_{qq} \\ G''_{pp} = G'_{pp} - 2\beta\sin^2\theta'\, G'_{qp} + (\beta\sin^2\theta')^2\, G'_{qq} \\ G''_{qp} = G'_{qp} - \beta\sin^2\theta'\, G'_{qq} \end{cases} . \tag{3.53b}$$

The details of the calculation are reported in Appendix C.1. Together with Eqs.(3.52) and the appropriate initial conditions, they give a complete description of the semiclassical dynamics of the quantum kicked top at stroboscopic times. This analysis is valid before the Ehrenfest time scale T_{Eh}.

3.3.2 Numerical simulations

We compare the predictions of the semiclassical dynamics with the entanglement and chaos indicators obtained via exact numerical computations, specifically via exact diagonalization (ED).

Our general scheme is the following. We start from an initially polarized state on the Bloch sphere, which corresponds to a spin-coherent state parametrized by the two spherical angles angles (θ_0, ϕ_0) as

$$|\psi_0\rangle = |\theta_0, \phi_0\rangle = e^{i\phi_0 \hat{S}_z}\, e^{i\theta_0 \hat{S}_y}\, |S, S\rangle \ , \tag{3.54}$$

where $\hat{\mathbf{S}}$ are the collective spin operators in Eq.(2.18) and $|S, S\rangle = |S = N/2, S_z = N/2\rangle$ is the fully polarized state in the z direction.

Then, we let it evolve with the Floquet operator (3.51) generated by the Hamiltonian (3.50), and we compute the stroboscopic time-evolution of the entanglement entropy (1.24), the QFI (1.38) and the square commutator (1.45), at times $t_n = n\tau = 0, 1, 2, \dots$ (recall that we have fixed $\tau = 1$). In all our simulations, we fix $\alpha = \pi/2$, while β ranges in a sufficiently large interval to appreciate the order/chaos transition in the classical limit.

Let us provide a few details on the ED simulations. We construct the initial state in Eq.(3.54) following Ref.[360] and compute the entanglement entropy using the decomposition in Ref.[103]. The numerical QFI is given by the maximal eigenvalue of the covariance matrix $\mathrm{Cov}(\hat{A}, \hat{B}) = 4\langle \hat{A}\hat{B}\rangle - 4\langle \hat{A}\rangle\langle \hat{B}\rangle$ with $\hat{A}, \hat{B} = \hat{S}^{x,y,z}$ [343]. For the square commutator (1.45), we choose $\hat{A} = \hat{B} = \hat{S}^z/S$, for definiteness.

For the semiclassical analysis, we apply the discrete-time map in Eqs.(3.52a-3.52b) for the classical phase space — the Bloch sphere, parameterized by the canonically conjugated variables $\cos\theta$ and ϕ as in Eqs.(3.52) — and in Eqs.(3.53) for the quantum fluctuations. The initial conditions are $(\cos\theta(0), \phi(0), G_{qq}(0), G_{pp}(0), G_{qp}(0)) = (\cos\theta_0, \phi_0, 1/2, 1/2, 0)$, which represent the state in Eq.(3.54). From the time evolution, we directly compute the entanglement entropy, QFI and $c_{zz}(t)$ from Eqs.(3.21-3.22), Eq.(3.25) and Eq.(3.28), respectively.

A remark is in order concerning the semiclassical numerical methods. For this kind of simulations, it is crucial that numerical integration is symplectic. For single degrees of freedom, simplecticity reduces to the conservation of the volume in phase space, i.e., $\det G(t) \equiv 1/4$. Although the map in Eqs.(3.53) is exact, we find violations of this conservation law after a few kicks in the chaotic regime, due to machine-precision errors. To the aim of presenting accurate results for the time windows shown in the figures below, we have resorted to a multi-precision arithmetic library [361] and fixed the precision to at least 400 digits.

3.3.3 Discussion

We study, as a function of the kicking strength β, how the qualitative change in the semiclassical phase space across the order/chaos transition determines a change in the dynamics of the entanglement.

In Figure 3.5 we present the numerical results deep in the two orderly and chaotic phases. For small β (left panels), the phase-space trajectories are mostly regular KAM tori. In this case, the classical Lyapunov exponent is vanishing.

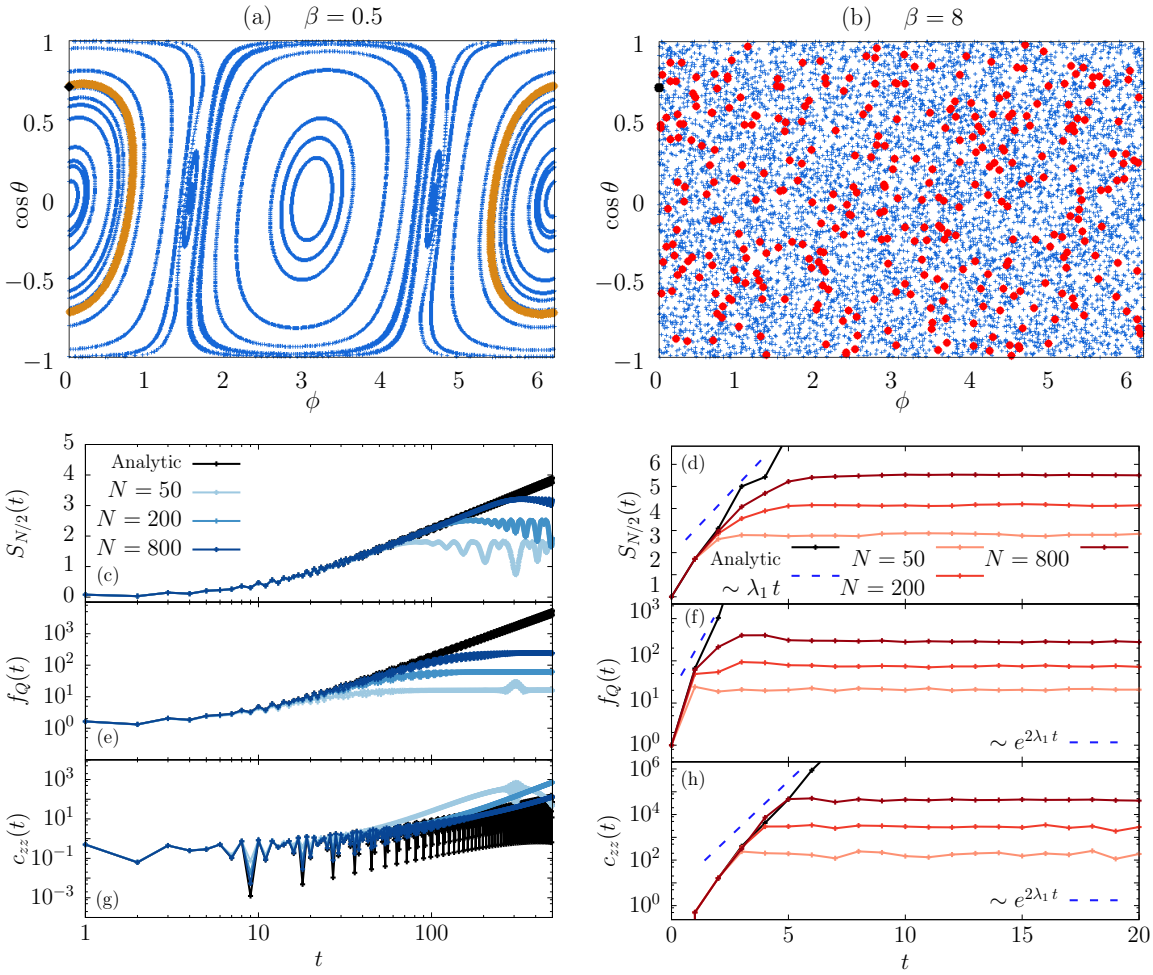

Figure 3.5: Dynamics of the quantum kicked top with $\tau = 1$ and $\alpha = \pi/2$, in the predominantly ordered and chaotic regimes with $\beta = 0.5$ and 8, respectively. Top panels: Poincarè map (stroboscopic phase-space trajectory) for the regular and chaotic dynamics, on the left (a) and right (b) panels, respectively. The black diamond and dot represent the initial condition of the orange and red trajectory, respectively. This initial condition ($\phi_0 = 0$ and $\theta_0 = \pi/4$) corresponds to the initial state for the quantum simulations in the bottom panels via Eq.(3.54). Bottom panels: We compare the corresponding analytical prediction for the entanglement entropy (c,d), quantum Fisher information (e,f) and square commutator (g,h), valid in the thermodynamic limit, with exact computations at finite system size $N = 50,\ 200,\ 800$. Here $\lambda_1 = 1.12$ is the maximal Lyapunov exponent computed in the Appendix C.4.

Accordingly, the asymptotic growth of quantum fluctuations in the semiclassical regime is polynomial in time. The theory in Section 3.1 predicts a logarithmic growth of the bipartite entanglement entropy and an exponential growth of the quantum Fisher information and of the square commutator. As shown in panels (c,e,g), the ED numerical data follow the semiclassical curves for a time window $T_{\rm Eh}(N) \sim \sqrt{N}$ that increases with the system size.
Conversely, for large β (right panels), chaos is fully developed in the classical phase space, and the motion is practically ergodic. The Lyapunov exponent λ is thus positive and almost uniform.

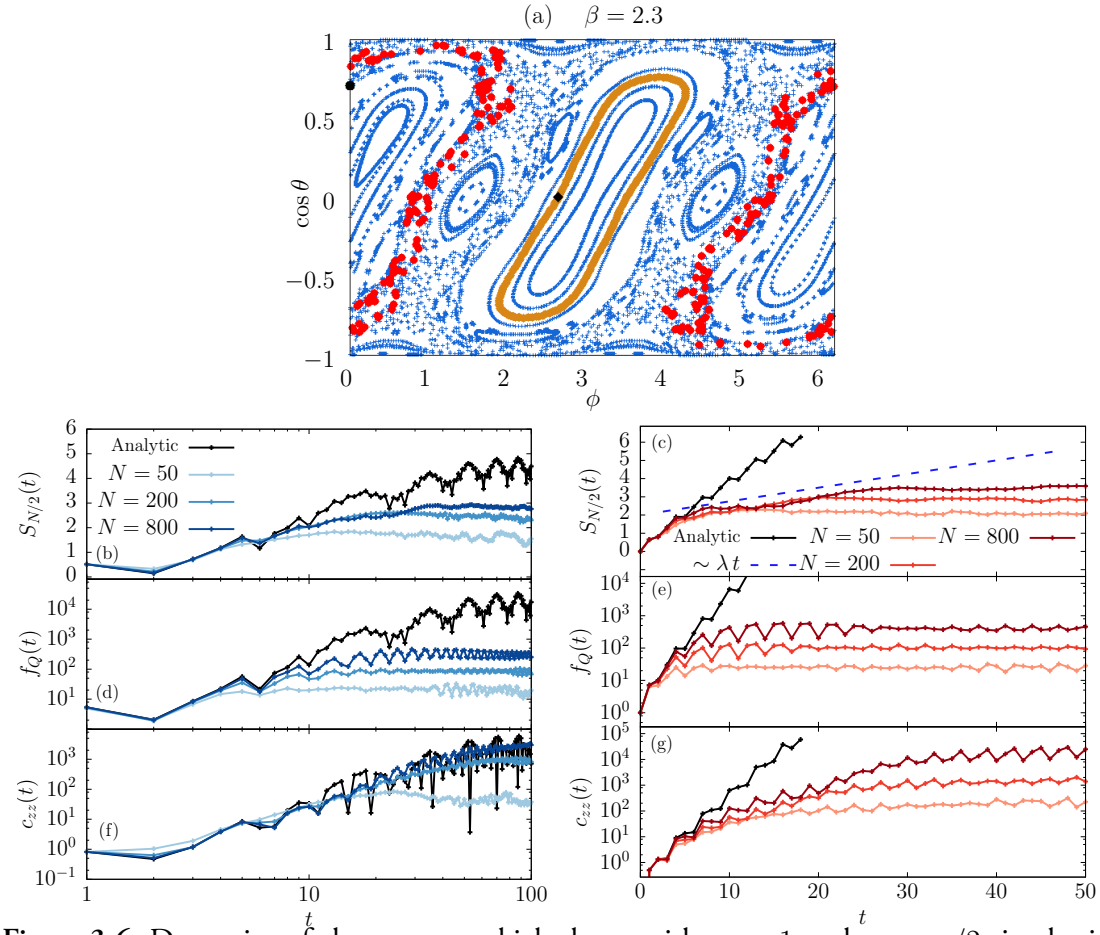

Figure 3.6: Dynamics of the quantum kicked top with $\tau = 1$ and $\alpha = \pi/2$, in the intermediate regime across the order/chaos transition, with $\beta = 2.3$. Top panel (a): Poincarè map (stroboscopic phase-space trajectories). The black dot and diamond (giving rise to the red and orange trajectories) indicate the initial condition of the simulations in the bottom panels. Bottom panels: Comparison between the analytical prediction for the entanglement entropy (b,c), quantum Fisher information (d,e) and square commutator (f,g), valid in the thermodynamic limit, and exact computations at finite $N = 50, 200, 800$. Left panels: Initial condition $\theta_0 = \pi/4$, $\phi_0 = 0$ corresponding to a regular trajectory. Right panels: Initial condition $\theta_0 = \pi/4$, $\phi_0 = 2.7$ corresponding to a chaotic trajectory. Here $\lambda_1 = 0.08$ is the maximal Lyapunov exponent computed in the Appendix C.4.

The theory in Section 3.1 predicts a linear growth of the bipartite entanglement entropy, with an asymptotic average slope λ, and an exponential growth of the quantum Fisher information and of the square commutator, with an asymptotic average rate 2λ. As shown in panels (d,f,h), the ED numerical data follow the semiclassical curves for a time window $T_{\rm Eh}(N) \sim \ln N$ that increases slowly with the system size. Hence, we turn to the intriguing intermediate regime across the order/chaos transition, characterized by a complex structure of phase-space trajectories featuring persisting KAM tori forming stability islands in a growing chaotic sea (we adopt here the standard figurative terminology in the literature). It is widely known that the

point-to-point and finite-time fluctuations of the Lyapunov spectrum are typically strong in Hamiltonian systems with a mixed phase space.

The comparison in Figure 3.6 allow us to test the theory of Section 3.1. Even in this case, the finite-size numerical data of the quantum evolution approach the result of the semiclassical computation as $N \to \infty$ for an increasing time window.

The behavior of the entanglement and chaos indicators for both the sample regular and chaotic initial states are partially masked by enhanced oscillations as compared to the corresponding evolution in Figure 3.5. Despite this effect, the distinction between the two qualitative behaviors is apparent.

In all cases, we observe some extent of discrepancy between the slope or rate of the transient growth of our indicators, and those compatible with the asymptotic Lyapunov exponent. This discrepancy is typically more pronounced when the phase space is complex and mixed [cf. Figure 3.6] than in a fully chaotic phase space [cf. Figure 3.5]. In Appendix C.4 we show that this is reflected in the rate of convergence of the numerical computations of λ.

3.4 The Dicke model

As a second illustrative example, we consider a conservative system: the Dicke model. The latter was originally defined [325] as an ensemble of two-level atoms collectively interacting with a single mode of the quantized electromagnetic field. Representing the atoms as spins-1/2, one can write the Dicke Hamiltonian as [9]

$$\hat{H} = \omega_0 \hat{S}^z + \omega \hat{b}^\dagger \hat{b} + \frac{\gamma}{\sqrt{N}} \frac{\hat{b}^\dagger + \hat{b}}{\sqrt{2}} \hat{S}^x, \tag{3.55}$$

where $\hat{S}^{x,y,z}$ are spin-1/2 collective operators as in Eq.(2.18) and $\hat{b}^\dagger$, $\hat{b}$ are creation and annihilation operators of a bosonic mode. For convenience, we define the real quadrature operators $\hat{Q} = (1/\sqrt{2})(\hat{b} + \hat{b}^\dagger)$, $\hat{P} = (1/i\sqrt{2})(\hat{b} - \hat{b}^\dagger)$. The Dicke model has interesting equilibrium and nonequilibrium properties. At zero temperature, the system undergoes a phase-transition at $\gamma_c = \sqrt{\omega\omega_0}/2$, between a normal phase ($\gamma < \gamma_c$) to a super-radiant one ($\gamma > \gamma_c$) [325]. Furthermore, in the classical limit the accessible phase space may undergo a progressive regular-to-chaotic transition upon varying the energy E and/or the coupling γ [326, 362]. Its bipartite [186, 304, 363–365], multipartite entanglement [186, 366–371] and scrambling dynamics [185, 186, 372, 373] have been intensively explored.

The dynamics of the Dicke model approach their classical limit for $N \to \infty$, described by the classical Hamiltonian $\hat{H}/N \to \mathcal{H}_{\rm cl}$

$$\mathcal{H}_{\rm cl} = \omega_0 \mathcal{S}^z + \omega \frac{\mathcal{Q}^2 + \mathcal{P}^2}{2} + \gamma \mathcal{Q} \mathcal{S}^x \,, \tag{3.56}$$

with

$$\hat{\mathbf{S}} \sim \frac{N}{2} \mathbf{Z}(t) \,, \quad \hat{Q} \sim \sqrt{N} \mathcal{Q}(t) \,, \quad \hat{P} \sim \sqrt{N} \mathcal{P}(t) \,, \tag{3.57}$$

[9] The Dicke model is often used in cavity-QED setups, where photon pumping and leakage require a Lindblad description of the dynamics. Here, we will only be concerned with ideally isolated systems, as relevant, e.g., for trapped-ions experiments.

where $\mathbf{Z}(t)$ represents the direction of the average collective spin and it is parametrized by the time-dependent angles $\phi(t)$, $\theta(t)$ [cf. Eq.(2.73)]. The functions $\mathcal{Q}(t)$, $\mathcal{P}(t)$ describe the limiting classical dynamics of the bosonic mode. The $\sqrt{N}$ scaling may be understood as the occurrence that all terms in the Hamiltonian are extensive and balance each other in equilibrium. The rescaling in Eq.(3.57) renders the emergence of the effective Planck constant $\hbar_{\text{eff}} = 1/N$ manifest.

The classical limit of the Hamiltonian governs the coupled dynamics of the atoms and the radiation field via the Hamilton equations

$$\begin{cases} \dot{\mathcal{Q}} = \omega \mathcal{P} \\ \dot{\mathcal{P}} = -\omega \mathcal{Q} - \dfrac{\gamma}{2} \sin\theta \cos\phi \\ \dot{\phi} = -\omega_0 \tan\theta + \gamma \mathcal{Q} \cos\phi \\ \dot{\theta} = -\gamma \mathcal{Q} \sin\phi \end{cases} . \tag{3.58}$$

See Appendix C.2 for the derivation.

3.4.1 Evolution of the quantum fluctuations

The evolution of the quantum fluctuations around the classical coupled evolution of the collective spin and of the cavity mode (3.58) can be obtained by adapting the method of Sections 3.1.2 and 3.1.3. The collective spin fluctuations may be described via a Holstein-Primakoff expansion around the time-dependent direction of the average spin orientation $\vec{\mathcal{S}}(t) \equiv \langle \hat{\mathbf{S}}(t) \rangle \propto \mathbf{Z}$, i.e. Eq.(3.11). The cavity-mode fluctuations are represented by deviations away from its macroscopic expectation value (3.57)

$$\begin{cases} \hat{Q} = \sqrt{N}\mathcal{Q}(t) + \delta\hat{Q} \, , \\ \hat{P} = \sqrt{N}\mathcal{P}(t) + \delta\hat{P} \, . \end{cases} \tag{3.59}$$

The quantum fluctuations are thus compactly denoted by $\delta\hat{\boldsymbol{\xi}} = (\delta\hat{Q}, \delta\hat{P}, \delta\hat{q}, \delta\hat{p})$. Conversely, typical quantum fluctuations in equilibrium, quantified by the expectation values of quadratic bosonic operators, are of order $\mathcal{O}(1)$, i.e., subextensive. This corresponds to having an effective Planck constant $\hbar_{\text{eff}} = 1/N$.

By substituting the expansions in Eqs. (3.11) and (3.59) into the Dicke Hamiltonian (3.55) and truncating it at the quadratic order, one finds the same structure as in Eq. (3.13). The classical trajectory $\mathcal{Q}(t), \mathcal{P}(t)$ and $\mathbf{Z}(t)$ is determined by the vanishing of the linear term in the quantum fluctuations, i.e., $\hat{H}_1(t) \equiv 0$. Their dynamics are thus regulated by the quadratic Hamiltonian $\hat{H}_2(t)$, from which we find Eq.(3.14), i.e.

$$\frac{d}{dt}\delta\hat{\boldsymbol{\xi}} = A(t)\, \delta\hat{\boldsymbol{\xi}} \, , \tag{3.60}$$

with

$$A(t) = \begin{pmatrix} 0 & \omega & 0 & 0 \\ -\omega & 0 & -\frac{\gamma}{\sqrt{2}} \cos\theta \cos\phi & \frac{\gamma}{\sqrt{2}} \sin\phi \\ -\frac{\gamma}{\sqrt{2}} \sin\phi & 0 & 0 & -\gamma\mathcal{Q}\frac{\cos\phi}{\sin\theta} \\ -\frac{\gamma}{\sqrt{2}} \cos\theta \cos\phi & 0 & +\gamma\mathcal{Q}\frac{\cos\phi}{\sin\theta} & 0 \end{pmatrix} . \tag{3.61}$$

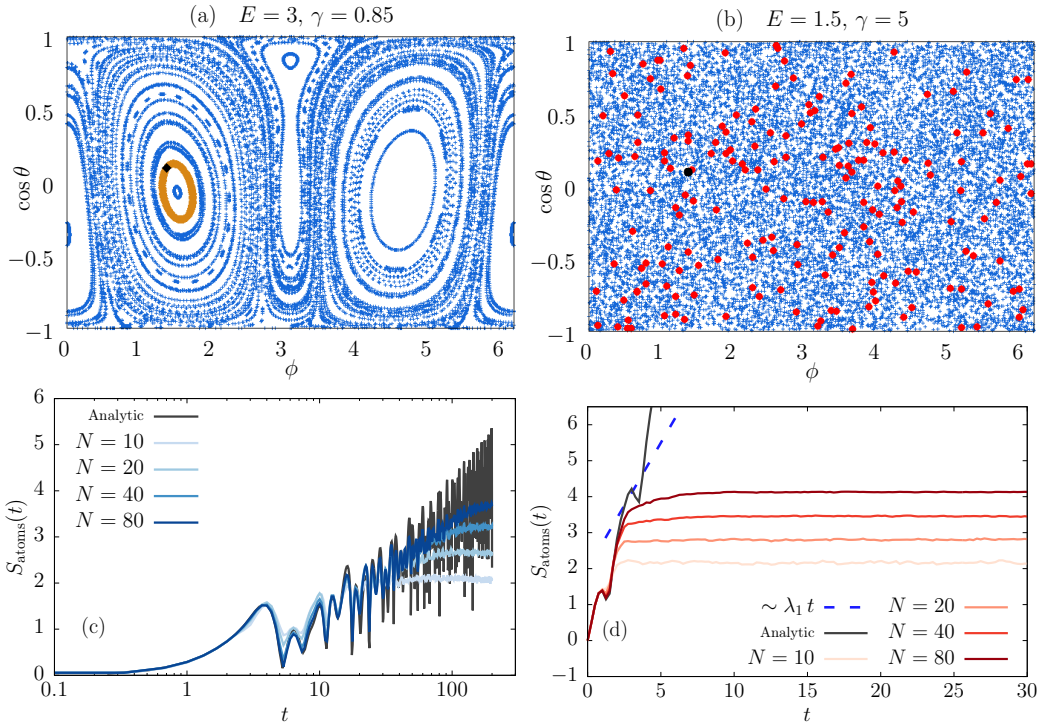

Figure 3.7: Entanglement dynamics for the Dicke model in the regular (a) and chaotic (b) regime with $E = 3$, $\gamma = 0.85$ and $E = 1.5$, $\gamma = 5$. (a-b) Poincarè maps with $\mathcal{P} = 0$ and $\mathcal{Q} > 0$ at fixed energies. The black diamond and dot correspond to the initial condition $(Q_0, P_0, \theta_0, \phi_0) = (Q(E, \theta_0, \phi_0),\, 0.,\, \theta_0, \phi_0)$ with $\theta_0 = \arccos(0.1)$ and $\phi_0 = 1.4$ chosen for the simulation of the entanglement entropy below. (c-d) Comparison between the semiclassical result with exact ED computations at finite $N = 10,\, 20,\, 40,\, 80$. (c) Dynamics in regular phase-space $E = 3$, $\gamma = 0.85$. (d) Dynamics in chaotic phase-space $E = 1.5$, $\gamma = 5$. Here $\lambda_1 = 0.7$ is the maximal Lyapunov exponent computed in the Appendix C.4.

Hence, the evolution of the correlation matrix $G(t)$ is determined via Eq.(3.17) from $A(t)$ by integrating Eq.(3.60). The details of the calculation to obtain Eq.(3.61) are reported in Appendix C.2. Together with Eqs.(3.58) and with the appropriate initial conditions, Eqs.(3.60,3.61) give a complete description of the semiclassical dynamics of the Dicke model, before the Ehrenfest time scale T_{Eh}.

3.4.2 Numerical simulations

We start from an initial state, which is a tensor product of a spin coherent state of the atomic ensemble and a bosonic coherent state for the cavity, namely

$$|\Phi_0\rangle = |\theta_0, \phi_0\rangle \otimes |\alpha\rangle \quad \text{with} \quad \alpha = \frac{\mathcal{Q}_0 + i\mathcal{P}_0}{\sqrt{2}}\,, \tag{3.62}$$

where $|\theta_0, \phi_0\rangle$ is the spin coherent state defined in Eq.(3.54), while the bosonic coherent state $|\alpha\rangle = e^{i(\alpha \hat{b}^\dagger + \alpha^* \hat{b})}|0\rangle$ is obtained by displacing the standard bosonic coherent vacuum $|0\rangle$ (defined by $\hat{b}|0\rangle = 0$, $\langle 0|0\rangle = 1$) by the complex vector α. This quantum initial state corresponds to a minimal-uncertainty Gaussian distribution

in the classical phase space, centered around the point $(\mathcal{Q}_0, \mathcal{P}_0, \cos\theta_0, \phi_0)$ (see e.g. Refs.[304, 326]). Then, we let evolve the system with the Dicke Hamiltonian (3.55) and we study the temporal development of quantum correlations.

We perform exact diagonalization using QuTip, open-source software for quantum optics dynamics [374, 375]. The spin Hilbert space is treated exactly, while we set a large cutoff N_{cut} on the photon Hilbert space, checking that the results are converged upon increasing N_{cut}. In all simulations, we take a maximum $N_{\text{cut}} = \Delta \times N$, where N is the number of spins and $\Delta \sim 4 \div 8$ varies depending on the trajectory. A convenient way to a priori estimate the needed magnitude of Δ is to evaluate the maximum of $(\mathcal{Q}^2(t) + \mathcal{P}(t)^2)/2$ along the reference classical trajectory in the target time window.

In the semiclassical simulations, we start from the classical initial conditions corresponding to the quantum state (3.62). We fix $\mathcal{P}_0 = 0$ and the value of the energy E. The classical initial condition is then $(\mathcal{Q}_0(E, \phi_0, \theta_0), 0, \cos\theta_0, \phi_0)$. We then numerically integrate Eqs.(3.58),(3.60). Since the Dicke Hamiltonian (3.55) is non-separable — i.e., it *cannot* be decomposed as $\mathcal{H}(\mathbf{q}, \mathbf{p}) = K(\mathbf{p}) + V(\mathbf{q})$ — efficient symplectic integrators are not available. For this reason, we employ an auto-adaptive fourth-order Runge-Kutta algorithm, fixing the relative and absolute accuracy to 10^{-14}. The lack of symplecticity of the numerical integration is witnessed, e.g., by violations of the phase-space volume conservation. This limitation restricts the validity of the classical simulations to relatively short times in the chaotic regimes.

Time-evolution is visualized via Poincaré sections at fixed energy $E = H(\mathcal{Q}_0, 0, \cos\theta_0, \phi_0)$ and $\mathcal{P} = 0$ in the four-dimensional phase space: the diagrams trace out the sequence of points in the $\cos\theta - \phi$ plane where the trajectory pierces the Poincaré section with $\mathcal{Q} > 0$. The natural entanglement bipartition in the Dicke model consists of subdividing the degrees of freedom of the atoms and the cavity mode. For any initial state (3.62), the semiclassical entanglement entropy is thus computed from Eq.(3.21).

3.4.3 Discussion

Similarly to the analysis of the quantum kicked top, we investigate all the qualitative dynamical regimes of the Dicke model and validate the correspondence between the entanglement dynamics and chaoticity properties in the semiclassical regime. Unlike the quantum kicked top, the Dicke model represents an isolated (undriven) system, so the energy is conserved. As its value of E and/or of the coupling γ is varied, the accessible phase space may undergo a progressive order/chaos transition [362]. This allows us to test the theoretical conclusions of Section 3.1 for autonomous dynamics.

In Figure 3.7, we show the Poincaré sections in two limiting cases of predominantly regular and chaotic behavior, in the top left and right panels, respectively. The initial state in Eq.(3.62) associated with the classical phase-space point denoted by a black marker is selected and the corresponding time-evolution of the von Neumann entanglement entropy between atoms and cavity mode is shown in the bottom panels. As it is apparent, the relation between orderly collective motion and slow logarithmic growth of entanglement on one side, and between collective chaos and fast linear growth of entanglement on the other side, is strongly corroborated by the outcome of the simulations.

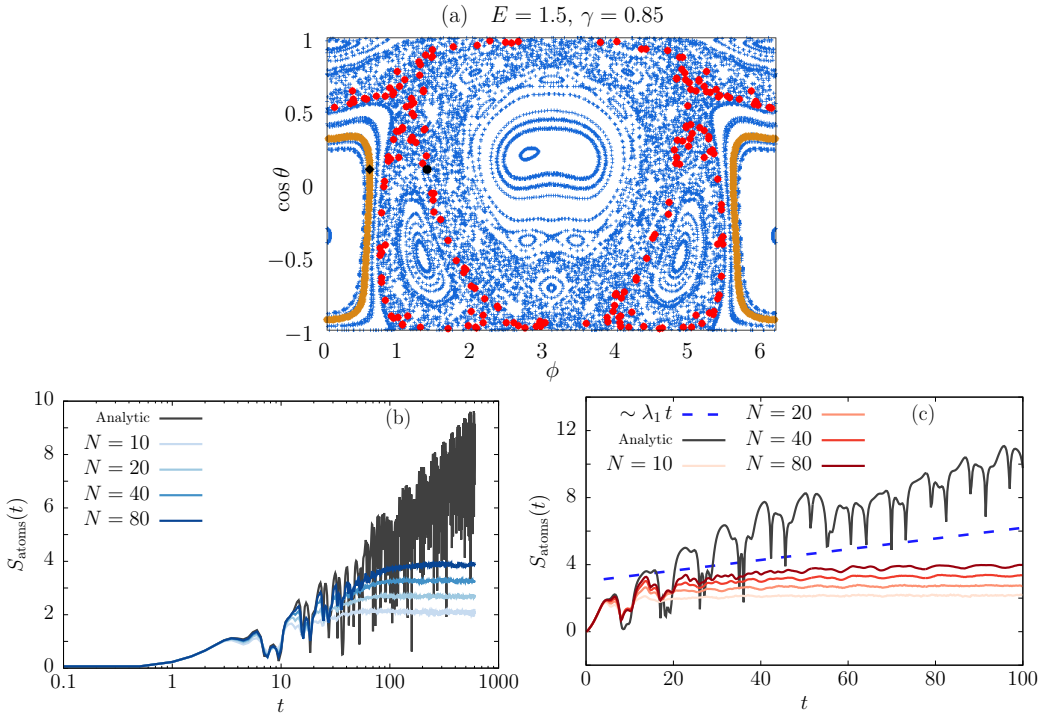

Figure 3.8: Entanglement dynamics for the Dicke model in the mixed regime with $E = 1.5$ and $\gamma = 0.85$. (a) Poincarè map with $\mathcal{P} = 0$ and $\mathcal{Q} > 0$ at fixed energy $E = 1.5$ with $\gamma = 0.85$. The black diamond (dot) correspond to regular (chaotic) initial conditions $(Q_0, P_0, \theta_0, \phi_0) = (Q(E, \theta_0, \phi_0), 0., \theta_0, \phi_0)$ with $\theta_0 = \arccos(0.1)$ and $\phi_0 = 0.6$ ($\phi_0 = 1.4$). (b-c) Comparison between the semiclassical entanglement entropy with exact ED computations at finite $N = 10, 20, 40, 80$. (b) Dynamics starting from the regular initial condition $\phi_0 = 0.6$ (diamond in (a)). (c) Dynamics starting from the chaotic initial condition $\phi_0 = 1.4$ (dot in (a)). Here $\lambda_1 = 0.03$ is the maximal Lyapunov exponent computed in the Appendix C.4.

In Figure 3.8 we turn to the intermediate regime of mixed classical phase-space across the order/chaos transition. The system is prepared in the two initial states corresponding to the phase-space points marked in black in the Poincaré section (top panel), representative of regular and chaotic trajectories, and the relative nonequilibrium dynamics of the entanglement entropy between atoms and cavity is displayed in the bottom panels. Similarly to the case of the quantum kicked top, the asymptotic growth of the entanglement entropy is partly obscured by pronounced oscillations and strong finite-time fluctuations. However, convergence to the semiclassical prediction upon increasing the number N of atoms is observed over an increasing time window.

As in the case of quantum kicked top, we observe deviations between the slope or rate of the transient growth of the entanglement entropy, and that compatible with the asymptotic Lyapunov spectrum. Even in this case, this effect tends to be more pronounced when the phase space is complex and mixed [cf. Figure 3.8] than in a fully chaotic phase space [cf. Figure 3.7]. Appendix C.4 discusses the rate of convergence of the numerical computations of the Lyapunov spectrum, highlighting the connection with the discrepancies presented in Figures 3.7 and 3.8.

3.5 Summary, interpretation and perspectives

In this work, we presented a unifying framework underlying the growth of entanglement in systems characterized by a well-defined classical limit, in agreement with previous suggestions in the literature [186, 298, 320]. Quantum entanglement indicators approach a finite limit as the effective Planck constant vanishes, $\hbar_{\text{eff}} \to 0$ [299, 315], and this limit possesses a clean interpretation in terms of the subsystem quantum fluctuations around the classical trajectory. Their temporal growth is precisely associated with the chaoticity properties of the underlying classical phase space. This allows us to make clear quantitative predictions on the asymptotic entanglement growth, based on the knowledge of the classical limit: Before the Ehrenfest time, for regular dynamics the entanglement entropy $S_A(t)$ grows only logarithmically in time, while the QFI and the square commutator polynomially; for chaotic dynamics, $S_A(t)$ undergoes a linear growth with a coefficient given by the classical Kolmogorov-Sinai entropy rate, while the QFI and the square commutator grow exponentially with a rate set by twice the largest classical Lyapunov exponent. This discussion is summarized in Table 3.1. For the entanglement entropy dynamics, this classification builds on the results of Ref. [320, 322] for quadratic bosonic Hamiltonians. We further discussed the finite-time fluctuations of entanglement quantifiers, crucial in finite quantum systems with a relatively short saturation time, and relate them to the underlying classical trajectories. We finally corroborated our analysis via detailed numerical computations in paradigmatic many-body collective quantum systems of current experimental relevance that undergo an order/chaos transition, namely the quantum kicked top and the Dicke model, finding excellent agreement with the analytical predictions in all dynamical regimes.

One can interpret these results in an appealing and experimentally natural way, as depicted in Figure 3.9. In fact, the central result for quadratic bosonic Hamiltonians of Refs. [320, 322] (see Section 3.1) states that the *entanglement entropy of a subsystem A, $S_A(t)$, asymptotically coincides with the logarithm of the phase space volume* spanned by the quantum fluctuations of the subsystem degrees of freedom. Hence, entanglement increases because of the growth in time of this "reduced" volume, while the global phase-space volume is always conserved. (Notice the interesting correspondence with the quantum Liouville theorem of Ref.[376] in the operator-spreading perspective.) This picture corresponds to the well-known identification of entanglement generation with the decoherence of the subsystem, illustrated in Figure 3.9. In an isolated spin system, such as the quantum kicked top, the uncertainty growth of a subset in the collective spin turns out to be dictated by the stretching of the global quantum fluctuations on the Bloch sphere, referred to as spin squeezing. Consequently, all the entanglement and chaos indicators in this semiclassical regime can be reduced to the rate of spin squeezing, which is accessible via standard experimental tools. Concerning spin-boson systems, such as the Dicke model, the bipartite entanglement entropy between the spins and the boson can be read out from the growth of the volume spanned by the collective spin fluctuations. In fact, as illustrated in Figure 3.9, the area covered by spin fluctuations progressively expands during the nonequilibrium evolution, due to the growth of the entanglement with the cavity mode. (This is in contrast to an isolated spin sys-

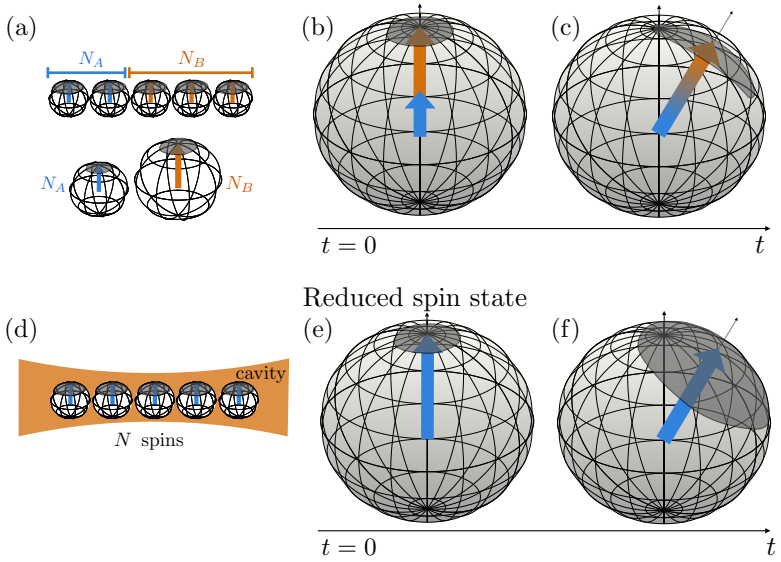

Figure 3.9: Illustration of the temporal growth of quantum fluctuations and the associated entanglement generation in spin systems with direct interactions (a-c) or with interactions mediated by bosonic "cavity" modes (d-f). The collective spin can be represented through an extended grey region on the Bloch sphere surrounding the point identified by its average polarization $\langle \hat{\mathbf{S}}(t) \rangle$. The grey region represents the uncertainty of the collective spin polarization due to quantum fluctuations. Top panels (a-c): spin-spin interactions lead to a progressive stretching of the spin fluctuations, or spin squeezing, which determines the growth of bipartite (between subsets of spins A and B) and of multipartite entanglement. Bottom panels (d-f): the entanglement between the spins and the bosonic cavity mode can be read out from the area covered by spin fluctuations on the Bloch sphere.

tem, where the area spanned by collective spin fluctuations gets stretched in time but is conserved — compare to Figure 3.9(b-c).) This principle has already been exploited to access bipartite entanglement between the nuclear and the electronic spin in experiments with single atoms [351]. Similar ideas have also been applied to access entanglement dynamics and chaos in experiments with trapped-ion systems described by the Dicke model [186, 377].

We also show that the correspondence between entanglement and scrambling ceases to be valid after the Ehrenfest time, where the square commutator displays a fully quantum regime describing the non-local growth of the operator support.

The same semiclassical approach could be applied to the entanglement growth in open systems, where it has been already shown that quantum fluctuations around the mean-field observables are the responsible for the growth of the entanglement negativity [332]. A very challenging and interesting problem is to understand how quantum interference effects enter the game after the Ehrenfest time, causing saturation of the entanglement quantifiers [378]. It is worth stressing that our results contribute to establishing a clear predictive framework for the study of entanglement dynamics in more general semiclassical approaches, such as those based on time-dependent variational principles [335, 379, 380]. Also, they can likely be ex-

tended to match complementary approaches to entanglement dynamics such as that in Ref. [352].

We finally reiterate that the connection between entanglement dynamics and chaos studied here, has direct experimental relevance for the detection of entanglement and its dynamics via measurements of collective quantities [158, 261, 381], the experimental accessibility of which is well-established with standard techniques and tools of quantum atomic experiments — see Figure 3.9 and the relative discussion.

Chapter 4

Scrambling and entanglement spreading in long-range spin chains

The goal of this chapter is the study of scrambling and entanglement spreading beyond the fully connected semiclassical regime. We first discuss the difference between entanglement and scrambling for infinite-range spin systems beyond the Ehrenfest time. Secondly, we consider the scrambling and entanglement growth of long-range spin chains with interactions decaying algebraically with the distance between two sites.

In the previous chapter, we have illustrated a semiclassical framework for the dynamics of entanglement before the Ehrenfest time, for systems characterized by permutational symmetry via all-to-all interactions. We are now interested in understanding the entanglement spreading beyond the Ehrenfest time and the impact of slowly-decaying interactions that decay algebraically with the distances r as $1/r^{\alpha}$, with exponent α [1].

In the quantum domain, long-range systems have been the focus of a great deal of attention only relatively lately, as a result of their experimental simulability with different platforms [258, 382–384]. These systems allow the controlled study of quantum dynamics in the absence of significant decoherence, a property that allows the explore of a number of important phenomena as, for example, dynamical phase transitions [29, 290, 385–387] or the dynamics of correlations [388–398] in a situation where Lieb-Robinson bounds do not apply [36, 399]. As far as entanglement entropy is concerned, very little is known both in [218, 400–408] and out-of-equilibrium [341, 342, 409–411]. At the same time, scrambling has been intensively studied in connection to correlation bounds [412–418] and its time average as a probe of criticality, see e.g. Ref.[419]. However, an analysis of the dynamics and the relevant time-scales in relation to the different processes involved in the spreading of information is still missing.

As we have thoroughly shown in the previous chapter, the early-time behavior of the entanglement quantifiers and the square commutator are connected to the chaotic properties of the underlying semiclassical limit. However, in view of the various forms in which quantum correlations manifests in a many-body system, it is

[1] The fully-connected limit of the previous chapter is retrieved by setting $\alpha = 0$.

important to understand how entanglement is connected to the scrambling beyond the fully-connected semiclassical regime.

In this chapter, we address these issues by studying numerically bipartite and multipartite entanglement propagation and scrambling in spin chains with long-range interaction with exponent α. We begin by reviewing the salient features of quantum long-range spin systems, as they will be the subject also of the next chapters. Then, we will present results for the entanglement dynamics of the quantum Fisher information, the tripartite mutual information and operator scrambling, studied via the square commutator.

We discuss the difference between entanglement and scrambling after the Ehrenfest time, considering as illustration the LMG model, defined in Section 3.2. As we are going to show in the rest of the chapter, scrambling and entanglement dynamics turn out to be very different. Interestingly, this becomes glaringly obvious in the regular regime, rather than in the chaotic one. In fact, the difference between entanglement and scrambling becomes noticeable *after* the Ehrenfest time $T_{\rm Ehr}$, where the entanglement quantifiers saturate, while the square-commutator undergoes to a fully quantum non-perturbative polynomial growth (saturation for chaotic dynamics), symmetric around $t^* = t_{\rm rec}/2$ the *recurrence time* $t_{\rm rec}$.

Secondly, we report numerical results in one-dimensional systems upon varying the range of interactions for $\alpha > 0$. We find that bipartite and multipartite entanglement display the same qualitative dynamics of short-range interacting systems for $\alpha > 2$. On the other hand, they posses a clear semiclassical behavior for $\alpha \leq 1$, with dinstinct logarithmic entanglement entropy growth and polynomial quantum Fisher information before saturation.

Entanglement in long-range spin chains is also discussed in two other chapters of the thesis.
The next Chapter 5 is devoted to an analitical understanding of the origin of such slow growth of entanglement for long-range systems, which was also reported by other numerical simulations[341, 342].
We conclude the study of clean long-range systems by shifting our focus on *ground state* entanglement. With this aim, we analyze in Chapter 7 the ground state von Neumann entropy of the Dyson hierarchical model.

The rest of the chapter is organized as follows. In Section 4.1, we recall the salient features of quantum long-range spin systems. In Section 4.2 we discuss the difference between entanglement and scrambling beyond the Ehrenfest time, considering the LMG model as an illustration. In Section 4.3, we report some numerical findings on long-range systems characterized by algebraically decaying interactions with exponent $\alpha > 0$.

4.1 Quantum long-range systems

Long-range interacting systems, because of their unconventional static and dynamical properties, have been extensively studied in classical statistical mechanics for many decades [47]. They display a plethora of interesting phenomena, such as

non-additivity of energy, slow relaxation, or ergodicity breaking, which do not have a counterpart in standard short-range statistical mechanics. In the quantum domain, atomic, molecular, and optical systems (AMO), as well as synthetic ones, are often described by long-range interactions. Yet, they have been a focus of great attention only relatively recently, as a consequence of their experimental implementation in different physical setups of many-body AMO systems, such as Rydberg atoms [420, 421], dipolar molecules [422, 423] or trapped ions [258, 382–384, 424]. In particular trapped ions, effectively described by ferromagnetic Ising long-range interactions (see below Eq.(4.1)), represent one of the most promising platforms for quantum computation [425, 426]. These experimental advances motivated an increasing interest towards the understanding of quantum systems with long-range interactions both in thermodynamic equilibrium [218, 400, 402–408, 427–436] and in several non-equilibrium situations [341, 342, 390, 391, 394, 405, 410, 437–453].

The prototypical Hamiltonian for such studies is the spin-1/2 Ising chain in transverse field with long-range interactions, defined as

$$\hat{H} = -\frac{J}{\mathcal{N}_{\alpha,N}} \sum_{i<j}^{N} \frac{\hat{\sigma}_i^x \hat{\sigma}_j^x}{|i-j|^\alpha} - h \sum_{i}^{N} \hat{\sigma}_i^z, \tag{4.1}$$

where $\hat{\sigma}_i^{x,z} = 2\hat{s}_i^{x,z}$ are Pauli matrices on sites $i = 1, \dots, N$ of the chain, h is the global transverse magnetic field. Notice the *Kač rescaling factor* $1/\mathcal{N}_{\alpha,N}$ given by

$$\mathcal{N}_{\alpha,N} = \frac{1}{N} \sum_{i \neq j} \frac{1}{|\mathbf{r}_i - \mathbf{r}_j|^\alpha} \,. \tag{4.2}$$

which replaces the $1/N$ factor in Eq. (2.17), ensuring the extensivity of the Hamiltonian for $\alpha \leq d$ [454]. The fully-connected limit is recovered by letting $\alpha \to 0$.

This model (in its classical and quantum version) has been extensively studied at *thermal equilibrium*, in particular in connection to the change of the universality classes due to the presence of long-range interactions. Qualitatively, it is well-known that a long-range interacting system may be equivalent to a short-range interacting one with an increased effective dimensionality [455–457]. In general, universality classes depend on the exponent α and one can identify two values $\alpha^{\pm}(d)$ depending on the dimensionality d, with $d \leq \alpha^{\pm}(d) \leq \alpha^{+} \leq d+2$. The universal behavior is described by mean-field theory for $\alpha < \alpha^{-}(d)$, by the short-range exponents in the same spatial dimensions for $\alpha > \alpha^{+}(d)$, while for $\alpha^{-}(d) < \alpha < \alpha^{+}(d)$ it is characterized by peculiar long-range exponents [429, 458]. One of the main effects of long-range interactions is the possible existence of long-range order at finite temperature. This occurs every time the dimensionality d is smaller than the upper critical dimension of the short-range model and one can effectively map the system onto an effective dimension which varies continuously with α, i.e. $d_{\text{eff}}(\alpha)$. For instance, in classical and quantum one-dimensional systems it is well-known that long-range order can be stabilized for $\alpha < 2$. This implies the existence of long-range order for highly-excited states. Such property constitutes one of the distinctive features of long-range interacting quantum systems.

More recently, also the *out-of-equilibrium* physics of quantum long-range Hamiltonians have been intensively scrutinized. As already mentioned in the first chapter,

all the standard paradigm of quantum thermalization – which relies on the presence of local Hamiltonians – does not apply to long-range interacting systems. Fundamental theorems, such as the Lieb-Robinson bound (1.3) or area law (1.46), are no longer valid. Also ETH [cf. (1.12)] has not been put on solid grounds in this case, besides few exceptions, e.g. [459].
However, quantum long-range systems are now known to display several interesting non-equilibrium phenomena, ranging from exotic correlation spreading [388–396] to new dynamical phases [290, 385–387, 460], as well as confinement [438, 461]. For instance, dynamical phase-transitions [32] persist also at finite α [290, 385, 448]. As discussed in Section 3.2 for fully-connected Hamiltonians $0 < \alpha \leq d$, with dynamical phase-transitions we refer to the existence of a finite order parameters out-of-equilibrium. For $\alpha \neq 0$, such phenomenon has been investigated numerically by means of TDVP in Ref.[385] or with semiclassical methods in Ref.[290] more recently.
A very interesting research direction concerns how long-range interactions affect the spreading of quantum correlation and entanglement growth. In fact, they pose a conceptually different and challenging problem. On one side, their non-local interactions allow quantum correlations between distant degrees of freedom to build up very quickly. This leads to violations of the Lieb-Robinson bound (1.3), and nonlinear light-cone spreading of quantum correlations [388–398, 410]. On the other, several numerical simulations have shown that entanglement entropy growth after a quench features a dramatic counterintuitive slowdown as the range of interactions is increased: It becomes as slow as logarithmic when the couplings decay algebraically with the distances with α smaller than the spatial dimensionality d, even in the absence of disorder [341, 342]. Understanding such a slow-growth of entanglement is one of the goals of the present and next chapters.

4.2 Scrambling beyond the Ehrenfest time

In this section, we consider the fully connected case for $\alpha = 0$ and focus on scrambling beyond the Ehrenfest time (2.7), where the differences with entanglement dynamics become more evident. The phase diagram of this model for $\alpha = 0$ has been described in Section 3.2, which we refer to. As we have thoughtfully illustrated, the entanglement dynamics reflect the semiclassical nature of the system: for general questions it is weak, slowly growing, and saturating at the Ehrenfest time T_{Ehr}.

On the other hand, the square commutator is characterized by two different regimes: a first semiclassical growth up to the T_{Ehr} (exponential for chaotic dynamics), followed by a fully quantum non-perturbative polynomial growth (saturation for chaotic dynamics), symmetric around $t^* = t_{\text{rec}}/2$ the *recurrence time* t_{rec}. The first regime is fully-semiclassical, as characterized by the theory of Section 3.2. As we have already discussed, such initial growth encodes the nature of classical orbits and can be exponential also for regular integrable dynamics, provided they have some classical instabilities. Conversely, the second regime accounts for the quantum chaoticity of the dynamics and it can not be reproduced by semiclassical approaches.

This reiterates that the state's entanglement growth and operator scrambling are

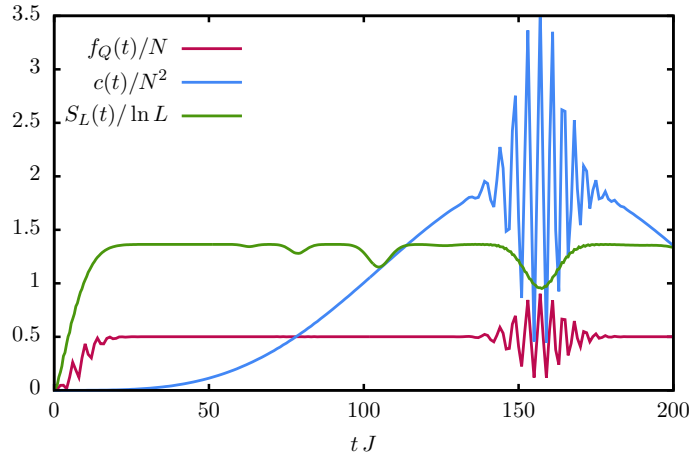

Figure 4.1: Quantum information dynamics for the regular dynamics in the LMG model. The entanglement quantities, entanglement entropy and QFI (green and red), saturate at T_{Ehr}, while the square commutator of the longitudinal magnetization operator (blue) goes beyond semi-classics and keeps growing up to t^*. Exact diagonalization results for $N = 100$, $h_f = 2$, S_L with $L = 5$.

two distinct, apparently disconnected phenomena beyond the classical limit. Interestingly, this becomes glaringly obvious in the regular regime, rather than in the chaotic one, see Figure 4.1.

Let us now finally describe in more detail the results obtained for the scrambling dynamics. We study the square commutator (1.45) between the collective operators along z, i.e. choosing $\hat{A} = \hat{B} = \hat{S}^z/S$, where $\hat{S}^z = \sum_i \hat{s}_i^z$ and $S = N/2$.

In the case of the quench dynamics, in the regular regime (above the dynamical critical point $h_f \gg h_c$) the square commutator is characterized by a first semiclassical quadratic growth $c(t) \propto t^2/N^3$ until $T_{\text{Ehr}} \propto \sqrt{N}$. In this regime, semiclassical approximations describe very well the evolution of $c(t)$ and we chose to employ the DTWA, i.e. the discrete truncated Wigner approximation introduced in Section 2.2.2. To this end, we generalized the corresponding expression for the square commutator to the discrete phase space representation

$$c(t) \sim \frac{\hbar^2}{N^4} \sum_{i,j,k,m} \overline{\left[\delta_{ij}^{xzy}(t) - \delta_{ij}^{yzx}(t)\right]\left[\delta_{km}^{xzy}(t) - \delta_{km}^{yzx}(t)\right]} \tag{4.3}$$

where $\delta_{ij}^{\alpha\beta\gamma}(t) = \sigma_i^{\alpha}(0)\frac{\partial\sigma_j^{\beta}(t)}{\partial\sigma_i^{\gamma}(0)}$, with $\sigma_i^{x,y,z}$ the Weyl transform of the spin operators and the average $\overline{(\cdot)}$ is computed over the initial discrete Wigner distribution given by Eq.(2.59). Note that the square commutator can be expressed within the phase-space formalism in terms of the Bopp operators, as shown in the Appendix B.
At T_{Ehr}, the quantum regime starts, characterised by a polynomial growth $\sim (t/N)^4$ up to a maximum $c(t_*) \sim 2$. At this time, the square commutator is independent of the system size. Even the DTWA, that perfectly reproduces multipartite entanglement dynamics up to T_{Ehr} (see Figure 2.1 in Section 2.2.4) is not able to reproduce the long time dynamics of the square commutator, see Figure 4.2. Indeed DTWA, despite keeping N discrete trajectories, represents all operators as factorised on each

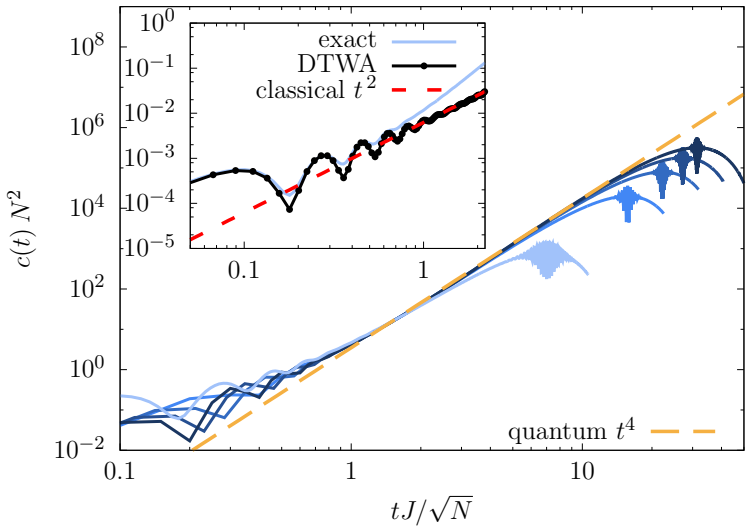

Figure 4.2: The two-times regime of the square commutator in the LMG model after a quantum quench with $h_f = 2$. In the main plot the quantum regime of $c(t)$ for different N: this regime starts at $\sqrt{N}$ and then $c(t)$ grows polynomially as t^4. ED results in blue for $N = 20, 100, 200, 300, 400$ (increasing color darkness), dashed yellow line for the polynomial fit. In the insert we show the semiclassical regime, comparing the exact $c(t)$ with DTWA, which predicts the $\sim t^2$ power-law growth, dashed in the plot. Here $N = 20$ and DTWA obtained with $N_{\rm sim} = 5 \cdot 10^3$ samplings.

site at any time [cf. Eq.(2.63)], see e.g. Ref.[284]. At times longer than $T_{\rm Ehr}$, the operator expansion starts developing longer and longer strings and the square commutator re-sums all the correlations, until t_*, which corresponds to the time at which the string of length N occurs. As we have shown in Section 2.2.4, such non-local growth of the operator can be captured for instance by the CTWA with increased cluster size, see e.g. Figure 2.2. Quenches to $h_f \ll h_c$, are characterized by the same time-scales $T_{\rm Ehr}$ and t_* and the same semiclassical regime $\sim t^2/N^3$ up to $T_{\rm Ehr}$. The result at long-times is qualitatively different: the quantum regime is $\sim t^3/N^4$ and $c(t_*) \sim 10^{-3}/N$ goes to zero at all times in the thermodynamic limit. This is a direct consequence of the existence of the dynamical transition, which is detected by scrambling [419]. Due to the presence of a macroscopic magnetization, the support of the operators has constrained dynamics and it will not acquire a string of length N.

A special case is represented by the quench at the dynamical critical point $h_f = h_c$. Despite the integrability of the quantum system, we find that the square commutator grows exponentially in time up to $T_{\rm Ehr} \propto \ln N$ as $c(t) = e^{2t}/N^3$. This is due to the existence of an unstable trajectory in the classical dynamics. The exponent is twice the eigenvalue of the instability matrix of the separatrix trajectory λ_{h_c} in Eq.(3.38) for $h_c = 1/2$. This is valid in general for all the classical trajectories associated with DPT. To our knowledge, this is the first example of an early time exponential growth in a many-body regular system to be reported. After $T_{\rm Ehr}$, $c(t)$ keeps growing linearly in time up to the t_*^r and then it goes back, see Figure 4.3.

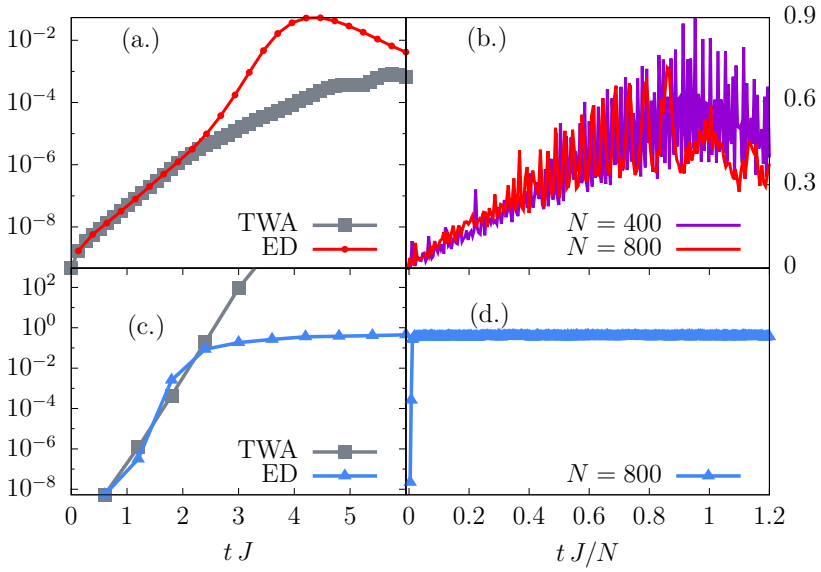

Figure 4.3: Square commutator dynamics $c(t)$ for the LMG model after a quantum quench to the DPT point (a., b.) and for the kicked top with $\beta = 20$, $\tau = 0.6$ (c., d.). At early times (a., c.), they are both characterized by an exponential growth up to T_{Ehr}, see the right side with the log-scale on the y axis. This regime can be perfectly reproduced by the TWA. (b., d.) At long times the behavior is different depending on the quantum integrability properties. In (c.) the time is rescaled by N in order to show that $c(t)$ grows up to a maximum at t_*. (d.) In the Kicked top the $c(t)$ stays constant also at very long times. Here, $N = 800$ and the TWA was obtained with $N_{\text{sim}} = 10^4$ samplings.

We conclude by considering the kicked top, which undergoes to a chaotic dynamics as discussed in Section 3.3. As expected, $c(t)$ is initially dominated by the classical exponential growth, then, after T_{Ehr}, quantum interference effects appear and the square commutator saturates to a constant value [161], see Figure 4.3 (lower panels). In the quantum chaotic regime, the dynamics are reproduced by the semiclassical approximation, which predicts the initial time growth of the square-commutator. After T_{Ehr}, the TWA loses any physical meaning. The quantum $c(t)$ remains constant and finite in the thermodynamic limit, meaning that the operator support is spread up to the longest string already from T_{Ehr}.

4.3 Entanglement dynamics for finite range α of interactions

In this section, we report the numerical findings on how entanglement grows and spreads in Ising spin chains with two-body power-law decaying interactions, $J_{ij} \propto |i-j|^{-\alpha}$ and after the semiclassical regime. We consider for definiteness the case in which an initial separable state, i.e. $|\psi_0\rangle = |\uparrow\uparrow \ldots \uparrow\rangle$, is brought out-of-equilibrium by means of a quantum quench with the Ising long-range Hamiltonian (4.1). In particular, we will focus on the quantum Fisher information (1.35) for $\hat{O} = \hat{S}^z$ and on the tripartite mutual information I_3 (1.26).

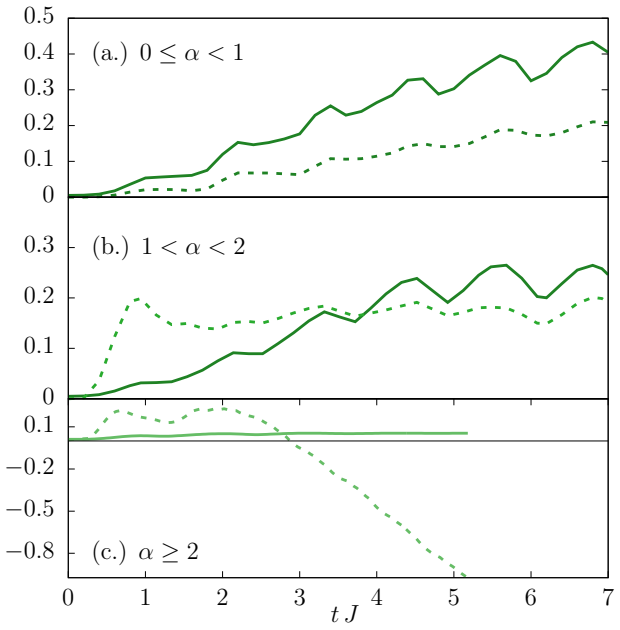

Figure 4.4: We plot the minimal TMI (dotted lines) and the $f_Q(t)/N$ (full lines) as a function of time, varying the range of interaction α. We obtained the minimal TMI by calculating the tripartite mutual information for all possible partitions A,B,C,D of the system and then taking the minimum. For $0 \leq \alpha < 1$ (a.) the dynamics is the same as the LMG model. For $1 \leq \alpha < 2$ (b.) we observe quadratic growth of the QFI with time, whereas the minimum of the tripartite mutual information remains bounded with time. When $\alpha > 2$ (c.), the QFI does not scale with the system size and remains bounded, whereas the minimum of the TMI decreases linearly with time and becomes negative for longer times. The parameters of the evolution are: $\alpha = 0.5$, $\alpha = 1.5$, $\alpha = 2.5$, $h_f = 0.75$. Data obtained with TDVP for system sizes $N = 200$ and bond dimension $D = 256$ (or $N = 100$, $D = 512$ for $\alpha = 2.5$).

As we have anticipated, the dynamics of the information spreading changes with the range of interaction α, as shown in Figure 4.4.

The Hamiltonian with $0 \leq \alpha < 1$ is dominated by the classical limit and the structure of entanglement and scrambling is the same as in the infinite range case. The QFI grows polynomially in time up to an extensive value $\overline{f_Q} \sim N$, signaling genuine multipartite entanglement of the asymptotic state. In this case, TMI increases logarithmically in time up to a constant positive value. The TMI gives complementary information: being positive, $\overline{I_3} > 0$ it shows that the information of the initial state is not delocalized across the system, see Figure 4.4 (a).

On the other hand, for $\alpha \geq 1$ the dynamics of entanglement changes. Let us first discuss $1 \leq \alpha < 2$. In this case, the QFI has the same structure as for $\alpha < 1$: it grows polynomially in time and saturates to an extensive value. On the other hand, the TMI grows linearly in time, but it still saturates to a positive value $\overline{I_3} > 0$, see Figure 4.4 (b).
Decreasing the range of interaction the situation changes drastically: for $\alpha \geq 2$ the state displays the typical dynamics and structure of short-range interacting systems.

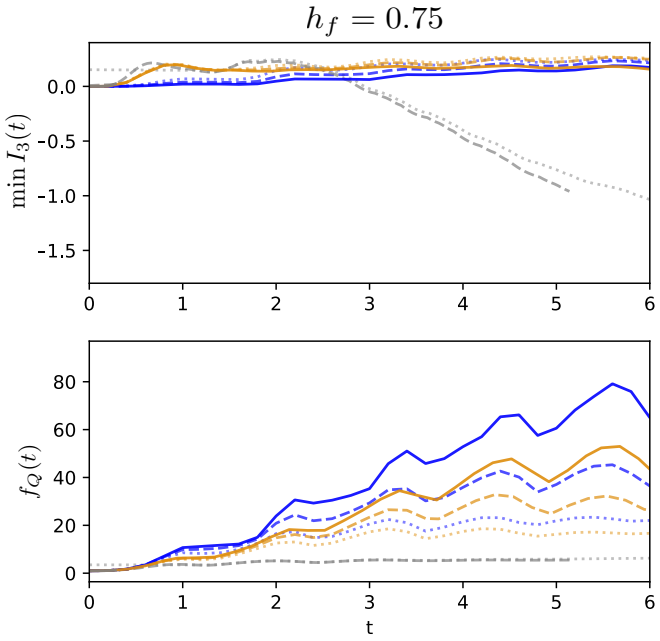

Figure 4.5: Scaling of the QFI and the tripartite mutual information with the system size for long-range hamiltonians for $\alpha \neq 0$. We observe that whenever the $f_Q(t)$ increases with the system size the minimum of the tripartite mutual information becomes independent of the system size and vice versa. The colors correspond to different interaction ranges: $\alpha = 2.5$ (gray) $\alpha = 1.5$ (orange) and $\alpha = 0.5$ (blue). The brightness and line style correspond to different system sizes $n = 50, 100, 200$ from bright to dark (or dotted to full lines). All data is converged with the bond dimension $D = 256$, except the data for $\alpha = 2.5$ where bond dimension 512 had to be used.

In fact, the QFI only displays intensive multipartite entanglement $\overline{f_Q} \sim$ const. and the TMI initially grows linearly in time. Interestingly, for this range of parameters, one finds $\overline{I_3} < 0$ signaling that the information about the initial condition is spread throughout the degrees of freedom of the state, see Figure 4.4 (c).

In Figure 4.5, we show the scaling of the QFI and the tripartite mutual information with the system size for long-range hamiltonians for finite size systems with $N = 50, 100, 200$. All the numerical results are obtained with TDVP algorithms, checking that the results are converged upon increasing the bond dimension. See Figure 4.5 for a brief discussion of the convergence of the method.

Long-range interactions do not change drastically the dynamics of the square commutator. In the range $\alpha \leq 1$, the early time dynamics are the same as those described before. The square commutator grows like a power law at small times, even for $\alpha > 2$.

Chapter 5

Semiclassical dynamics of long-range spin systems

In this chapter, we study the effect of slowly-decaying interactions on the entanglement entropy growth for $\alpha \leq d$. We discuss the existence of a long prethermalization regime where the dynamics are dominated by collective behavior, as a result of the quasi-conservation of finite-wavelength excitations. This explains the counterintuitive logarithmic entanglement growth reported by several numerical simulations.

In the previous chapter, we analyzed numerically the entanglement spreading in long-range systems, with interactions decaying as $1/r^\alpha$. Here, we focus on the entanglement entropy in the fully long-range regime for $\alpha \leq d$. We show that the dynamics are dominated by the semiclassical collective zero-mode, whose out-of-equilibrium properties have been the subject of Chapter 3.

When interactions decay with the distance between spins, the full permutational symmetry of the infinite-range Hamiltonian (2.17) is broken and the finite-wavelength spin modes participate in the dynamics. These excitations now allow the system to explore the full Hilbert space beyond the Dicke manifold, i.e., "inside the Bloch sphere". Hence, the system may be expected to thermalize by accumulating extensive entanglement entropy, as outlined in Chapter 1. However, when the range of interactions is sufficiently long, various numerical works have reported hints of ergodicity breaking [289, 341, 342, 383–385, 408, 438, 453, 461–463]. Firstly, as also discussed in the previous Chapter 4, several simulations have shown a logarithmic slowdown of entanglement entropy growth after a sudden quench [341, 342], similarly to the one of many-body localized systems [cf. Section 1.3.3]. In the same regime, various semiclassical approaches have shown to correctly capture the dynamics of local observables up to very long-times, see e.g. Refs.[284, 289, 290].

In this chapter, we address the impact of long-range interactions on the semiclassical entanglement dynamics. We use the general framework of Section 2.3.2 to study the contribution of spin-waves excitations on top of the infinite-range model. This allows us to demonstrate the existence of a long "prethermalization" regime, where spin-waves are mostly suppressed in typical quenches. This quasi-conservation is supplemented by a stability analysis. As a consequence, spin-waves yield only a bounded contribution to entanglement growth on top of the leading collective spin squeezing entanglement introduced in Chapter 3.

Therefore, this picture leads to a universal logarithmic growth of S_A in the absence of semiclassical chaos for $\alpha \leq d$, as reported numerically [341, 342]. The theory further predicts fast entanglement growth in the vicinity of critical quenches. As such, our findings identify a qualitative change to respect to the standard quasiparticle picture of entanglement dynamics [cf. Section 1.3.3], induced by long-range interactions.

The analytical results agree with numerical computations for quantum Ising chains with long-range couplings, obtained via TDVP algorithm. In particular, we analyze the standard long-range Ising model with the transverse field and the one with the tilted fields. We also study how short-range interactions affect this picture, restoring the standard quasi-particle picture [cf. Section 1.3.3] which results in linear growth of the entanglement entropy.

The rest of the chapter is organized as follows. In Section 5.1, we illustrate our approach to the study of the quasi-conservation of spin-waves and their corresponding impact on the bipartite entanglement dynamics. In Section 5.2, we exemplify our findings applying the above formalism to three different long-range spin-chains. We first analyze the long-range Ising chain with transverse and tilted field in Sections 5.2.1 and 5.2.2 respectively. Then, in Section 5.2.3 we consider the impact of short-range interactions.

5.1 Quasi-conservation of spin waves for $\alpha \leq d$

In this section, we aim at describing the persistence of the collective behavior of long-range systems for finite $0 \leq \alpha < d$.
To keep the discussion general, let us re-define the long-range Hamiltonian in arbitrary dimensions d. For definiteness, we deal with a quantum spin-$1/2$ system on a d-dimensional cubic lattice of size L governed by a Hamiltonian of the form

$$\hat{H} = -\frac{1}{\mathcal{N}_{\alpha,N}} \sum_{\mu,\nu=x,y,z} J_{\mu\nu} \sum_{i\neq j}^{N} \frac{\hat{s}_i^\mu \hat{s}_j^\nu}{|\mathbf{r}_i - \mathbf{r}_j|^\alpha} - \sum_{\mu=x,y,z} h_\mu \sum_{i}^{N} \hat{s}_i^\mu \,, \tag{5.1}$$

where the exponent $\alpha \geq 0$ characterizes the algebraic decay of spin-spin interactions. The distance $|\mathbf{r}_i - \mathbf{r}_j|$ between two sites on the periodic lattice is taken as

$$|\mathbf{r}_i - \mathbf{r}_j| = \sqrt{\sum_{\mu=1}^{d} \left[\min(|r_i^\mu - r_j^\mu|, L - |r_i^\mu - r_j^\mu|)\right]^2} \,. \tag{5.2}$$

The Hamiltonian (5.1) is rescaled by the Kač normalization defined in Eq.(4.2).

We study the impact of long-range interactions by using the formalism introduced in Section 2.3.2. First of all, one performs the Fourier transform of the long-range Hamiltonian (5.1). In the Ising long-range Hamiltonian (4.1), for example, this leads to the same equations of (2.96), where now $\tilde{J}_0 = J$ and the spin-waves

couplings $\tilde{J}_k = \widetilde{f}_{\alpha,k}$ with

$$\widetilde{f}_{\alpha,\mathbf{k}} = \frac{1}{\mathcal{N}_{\alpha,N}} \sum_{j(\neq i)} \frac{e^{-i\mathbf{k}\cdot(\mathbf{r}_j - \mathbf{r}_i)}}{|\mathbf{r}_j - \mathbf{r}_i|^\alpha}. \tag{5.3}$$

Then, one expands the individual spins around the classical direction via Holstein-Primakoff transformations, obtaining the generic transformed Hamiltonian (2.98), i.e.

$$\widetilde{\hat{H}}(t) = \widetilde{\hat{H}}_0(t) - \sum_{\mathbf{k}\neq 0} \widetilde{f}_{\alpha,\mathbf{k}} \left[J_{qq}(\theta,\phi)\, \frac{\tilde{q}_{\mathbf{k}}\tilde{q}_{-\mathbf{k}}}{2} + J_{pp}(\theta,\phi)\, \frac{\tilde{p}_{\mathbf{k}}\tilde{p}_{-\mathbf{k}}}{2} + J_{qp}(\theta,\phi)\, \frac{\tilde{q}_{\mathbf{k}}\tilde{p}_{-\mathbf{k}} + \tilde{p}_{\mathbf{k}}\tilde{q}_{-\mathbf{k}}}{2} \right] + \mathcal{O}\left(\frac{1}{\sqrt{N}}\right), \tag{5.4}$$

where J's are coefficients depending on the classical degrees of freedom $(\theta(t), \phi(t))$ and $\widetilde{\hat{H}}_0(t)$ is the collective-mode Hamiltonian that encodes for the infinite-range part $\widetilde{f}_{\alpha,\mathbf{0}}\, \delta_{\mathbf{k},\mathbf{0}} \equiv \delta_{\mathbf{k},\mathbf{0}}$ of the interaction $\widetilde{f}_{\alpha,\mathbf{k}}$ [1]. In the above equations, it is assumed that the motion of the angles $\theta(t)$ and $\phi(t)$ is fixed in such a way that linear terms in the collective quantum fluctuations $Q \equiv \tilde{q}_{\mathbf{0}}$ and $P \equiv \tilde{p}_{\mathbf{0}}$ vanish. This is equivalent to the self-consistency requirement $\langle \hat{S}^X(t) \rangle \equiv \langle \hat{S}^Y(t) \rangle \equiv 0$. We recall that the collective Hamiltonian $\widetilde{\hat{H}}_0(t)$ conserves the bosonic occupation numbers of all the other spin-wave modes at finite wavelength,

$$\hat{n}_{\mathbf{k}\neq\mathbf{0}} \equiv \frac{\tilde{q}_{\mathbf{k}}\tilde{q}_{-\mathbf{k}} + \tilde{p}_{\mathbf{k}}\tilde{p}_{-\mathbf{k}} - 1}{2}\,. \tag{5.5}$$

as $\left[\hat{n}_{\mathbf{k}}, \widetilde{\hat{H}}_0\right] = 0$ for all $\mathbf{k} \neq 0$.

The dynamical excitation of spin waves with finite wavelengths for $\alpha > 0$ is responsible for modifications to the semiclassical dynamics. As is evident in Eq. (5.4), their impact is controlled by the strength of the finite-range part $\widetilde{f}_{\alpha,\mathbf{k}\neq\mathbf{0}}$ of the interaction. These couplings are vanishing in the infinite-range model with $\alpha = 0$. Remarkably, they turn out to be suppressed in the thermodynamics limit $N \to \infty$ also for $0 < \alpha \leq d$. See Figure 5.1 for an illustration of the behavior of the function $\widetilde{f}_{\alpha,k}$ in $d = 1$.
Furthermore, in Appendix F we rigorously derive the following bounds $\alpha < d$

$$\left|\widetilde{f}_{\alpha,\mathbf{k}\neq\mathbf{0}}\right| \leq \begin{cases} \text{const} \times \dfrac{1}{(|\mathbf{k}|L)^{\frac{d+1}{2}}} & \text{for } \alpha \leq \dfrac{d-1}{2}, \\ \text{const} \times \dfrac{1}{(|\mathbf{k}|L)^{d-\alpha}} & \text{for } \dfrac{d-1}{2} < \alpha < d, \\ \text{const} \times \dfrac{\left|\ln|\mathbf{k}| + \tilde{F}(|\mathbf{k}|)\right|}{\ln L} & \text{for } \alpha = d\,. \end{cases} \tag{5.6}$$

[1] Notice that in Eq.(5.4) we are neglecting U_3 and U_4 in Eq.(2.98) which account for the feedback of the quantum fluctuations. Their contributions is sub-leading to respect to the Hamiltonian (5.4). This follows from the specific analytic structure of $\widetilde{f}_{\alpha,\mathbf{k}\neq\mathbf{0}}$ that we discuss below.

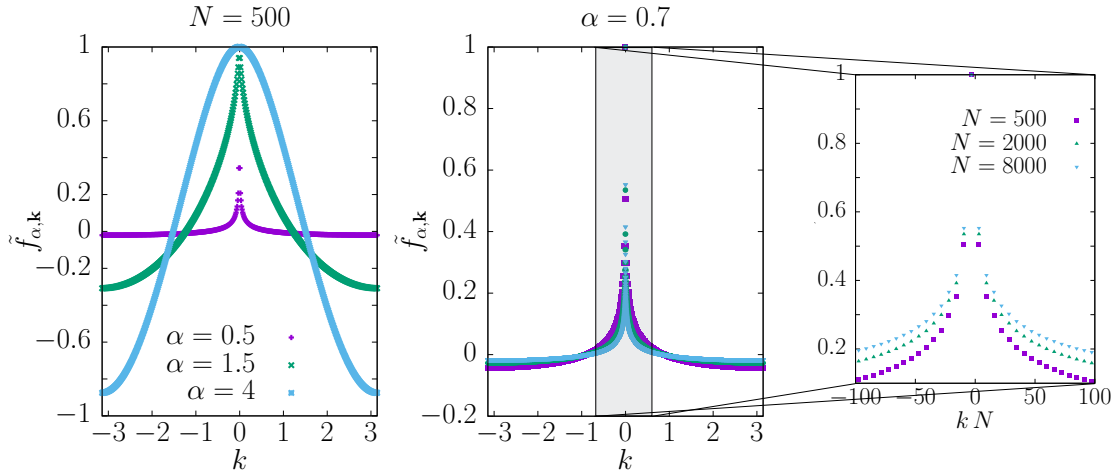

Figure 5.1: Plots of the function $\widetilde{f}_{\alpha,k}$ (5.3) for $d = 1$. (Left panel): $\widetilde{f}_{\alpha,k}$ is shown for several values of α, for $N = L = 500$. The function squeezes towards $k = 0$ for $0 \leq \alpha \leq 1$. For $1 < \alpha < 2$, $\widetilde{f}_{\alpha,k}$ becomes a finite function with a cusp behavior for small k, while for $\alpha \gg 2$ is a cosine-like function. (Central panel): $\widetilde{f}_{\alpha,k}$ is shown for $\alpha = 0.7$ and increasing values of N. Qualitatively similar behavior occurs for $0 \leq \alpha \leq 1$. Squeezing towards a delta function as $N \to \infty$ occurs with a speed $N^{-(1-\alpha)}$ for $\alpha < 1$ and $1/\ln N$ for $\alpha = 1$. (Right panel): a "zoom" of the plot in the bottom left panel is shown, for larger values of N. The *rescaled* function in the vicinity of $k = 0$ converges to a finite limiting curve as $N \to \infty$. This discrete structure approaches a continuum as $\alpha \nearrow 1$.

These implies that for all fixed $\mathbf{k} \neq \mathbf{0}$, the coupling $\widetilde{f}_{\alpha,\mathbf{k}}$ is vanishingly small in thermodynamic limit $L \to \infty$ whenever $\alpha \leq d$, and hence the associated number of bosonic excitations is an approximate constant of motion,

$$\left| \left\langle \left[\hat{n}_{\mathbf{k}\neq\mathbf{0}}, \widetilde{\hat{H}}(t) \right] \right\rangle \right| \leq \frac{\text{const}}{(|\mathbf{k}|L)^{\beta}} , \quad \text{with} \quad \beta \equiv \min\left(d - \alpha, (d+1)/2\right) . \tag{5.7}$$

Therefore, there exists a long time scale

$$T_{\text{sw}} \sim N^{\beta/d} , \tag{5.8}$$

during which the dynamical excitation of spin waves with finite wavelengths is suppressed [2] (note the interesting relation to the *prethermalization* time in Ref. [289]). As such, the total number of spin waves excitations $\hat{n}_{\text{sw}}$ at finite wavelength (5.5) remains small during the dynamics, i.e.

$$\hat{n}_{\text{sw}} = \sum_{k\neq 0} \hat{n}_k \ll N . \tag{5.9}$$

An equivalent statement is that that the collective spin, in Eq.(2.103), remains close to the maximal value $N/2$ during the pre-thermal regime, that is

$$\langle \hat{\mathbf{S}}(t)^2 \rangle = \left(\frac{N}{2} - \langle \hat{n}_{\text{sw}}(t) \rangle \right) \left(\frac{N}{2} - \langle \hat{n}_{\text{sw}}(t) \rangle + 1 \right) . \tag{5.10}$$

[2] Note that this justifies a posteriori the Holstein-Primakoff approach, as the density of spin waves remains small over a long time window

However, permutational symmetry may severely break over large length scales via excitations with $|\mathbf{k}| \propto 1/L$. As we discuss in detail in the next section, their dynamics is governed by the Hamiltonian (5.4) and it is equivalent to a *discrete* set of periodically driven quantum oscillators, the drive being induced by the precession of the collective spin. From a stability analysis, we find that for typical quenches these long-wavelength spin-wave modes are non-resonantly driven and hence weakly excited. Their resulting contribution to entanglement dynamics amounts to bounded oscillations on top of the dominant, the semiclassical induced logarithmic growth. Near dynamical criticality, however, resonant excitation of these modes may lead to exponentially growing quantum fluctuations (cf. Ref. [289]) and hence linear increase of the entanglement entropy, see e.g. the example in Section 5.2.2.

5.1.1 Stability analysis of spin-waves

We can now analyze the full contribution of the spin waves to the quantum dynamics. To this end, we start by discussing the evolution of the population of the spin waves after a quench.

The time-dependent Hamiltonian (5.4) shows that, within the linear spin-wave analysis, the system is equivalent to a set of *periodically driven quantum harmonic oscillators*, labelled by the quasimomentum $\mathbf{k}$. The classical evolution of the collective spin, described by the periodic dynamics of the angles $\theta(t)$, $\phi(t)$ with a frequency $\omega_{\rm cl} \equiv 2\pi/T_{\rm cl}$, acts as a drive on these bosonic modes described by the variables $(\tilde{q}_{\mathbf{k}}(t), \tilde{p}_{\mathbf{k}}(t))$. The driving frequency $\omega_{\rm cl}$ is common to all $\mathbf{k}$'s and depends only on the quench, while the driving amplitude depends both on the quench and on $\mathbf{k}$ via the coupling strength $\widetilde{f}_{\alpha,\mathbf{k}}$. As a consequence of the bounds in Eqs. (5.6), the driving amplitude is vanishingly small in the thermodynamic limit for all fixed $\mathbf{k}$'s when $\alpha < d$, which implies that the excitation of all finite-wavelength modes is vanishingly weak, so that their effects are generically negligible for large N, and in any case delayed to the divergent time scale $T_{\rm sw}$ in Eq.(5.8). However, long-wavelength modes with $|\mathbf{k}| \propto 1/L$ are driven with a finite intensity. Therefore, in the presence of long-range interactions with $\alpha < d$, the description of the system dynamics effectively reduces to a *discrete* set of driven quantum oscillators, corresponding to spin fluctuations with $k_\mu = 0, \pm 2\pi/L, \pm 4\pi/L, \ldots, \pm 2\pi n^*/L$, for $\mu = 1, \ldots, d$, where the cutoff $n^* \gg 1$ can be taken independent of L, see the right panel of Figure 5.1. This is in contrast with systems with shorter-range interactions (i.e., with $\alpha > d$), in which a *continuum* of traveling quasiparticles generate linear growth of entanglement entropy through the standard Calabrese-Cardy mechanism [102], see also Section 1.3.3.

For a large set of initial conditions, spin waves are *stable*, and consequently, their population remains bounded in time. However, particular quenches typically near mean-field dynamical critical points, may give rise to a *runstable* of long-wavelength spin waves, leading to an exponentially growing population thereof. This effect is a hallmark of semiclassical chaos induced by the finiteness of the interaction range and is associated with a linear increase of entanglement entropy in time (see below).

A *stability analysis* of the spin-wave excitations allows one to predict the nature of the dynamics and correspondently of the entanglement growth (logarithmic or linear) for any given quench. It can be performed as follows. For any long-range spin

Hamiltonian, one can perform a nonequilibrium spin-wave expansion as explained in Section 5.1 above, and compute the time-evolution

$$\begin{pmatrix} \tilde{q}_{\mathbf{k}}(t_0+T_{\rm cl}) \\ \tilde{p}_{\mathbf{k}}(t_0+T_{\rm cl}) \end{pmatrix} = U_{\mathbf{k}}(T_{\rm cl}) \cdot \begin{pmatrix} \tilde{q}_{\mathbf{k}}(t_0) \\ \tilde{p}_{\mathbf{k}}(t_0) \end{pmatrix} \tag{5.11}$$

of each spin-wave mode over one classical period $T_{\rm cl}$. Hence, one obtains the eigenvalues $e^{\pm\lambda_{\mathbf{k}}T_{\rm cl}}$ of the 2×2 matrix $U_{\mathbf{k}}(T_{\rm cl})$. The number $\lambda_{\mathbf{k}}$, known as the *Floquet quasi-frequency* (see, e.g., Refs. [464, 465]) of the driven oscillator, determines the resonance condition of the driven oscillator. If $\lambda_{\mathbf{k}} = i\omega_{\mathbf{k}}$ is *purely imaginary*, then the mode is stable and its amplitude remains bounded in time, oscillating at a frequency $|\omega_{\mathbf{k}}|$. On the contrary, if $\lambda_{\mathbf{k}}$ is *real*, the mode in unstable and its amplitude grows exponentially fast in time with a rate $|\lambda_{\mathbf{k}}|$. Isolated resonances may in principle occur for particular trajectories. It seems to be typically the case (see the examples below) that quenches *near* dynamical criticality give rise to unstable excitation of spin waves. In other words, the classical separatrix of the mean-field dynamics for $\alpha = 0$ broadens to a *finite* layer of instability (chaoticity) for $\alpha > 0$.

To quantify the stability of a given quantum quench, one can study the Kolmorgorov-Sinai entropy defined in Eq.(3.7). In particular, we will study its dependence as a function of the initial configurations on the Bloch sphere, i.e.

$$\Lambda_{\rm KS}(\theta_0,\phi_0) = \sum_{k:\lambda_k>0} {\rm Re}[\lambda_k(\theta_0,\phi_0)] \, . \tag{5.12}$$

5.1.2 Entanglement dynamics

The above discussion allows us to understand the full spin-wave time-dependent entanglement entropy, using known mathematical results for quadratic bosons [322]. Even for $\alpha > 0$, the entanglement between two subsets of quantum spins is encoded in the entanglement between their respective bosonic fluctuations. For a general system of quadratic bosons, $S_A(t)$ can be computed with standard techniques, that we already used in Section 3.1.3, see, e.g., Refs. [322, 466, 467]. We briefly recall how this computation can be performed for translation-invariant Hamiltonians such as Eq. (5.4). The time evolution is diagonal in Fourier space, and one integrates N decoupled pairs of equations of motion for $(\tilde{q}_{\mathbf{k}}(t), \tilde{p}_{\mathbf{k}}(t))$ to obtain the time-evolved Gaussian state of each Fourier mode, described by the correlations $(\tilde{G}^{qq}_{\mathbf{k}}(t), \tilde{G}^{qp}_{\mathbf{k}}(t), \tilde{G}^{pp}_{\mathbf{k}}(t))$ defined by

$$\tilde{G}^{\alpha\beta}_{\mathbf{k}}(t) = \frac{1}{2}\Big\langle \tilde{\alpha}_{\mathbf{k}}(t)\tilde{\beta}_{-\mathbf{k}}(t) + \tilde{\beta}_{\mathbf{k}}(t)\tilde{\alpha}_{-\mathbf{k}}(t) \Big\rangle \tag{5.13}$$

for $\alpha,\beta = q,p$. The time-evolved operators $\tilde{q}_{\mathbf{k}}(t)$, $\tilde{p}_{\mathbf{k}}(t)$ are linearly related to those at time $t = 0$ via the solution to the Heisenberg equations of motion $\dot{\tilde{\alpha}}_{\mathbf{k}}(t) = -i\big[\tilde{\alpha}_{\mathbf{k}}(t), \widetilde{H}(t)\big]$ with the generator $\widetilde{H}(t)$ in Eq. (5.4). Within the linear spin-wave analysis, the state of a subsystem composed of $M < N$ spins contained in a region A of the lattice is a Gaussian bosonic state determined by the instantaneous correlations

$$\Big\{ G^{\alpha\beta}_{ij}(t) = \big\langle \alpha_i(t)\beta_j(t) + \beta_i(t)\alpha_j(t) \big\rangle \Big\}_{\substack{i,j\in A \\ \alpha,\beta=q,p}} \tag{5.14}$$

between them, which can be expressed in terms of $\tilde{G}^{\alpha\beta}_{\mathbf{k}}(t)$ via Fourier antitransform

$$G^{\alpha\beta}_{ij}(t) = \frac{2}{N}\sum_{\mathbf{k}} e^{i\mathbf{k}(\mathbf{r}_i-\mathbf{r}_j)}\tilde{G}^{\alpha\beta}_{\mathbf{k}}(t) \equiv G^{\alpha\beta}_{\mathbf{r}}(t)\Big|_{\mathbf{r}=\mathbf{r}_i-\mathbf{r}_j} . \tag{5.15}$$

This set of correlations for $i,j \in A$, collected in a $2M \times 2M$ matrix G_A, uniquely identifies the reduced density matrix $\hat{\rho}_A(t)$. The von Neumann entropy of this Gaussian bosonic state can be computed via Eq.(3.20), namely

$$S_A = \sum_{i=1}^{M} S(\nu_i) , \quad \text{with} \quad S(\nu_i) = \frac{\nu_i+1}{2}\ln\frac{\nu_i+1}{2} - \frac{\nu_i-1}{2}\ln\frac{\nu_i-1}{2} , \tag{5.16}$$

where ν_i are the symplectic eigenvalues of the correlation matrix, see e.g. the Note 5.

For long-range interactions with $0 < \alpha \leq d$, the growth of $S_A(t)$ turns out to be determined by the stability of the discrete set of long-wavelength excitations, expressed by the Floquet quasi-frequencies $\lambda_{\mathbf{k}}$ with $|\mathbf{k}| \propto 1/L$: see the above discussion and Figure 5.1 in the previous section. In particular, one can use the general semiclassical description of the previous chapter, summarized in Table 3.1.

If all the modes are imaginary (i.e., all are stable), then $S_A(t) \sim \ln t$ exhibits a slow growth dominated by the collective spin fluctuations with $k = 0$. On the other hand, if some of them are real (i.e., some modes are unstable), then $S_A(t) \sim \Lambda_{\rm KS}\, t$ exhibits a fast growth dominated by the unstable quantum fluctuations [cf. Eq.(3.31)].

In view of the above discussion of the evolution of the k-resolved spin-wave population after a quench, we conclude that typical quenches in a long-range interacting quantum spin-1/2 system yield a logarithmic growth of the von Neumann entanglement entropy, as argued in the main text. See below for a numerical illustration.

5.2 Application to long-range spin chains

To show the validity of our analysis, we apply it to a variety of spin models and quenches. As explained in Section 2.1.2, their fully connected limit is mapped into a single classical degree of freedom. Being integrable, they generically display a logarithmic growth of the entanglement entropy, with the exception of the classical unstable trajectory. For an illustration of the case with $\alpha = 0$ see Figures 3.1 and 3.2.

5.2.1 Long-range quantum Ising chain in a transverse field

We first consider the long-range quantum Ising chain in a transverse field [cf. Eq.(4.1) of the first section]. In this case, the fully-connected limit is given by the LMG model discussed in Section 3.2.

First of all, the equation of motion for the spin-wave correlations in k-space $\tilde{G}^{\alpha\beta}_{k}(t)$ for $\alpha,\beta = q,p$ in Eq.(5.13) ca be computed following Section 2.3.2. For the

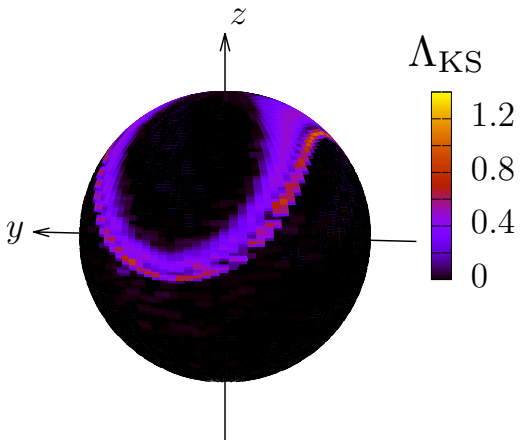

Figure 5.2: Density plot of the Kolmogorov-Sinai entropy rate $\Lambda_{KS}(\theta_0, \phi_0)$ for different initial conditions (θ_0, ϕ_0) on the Bloch sphere for $\alpha = 0.7$, $h = 0.5J$. The picture is converged with respect to refining the k-space discretization (here $N = 100$).

Hamiltonian (4.1), they had been already derived in Eqs.(2.107) and read

$$\begin{cases} \dfrac{d}{dt}G_k^{qq} = 4\tilde{J}_k \cos\theta\cos\phi\sin\phi\, G_k^{qq} + 4\left(J\cos^2\phi - \tilde{J}_k \sin^2\phi\right) G_k^{qp}, \\ \dfrac{d}{dt}G_k^{pp} = -4\left(J\cos^2\phi - \tilde{J}_k \cos^2\theta\cos^2\phi\right) G_k^{qp} - 4\tilde{J}_k \cos\theta\cos\phi\sin\phi\,\Delta_k^{pp}, \\ \dfrac{d}{dt}G_k^{qp} = -2\left(J\cos^2\phi - \tilde{J}_k \cos^2\theta\cos^2\phi\right) G_k^{qq} + 2\left(J\cos^2\phi - \tilde{J}_k \sin^2\phi\right) G_k^{pp} \end{cases} \tag{5.17}$$

where $\tilde{J}_k \equiv J\widetilde{f}_{\alpha,k}$ and the periodic time-dependence of the angles $(\theta(t), \phi(t))$ are determined by the classical precession of the collective spin described by Eqs.(2.89). The Fourier antitransform of $\tilde{G}_k^{\alpha\beta}(t)$ leads to the real-space correlation functions (5.15), which enter the computation of the entanglement entropy via Eq. (5.16).

Following the discussion above, we first perform a global Floquet stability analysis. For illustration purposes, we focus on quenches to the ferromagnetic phase with $\alpha = 0.7$, $h = 0.5J$ starting from generic fully-polarized spin states, characterized by angles (θ_0, ϕ_0) spanning the entire Bloch sphere. The spherical plot in Figure 5.2, shows the value of $\Lambda_{\rm KS}(\theta_0, \phi_0)$ as a function of the initial conditions in Eq.(5.12). This quantity is vanishing for regular evolutions free of dynamically unstable excitation modes (i.e., with an entirely real Floquet dispersion relation $\{-i\lambda_k \equiv \omega_k\}_k$), whereas it is strictly positive when at least one mode k^* is unstable [i.e., $\mathrm{Re}(\lambda_{k^*}) \neq 0$]. The results show that only quenches near dynamical criticality give rise to unstable excitation of spin waves. They correspond to initial configurations close to the classical separatrix of the mean-field dynamics, as shown by the purple region on in Figure 5.2. In other words, the single unstable trajectory for $\alpha = 0$ broadens to a finite layer of instability for $\alpha > 0$. However, for typical quenches well away from criticality (the black region on the sphere in Figure 5.2), spin waves are stable.

As results from the above discussion, we can extend the entanglement analysis to varying α and h. We find that, for typical quenches, the population $\langle \hat{n}_{k\neq 0}\rangle$ of spin

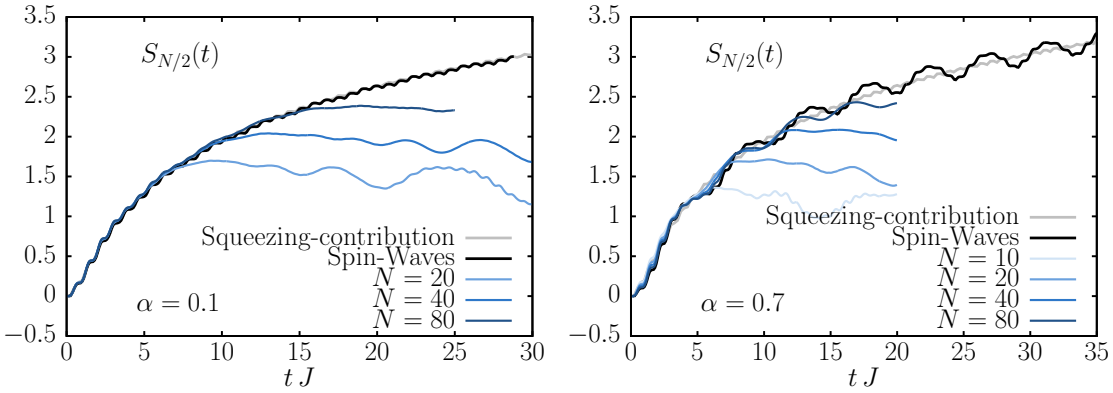

Figure 5.3: Comparison between finite-size MPS-TDVP numerical data (light-to-dark blue curves for increasing N), the spin-squeezing contribution (grey) and full spin-wave entanglement (black), for $\alpha = 0.1$ (left panel) and 0.7 (right panel), for the quench $h_0 = 0 \to h_f = 2J$, with $N = 500$.

waves remains bounded in time, whereas the collective fluctuations $\langle \hat{n}_{k=0} \rangle \equiv \langle \hat{n}_{\rm exc} \rangle$ grow polynomially in time as t^2, as discussed in general in Section 3.1.4. Consequently, entanglement entropy growth is dominated by the spin-squeezing collective contribution, and spin-wave excitations generate a finite correction, the impact of which grows as α increases. This scenario is illustrated in Figure 5.3, where we compare the full spin-waves calculation with the MPS-TDVP data obtained using periodic boundary conditions. These plots highlight that: *i*) the spin-squeezing contribution captures the leading behavior of the time-dependent entanglement entropy for all $\alpha < 1$, provided long-wavelength modes are stable, as occurs in typical quenches; *ii*) the full spin-wave entanglement entropy calculation *quantitatively* reproduces the numerical data before saturation as N is increased. These two occurrences strongly support the effectiveness of the nonequilibrium spin-wave analysis of entanglement entropy growth. To fully corroborate the above picture, we report in Figure 5.4 the time evolution of the k-resolved spin-wave population for the same quench.

5.2.2 Long-range quantum Ising chain in a tilted field

We further discuss the quenches in long-range quantum Ising chains in a tilted magnetic field, described by the following Hamiltonian

$$\hat{H} = -\frac{J}{\mathcal{N}_{\alpha,N}} \sum_{i<j}^{N} \frac{\hat{\sigma}_i^x \hat{\sigma}_j^x}{|i-j|^\alpha} - h_z \sum_i^N \hat{\sigma}_i^z - h_x \sum_i^N \hat{\sigma}_i^x \,, \tag{5.18}$$

where now h_z and h_x are respectively the transverse and longitudinal field and $\mathcal{N}_{\alpha,N}$ is the Kač normalization (4.2). This model has been considered by T.Mori in Ref.[289]. There, it is argued that the non-equilibrium dynamics of a long-range quantum Ising chain (with $0 < \alpha < 1$ and with transverse field $h_z = 0.32J$ and longitudinal field $h_x = 0.26J$) shows signatures of many-body chaos. The dynamics are studied by starting from the paramagnetic state with spins fully polarized along

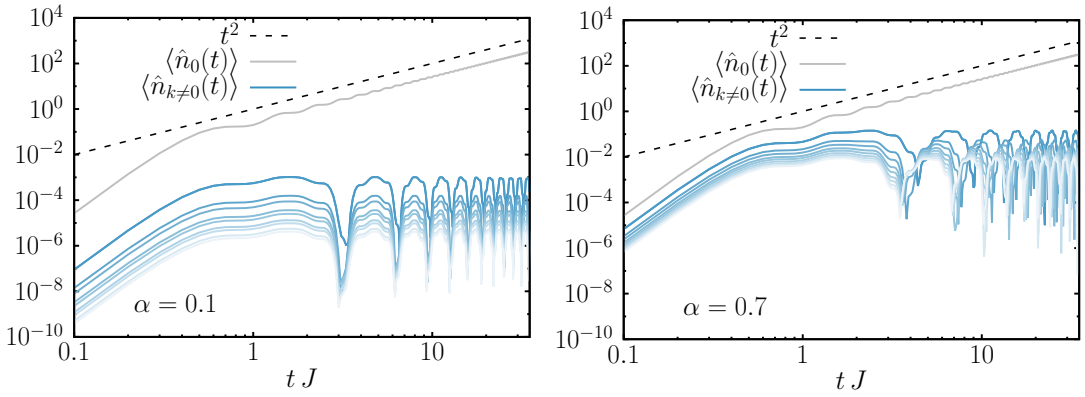

Figure 5.4: Time-dependent k-resolved spin-wave population for $\alpha = 0.1$ (left panel) and $\alpha = 0.7$ (right panel) after a quench from $h_0 = 0$ to $h_f = 2J$. The blue color gradient for the spin-wave populations in Fourier modes follows the quasimomentum $|k|$ from the darkest ($k = \pm 2\pi/L$) down to smaller-wavelength modes with larger $|k|$ (only the first 20 modes out of $N = 500$ are shown).

the z axis, i.e., from $h_{z,0} = \infty$. (Note that $x \leftrightarrow z$ have been exchanged in our conventions.)

We apply here the non-equilibrium spin-wave theory and the theory of entanglement dynamics developed in the present chapter. Upon adding a longitudinal field, the classical equation of motion of the collective spin [cf. Eq.(3.35) of Section 3.2] now reads

$$\begin{cases} \dot{\theta} = 2J \sin\theta \cos\phi \sin\phi + 2h_x \sin\phi \\ \dot{\phi} = -2h_z + 2J \cos\theta \cos^2\phi + 2h_x \dfrac{\cos\theta}{\sin\theta} \cos\phi \ . \end{cases} \tag{5.19}$$

and the evolution equations for the spin-wave correlations, ($\tilde{J}_k \equiv J\widetilde{f}_{\alpha,k}$) are

$$\begin{cases} \dot{G}^{qq}_k = 4\tilde{J}_k \ \cos\theta \cos\phi \sin\phi \ \tilde{G}^{qq}_k + 4\left(J\cos^2\phi + h_x \dfrac{\cos\phi}{\sin\theta} - \tilde{J}_k \ \sin^2\phi \right) \tilde{G}^{qp}_k , \\ \dot{G}^{pp}_k = -4\left(J\cos^2\phi + h_x \dfrac{\cos\phi}{\sin\theta} - \tilde{J}_k \ \cos^2\theta \cos^2\phi \right) \tilde{G}^{qp}_k - 4\tilde{J}_k \ \cos\theta \cos\phi \sin\phi \, \tilde{G}^{pp}_k \\ \dot{G}^{pq}_k = -2\left(J\cos^2\phi - \tilde{J}_k \ \cos^2\theta \cos^2\phi \right) \tilde{G}^{qq}_k + 2\left(J\cos^2\phi + h_x \dfrac{\cos\phi}{\sin\theta} - \tilde{J}_k \ \sin^2\phi \right) \tilde{G}^{pp}_k \end{cases} . \tag{5.20}$$

We first study the mean-field case $\alpha = 0$, verifying that the growth of entanglement entropy is logarithmic for the considered quench, see Figure 5.5, as follows from our predictions. However, due to the closeness to a nearby dynamical critical point, the short-time dynamics of entanglement is fast, and the universal logarithmic behavior emerges only over longer times. In agreement with our theory, larger system sizes are required to observe the asymptotic behavior, as confirmed by the ED numerical results. Because of these strong finite-size effects, we did not attempt for $\alpha > 0$ numerical investigations with MPS-TDVP, limited to $N \lesssim 100$, but directly studied the limiting behavior in the thermodynamic limit via a full spin-wave calculation of entanglement dynamics. The results are shown in Figure 5.6, left

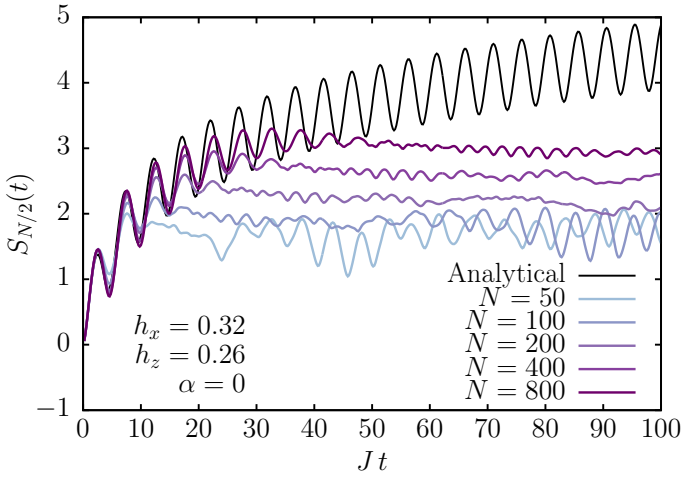

Figure 5.5: Comparison between entanglement entropy growth computed numerically (ED) and analytically (semiclassical formula) for $\alpha = 0$, for the quenches in Ref.[289] [Eq. (5.18) with $h_z = 0.32J$, $h_x = 0.26J$, initial state polarized along z]. The growth is logarithmic, but finite-size effects are strong due to closeness to a mean-field dynamical critical point.

panel, for increasing values of α, and they confirm that the growth of entanglement entropy is linear for $\alpha > 0$, as suggested by the results of Ref. [289] in view of the interpretation provided by the theory presented here.

To fully corroborate this picture, we presented a similar analysis to that outlined above for the Ising chain in a transverse field. In Figure 5.7, we report the time evolution of the k-resolved spin-wave population for the same quench. The dynamical production of long-wavelength spin-wave excitations is unstable, i.e., exponentially growing. This occurrence hints at the fact that the quench considered in Ref. [289] falls into a layer of instability of the many-body semiclassical dynamics, characterized by a positive Kolmogorov-Sinai entropy rate (5.12) and hence a linear growth of entanglement entropy in time. This is confirmed by the spherical plot in Figure 5.6, right panel, of the Kolmogorov-Sinai entropy rate $\Lambda_{\rm KS}$ as a function of the initial configuration on the Bloch sphere (5.12). The considered quench falls inside the instability layer which opens up around the classical separatrix upon increasing $\alpha > 0$. However, we emphasize that a large set of initial configurations show a stable generation of spin waves, and hence slow logarithmic growth of entanglement entropy, even for this Hamiltonian (the black region in the spherical plot).

5.2.3 Short-range perturbations to collective spin models

The above analysis shows that slow logarithmic growth of the entanglement entropy can be expected in the quench dynamics of spin-1/2 systems with long-range interactions. The underlying mechanism involves the existence of a *discrete* set of excitation modes (the long-wavelength spin waves) which yield a bounded, subleading contribution to entanglement when non-resonantly driven by the collective spin dynamics. However, this is an intrinsic property of slowly-decaying interactions, which generically fails for other types of perturbations of infinite-range models.

To explicitly show this, we consider *additional* finite-range interactions as perturbations to an integrable system with collective interactions. To be specific, we

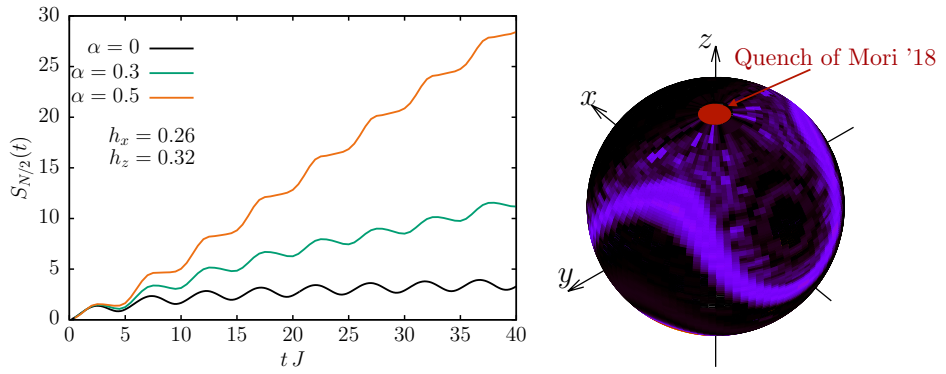

Figure 5.6: Left panel: Comparison between entanglement entropy growth obtained via the full spin-wave computation with $N = 500$, for increasing $\alpha = 0$, 0.3 and 0.5, for the quenches in Ref. [289] [Eq. (5.18) with $h_z = 0.32J$, $h_x = 0.26J$, initial state polarized along z]. While the growth is logarithmic in the integrable case $\alpha = 0$, the breaking of integrability induced by a finite range triggers a linear growth of $S(t)$, due to unstable excitation of long-wavelength spin waves: see the text and Figure 5.7. Right panel: Spherical plot of the Kolmogorov-Sinai entropy rate $h_{KS}(\theta_0, \phi_0)$ versus the initial spin-polarized configuration, for $\alpha = 0.7$.

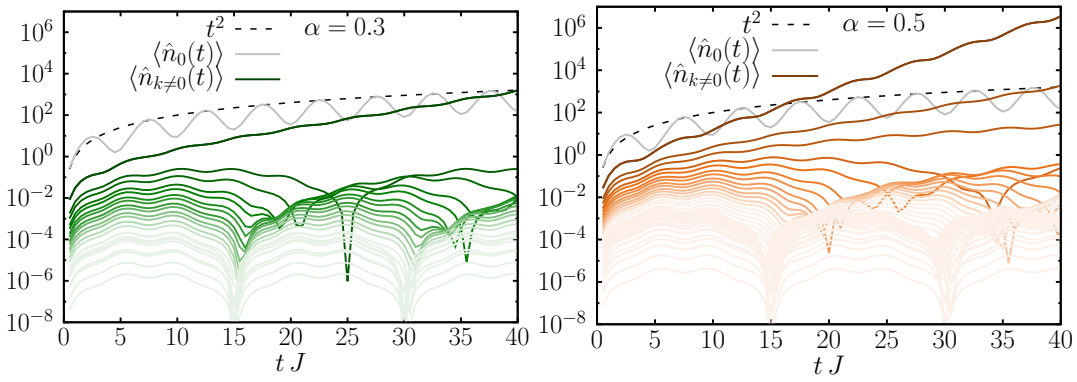

Figure 5.7: Time-dependent k-resolved spin-wave population for the quenches in Ref. [289] [Eq. (5.18) with $h_z = 0.32J$, $h_x = 0.26J$, initial state polarized along z]. Collective quantum fluctuations with $k = 0$ grow polynomially, whereas the long-wavelength modes $k = \pm 2\pi/L$ (left, $\alpha = 0.3$) and $k = \pm 2\pi/L, 4\pi/L, 6\pi/L$ (right, $\alpha = 0.5$), diverge exponentially fast in time. Here we have set $N = 500$.

consider a Hamiltonian of the form

$$\hat{H}_{lr+sr} = \hat{H}_\alpha - \lambda \sum_i \hat{\sigma}_i^x \, \hat{\sigma}_{i+1}^x \,, \tag{5.21}$$

where $\hat{H}_\alpha$ is the long-range quantum Ising chain in Eq.(4.1). In Refs. [293, 294], it has been shown that the nonequilibrium spin-wave approach adequately describes the dynamics of this Hamiltonian when $\lambda \ll J$. We show that the two kinds of perturbations, corresponding to raising α or λ from 0, respectively, lead to a radically different scenario of entanglement growth, in accordance with the theory developed above.

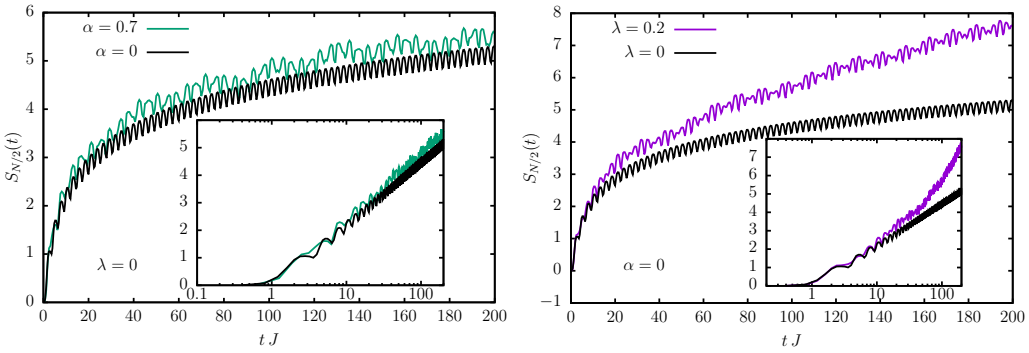

Figure 5.8: Entanglement entropy growth obtained via the full spin-wave analysis, for quenches $h_0 = 0 \to h_f = 0.7J$ in the Hamiltonian (5.21). We compare the effects of the two kinds of perturbations to the fully-connected quantum Ising model with $\alpha = 0$, $\lambda = 0$: *i)* $\alpha = 0.7$, $\lambda = 0$, i.e., a slow spatial decay of interactions (left); *ii)* $\alpha = 0$, $\lambda = 0.2J$, i.e., additional weak nearest-neighbor interactions (right). In both plots, the black lines represent the behavior of the fully-connected quantum Ising model with $\alpha = 0$, $\lambda = 0$, for comparison. It is apparent that the former α-perturbation (top) provides only bounded corrections to the logarithmic growth of the permutationally-invariant limit, whereas the latter λ-perturbation clearly exhibits the onset of a linear-in-time growth (with a small slope) which can be appreciated at long times. The insets report the same data on a logarithmic time scale, highlighting the different behavior. In this computation $N = 500$.

For the spin-wave analysis of the Hamiltonian H_{lr+sr} in Eq. (5.21), it is actually sufficient to substitute $J_{k\neq 0} = J\widetilde{f}_{\alpha,k} + \lambda \cos k$ in Eqs. (5.20). In the case $\alpha = 0$, $\lambda \neq 0$, the spin-wave Hamiltonian features two fundamental differences: firstly, it is equivalent to a system of quantum oscillators with short-range interactions, hence described by a *continuous* dispersion relation with a finite bandwidth (apart from the singular $k = 0$ mode); secondly, all excitations with $k \neq 0$ now live on a widely separated energy scale $\lambda \ll J$ with respect to the classical drive. Therefore, away from fine-tuned resonances, the system typically behaves as a standard model of free bosonic excitations, where the fast, non-resonant drive amounts to modifying their effective dispersion relation. Such a system is expected to exhibit light-cone spreading of quantum correlations and linear growth of entanglement entropy, according to the standard Calabrese-Cardy quasiparticle picture [cf. Section 1.3.3], in stark contrast to the perturbation with $\alpha > 0$, $\lambda = 0$ discussed above.

To be fair, it should be noted that the λ-perturbed model features a coexistence of two mechanisms, namely the spin squeezing associated with the singular $k = 0$ mode and the traveling quasiparticles associated with the all the remaining $k \neq 0$ modes. Although the second mechanism is clearly dominant [linear over logarithmic $S(t)$], for tiny perturbations $\lambda \ll J$, a long time is required to appreciate this distinction. In practice, for small sizes, short times, weak quenches, and/or weak perturbations, one will always observe a crossover from initial logarithmic growth to an asymptotic linear growth.

We verified the predictions above explicitly: see the comparison between the two perturbations in Figure 5.8. We conclude that, as expected based on the present

analysis, the nature of the integrability-breaking perturbation is crucial, and the slow growth of entanglement analyzed is a characteristic property of long-range interactions.

5.3 Conclusions

The mechanism underlying entanglement growth in long-range interacting quantum systems complements the available paradigms for entanglement dynamics characterizing systems with local interactions [102, 216, 224, 233, 234, 247, 468] and, at the same time, improves the current understanding of the efficiency of "classical" simulations of quantum long-range interacting spin chains with matrix-product-state techniques [212, 213]. In connection with known instances of ergodicity breaking stemming from long-range interactions [289, 341, 342, 383, 385, 400, 408, 438, 448, 453, 461–463], the suppression of spin-wave excitations demonstrated in this chapter clarifies the role of long-range interactions in constraining quantum dynamics to small portions of the many-body Hilbert space in the relevant time regime. Such quasi-conservation shows that the quantum dynamics subject to long-range interactions are constrained to small portions of the many-body Hilbert space in the correct time regime. Concerning the slow entanglement growth, this is reminiscent of localized or glassy dynamics

Therefore it becomes crucial to understand whether this effect exists only in a prethermalization regime or whether it has a corresponding impact also to the many-body eigenstates. This issue is subject of current work.

Chapter 6

Scrambling dynamics in the Sherrington Kirkpatrick model

In this chapter, we study the echo dynamics in the Sherrington-Kirkpatrick (SK) model, where the validity of the semiclassical approach is ensured by the large N limit. We explore the requirements under which the echo of observable grows exponentially fast in time. These are determined by the nature of the observable and of the initial state and by the existence of a well-defined semiclassical limit. We also discuss a short-range version of the SK model, where the quantum echo grows only polynomially in time.

In the previous chapters, semiclassical approaches have been applied to fully connected systems or long-range models with clean interactions. In this chapter, we will apply the TWA [cf. Section 2.2.1] to a many-body problem of fully disordered interacting spins, where the large N limit ensures the validity of the semiclassical analysis. In particular, we will focus on irreversibility and scrambling dynamics as witnessed by the echo observable (1.44), introduced in Section 1.2.4.

As discussed above, understanding the footprints of chaos in quantum-many-body systems has been under debate for a long time. Here, we investigate how chaotic many-body quantum dynamics leads to the exponential divergence of the echo of observables in the transverse quantum Sherrington-Kirkpatrick (SK) spin model with long-range interactions. This model can be experimentally realized over different atomic platforms ranging from cavity QED to Rydberg atoms. Theoretically, it has many analogies with the Sachdev-Ye-Kitaev (SYK) model [1], as it shares the feature of having non-local all-to-all random interactions. At the same time, there are important differences between them: while the SK displays a quantum phase transition towards a quantum glass phase below a critical transverse field [469–471], the SYK remains critical and scale-invariant at all temperatures. Because of nonuniform couplings, the SK model can not be mapped to that of a large spin and for this reason, there is no simple classical limit, in a way similar to the situation in the SYK model. Yet we show the validity of the semiclassical expansion, such as the truncated Wigner approximation [c.f. Section 2.2.1], both analytically and numerically. Hence, TWA can accurately reproduce both the forward evolution of

[1] As mentioned in Section 1.2.4, we recall that the SYK model is a solvable model of all-to-all interacting Maiorana fermions. Among its properties, it is well-known because its OTOC grows exponentially fast with a rate that saturates the "bound to chaos", i.e. $\lambda = 2\pi T/\hbar$ [147].

observables like magnetization (essentially up to infinitely long times) and the echo and hence the OTOC up to the Ehrenfest time. In this sense, even in the absence of a clear mapping to a classical Hamiltonian, the large N limit of the SK model is semiclassical, similarly to the SYK model [183].

The availability of a semiclassical limit is, also in this case, the most important ingredient to see an exponential growth of the echo of observables (and of the OTOC). As in recent studies of the SYK model, we find that to have exponential behavior of the OTOC it is necessary to have long-range interactions in the system, correctly captured by semiclassical TWA dynamics. In this way, even in the absence of an obvious classical limit in the system, $1/N$ serves as an effective Planck's constant $\hbar$. To further confirm the crucial role of a well-defined semiclassical limit, we also considered a short-range version of the SK model with random couplings between sites decaying gaussianly as a function of their distance. In this case, the semiclassical description fails to correctly reproduce the echo dynamics, which do not show exponential sensitivity to the protocol time. Our work, therefore, confirms that the existence of quantum Lyapunov exponents is closely related to the proximity of the model to the semiclassical limit, coinciding with the corresponding classical exponents [184–187] (c.f. Ref. [183] for the SYK model).

We also find that the nature of the initial state and the observable are crucial to observe exponential echo response in this and other large N models. To see the exponential growth of the OTOC, the operator on the initial state has, in loose terms, to give enough "space" to the OTOC to develop an exponential growth. This means quantitatively that the intermediate time window separating the early perturbative power-law growth of the latter and its eventual saturation at long times has to be long and eventually divergent in the thermodynamic limit. This is impossible in quantum systems with a bounded local Hilbert space size like in spin $1/2$ chains or Hubbard like models of interacting fermions if we choose observables which are local in space. Such operators are bounded by the corresponding finite operator norms at long times and generically do not give room for exponential growth. In Ref. [194] it was thus argued that collective observables such as the sums of local observables, which can become arbitrarily large with the number of degrees of freedom, are better candidates for observing universal, non-perturbative behavior of OTOC. Thus, given a collective observable, one has to require that the long-time saturation value of the OTOC has a parametrically larger value in the system size N than the coefficient governing the initial perturbative short-time behavior. Interestingly, such requirements simultaneously constrain the nature of the initial state and the observable. In particular, we find that for a collective observable the "good" initial state must be such that there is an extensive difference between the initial and the equilibrium (long time) values of the observable. For example, if we choose the total (non-conserved) magnetization as an observable, which decays to zero under forward evolution, one could start from an initially magnetized state. In the case of the current, a good initial state will be the one with a macroscopic current, and so on.

Such initial states naturally generalize those proposed by Rozenbaum et al. in Ref. [472], where the authors associated the existence of an exponential regime with the choice of the "classical" initial conditions localized in phase space, where the position and the momentum of the particle acquire non-zero expectation values. This

choice of initial conditions is very similar to that proposed in Ref. [181] for studying the echo based on more intuitive considerations. Notice that in Ref. [473] it was argued that classical Lyapunov exponents can exceed the quantum one in the SYK model. However, the authors of that paper considered initial conditions sampled according to the classical thermal Gibbs distribution rather than the corresponding Wigner function. The two choices can lead to inconsistencies between the conclusions since the exponential growth crucially depends on the initial state.

The rest of the paper is organized as follows. In Section 6.1 we discuss the requirements on the initial state and the observables. Then, in Section 6.2 we describe the Sherrington-Kirkpatrick (SK) model and its short-range version. In the following Section 6.3, we discuss the application of TWA to the SK model and its failure for the short-range case. Finally in Section 6.4, we show numerical results and determine the Lyapunov exponent for the long-range model.

6.1 The choice of the initial state and the observable

The typical time dependence of the echo of observables (as well as that of other OTOCs) is divided into three regimes: an initial perturbative one, reaching times of the order of the inverse coupling constant, where the echo grows as a power law, and an eventual saturation at long-times (beyond the Ehrenfest time) separated by an intermediate regime, where the presence of quantum chaos is manifest as exponential growth. It is clear that, for such exponential behavior to be seen, the long-time saturation value of the echo has to be parametrically larger in the system size N than the coefficient governing its initial perturbative short-time expansion. This requirement puts some well-defined constraints on the type of observables and of initial states to be considered.

Let us now explain quantitatively this point by first analyzing the short-time regime with perturbation theory and then the long-time saturation value, evaluated with the Eigenstate Thermalization Hypothesis, introduced in Section 1.1.2. We will show in the generic case of a sufficiently chaotic spin Hamiltonian satisfying ETH, that the conditions above are met if one chooses i) either the perturbation $\hat{B}$ or the observable $\hat{A}$ to be collective (sum of local operators), ii) the initial expectation value of $\hat{A}$ in the state $|\psi_0\rangle$ far from the long-time (thermal) saturation value. As we already mentioned above, while it is not required the analysis significantly simplifies if the initial state is the eigenstate of $\hat{A}$

$$|\psi_0\rangle = |\alpha_0\rangle \quad : \quad \hat{A}|\alpha_0\rangle = \alpha_0 |\alpha_0\rangle \, . \tag{6.1}$$

6.1.1 Early-time growth

Let us start with the initial growth. Using Eq.(6.1), the average of the echo operator in Eq.(1.44) becomes

$$\mu(t) = \langle \hat{B}(t)\hat{A}\hat{B}(t)\rangle - \alpha_0 \langle \hat{B}^2(t)\rangle \, . \tag{6.2}$$

In order to derive the early-time behavior, it is more convenient to work in the eigenbasis of the operator $\hat{A}$, i.e. $\hat{A}|\alpha_\lambda\rangle = \alpha_\lambda |\alpha_\lambda\rangle$ with $\lambda = 0, \ldots, D-1$, where D is

the Hilbert space dimension ($D = 2^N$ for a system of N spins $1/2$). The early-time expansion of the operator $\hat{B}(t)$ can be obtained via the Baker–Campbell–Hausdorff formula. Up to second order in time it reads

$$\hat{B}(t) = \hat{B} - it[\hat{H}, \hat{B}] - t^2/2\,[\hat{H}, [\hat{H}, \hat{B}]] + \mathcal{O}(t^3)\ . \tag{6.3}$$

We will further assume that the operators $\hat{A}$ and $\hat{B}$ commute at $t = 0$. This guarantees that $\mu(0) = 0$, i.e. that the echo signal in $\hat{A}$ only appears after some propagation time. For this reason, the operators $\hat{A}$ and $\hat{B}$ can be simultaneously diagonalized such that $\hat{B}|\alpha_\lambda\rangle = \beta_\lambda|\alpha_\lambda\rangle$. At short times, the average of the echo operator (6.2) reads

$$\mu(t) = t^2 \sum_{\lambda\neq 0} |\hat{H}_{0\lambda}|^2\,(\beta_\lambda - \beta_0)^2(\alpha_\lambda - \alpha_0)\ + \mathcal{O}(t^4)\ , \tag{6.4}$$

where $|\hat{H}_{0\lambda}| = \langle\alpha_0|\hat{H}|\alpha_\lambda\rangle$ are the matrix elements of Hamiltonian matrix elements in the eigenbasis of $\hat{A}$.

6.1.2 Long time saturation

Let us now turn to the analysis of the long time saturation of the echo, or more precisely of the infinite time average as defined in Eq.(1.6) of Eq.(1.44). It is convenient to work in the eigenbasis of the Hamiltonian, i.e. $\hat{H}|E_n\rangle = E_n|E_n\rangle$. Hence, Eq. (6.2) can be re-written as

$$\mu(t) = \sum_{nmpq} c_n\, c_q^*\, B_{nm}A_{mp}B_{pq}\, e^{i(E_n - E_m + E_p - E_q)\,t} - \alpha_0 \sum_{nmp} c_n\, c_m^*\, B_{np}B_{pm}\, e^{i(E_n - E_m)\,t}\ , \tag{6.5}$$

where $c_n = \langle\psi_0|E_n\rangle$, $B_{nm} = \langle E_n|\hat{B}|E_m\rangle$ and $A_{nm} = \langle E_n|\hat{A}|E_m\rangle$. We will assume that the Hamiltonian $\hat{H}$ is chaotic satisfying ETH [cf. Eq.(1.12)] and in particular that it has no degeneracies. With this choice, the time average of Eq.(6.5) is non-zero only if the energies appearing in the exponentials are equal to each other pairwise,[17, 44] such that

$$\overline{e^{i(E_n - E_m + E_p - E_q)\,t}} = \delta_{nm}\delta_{pq} + \delta_{nq}\delta_{mp} - \delta_{nmpq}\ ,$$

where δ_{nmpq} implies that all four indices are equal to each other. Likewise

$$\overline{e^{i(E_n - E_m)\,t}} = \delta_{nm}\ .$$

Then

$$\begin{aligned}\overline{\mu} &= \sum_{nm} c_n\, c_m^*\, B_{nn}A_{nm}B_{mm} + \sum_{nm} |c_n|^2|B_{nm}|^2A_{mm} - \sum_{n} |c_n|^2B_{nn}^2A_{nn} - \alpha_0 \sum_{nm} |c_n|^2\,|B_{nm}|^2 \\ &= \sum_{nm} c_n\, c_m^*\, B_{nn}A_{nm}B_{mm} - \alpha_0 \sum_{n} |c_n|^2|B_{nn}|^2 + \sum_{n\neq m} |c_n|^2\,(A_{mm} - \alpha_0)\,|B_{nm}|^2\ .\end{aligned} \tag{6.6}$$

This expression further simplifies if we assume that the diagonal matrix elements B_{nn} are smooth functions of E_n, an assumption always justified within ETH. As

discussed in Section 1.1.1, typical initial states are characterized by subextensive energy fluctuations, i.e. $\delta^2 E/E^2 \sim 1/N$ [cf. Eq.(1.9)]. Therefore, owing to the fact that $\sum_{nm} c_n\, c_m^* A_{nm} = \alpha_0$ and $\sum |c_n|^2 = 1$, the first two terms in Eq.(6.6) cancel each other and we get

$$\bar{\mu} \approx \sum_{n \neq m} |c_n|^2 \, (A_{mm} - \alpha_0) \, |B_{nm}|^2 \ . \tag{6.7}$$

We can now compute the long-time saturation value using the ETH ansatz for the matrix elements of observables in the eigenbasis of the Hamiltonian. Substituting Eq.(1.12) into E.(6.7), one obtains

$$\bar{\mu} = \sum_{n \neq m} |c_n|^2 \, [\mathcal{A}(E_n + \omega_{nm}) - \alpha_0] \, |f_{\hat{B}}(E_n + \omega_{nm}/2, \omega_{nm})|^2 \ e^{-S(E_n + \omega_{nm}/2)} \ . \tag{6.8}$$

where we have replaced R_{mm} ($|R_{nm}|^2$) with its statistical zero (unit) average and $\bar{E} = E_n + \omega_{nm}/2$ and $E_m = E_n + \omega_{nm}$. We now write each sum as an integral with the suitable density of states, $\sum_m \to \int_0^\infty dE_m \, e^{S(E_m)} = \int d\omega e^{S(E+\omega)}$. We therefore have

$$\bar{\mu} = \sum_n |c_n|^2 \int d\omega \ [\mathcal{A}(E_n + \omega) - \alpha_0] \, |f_{\hat{B}}(E_n + \omega/2, \omega)|^2 \ e^{-S(E_n+\omega/2)+S(E_n+\omega)} \ . \tag{6.9}$$

Since $f_{\hat{B}}(E, \omega)$ decays rapidly enough at large ω [474], we can expand in powers of ω

$$\mathcal{A}(E_n + \omega) = \mathcal{A}(E) + \frac{\partial \mathcal{A}}{\partial E}\, \omega + O(\omega^2) \ . \tag{6.10a}$$

The term containing the energy derivative become irrelevant in the thermodynamic limit, both if $\hat{A}$ is a local operator, or a sum of local operators [17]. Substituting back, we obtain

$$\begin{aligned} \bar{\mu} &= \sum_n |c_n|^2 \, [\mathcal{A}(E_n) - \alpha_0] \int \mathrm{d}\omega \ |f_{\hat{B}}(E_n + \omega/2, \omega)|^2 \ e^{-S(E_n+\omega/2)+S(E_n+\omega)} \\ &= \sum_n |c_n|^2 \, [\mathcal{A}(E_n) - \alpha_0] \ \langle E_n | \Delta \hat{B}^2 | E_n \rangle \ , \end{aligned} \tag{6.11}$$

where we have replaced the frequency integral by the variance over a single energy eigenstate $\langle E_n | \Delta \hat{B}^2 | E_n \rangle = \langle E_n | \hat{B}^2 | E_n \rangle - \langle E_n | \hat{B} | E_n \rangle^2$, see Ref.[17]. Performing now an expansion around the average energy $E = \langle \psi_0 | \hat{H} | \psi_0 \rangle$

$$\mathcal{A}(E_n) = \mathcal{A}(E) + (E_n - E)\, \mathcal{A}'(E) + \frac{1}{2}\,(E_n - E)^2\, \mathcal{A}''(E) + \dots \tag{6.12}$$

where $\mathcal{A}'(E) = \partial \mathcal{A}/\partial E|_E$ and $\mathcal{A}''(E) = \frac{\partial^2 \mathcal{A}}{\partial E^2}|_E$. One then obtains

$$\bar{\mu} = (\mathcal{A}(E) - \alpha_0)\, \Delta B^2(E) + \delta E^2 \left[(\mathcal{A}(E) - \alpha_0)\, (B'(E))^2 + \frac{1}{2} \mathcal{A}''(E)\, \Delta B^2(E) \right] \ , \tag{6.13}$$

where we isolated the corrections proportional to δE^2. If $\hat{B}$ is a local operator, these corrections are suppressed by a factor of N compared to the first leading term. On the other hand, when $\hat{B}$ is a sum of local operators, then the correction (proportional to $B'(E)$) scales with N in the same way as the first leading term.

6.1.3 Existence of a parametric window for the echo growth

We are now in the position to compare the short and the long-time behavior and find the conditions under which there is a parametric window for the growth of the echo. A simple qualitative criterion, which is at the same time a necessary condition, for the existence of such a window is

$$|\mu(t^*)| \sim N^{-\ell}|\bar{\mu}| \ ,$$

where ℓ is a positive power and t^* is the time of breakdown of the short time expansion. We will focus only on a class of operators $\hat{A}$ and $\hat{B}$ which are either local in spins or can be represented as sums of local terms, i.e. we will focus on most common and measurable operators representing physical observables. Also, we will also assume that the Hamiltonian contains sums of few spins (fermion) terms, i.e. it can contain an external field and two or three spin interactions, which may not necessarily be local in space. Under these assumptions, the Hamiltonian can flip at most few spins. Therefore, for the states connected by the nonzero matrix element $|H_{0\lambda}|^2$, the differences $\alpha_\lambda - \alpha_0$ and $\beta_\lambda - \beta_0$ are non-extensive irrespective on whether $\hat{A}$ or $\hat{B}$ are local or sums of local terms. Therefore $|\alpha_\lambda - \alpha_0|$ and $|\beta_\lambda - \beta_0|$ are bounded by some non-extensive constants $M_A = \text{Max}_\lambda|\alpha_\lambda - \alpha_0|$ and $M_B = \text{Max}_\lambda|\beta_\lambda - \beta_0|$.

Let us start by estimating the short time expansion using Eq.(6.4) distinguish three different possibilities, which we discuss one by one: (i) both $\hat{A}$ and $\hat{B}$ are collective operators, (ii) one of the operators is global one is local and (iii) both $\hat{A}$ and $\hat{B}$ are local.

(i) $\hat{A}$ and $\hat{B}$ are global operators. In this case at short times

$$\begin{aligned} \mu(t) &\leq t^2 \sum_{\lambda\neq 0} |\hat{H}_{0\lambda}|^2 \, |\beta_\lambda - \beta_0|^2 |\alpha_\lambda - \alpha_0| \\ &\leq t^2 \, M_A \, M_B^2 \sum_{\lambda\neq 0} |\hat{H}_{0\lambda}|^2 \sim Ct^2 N, \end{aligned} \tag{6.14}$$

where we used the standard normalization of the Hamiltonian such that it has an extensive energy variance

$$\langle\psi_0|\hat{H}^2|\psi_0\rangle = \sum_\lambda |\hat{H}_{0\lambda}|^2 \propto N \ .$$

We note that this scaling with N can be reduced further if $\alpha_\lambda - \alpha_0$ has an alternating sign between different eigenstates α_λ. The time t^* defining the validity of the short time expansion can be estimated from the decay of the expectation value of $\hat{B}(t)$, which is readily obtained from Eq. (6.3)

$$\langle\psi_0|\hat{B}(t)|\psi_0\rangle = \beta_0 + t^2 \sum_\lambda |H_{0\lambda}|^2(\beta_\lambda - \beta_0) + O(t^3) \ .$$

By equating the first and the second term in the expansion and by the same arguments of extensivity of the energy variance in the initial state we see that the time t^* is N-independent.

(ii) One of the operators $\hat{A}$ or $\hat{B}$ is local and the other is extensive. In this case locality of one of the operators $\hat{A}$ or $\hat{B}$ (let us say $\hat{B}$ for concreteness) restricts the eigenstates $|\alpha_\lambda\rangle$ in Eq. (6.14) to those where one of the local degrees of freedom (e.g. a spin) is localized. This additional selection rule removes a factor of N from the sum in Eq. (6.14) leading to the following estimate

$$\mu(t) \sim Ct^2 \ . \tag{6.15}$$

It is easy to see that the time scale t^* is N-independent irrespective of whether the operator $\hat{B}$ is extensive or global.

(iii) Both $\hat{A}$ and $\hat{B}$ are local. We will focus on operators that are not spatially separated. The OTOC for spatially separated operators was analyzed in the literature, see e.g. Ref. [116]. In these situations, there is a possibility for exponential echo growth, related to the out of the light cone dynamics and not generally connected to the existence of chaos. Assuming that there is no spatial separation, we can easily check that the Eq. (6.15) still holds.

Let us now determine the long time asymptotes of $\mu(t)$ from Eq. (6.7) for the three cases. As already mentioned, the scaling of these asymptotes with N sets the condition for the initial state and operator. The best initial state to have the maximal room for the non-perturbative growth of the echo is such that the difference between the initial value and its long time limit $|\mathcal{A}(E)-\alpha_0|$ appearing in Eq.(6.13) is maximal. In the case of a global operator $\hat{A}$, the maximum possible difference is extensive $|\mathcal{A}(E)-\alpha_0| \propto N$; for a local operator the maximal possible difference is of the order of one: $|\mathcal{A}(E)-\alpha_0| \propto N^0$. Then we immediately find for Eq. (6.7) that for the case (i) $\bar{\mu} \propto N^2$. Likewise for the case (ii), i.e. when either $\hat{A}$ or $\hat{B}$ is an extensive operator we have $\bar{\mu} \propto N^1$ and finally for the case (iii) $\bar{\mu} \propto N^0$. Comparing these asymptotes with the short time expansions of $\mu(t)$ discussed above we see that in order to have a non-perturbative growth of echo one should chose either the possibility (i) or (ii), i.e. at least one of the two operators $\hat{A}$ or $\hat{B}$ should be extensive. In particular, a very convenient choice we will use most extensively below is (i) where $\hat{A} = \hat{B}$ are the global magnetization along a particular direction:

$$\hat{A} = \hat{S}^\alpha = \sum_{i=1}^{N} \hat{\sigma}_i^\alpha \quad \text{with} \quad \alpha = x, y, z \ . \tag{6.16}$$

This choice is analogous to the one used in Refs. [181] and [194] and with that of standard echo-experiments [177–180]. We will also show results for the other cases ((ii) and (iii)). Of course, the existence of a parametric large in N time window is only a necessary condition for the exponential growth of the echo (OTOC) but a not sufficient one. If, however, the dynamics in the large N limit are semiclassical and chaotic, then we generally expect a regime of the exponential growth of $\mu(t)$.

Conversely if in the large N limit dynamics remains quantum, there is no a-priory reason to expect any exponential behavior of $\mu(t)$. As we show below this is indeed the case in the SK model with local couplings, where the non-perturbative growth regime of $\mu(t)$ is a power law with a small non-integer exponent.

6.2 The Sherrington-Kirkpatrick model in transverse field

We will now corroborate our general discussion with an analysis of the Sherrington-Kirkpatrick (SK) model, describing a set of spins with infinite-range disordered interactions in their z-components. To make this model dynamical we add a uniform transverse field. Below we will also analyze a version of this model with local interactions that decay in space according to a Gaussian law.

The Hamiltonian of the SK model in the transverse field reads

$$\hat{H} = -\frac{1}{2}\sum_{i\neq j}^{N} J_{ij}\hat{\sigma}_i^z\hat{\sigma}_j^z - h\sum_{i=1}^{N}\hat{\sigma}_i^x \,, \tag{6.17}$$

where $\hat{\sigma}_i^z$, $\hat{\sigma}_i^x$ are the Pauli matrices and the couplings J_{ij} are random symmetric numbers distributed according to the Gaussian probability with zero mean and the variance J^2/N as

$$J_{ij} = \frac{J}{\sqrt{N}}\, g_{ij} \,, \tag{6.18}$$

where g_{ij} are Gaussian random numbers with zero average and unit variance. At equilibrium, the phase-diagram of the SK model has been extensively studied [469–471]. In the limit of zero transverse field ($h = 0$), one recovers the classical SK model [475, 476], which has a glass transition at the critical temperature $T_c = J$. The SK model in transverse field has a zero-temperature quantum phase transition at a critical magnetic field $h_c(T = 0) \sim 1.52J$ [470]. Away from equilibrium, this model was explored in Refs. [477–480].

In what follows, we will also analyze a *short-range version* of the SK model. It is described by the same spin Hamiltonian (6.17), but the random couplings J_{ij} connecting the sites $i\,, j$ now decay with the distance r_{ij} according

$$J_{ij} = \frac{J}{\sqrt{N(\sigma)}}\, e^{-\frac{r_{ij}^2}{2\sigma^2}}\, g_{ij} \,, \tag{6.19}$$

where σ is a parameter defining the interaction range. In one dimension with periodic boundary conditions the distance between any two sites is taken to be

$$r_{ij} = \min\left(|i-j|, N-|i-j|\right).$$

We normalize the couplings by the effective number of spins within the correlation length σ: $N(\sigma) = \sum_{i\neq j} e^{-r_{ij}^2/2\sigma^2}/N \sim \sqrt{\pi}/2\,\sigma\,\mathrm{Erf}(N/\sigma)$. This choice correctly interpolates between the short range ($\sigma \approx 1$) and the long range ($\sigma \to \infty$) limits of the SK model. In the infinite range limit $\sigma \to \infty$, the standard SK model is recovered (6.18) and $N(\sigma) = N$. In the opposite case when $\sigma \ll N$, the normalization is simply a constant $N(\sigma) \sim 2/\sqrt{\pi}\,\sigma$.

6.3 Semiclassical dynamics in the large N-limit

To connect the exponential growth of the echo with the availability of a semiclassical limit, we will combine exact diagonalization with the semiclassical truncated Wigner approximation [195, 277, 278, 282–284], which we have introduced and described in Section 2.2.1.

As discussed above, the semiclassical approach is expected to hold at short times, namely, before the Ehrenfest time scale $T_{\rm Ehr}$ [cf. Eq.(2.7)] which diverges for $\hbar_{\rm eff} \to 0$. In this case, the role of the effective Planck's constant $\hbar_{\rm eff}$ is played by $1/N$, as for the fully connected case[2], see also Section 2.1.2. We find that, even when couplings are randomly distributed as in Eq.(6.18), the situation does not change qualitatively, as long as the interactions are sufficiently long-ranged. This is demonstrated numerically in the following section. Furthermore, as we discuss in more detail in the Appendix D.1, TWA can be rigorously derived for the SK model in the large N-limit, where $1/N$ serving as a proper saddle point parameter. Similar findings for the SYK model were reported recently in Ref [183]. In this sense, the situation is similar to equilibrium, where the large N-limit ensures the validity of the saddle point mean-field approximation.

In the next sections, we outline the application of the TWA to the models described in this chapter.

6.3.1 TWA for the SK model

Let us now apply the general TWA formalism of Section 2.2.1 to the SK model. The Weyl symbol of the SK Hamiltonian (6.17) is simply obtained by replacing the spin (angular momentum) operators by the classical spin variables. It reads

$$H^{\rm w} = -2\sum_{i\neq j}^{N} J_{ij} s_i^z\, s_j^z \; - 2\,h \sum_{i=1}^{N} s_i^x \;, \tag{6.20}$$

with J_{ij} the same random couplings as in Eq.(6.18). The spin variables evolve in time according their classical equations of motion (2.46), i.e.

$$\frac{d\vec{s}_i}{dt} = \frac{\partial H^{\rm w}(\{\vec{s}\})}{\partial \vec{s}_i} \times \vec{s}_i \;. \tag{6.21}$$

These are supplemented with the initial conditions distributed according to the Wigner function. For simplicity we will consider simple product initial states $|\psi_0\rangle$, whose Wigner function $W(\{s_i^\alpha(0)\})$ also factorizes. Instead of the exact Wigner function, we choose its Gaussian approximation, see e.g. Eq.(2.48). Alternatively one can use a discrete Wigner function or DTWA, introduced in Section 2.2.2. We checked numerically that the results obtained using the Gaussian and the discrete Wigner functions do not have noticeable differences.

The equations of motion (6.21) are integrated numerically and averaged at each time t over $N_{\rm sim}$ trajectories, as in Eq.(2.44). For each of them, the initial conditions

[2]Notice that the fully connected model is retrieved by considering uniform couplings $J_{ij} = 1/N$ in the Hamiltonian (6.17).

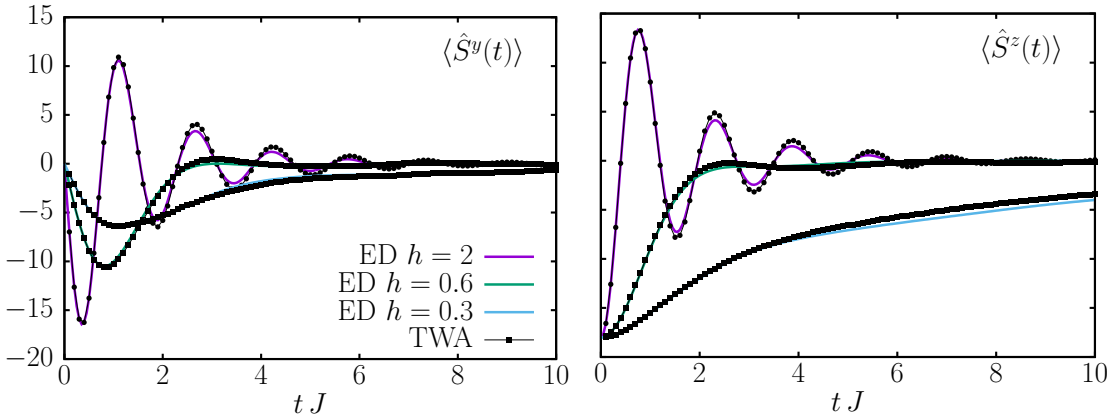

Figure 6.1: Comparison of TWA results to exact magnetization dynamics with SK couplings (6.18) for a fixed disorder realization at different transverse fields h for $N = 18$ spins. The left (right) panels show the total magnetization along y (z) direction: $\langle \hat{S}^y(t) \rangle$ ($\langle \hat{S}^z(t) \rangle$). Full lines ED simulations, dotted lines correspond to TWA simulations with $N_{\rm sim} = 8000$.

are sampled from to the initial Wigner function (2.48). For numerical integration, we use an adaptive fourth-order Runge-Kutta algorithm, fixing the error to 10^{-12}.

Before analyzing the echo, let us consider the magnetization dynamics (6.16) with forward evolution, where we suddenly quench the system to the SK Hamiltonian (6.20). We check the validity of the TWA by comparing it with exact diagonalization (ED) [3]. In what follows, we focus for concreteness on the initial product state, where all the spins are polarized along the z-axis: $|\psi_0\rangle = |\downarrow\downarrow \ldots \downarrow\rangle$, but the validity of the method does not depend on this choice. In Figure 6.1, we show results of the time evolution of the total spin components along the y and z axes for a fixed realization of the spin-spin couplings in the SK Hamiltonian. As expected, the TWA gives an excellent quantitative description of the forward time evolution of the magnetization for all simulated times and for different values of the transverse field h, covering both glassy and normal phases of the Hamiltonian. Furthermore, by increasing the system size N, TWA asymptotically approaches the exact quantum dynamics. This is shown in Figure 6.2, where we compare TWA to ED for fixed h increasing N. In the inset of the same figure, we plot the absolute value of the difference between the two results Diff($\langle S_z(t) \rangle$), which clearly decreases with N.

[3] We address the exact quantum dynamics by employing the method of Krylov sub-spaces to avoid full diagonalization, see e.g. Ref.[481].

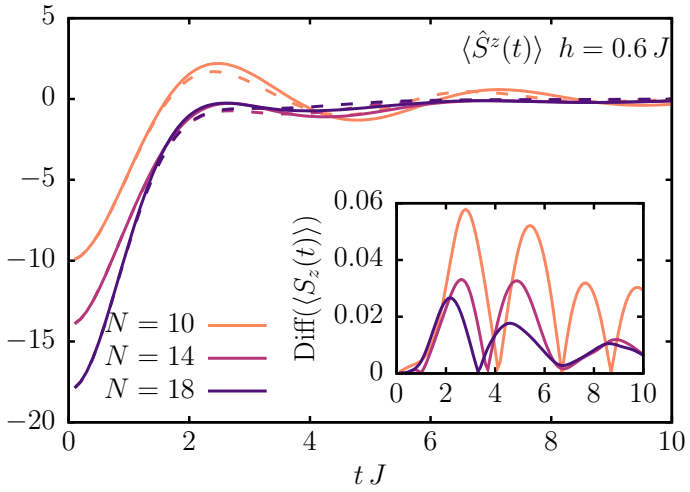

Figure 6.2: Comparison between ED (solid lines) and TWA (dashed lines) dynamics for $\langle \hat{S}^z(t) \rangle$ for the SK model (6.18) with a fixed disorder realization, fixed $h = 0.6\,J$, and with different $N = 10\,, 14\,, 18$. In the inset we plot the absolute value of the difference between the two results. TWA simulations with $N_{\rm sim} = 8000$.

As evident from the data, the TWA error reaches the maximum at an intermediate, system size-independent time before decreasing again at late times. The maximal (and the average) error diminishes with N. Interestingly, there is no clear signature of the Ehrenfest time $T_{\rm Ehr}$ in the forward evolution. Correspondingly, the TWA correctly reproduces the magnetization dynamics at all times at sufficiently large N. This is to be contrasted with the echo dynamics, analyzed in the next section, where we will see that TWA breaks down after $T_{\rm Ehr}$, which for these parameters and largest analyzed $N = 20$ is given by $JT_{\rm Ehr} \approx 2$ (c.f. Figure 6.5).

6.3.2 TWA for the short-range model

In the case of the short-range Hamiltonian, the TWA approach is the same as the one illustrated in the previous section, with the only difference of the short-range couplings as given by Eq.(6.19). In this case, $1/N(\sigma) \sim 1/\sigma$ acts an effective Plank constant $\hbar_{\rm eff}$ and TWA is expected to fail at a time-scale set by σ, which is N-independent. In the short-range limit, for fixed finite σ, the semiclassical approximation does not reproduce the exact quantum dynamics in the thermodynamic limit. Indeed, in Figure 6.3(a.), we show the comparison of the TWA with the ED dynamics for $\langle \hat{S}_z(t) \rangle$ from the initial state $|\psi_0\rangle = |\downarrow\downarrow \ldots \downarrow\rangle$ at fixed $\sigma = 1$ varying $N = 10 \div 18$. The results might seem qualitatively in agreement with the exact dynamics. However, they do not improve with increasing the system size, as shown in the inset. When $N(\sigma) \sim \sigma$ is big enough, the TWA is accurate both at short and at long-times. In Figure 6.3(b.), we plot $\langle \hat{S}_z(t) \rangle$ at fixed $N = 18$ for different $\sigma = 1,\, 2,\, 6$. The difference between ED and TWA (displayed in the inset) shows how the reliability of the TWA grows by increasing σ.

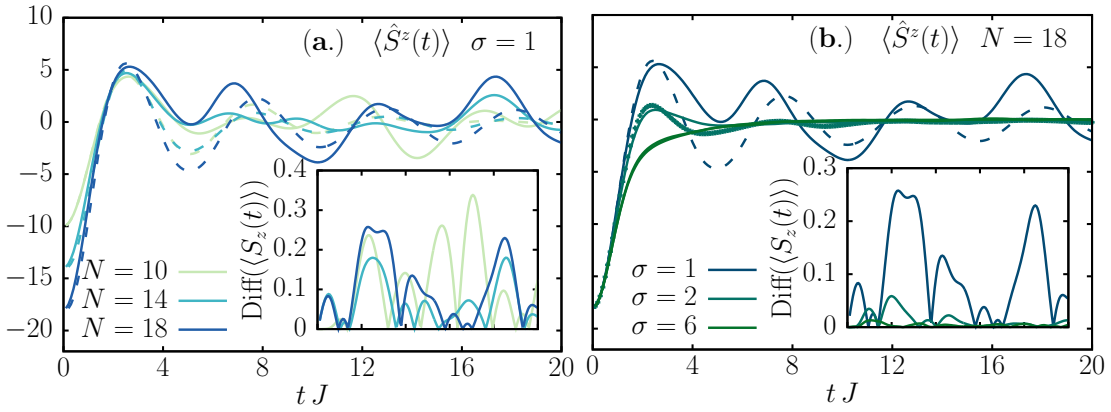

Figure 6.3: Comparison of ED (solid lines) and TWA (dashed lines) dynamics of $\langle \hat{S}^z(t) \rangle$ for a single realization of the short-range gaussian couplings (6.19) at $h = 0.6\,J$. TWA breakdown is set by $N(\sigma) \sim \sigma$, which is N-independent. (a.) Short-range couplings for fixed $\sigma = 1$ with different $N = 10\,, 14\,, 18$. In the inset, we plot the absolute value of the difference between the two results as a function of time. (b) Same as in a) but for fixed $N = 18$ and different range of interactions $\sigma = 1, 2, 6$. TWA simulations with $N_{\text{sim}} = 8000$.

6.4 Scrambling in the SK model

Let us now turn to the dynamics of the echo in the SK model and its short-range version. In particular, we will study numerically the role of the number of spins N, the choice of the operator and the range interactions for both observing the exponential growth of OTOC and for the validity of the semiclassical TWA approach. We first discuss the echo dynamics under the evolution of the all-to-all SK Hamiltonian given by Eq.(6.17).

Let us start by analyzing possible choices of the operators $\hat{A}$ and $\hat{B}$ according to the cases (i), (ii) and (iii) discussed in Section 6.1. We wish to compare the scaling with N of the early and long-time behavior of the echo in these three alternatives. For definiteness, we focus on the magnetization along the z axis and we consider (i) extensive-extensive $\hat{A} = \hat{B} = \hat{S}^z = \sum_j \hat{\sigma}_j^z$ [c.f. Eq. (6.16)], (ii) extensive-local $\hat{A} = \hat{S}^z$ with $\hat{B} = \sigma_i^z$ and (iii) local-local $\hat{A} = \hat{B} = \hat{\sigma}_i^z$, where the site i is chosen randomly for each disorder realization. Notice that another possibility for (ii) discussed in Section 6.1 is $\hat{A} = \hat{\sigma}_j^z$ local with $\hat{B} = \hat{S}^z$ extensive. This choice in fact yields results identical to those of (i) with the $\langle A(t) \rangle$ and $\mu(t)$ simply scaled down by a factor of N. This follows from the fact that the expression for the echo (1.44) is linear in $\hat{A}$. We consider a fully polarized product initial state $|\psi_0\rangle = |\downarrow\downarrow \ldots \downarrow\rangle$, which automatically satisfies the requirement (6.13) and maximizes the difference between the initial and asymptotic value $\mathcal{A}(E) - \alpha_0 \sim -\alpha_0$ [c.f. Eq.(6.13)]. In fact, the energy of this fully polarized state lies in the middle of the spectrum of the Hamiltonian, therefore $\mathcal{A}(E) \sim 0$. This represents a generic choice suitable for studying the echo dynamics.
At early times the echo grows quadratically as predicted by Eq.(6.4), which in this case can be computed explicitly yielding (i) $\mu(t) = 8\,N\,h^2\,t^2$ and (ii-iii) $\mu(t) = 8\,h^2\,t^2$.

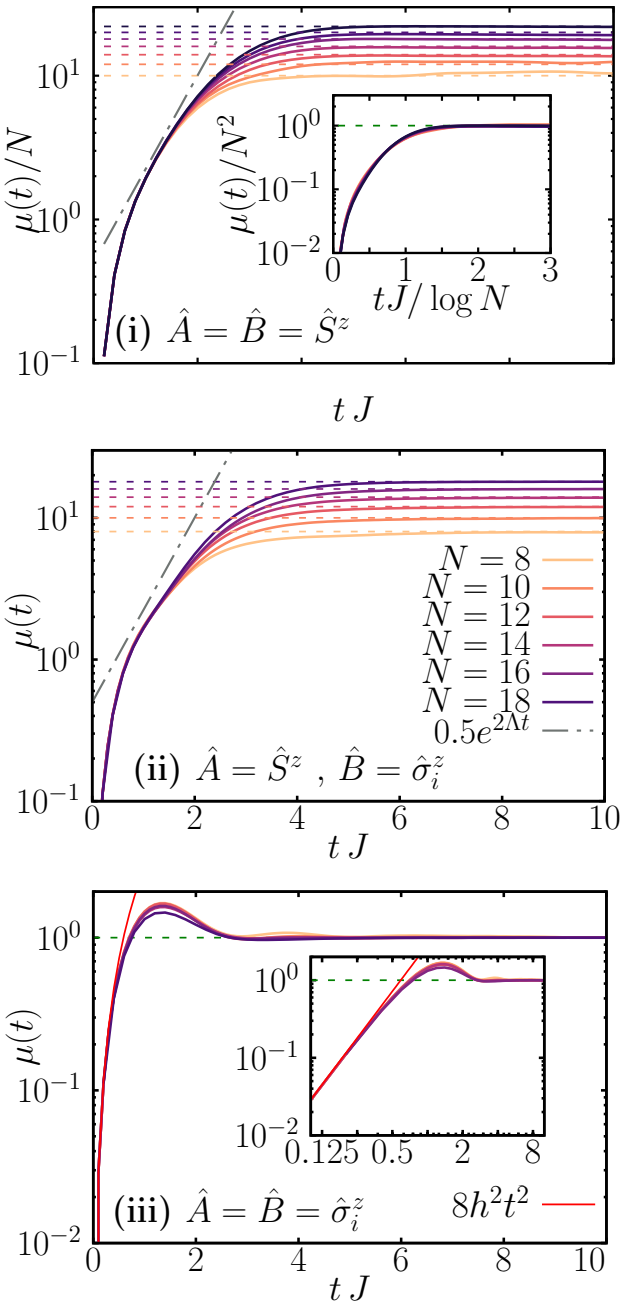

Figure 6.4: Exact scrambling dynamics $\mu(t)$ for different observables realizing three different scenarios (i-iii) discussed in Section6.1.3, for system sizes $N = 8 \div 18$. The saturation value as predicted by the ETH ansatz [cf. Eq.(6.7)] is illustrated by the dashed lines. To guide the reader's eyes, in (i-ii) we show an exponential function $f(t) = e^{2\Lambda t}/2$ in grey. The rate $2\Lambda = 1.5$ is extracted within TWA (see below). In (iii) the early time quadratic growth is plotted in red. (Top panel) (i) $\mu(t)/N$ for extensive-extensive operators $\hat{A} = \hat{B} = \hat{S}_z$. (Center panel) (ii) $\mu(t)$ for extensive-local operators $\hat{A} = \hat{S}^z$ with $\hat{B} = \sigma_i^z$. (Bottom panel) (iii) $\mu(t)$ for local-local $\hat{A} = \hat{B} = \hat{\sigma}_i^z$. In the inset of (i) we show $\mu(t)/N^2$ as a function of the rescaled time $tJ/\ln N \sim tJ/T_{\rm Ehr}$ showing the long time scaling collapse of the echo for different values of N. (iii) The echo saturates to unity (green dashed line), while in the inset the same data are plotted in a doubly logarithmic scale. The plotted results correspond to a fully polarized initial state with $h = 0.6\,J$, averaged over 50 disorder realizations (see text for details).

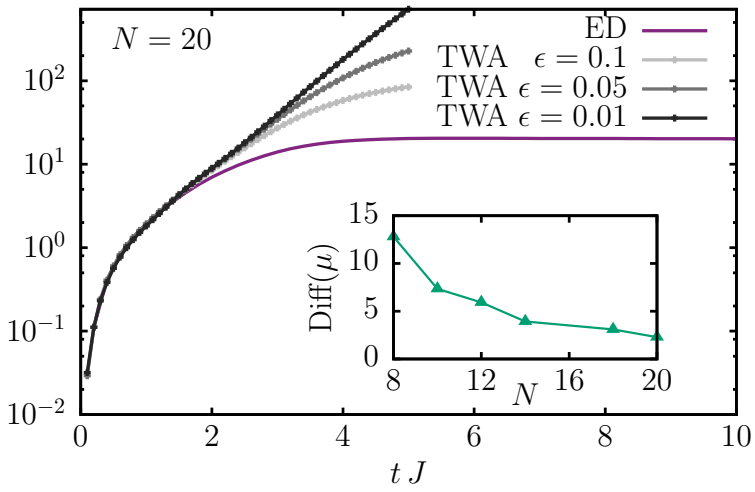

Figure 6.5: Comparison between the TWA scrambling dynamics $\mu(t)/N$ and the exact results at $N = 20$ varying ϵ. An exponential fit of the TWA data for $\epsilon = 0.01$ with $f(x) = ae^{2\Lambda x}$ yields the exponent $2\Lambda = 1.5/J$. In the inset we show the difference between the TWA and ED results at fixed time $t = 2$ as a function of the system size N. At larger N, the quantum echo approaches the exponentially growing TWA prediction and then saturates. The results correspond to a fully polarized initial state with $h = 0.6\,J$ for a single disorder realizations. TWA with $N_{\rm sim} = 20000$.

This perturbative expansion breaks down at $t^* \sim 1/\sqrt{J^2 + 4h^2}$. After t^*, $\mu(t)$ enters a non-perturbative regime, until it saturates at long-times to the value: (i) $\overline{\mu} \approx N^2$, (ii) $\overline{\mu} \approx N$, and (iii) $\overline{\mu} \approx 1$, as immediately follows from Eq. (6.7) for an infinite temperature state which has no magnetization correlations between different spins. This general behavior is exemplified in Figure 6.4, where we show the exact quantum dynamics of the echo observable for (i-iii) for finite system sizes up $N = 8 \div 18$ for $h = 0.6\,J$, averaged over 50 disorder realizations. The figure further shows how the early time quadratic growth — red in the plot (iii) — breaks at a time, which is N-independent, the same is true for the collective observables. For (i-ii), the saturation value predicted by ETH is represented by dashed lines for each N at the corresponding color, displaying the existence of a parametric window that scales with N that gives "room" for chaos to develop. On the other hand, the panel (iii) shows the saturation of the echo to one (green dashed line) leading the same dynamical behavior of the echo, which is independent of N. From this ED preliminary analysis for small system sizes, the echo observable already shows hints of exponential growth in the case of collective observables, see Figure 6.4 (i-ii). As evident from the data, this is possible due to the $N-$dependent saturation between the early-time and long-time behavior.

Let us now focus on the case (i) for $\hat{A} = \hat{B} = \hat{S}^z$. By increasing N, the non-perturbative time-regime extends and the late time dynamics collapses if we plot $\mu(t)$ vs $tJ/\ln(N)$, as shown in the inset of the same Figure 6.4 (i). This time-scale is compatible with the Ehrenfest time (2.7), meaning that the echo has an asymptotic form $\mu(t) = N^2 f(tJ/T_{\rm Ehr})$. Hence this scaling analysis shows that the intermediate, non-perturbative regime of exponential growth extends for $t^* < t < T_{\rm Ehr}$, with the latter being divergent in the thermodynamic limit.

Since the quantum exponential growth is restricted in a time interval of width $\propto \ln N$, a very slow function of its argument, one needs a numerical approach alternative to ED to simulate sufficiently large N and fully appreciate the exponential growth numerically. To study the $\mu(t)$ dynamics before the Ehrenfest time, we resort to the TWA. As discussed in Section 6.3.1, for this model the semiclassical approach correctly describes the expectation value of the observables in this time-regime. In Figure 6.5, we show TWA results in comparison with ED, for a single-disorder realization at finite size $N = 20$. After a short transient time, the TWA data exhibit a clear exponential growth, whose extent is determined by the parameter ϵ, representing the strength of the perturbation, see Eq.(1.43). This situation is analogous to what happens in chaotic classical systems with compact phase-space. There, the ratio between the distance of two nearby trajectories, initially separated by ϵ, ultimately saturates at a typical value fixed by the maximum available separation. For larger ϵ this saturation happens earlier, hence there is a shorter domain of exponential growth. The difference between exact ED and TWA data at fixed time, Diff(μ) diminishes with the system size as indicated in the inset of Figure 6.5. This result is consistent with the asymptotic accuracy of the TWA in the large N-limit, as discussed above for the magnetization. However, for long times, unlike for the magnetization, this difference can be arbitrarily large as $\epsilon \to 0$.

Interestingly the TWA has an advantage over the ED method as it allows one to accurately extract the exponent characterizing the growth of the quantum echo in the thermodynamic limit even using relatively small system sizes (see also Ref. [183] for the related discussion on the SYK model). In the case of the transverse field $h = 0.6\,J$ as in Figure 6.5, an exponential fit yields $2\Lambda \sim 1.5/J$, while in general Λ is an increasing function of h. The rate Λ (sometimes referred to as the generalized Lyapunov exponent [482–484]) is related to the maximal Lyapunov exponent of the theory λ_1 defined in Section 3.1 [181, 183]. The difference between the two comes from the different order of operations of taking logarithm and ensemble averaging. We would also like to point out that TWA is more accurate in extracting the Lyapunov exponent Λ for the additional two reasons: 1) TWA does not know about the Ehrenfest time (a fully quantum time-scale) and its exponential growth lasts for many decades. 2) In TWA Λ becomes independent on the system size even for relatively small N, allowing a precise estimate.
To summarize this discussion, TWA for the echo indeed breaks down at $t \propto \ln N$, which are relatively short times unless N is very big. But it breaks down in a smart way, which allows predicting quantum dynamics when N becomes exponentially large. While this result seems to be paradoxical, it is correct and not incidental. By our arguments, it should apply to any large N model, which has a diverging Ehrenfest time. This loosely follows from the fact that the main role of N in dynamics is to set the value of $\hbar$, other corrections due to finite N are small and very quickly disappear as N becomes moderately large, of the order of 10. So the semiclassical-classical TWA dynamics effectively extrapolate $\hbar \to 0$ and is very efficient if we are interested in this limit.

The same considerations apply in the case of other observables, i.e. magnetization in the other directions $\hat{S}^x$, $\hat{S}^y$.

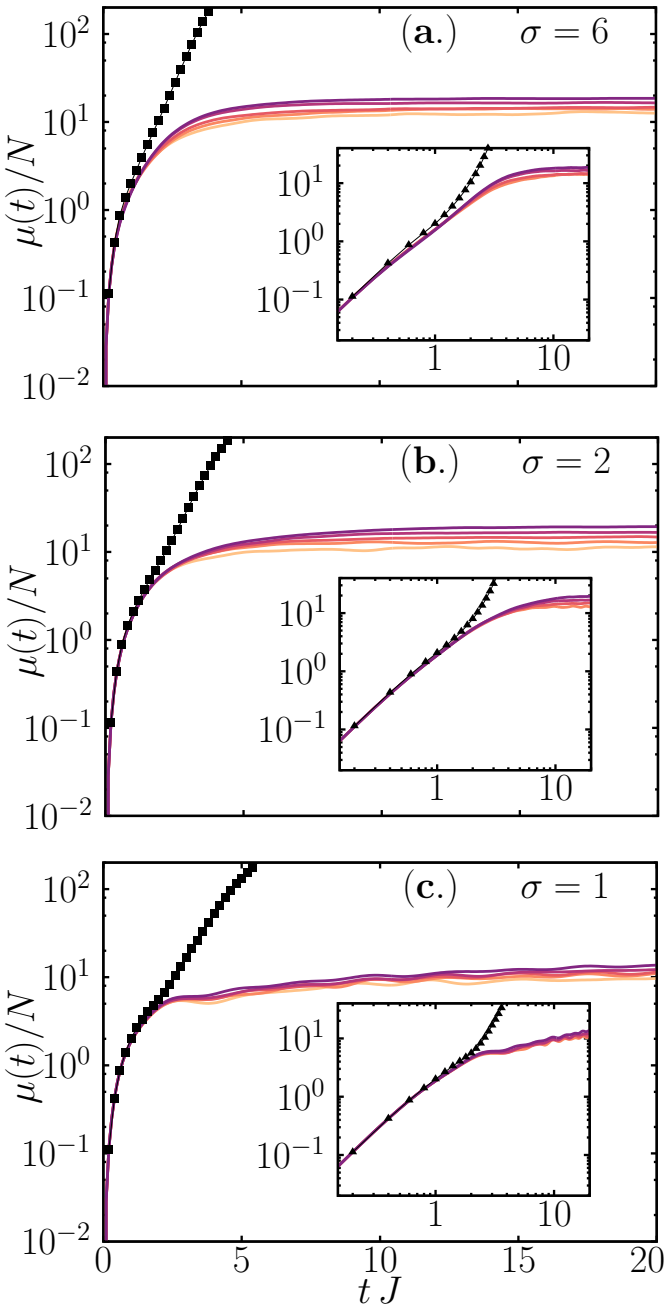

Figure 6.6: Absence of the exponential growth for the scrambling dynamics induced by short range couplings (6.19) for different σ. We compare exact quantum ED dynamics for different system sizes $N = 8 \div 16$ (increasing color intensity) with TWA results for $N = 16$ and $\delta = 10^{-2}$ (dotted black lines). Panels (a), (b), and (c) refer to decreasing interaction range $\sigma = 6\,, 2\,, 1$, respectively. The results correspond to a fully polarized initial state with $h = 0.6\,J$, averaged over 50 disorder realizations (see text for details).

6.4.1 Absence of exponential sensitivity in a short-range SK model

The exponential sensitivity of the echo disappears in the presence of local interactions. This happens simultaneously with the failure of the semiclassical TWA approximation. We consider the evolution of the same polarized initial state with the SK Hamiltonian with short-range Gaussian couplings (6.19). Short-range interactions result in at most a power-law growth of echo, in accordance with what was first observed in Ref. [181] and then proved in Ref [194]. In Figure 6.6, we show the quantum ED evolution for a fixed system size at different values $\sigma = 1, 2, 6$ and compare them to the corresponding TWA results. As the plots show, for the short-range model $\sigma = 1, 2$ the echo growth according to the initial perturbative power until it crossovers to a slower polynomial growth best fitted by $\mu(t) \propto t^{0.5}$ consistent with Refs.[181, 194] (see the inset) and the eventual saturation to the correct ETH value Eq. (6.12). As σ increases one can observe a slow emergence of the non-perturbative intermediate time dynamics of fast echo growth, which is expected to crossover to the exponential growth in the limit $\sigma \to \infty$. From this plot it is also evident that the TWA fails after a shorter (N-independent) time, incorrectly showing the persistence of exponential growth of the echo even for the short-range model. These results can be rephrased by saying that the effective Ehrenfest time becomes of the same order as the time of breakdown of the short time expansion, i.e. $T_{\text{Ehr}} \sim t^*$, leading to a lack of the semiclassical time-window necessary for the exponential quantum growth of the echo.

6.5 Discussion

In this work, we have studied the quantum echo dynamics and its exponential divergence in time in the Sherrington-Kirkpatrick model with the transverse field. We have argued that, by choosing collective observables and an initial state such that the initial value of the observable is thermodynamically different from its stationary value, the echo grows exponentially, with the same rate of the underlying semiclassical theory. On the other hand, the presence of short-range interactions results in the absence of exponential sensitivity in the quantum dynamics [181, 182] as a result of the lack of a well defined semiclassical limit. In this case, understanding the nature of the non-perturbative polynomial regime remains an open question, beyond the scope of the present work.

Overall, we would like to emphasize that the echo (and the OTOC in general) can be used as a precise probe of failure of classical analysis, exactly in the spirit of the seminal paper by Larkin and Ovchinnikov [160]. Indeed, the forward evolution of observables like the magnetization is reproduced by the semiclassical evolution up to times which go well beyond T_{Ehr} and can even extend to infinity. Conversely, the semiclassical description of the OTOC breaks down precisely at T_{Ehr} and it allows one to identify the Ehrenfest time as the breakdown time of the classical evolution. Interestingly, the same occurs for all the quantifiers of entanglement, as we have shown in detail in Chapter 3.

Because of the connection between the echo (the square commutator) and the expectation value (the variance) of the observables under effective time reversal, our findings are directly relevant to experiments allowing one to access exponential signa-

tures of chaos in atomic experiments. A more general and open question concerns the full distribution of the echo operator. We observed numerically that higher cumulants of the echo signal produce deviations between the ED and the TWA predictions even before the Ehrenfest time. We will leave this analysis for future work.

Chapter 7

Ground state entanglement entropy of the Dyson hierarchical model

The goal of this chapter is to get an analytical insight into the ground state entanglement entropy of long-range interacting systems. This is done by studying a renowned toy model: the Dyson hierarchical chain with algebraically decaying interactions. By exploiting the real-space renormalization group solution, we derive a manageable recursive expression for the reduced density matrix and hence for the entanglement entropy. Surprisingly, we find that at criticality the entanglement entropy obeys an area law.

As we have argued thoroughly in Section 1.3, a large amount of information about many-body systems can be inferred by their entanglement properties. The most useful quantity is surely the celebrated entanglement entropy S_A(1.24), introduced in Section 1.2.1. S_A is a very useful quantity, especially when A is a block of ℓ contiguous lattice sites in a one-dimensional chain. As stated above, the scaling entanglement entropy is tightly connected to the presence of quantum phase transitions for short-range systems. Indeed, while for gapped systems with short-range interaction S_ℓ obeys an area law [cf. Eq.(1.46)], it grows like $\ln \ell$ at the critical point, with a proportionality constant given by the central charge of the underlying conformal field theory.

On the other hand, the entanglement of long-range interacting systems represents an intriguing theoretical challenge, as we have discussed in Section 4.1. In fact, for this class of models, conformal invariance is broken as a consequence of the lack of Lorentz symmetry (rotational one in Euclidean spacetime) as explicitly manifested by a dynamical critical exponent $z \neq 1$ [485]. Hence unusual ground state entanglement properties are expected [400–407], as e.g. shown numerically for antiferromagnetic long-range one-dimensional systems, which violate area-law scaling also in the gapped phase [218, 400, 408]. On the other hand, the ferromagnetic mean-field Ising model has a critical entanglement entropy that scales with the logarithm of the number of spins in A [103, 486]. Beyond the mean-field, the scaling of entanglement entropy for ferromagnetic long-range interaction is still an open issue, also in one spatial dimension.

In this chapter, we address such a problem, by considering the quantum version of the ferromagnetic Dyson hierarchical model [487, 488]. Its classical version

was introduced by Dyson in 1969 [455, 456] and it provided, via an exact renormalization group (RG) approach, analytical insights about the critical behavior of long-range interacting one-dimensional spin chains. The quantum version has been recently solved by Monthus [487] using real-space renormalization and the critical properties of the ground state have been obtained by a recursive projection onto the low lying energy states.

Within this frame, we study the entanglement entropy of the renormalized ground state of the Dyson hierarchical model at criticality. The result depends on the choice of the subsystem because the model is not translationally invariant. Hence, we consider three types of partitions, and, for each of them, we determine recursively the reduced density matrix. We finally analyze the scaling of the entanglement entropy at the critical point and in some limits we derive analytical expansions. Our main and surprising result is that, although the correlation functions decay algebraically, the entanglement entropy obeys an area law. This is due to the hierarchical structure of the renormalized ground state that makes the rank of the reduced density matrix finite (the ground state is a tree tensor network [489–492] with finite bond dimension). Despite this saturation at the critical point, the renormalized ground-state reduced density matrix reproduces the power-law decay of the two-point correlation function with the exact critical exponent.

The chapter is organized as follows. In Section 7.1, we describe the model and the main steps of the real-space RG procedure. Section 7.2 contains all our results, including a description of the three considered partitions and the first discussion of our findings. This section is divided as: in Subsections 7.2.1-7.2.3 we derive recursively the reduced density matrix and the entanglement entropy for the three considered partitions; we then show by an elementary approach that the rank of the reduced density matrix is finite (Subsection 7.2.4) and that the correct power-law decay of the correlation functions follows from them (Subsection 7.2.5). In the closing section, we draw our conclusions and discuss some open questions. In the appendix, we report some technical details of the calculations.

7.1 The model

The Dyson hierarchical model was introduced by Dyson in 1969 [455, 456] to study phase transitions in one dimensional ferromagnetic Ising models with algebraically decaying interactions with exponent $\alpha = 1+\sigma$. A hierarchical Hamiltonian is defined with a tree structure on a spin chain of length $L = 2^n$, where blocks of spins are subject to an interaction that decays as a power-law of their distance. In the classical case, the hierarchical model reproduces well the critical properties of the long-range Ising Hamiltonian [493]. In fact, for $\sigma < 1/2$ the critical exponents of the former coincide with the mean-field of the latter. Furthermore, for $\sigma \geq 1/2$, the exponents of the two models coincide at first order in the $\epsilon = \sigma - 1/2$ expansion [494].

The quantum version of this model aims at reproducing the properties of the quantum long-range Ising Hamiltonian with a transverse field, defined in Eq.(4.1). It has been introduced and studied with real-space RG by Monthus in Refs.[487, 488]. Let us describe the Hamiltonian which is pictorially represented in Figure

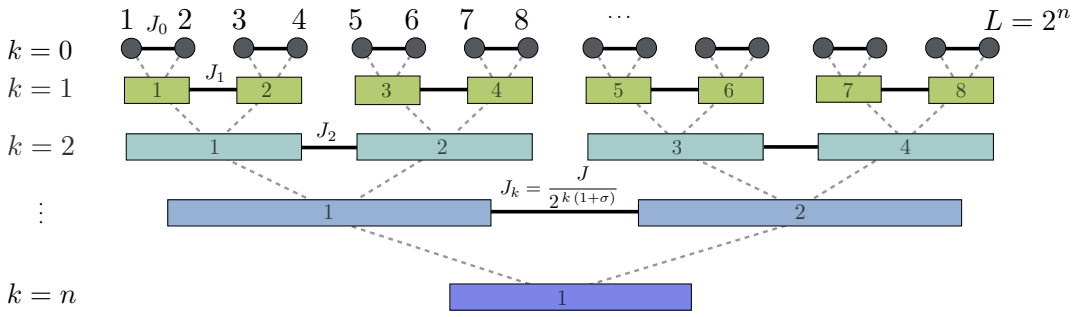

Figure 7.1: Tree structure of the Dyson hierarchical model. The Hamiltonian is a sum over different two-body interactions J_k between block variables at level k (full horizontal lines). The level $k = 0$ corresponds to the physical spins (top circles). At each layer, the block variables, represented by coloured boxes, interact with the coupling $J_k = J/2^{k(1+\sigma)}$. The dashed lines show which spins at level k form the blocks at level $k+1$. The real-space RG procedure consists of replacing each box with an effective spin. At the last step, there is a single spin left and the Hamiltonian is an effective transverse magnetic field h_n.

7.1. At step $k = 0$ each pair of spins at sites $2j - 1$ and $2j$ interacts with a coupling $J_0 = J$ as $J\hat{\sigma}^x_{2j-1i}\hat{\sigma}^x_{2j}$, where hereafter $\hat{\sigma}^\alpha_i$ denotes the Pauli matrices. The absence of interactions between the sites $2j$ and $2j + 1$ is the main difference from standard Ising models. At the following step $k = 1$, two blocks of two spins interact (always along x) with coupling $J_1 = J/2^{1+\sigma}$, then at $k = 2$ blocks of four spins interact with $J_2 = J/2^{2(1+\sigma)}$ and so on. Hence, the total hamiltonian is

$$\hat{H} = -\sum_{k=0}^{n-1} J_k \mu^2 \sum_{i=1}^{L/2^{k+1}} \Big(\sum_{j=0}^{2k} \hat{\sigma}^x_{2^k(2i-1)-j}\Big)\Big(\sum_{j=0}^{2k} \hat{\sigma}^x_{2^{k+1}i-j}\Big) - h \sum_{i=1}^{L} \hat{\sigma}^z_i , \tag{7.1}$$

where $J_k = J2^{-k(1+\sigma)}$ and we introduced the transverse field $h > 0$ and the magnetic moment μ (the latter will be set to 1, and it has been introduced for convenience in the renormalization procedure). The real-space RG of Ref. [487] is constructed by projecting (at each step k) the Hamiltonian $\hat{H}^{(k)}$ onto the two lower energy states. Hence at each RG step, we have half of the spins. The renormalized transverse field h_k and magnetic moment μ_k are obtained within this procedure.

7.1.1 Real-space RG for the Dyson hierarchical model

We report here the main ideas and the conceptual steps of the real-space RG approach. For all the details we refer to [487]. We rewrite the Hamiltonian (7.1) as a sum over the generations $k = 0, 1, .., n - 1$

$$\hat{H} = \sum_{k=0}^{n-1} \hat{H}^{(k)} , \tag{7.2}$$

where $\hat{H}^{(k)}$ for $k > 1$ is read off Eq. (7.1), and in particular $k = 0$ is

$$\hat{H}^{(k=0)} = -h \sum_{i=1}^{L} \hat{\sigma}^z_i - \sum_{i=1}^{L/2} J_0[\mu\, \hat{\sigma}^x_{2i-1}][\mu\, \hat{\sigma}^x_{2i}] = \sum_{i}^{L/2} \hat{H}^{(0)}_{2i} . \tag{7.3}$$

The Hamiltonians $\hat{H}^{(0)}_{2i}$ are unrelated and each pair of spins may be diagonalized independently. It is convenient to work in the basis of eigenstates of $\hat{\sigma}^z_i$, i.e. $\hat{\sigma}^z_i|\pm\rangle_{2i} = \pm|\pm\rangle_{2i}$. Then, the four eigenstates and eigenvalues of $\hat{H}^{(0)}_{2i}$ are

$$|\lambda^+_{\rm s/a}\rangle_{2i} = a_1|+\rangle_{2i-1}|+\rangle_{2i} \pm b_1\,|-\rangle_{2i-1}|-\rangle_{2i}\,, \qquad \lambda^+_{\rm s/a} = \mp\sqrt{(J_0\mu^2)^2+4h^2}\,, \tag{7.4a}$$

$$|\lambda^-_{\rm s/a}\rangle_{2i} = \frac{1}{\sqrt{2}}|-\rangle_{2i-1}|+\rangle_{2i} \pm \frac{1}{\sqrt{2}}\,|+\rangle_{2i-1}|-\rangle_{2i}\,, \qquad \lambda^-_{\rm s/a} = \mp J_0\,\mu^2\,, \tag{7.4b}$$

where "s/a" stands for the symmetric and anti-symmetric combination respectively and the coefficients are $a_1 = \sqrt{1/2 + h/\sqrt{(J_0\mu)^2+4h^2}}$, $b_1 = \sqrt{1-a_1^2}$. In the RG approach, we keep only the two lowest energy states $|\lambda^\pm_{\rm s}\rangle_{2i}$. Thus the RG transformation is the projection onto the symmetric subspace. The *renormalised spins* at level $k=1$ are then identified by the basis

$$|\pm\rangle^{[1]}_{2i} \equiv |\lambda^\pm_{\rm s}\rangle_{2i}\,. \tag{7.5}$$

They are related to the physical spins by Eq. (7.4) and are pictorially represented in Figure 7.1 by the green boxes. Hereafter, the superscript $[k]$ always refers to a renormalized spin at level k.

Eq. (7.5) allows us to define the projection operator

$$\hat{P}_1 \equiv \prod_i \hat{P}_{1,\,2i} = \prod_i |+\rangle\langle+|^{[1]}_{2i} + |-\rangle\langle-|^{[1]}_{2i}\,, \tag{7.6}$$

which implements the RG transformation and selects the two lowest energy states of $\hat{H}^{(0)}$. When applied to $\hat{H}^{(0)} + \hat{H}^{(1)}$ in Eqs. (7.2-7.3), the projection gives the renormalised Hamiltonians

$$\hat{H}^{(0)}_R + \hat{H}^{(1)}_R = -\frac{L}{2}e_1\,\hat{P}_1 - h_1\sum_i \hat{\sigma}^{z\,[1]}_{2i} - \sum_{i=1}^{L/4} J^{(1)}[\mu_1\,\hat{\sigma}^{x\,[1]}_{4i-2}][\mu_1\,\hat{\sigma}^{x\,[1]}_{4i}]\,, \tag{7.7}$$

where h_1, μ_1 are the renormalized magnetic field and moment while e_1 is the contribution of the previous generation to the ground state energy. It is then clear that the RG flow should be written in terms of the control parameter

$$K_k \equiv \frac{J_k\;\mu_k^2}{h_k}, \qquad \text{with} \quad K_0 = \frac{J_0\,\mu^2}{h} = \frac{J}{h}\,. \tag{7.8}$$

Hence, at level $k=1$ the renormalised parameter are

$$h_1 = \frac{\lambda^-_{\rm s} - \lambda^+_{\rm s}}{2} = -\frac{2h}{K_0 + \sqrt{K_0^2+4}}\,, \tag{7.9a}$$

$$e_1 = \frac{\lambda^-_{\rm s} + \lambda^+_{\rm s}}{2} = -h\,\frac{K_0+\sqrt{K_0^2+4}}{2}\,, \tag{7.9b}$$

$$\mu_1 = \mu\sqrt{2}\sqrt{1+\frac{K_0}{\sqrt{K_0^2+4}}}\,. \tag{7.9c}$$

In Eq. (7.7) the operators $\sigma_{2i}^{z/x\,[1]}$ are Pauli matrices acting on the renormalised spins at level $k=1$ as $\sigma_{2i}^{z\,[1]}|\pm\rangle_{2i}^{[1]} = \pm|\pm\rangle_{2i}^{[1]}$ and $\sigma_{2i}^{x\,[1]}|\pm\rangle_{2i}^{[1]} = |\mp\rangle_{2i}^{[1]}$. The renormalised Hamiltonian (7.7), besides the projector $\hat{P}_1$, has exactly the same structure of $\hat{H}^{(0)}$ in Eq. (7.3), being a sum of independent two-spin Hamiltonians. Eqs. (7.9) are the renormalization rules for the magnetic field, coupling, and energy.

The diagonalisation and projection transformations (7.4-7.7) are then applied again $n-1$ times on all the terms of the Hamiltonian (7.2). The k-th renormalized spin is the block of 2^k spins at level k. Its basis $|\pm\rangle_i^{[k]}$ is defined recursively as

$$|+\rangle_i^{[k]} = a_{k-1}|++\rangle_i^{[k-1]} + b_{k-1}|--\rangle_i^{[k-1]}\,, \tag{7.10a}$$

$$|-\rangle_i^{[k]} = \frac{1}{\sqrt{2}}|-+\rangle_i^{[k-1]} + \frac{1}{\sqrt{2}}|+-\rangle_i^{[k-1]}\,. \tag{7.10b}$$

Here $|a\,b\rangle_i^{[k-1]}$ stands for the tensor product of two adjacent $(k-1)$-th renormalised spins as $|a\,b\rangle_i^{[k-1]} = |a\rangle_{2i-1}^{[k-1]} \otimes |b\rangle_{2i}^{[k-1]}$. The parameters a_k, b_k are obtained from the diagonalization and read

$$a_k = \frac{1}{\sqrt{2}}\left(1+\frac{2}{\sqrt{K_k^2+4}}\right)^{1/2}\,, \qquad b_k = \frac{1}{\sqrt{2}}\left(1-\frac{2}{\sqrt{K_k^2+4}}\right)^{1/2}\,, \tag{7.11}$$

while the contribution of each projection to the ground state energy is

$$e_k = -h_k\frac{K_k+\sqrt{K_k^2+4}}{2}\,. \tag{7.12}$$

At every step, the renormalisation rules

$$h_{k+1} = \frac{2h_k}{K_k+\sqrt{K_k^2+4}}\,, \qquad \mu_{k+1} = \mu_k\sqrt{2}\sqrt{1+\frac{K_k}{\sqrt{K_k^2+4}}}\,, \tag{7.13}$$

give explicitly the recursion relation for the control parameter (7.8) as

$$K_k = \frac{K_{k-1}}{2^{1+\sigma}}\frac{\left(K_{k-1}+\sqrt{K_{k-1}^2+4}\right)^2}{\sqrt{K_{k-1}^2+4}} \equiv R[K_{k-1}]\,. \tag{7.14}$$

7.1.2 The RG ground state

After renormalisation, the hierarchical Hamiltonian (7.2) becomes

$$\hat{H}_R = -\sum_{k=1}^{n}\frac{L}{2^k}e_k\,\hat{P}_k - h_n\,\hat{\sigma}^{z\,[n]}, \tag{7.15}$$

where e_k is the energy contribution (7.12) of each renormalisation step, $\hat{P}_k$ is the projection operator onto the lowest energy eigenstates at level $k-1$ (i.e. the generalisation of Eq. (7.6)), h_n is the renormalised transverse field (7.13) and $\hat{\sigma}^{z\,[n]}$ is the Pauli matrix at level n. Hereafter, we will not use the subscript for the Pauli matrices

and eigenvectors at level n because there is a single spin at that level. Since $h_n > 0$, the ground state is simply

$$|\psi_{\rm GS}\rangle = |+\rangle^{[n]}, \tag{7.16}$$

and it can be written on the basis of the spins at the previous level using Eq. (7.10) as

$$|\psi_{\rm GS}\rangle = |+\rangle^{[n]} = a_{n-1}|++\rangle_1^{[n-1]} + b_{n-1}\,|--\rangle_1^{[n-1]}\,, \tag{7.17}$$

and the recursively up to writing it in the physical spins at level 0.

Note that not only the Hamiltonian has a binary tree form, but also the RG ground state has the structure of a *tree tensor network* where the isometries have all rank equal to two, see [489–492]. In fact, the transformations of Eq. (7.10) automatically define the isometric tensors in the sense of Ref. [489].

7.1.3 The critical point

The critical point and all the universal exponents are determined from the study of the flow induced by the RG equation (7.14). The critical point $K_c = R[K_c]$ depends on σ. For $\sigma \ll 1$, $K_c \to 0$ (aka h_c diverges) and all the spins align along the z direction. Conversely, for $\sigma \gg 1$, $K_c \to \infty$ (aka $h_c \to 0$). Hence, as in the usual quantum Ising model [69], the critical point separates a ferromagnetic phase, for $h < h_c$ or $K > K_c$, from a paramagnetic one, for $h > h_c$ or $K < K_c$. At the critical point, the ground-state wave function simplifies considerably. Since $K_k = K_c$ for all k, the coefficients of Eq. (7.11) do not depend on k, i.e. $a_k = a\,, b_k = b$ for all k and the recurrence relation (7.17) further simplifies, as we will exploit to calculate the entanglement entropy.

By linearising the flow equation (7.14) close to the fixed point, the critical exponents for the correlation length (ν_σ), correlation function (x_σ), and the dynamical one (z_σ) have been determined [487]. We will be interested in the longitudinal correlation function between two spins at distance r, that at the critical point, behaves as

$$\langle \hat\sigma_i^x\, \hat\sigma_{i+r}^x \rangle \sim \frac{1}{r^{2x_\sigma}}\,, \tag{7.18}$$

where the exponent x_σ is [487]

$$x_\sigma = \frac{1-\sigma}{4} + \frac{\ln(K_c^2+4)}{8\ln 2}\,. \tag{7.19}$$

We mention that in the limit $\sigma \ll 1$, all the critical exponents in [487] reproduce the mean-field results of [427, 428]. For larger σ, they are in good qualitative agreement with the values obtained numerically in a dissipative short-range model in the same universality class of the long-range Ising one [495–497].

7.2 The block entanglement entropy of the hierarchical model

In this section, we present the main results of this paper about the entanglement entropy of the RG ground state of the Dyson hierarchical model at the critical point.

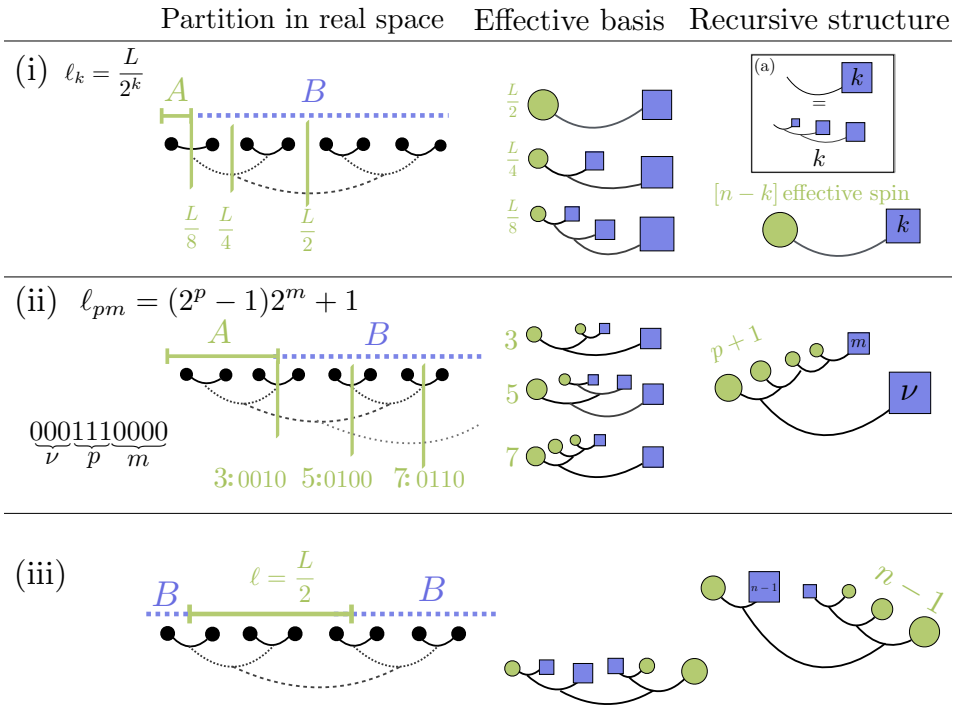

Figure 7.2: The partitions (1-3) of the ground state of the hierarchical model that we consider here. Left column: the partitions in real space. Central column: reduced density matrix in renormalized variables. The green circles indicate the block spins, whose basis is used to write the recursive density matrix. Each of them contributes with a factor two to the size of $\hat{\rho}_A$. Right column: recursive structure of the reduced density matrix. In the inset (a) we introduce the diagram for the recursive trace performed on a block-spin k times. (Top row) Partition (1) with an interval of size $\ell_k = 2^{n-k}$. The reduced density matrix is a 2×2-matrix in the basis of the renormalized spins at $(n-k)$-th level. (Middle) Partition (2) with an interval of length $\ell_{pm} = (2^p - 1)2^m + 1$. The reduced density matrix has effective size $2^{p+1} \times 2^{p+1}$. (Bottom) Partition (3) with an interval of length $\ell = L/2$ shifted by one site from the chain end. This partition always splits n effective spins and the reduced density matrix has size $L \times L$.

We mention that a very large literature exists about the characterisation of the entanglement in many-body systems by real space RG, but its main focus is disordered systems and strong disorder RG, see e.g. Ref.[498–506]. Although the employed techniques are different, there are many qualitative similarities that also helped our understanding of the hierarchical model.

We consider bipartitions of the chain into a block of spins A of length ℓ and the remainder B. The first step will be to reconstruct the reduced density matrix $\hat{\rho}_A$ of the ground state (7.16) as achieved using the recursive projection technique in the previous section. We then calculate the eigenvalues of $\hat{\rho}_A$ and consequently the entanglement entropy S_A, defined in Eq.(1.24). Since local transformations within the subsystems do not alter the entanglement between A and B, we will write $\hat{\rho}_A$ without tracing back all those renormalized spins that are not split by the bipartition: in tree tensor network language [489, 492], this means that all the isometries contained within A do not contribute to the entanglement and cancel

in the construction of the reduced density matrix. The size of the reduced density matrix is then determined by the number of the renormalized spins (7.10) that are split by the bipartition. As a simple example, let A be the block composed of the first $\ell = L/2$ sites. This partition spits only the n-th effective spin at level n, as in the top panel of Figure 7.2 for $k = 1$. Hence, the reduced density matrix $\hat{\rho}_A$ is a 2×2 matrix in the basis $|\pm\rangle_1^{[n-1]}$ and its eigenvalues will never change when rewriting in terms of the spins at lower levels up to the physical spins.

The same reasoning applies to all other kinds of intervals. However, since the model is not translationally invariant, the reduced density matrix depends not only on the length of the subsystems A, but also on its position in the chain. We consider the three following bipartitions as shown in Figure 7.2:

1. the interval of length $\ell_k = L/2^k = 2^{n-k}$ (with $k = 1, \dots n$) starting from left end of the chain as in the top panel of Figure 7.2;

2. the interval of length $\ell_{pm} = (2^p - 1)2^m + 1$ (with $m, p \geq 1$) again starting from left end of the chain as in the central panel of Figure 7.2;

3. the shifted interval of length $\ell = L/2$ starting from the second site of the chain as in the bottom panel of Figure 7.2.

For these three cases, we will construct the reduced density matrix $\hat{\rho}_\ell$ recursively.

The partition (1), as previously discussed for $\ell = L/2$, splits only one renormalised spin at level $n - k$. Hence, the reduced density matrix is conveniently written in the basis at this level when it is again a 2×2 matrix, whose elements will be obtained recursively.

Partition (2) instead cuts $p+1$ effective spins, hence it is a matrix of size $2^{p+1}\times 2^{p+1}$ in the basis given by the tensor product of the effective spins at corresponding levels (see below for details). Consequently the largest possible rank is obtained for $\ell = L/2 - 1$, i.e. $m = 1$ and $p = n - 2$.

The partition (3) is chosen in such a way to have maximum possible rank (as standard in tree tensor networks [489–492]). Indeed, this partition cuts by construction n effective spins and so $\hat{\rho}_A$ is, in principle, a $L \times L$ density matrix.

Numerical and analytical results for the entanglement entropy at criticality will be explicitly obtained in the following subsections for asymptotically large systems and subsystems. The most relevant and surprising result is that the reduced density matrix has always a finite rank (at most equal to 16), even for the case (3) when the rank naively might have been maximal, i.e. L. The natural question at this point is how well the fixed point ground-state entanglement correctly describes the one of the real model, without integrating out the high-energy physics in the renormalization procedure. To this aim, we compare the renormalized entanglement with the exact one. In Figure 7.3 we report the comparison with the data from numerical exact diagonalisation for $L = 16$ and partition (3) (because of the tree structure, the next possible size would be $L = 32$ that is hard to exactly diagonalize; alternatively one can use tree tensor networks to get very accurate estimates for a larger chain, but this is beyond the goal of this paper). We show the comparison for many values of σ. The two curves are qualitatively very similar, although S_A is non-monotonic in σ. While for large and small σ they compare very well, there are quantitative

differences for $\sigma \sim 1$. Most probably this is just a finite size effect and indeed it is remarkable that for such a small value of L, the two curves match so well. In the Figure report also the results from the renormalization group for larger L, showing that the saturation value is much larger for intermediate σ as we shall discuss.

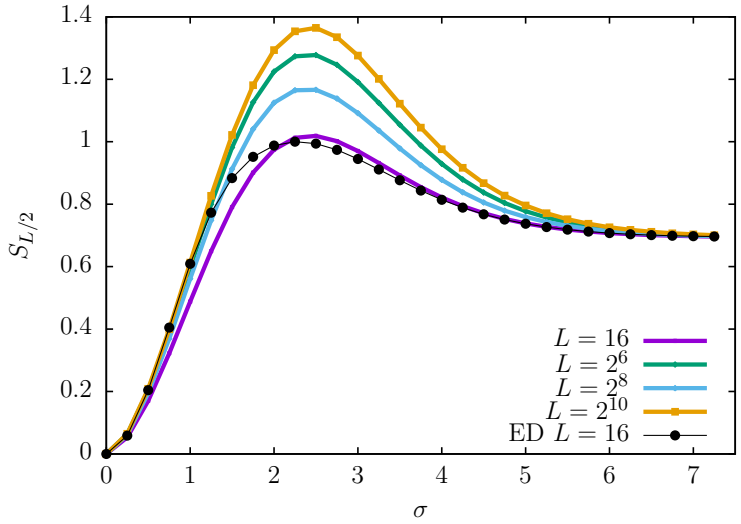

Figure 7.3: Entanglement entropy at the critical point for the partition (3) as a function of σ. S_A is non-monotonic. We compare numerical exact diagonalization results at $L = 16$ with the RG prediction. For intermediate σ, finite size effects are relevant.

Since in the following, we will only consider critical entanglement entropies, to lighten the notations we set $K_c = K$ to indicate the control parameter at the critical point and we set $J = 1$.

7.2.1 Entanglement entropy for the partition (1).

We first consider the reduced density matrix for an interval A of length $\ell_k = 2^{n-k}$ starting from the chain boundary. The partial trace over B (the complement of A, i.e. the last $L-\ell_k$ spins) may be obtained recursively by tracing away half of the spins at each step k times, as shown in the top panel of Figure 7.2. For later convenience, it is useful to define the auxiliary matrices $\hat{\tau}_i^{[k]}$, represented pictorially by the diagram (a) in the inset of Figure 7.2, as

$$\hat{\tau}_0^{[k]} \equiv \mathrm{tr}_B \, |+\rangle\langle+|^{[n]} \,, \quad \hat{\tau}_1^{[k]} \equiv \mathrm{tr}_B \, |-\rangle\langle-|^{[n]} \,, \tag{7.20a}$$

$$\hat{\tau}_2^{[k]} \equiv \mathrm{tr}_B \, |+\rangle\langle-|^{[n]} \,, \quad \hat{\tau}_3^{[k]} \equiv \mathrm{tr}_B \, |-\rangle\langle+|^{[n]} \,, \tag{7.20b}$$

where the states $|\pm\rangle^{[n]}$ are defined in Eq. (7.10). Notice that the k dependence is encoded in B. These matrix can be written explicitly in the basis of the first spin at level $n-k$ (i.e. in the basis $|\pm\rangle_1^{[n-k]}$) by recursion (see E.1) as

$$\hat{\tau}_0^{[k]} = \begin{pmatrix} c_k^+ & 0 \\ 0 & d_k^+ \end{pmatrix} \,, \quad \hat{\tau}_1^{[k]} = \begin{pmatrix} c_k^- & 0 \\ 0 & d_k^- \end{pmatrix} \,, \quad \hat{\tau}_2^{[k]} = \begin{pmatrix} 0 & e_k \\ f_k & 0 \end{pmatrix} \,, \quad \hat{\tau}_3^{[k]} = \left[\hat{\tau}_2^{[k]}\right]^{\mathrm{T}} \,, \tag{7.21}$$

with

$$\begin{cases} c_k^{\pm} = a^2\, c_{k-1}^{\pm} + \dfrac{1}{2}\, d_{k-1}^{\pm} \\ d_k^{\pm} = b^2\, c_{k-1}^{\pm} + \dfrac{1}{2}\, d_{k-1}^{\pm} \end{cases}, \qquad \begin{cases} e_k = \dfrac{a}{\sqrt{2}} e_{k-1} + \dfrac{b}{\sqrt{2}} f_{k-1} \\ f_k = \dfrac{b}{\sqrt{2}} e_{k-1} + \dfrac{a}{\sqrt{2}} f_{k-1} \end{cases}, \tag{7.22}$$

with initial conditions $c_0^+ = 1, d_0^+ = 0, c_0^- = 0, d_0^- = 1, e_0 = 1, f_0 = 0$. Here a, b are the coefficients in Eq. (7.11) evaluated at the critical point $K_k = K$. These recurrence relations admit the exact solution

$$\begin{cases} c_k^+ = \dfrac{1 + 2b^2\, e^{-k\alpha}}{1 + 2b^2} \\ d_k^+ = 2b^2 \dfrac{1 - e^{-k\alpha}}{1 + 2b^2} \end{cases}, \qquad \begin{cases} c_k^- = \dfrac{1 - e^{-k\alpha}}{1 + 2b^2} \\ d_k^- = \dfrac{2b^2 + e^{-k\alpha}}{1 + 2b^2} \end{cases}, \qquad \begin{cases} e_k = \dfrac{1}{2}\left(e^{-\beta k} + e^{-\gamma k}\right) \\ f_k = \dfrac{1}{2}\left(e^{-\beta k} - e^{-\gamma k}\right) \end{cases}, \tag{7.23}$$

with

$$\alpha \equiv \ln \sqrt{K^2 + 4}\,, \qquad \beta \equiv \ln \frac{\sqrt{2}}{a - b}, \qquad \gamma \equiv \ln \frac{\sqrt{2}}{a + b}\,. \tag{7.24}$$

Being the ground state $|\psi\rangle_{\rm GS} = |+\rangle^{[n]}$ as in Eq. (7.16), we just have $\hat{\rho}_A = \hat{\tau}_0^{[k]}$, which is already written in diagonal form. Hence, the exact fixed-point entanglement entropy for this bipartition is

$$S_A = -c_k^+ \ln c_k^+ - d_k^+ \ln d_k^+\,. \tag{7.25}$$

Note that, because of the tree structure of the ground state, S_A is a function only of k and not of k and n separately. For large k we have the exact asymptotic expansion

$$S_A = S_* + c_* e^{-k\alpha} + O(e^{-2k\alpha})\,, \tag{7.26}$$

with

$$S^* = \ln(1 + 2b^2) - \frac{2b^2}{(1 + 2b^2)} \ln 2b^2, \qquad c^* = \frac{2b^2 \ln 2b^2}{1 + 2b^2}. \tag{7.27}$$

Thus, the entanglement entropy saturates to a constant S^*, exponentially fast in k. Since $e^{-k \ln 2} = (\ell_k / L)$, Eq. (7.26) is an expansion for $\ell_k \ll L$.

In Figure 7.4, we plot the asymptotic fixed-point value S_* (7.27) as a function of σ. We also compare it with the exact diagonalisation results for $L = 8$ and $L = 16$ with all possible values of $\ell_k = 1, 2, 4$ and $\ell = 8$ for $L = 16$. Although the size of the system is very small, the results for small ℓ lie very close to the saturation value S^* (expected to be reached for $\ell_k \ll L$, but large L).

7.2.2 Entanglement entropy for the partition (2).

In this subsection, we obtain the renormalised reduced density matrix of the critical ground state (7.16) for a partition of length $\ell_{pm} = (2^p - 1)2^m + 1$. (We can also think to the bipartition as a binary number: the binary representation of $\ell_{pm} - 1$ is just p ones followed by m zeros – we can place $\nu = n - p - m$ zeros in front of it – the result does not depend on ν). The number of effective spins broken by the partition is $p + 1$, as it should be clear also from Figure 7.2. The rules to construct recursively the reduced density matrix are:

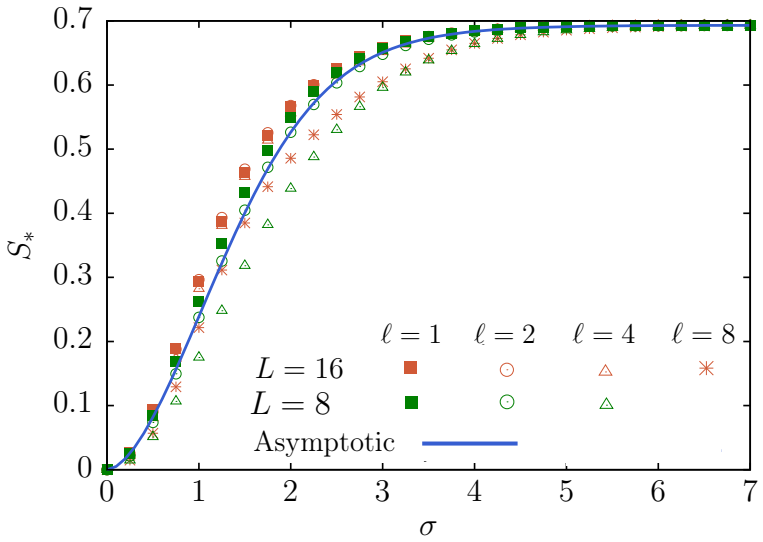

Figure 7.4: Critical entanglement entropy for $\ell_k = 2^{n-k}$ for different values of σ. We compare the results obtained by means of exact diagonalisation for $L = 8$ (green) and 16 (red) with $\ell = 1, 2, 4, 8$ with the asymptotic saturation value of the fixed-point entanglement entropy (7.26) (full line). Although the systems are very small, the results match quite well for $\ell \ll L$.

.

(a) Trace away recursively half of the spins $\nu = n - m - p$ times to get the reduced density matrix $\hat{\rho}_{(a)}$ of the first 2^{p+m} spins. $\hat{\rho}_{(a)}$ is a 2×2 matrix in the basis $|\pm\rangle_1^{[p+m]}$ as in Section 7.2.1.

(b) Trace out the $(m-1)$-th effective spin on the right. $\hat{\rho}_{(b)}$ is a $2^{p+1} \times 2^{p+1}$ matrix in the basis $|\pm\rangle_1^{[m+p-1]} \otimes |\pm\rangle_3^{[m+p-2]} \otimes \cdots \otimes |\pm\rangle_{2^p-1}^{[m]} \otimes |\pm\rangle_{2^{p+1}-1}^{[m-1]}$. This is the reduced density matrix of the first $2^{m+p} - 2^{m-1}$ spins at level zero.

(c) On the rightmost effective spin at level $m-1$, trace out all spins except one at level zero by means of the recurrence relations (7.20). This last step does not increase the size of the reduced density matrix because all involved effective spins have been already broken before. $\hat{\rho}_{(c)}$ is the desired $2^{p+1} \times 2^{p+1}$ density matrix in the basis $|\pm\rangle_1^{[m+p-1]} \otimes |\pm\rangle_3^{[m+p-2]} \otimes \cdots \otimes |\pm\rangle_{2^p-1}^{[m]} \otimes |\pm\rangle_{\ell_{pm}}^{[0]}$.

These three rules are pictorially summarised in Figure 7.5.

As an example, let us consider the case $p = 1$ and $m = 2$, i.e. an interval of length $\ell = 5$ (in a chain of arbitrary size L): $\ell - 1 = 4 \to \ldots 0100$, see also Figure 7.5 (bottom). (a) Compute first the 2×2 reduced density matrix of the first spin at level $p + m = 3$, i.e. $\hat{\rho}_{(a)} = a^2 |+\rangle\langle+|_1^{[3]} + b^2 |-\rangle\langle-|_1^{[3]}$. (b) Trace away the rightmost effective block-spin at level one. This yields the 4×4 matrix $\hat{\rho}_{(b)}$, in the basis $|\pm\rangle_1^{[2]} \otimes |\pm\rangle_3^{[1]}$. (c) Trace out the sixth physical spin from the block spin at level one. Hence $\hat{\rho}_{\ell=5}$ is then a 4×4 matrix in the basis $|\pm\rangle_1^{[2]} \otimes |\pm\rangle_5^{[0]}$.

Step (a) has been already discussed in Section 7.2.1. For the ground state (7.16), Eqs. (7.20-7.21) evaluated at $k = \nu$ read

$$\hat{\rho}_{(a)} = c_\nu^+ \, |+\rangle\langle+|_1^{[p+m]} + d_\nu^+ \, |-\rangle\langle-|_1^{[p+m]} \, , \tag{7.28}$$

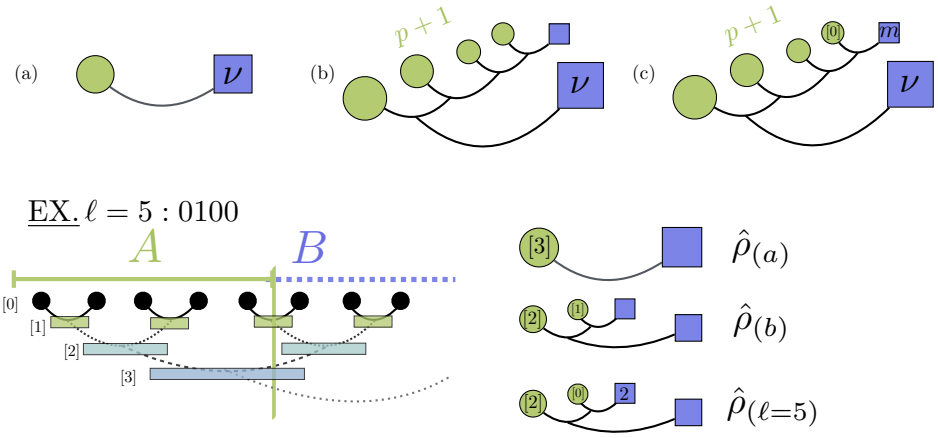

Figure 7.5: Pictorial representation of the construction of the reduced density matrix for the partition (2) of length $\ell_{pm} = (2^p - 1)2^m + 1$. The green circles represent the basis of the reduced density matrix, while the blue squares are the elements over which the trace has been performed. The label $[k]$ inside the green circles indicates that we refer to the k-th effective spin $|\pm\rangle^{[k]}$. (Top) General rules: (a) trace away 2^ν sites, (b) trace away the $(m-1)$-th effective spin on the right, and (c) trace out the remaining $2^m - 1$ physical sites from the last effective spin on the right. (Bottom) Example for $\ell = 5$ (the value of L is irrelevant) discussed in the main text.

where $c_\nu^\pm$ are given in Eq. (7.23). The reduced density matrix is a 2×2 matrix in the basis of the effective spin at level $n - \nu = p + m$.

Now we perform step (b) and construct $\hat\rho_{(b)}$. We trace away the rightmost $(m-1)$-th effective spins from the reduced density matrix in Eq. (7.28). Since the partial trace occurs at level m, it leaves untouched all the p effective spins on the left. The trace of the $(m-1)$-th right effective spin from the m-th yields

$$\begin{aligned}
\hat\rho_0^{[0]} &\equiv \mathrm{tr}_{m-1}\, |+\rangle\langle+|_1^{[m]} = \begin{pmatrix} a^2 & 0 \\ 0 & b^2 \end{pmatrix}, \quad \hat\rho_1^{[0]} \equiv \mathrm{tr}_{m-1}\, |-\rangle\langle-|_1^{[m]} = \frac{1}{2}\begin{pmatrix} 1 & 0 \\ 0 & 1 \end{pmatrix}, \\
\hat\rho_2^{[0]} &\equiv \mathrm{tr}_{m-1}\, |+\rangle\langle-|_1^{[m]} = \frac{1}{\sqrt{2}}\begin{pmatrix} 0 & a \\ b & 0 \end{pmatrix}, \quad \hat\rho_3^{[0]} \equiv \mathrm{tr}_{m-1}\, |-\rangle\langle+|_1^{[m]} = \left(\hat\rho_2^{[0]}\right)^T.
\end{aligned} \tag{7.29}$$

Let us now define for convenience the following matrices for a generic p

$$\begin{aligned}
\hat\rho_0^{[p]} &\equiv \mathrm{tr}_{m-1}\, |+\rangle\langle+|_1^{[p+m]}, \qquad \hat\rho_1^{[p]} \equiv \mathrm{tr}_{m-1}\, |-\rangle\langle-|_1^{[p+m]}, \\
\hat\rho_2^{[p]} &\equiv \mathrm{tr}_{m-1}\, |+\rangle\langle-|_1^{[p+m]}, \qquad \hat\rho_3^{[p]} \equiv \mathrm{tr}_{m-1}\, |-\rangle\langle+|_1^{[p+m]}.
\end{aligned} \tag{7.30}$$

They are obtained recursively as

$$\begin{aligned}
\hat{\rho}_0^{[p]} &= a^2 \begin{pmatrix} 1 & 0 \\ 0 & 0 \end{pmatrix} \otimes \hat{\rho}_0^{[p-1]} + b^2 \begin{pmatrix} 0 & 0 \\ 0 & 1 \end{pmatrix} \otimes \hat{\rho}_1^{[p-1]} + a\,b \begin{pmatrix} 0 & 1 \\ 0 & 0 \end{pmatrix} \otimes \hat{\rho}_2^{[p-1]} + h.c.\,, \\
\hat{\rho}_1^{[p]} &= \frac{1}{2} \begin{pmatrix} 1 & 0 \\ 0 & 0 \end{pmatrix} \otimes \hat{\rho}_1^{[p-1]} + \frac{1}{2} \begin{pmatrix} 0 & 0 \\ 0 & 1 \end{pmatrix} \otimes \hat{\rho}_0^{[p-1]} + \frac{1}{2} \begin{pmatrix} 0 & 1 \\ 0 & 0 \end{pmatrix} \otimes \hat{\rho}_3^{[p-1]} + h.c.\,, \\
\hat{\rho}_2^{[p]} &= \hat{\rho}_3^{[p]\,T} = \frac{a}{\sqrt{2}} \begin{pmatrix} 1 & 0 \\ 0 & 0 \end{pmatrix} \otimes \hat{\rho}_2^{[p-1]} + \frac{a}{\sqrt{2}} \begin{pmatrix} 0 & 1 \\ 0 & 0 \end{pmatrix} \otimes \hat{\rho}_0^{[p-1]} + \frac{b}{\sqrt{2}} \begin{pmatrix} 0 & 0 \\ 0 & 1 \end{pmatrix} \otimes \hat{\rho}_3^{[p-1]} \\
&\quad + \frac{b}{\sqrt{2}} \begin{pmatrix} 0 & 0 \\ 1 & 0 \end{pmatrix} \otimes \hat{\rho}_1^{[p-1]}\,,
\end{aligned} \tag{7.31}$$

with the initial conditions given by Eq. (7.29). At the end of the recursive construction, the reduced density matrix is a $2^{p+1} \times 2^{p+1}$ block-diagonal matrix with symmetric and anti-symmetric components

$$\hat{\rho}_{(b)} = \hat{\rho}_{l_{p1}} = c_\nu^+ \, \hat{\rho}_0^{[p]} + d_\nu^+ \, \hat{\rho}_1^{[p]} = \begin{pmatrix} \hat{\rho}_S^{[p]} & 0 \\ 0 & \hat{\rho}_A^{[p]} \end{pmatrix}\,, \tag{7.32}$$

as it follows from the fact that the Hamiltonian (7.3) is block-diagonal. The $\hat{\rho}_{S/A}^{[p]}$ are $2^p \times 2^p$ matrices given directly in terms of Eqs. (7.23-7.31).

We are ready for the final step (c). The reduced density matrix $\hat{\rho}_{(c)}$ is obtained by tracing away the remaining $2^m - 1$ physical spins from (7.32). This is achieved by means of the procedure (1) applied to the m-th effective spin $|\pm\rangle_{2^{p+1}-1}^{[m]}$. The final reduced density matrix then reads

$$\hat{\rho}_{(c)} = c_\nu^+ \, \hat{\rho}_0^{[p,m]} + d_\nu^+ \, \hat{\rho}_1^{[p,m]}\,, \tag{7.33}$$

where $\hat{\rho}_i^{[p,m]}$ are given by the recurrence relations (7.31) with initial conditions given by $\hat{\rho}_i^{[0,m]} = \hat{\tau}_i^{[m]}$ in Eq. (7.21).

At this point, we have a general recursive form for the reduced density matrix whose elements can be easily constructed. We diagonalize the reduced density matrix (7.33) to yield the entanglement entropy. The results of this procedure are shown in Figure 7.6 for various values of σ. We plot the entanglement entropy as a function of ℓ for several values of p and m (as we stressed, the value of L does not matter at the fixed point). For fixed p, S_A initially grows with m up to a saturation value depending on p. The same trend holds when p is varied at fixed m. The scaling with ℓ approaching its asymptotic value depends on σ. In fact, for small σ the entanglement entropy initially grows quickly and saturates after a given $\ell^*(\sigma)$. This saturation value $\ell^*(\sigma)$ increases as σ gets larger. Conversely, at large σ, we observe a very small growth, roughly compatible with a logarithmic behavior that persists for many decades (more than 15) before saturation. We will get an analytic understanding of this behavior from the expansion at large σ. For fixed ℓ and L, the dependence of the entanglement entropy on σ is very similar to the one in Figure 7.3: starting from zero, it grows with σ up to a maximum and then decreases.

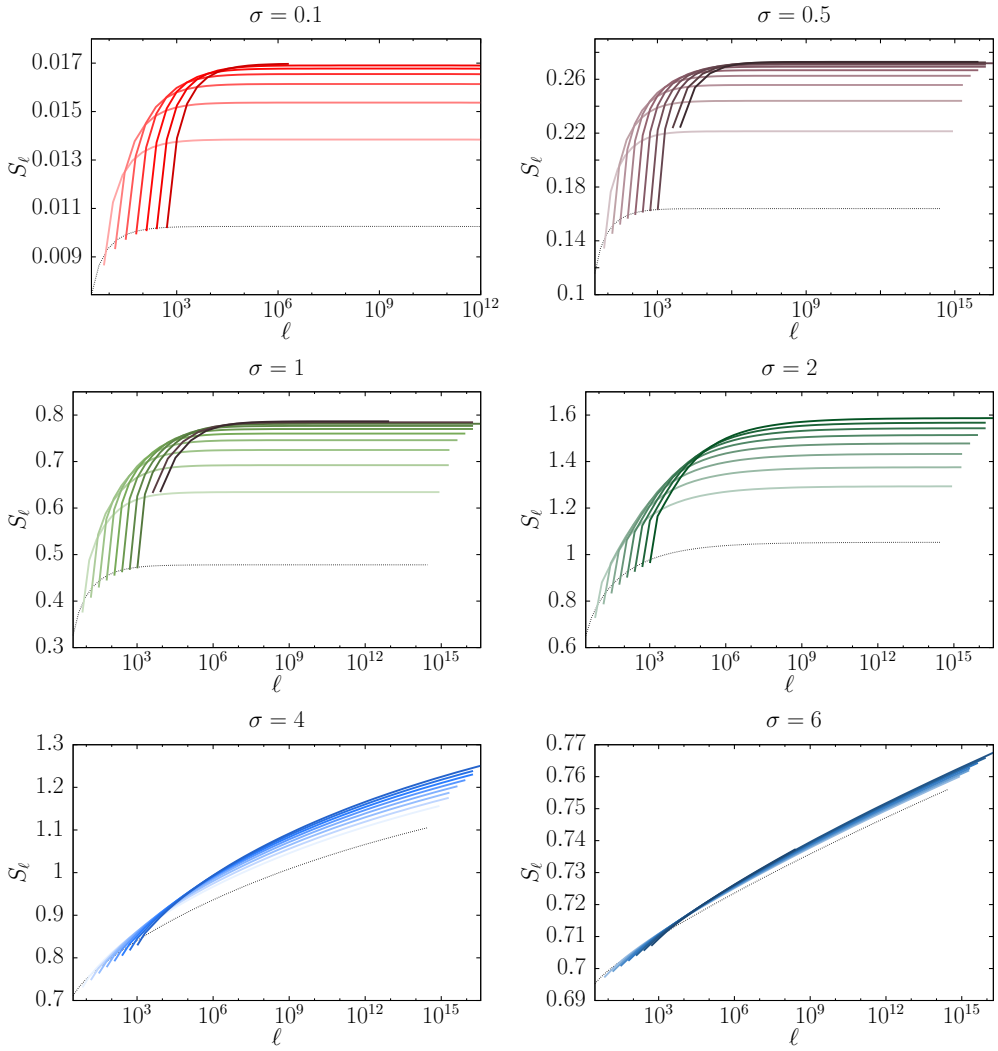

Figure 7.6: Fixed-point entanglement entropy for the partition (2). Each curve in the plot corresponds to a fixed value of p: ℓ_{pm} is changed varying m. Different curves refers to increasing values of $p = 1, \dots, 9$. The dotted black lines correspond to $p = 1$.

Some analytical expansions

We derive an analytical expression of the entanglement entropy in the case $p = 1$, which corresponds to an interval of length $\ell_m = 2^m + 1$. In this case, the reduced density matrix is just a 4×4 density matrix in the basis $|\pm\rangle_1^{[m]} \otimes |\pm\rangle_{\ell_m}^{[0]}$, whose elements are determined recursively via Eq. (7.33). These elements are easily worked out analytically and so are their expansion for $\sigma \ll 1$ and $\sigma \gg 1$. See E.2 for the derivation and the details.

For $\sigma \ll 1$, the critical coupling $K \to 0$, the expansion of the matrix elements (7.33) at order $\mathcal{O}(K^3)$ provides the following asymptotic expression for large ℓ_m

$$S_{\ell_m} = \frac{K^2}{4}\left(1 + \ln\frac{8}{K^2}\right) - \frac{K^2}{16}\frac{1}{\ell_m - 1}\left(\ln\frac{8}{K^2} + \frac{1}{4}\left[\log_2(\ell_m - 1) + 2\right]^2\right) + \mathcal{O}(K^3)\,. \tag{7.34}$$

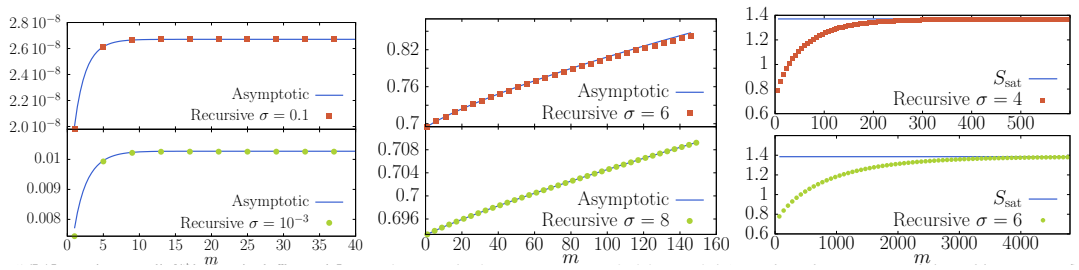

Figure 7.7: Entanglement entropy at the critical point for the partition (2) with $\ell_m = 2^m+1$. We compare the asymptotic expressions with the entanglement entropy obtained from the recursion relations (7.33). (Left) For $\sigma \ll 1$, the entanglement saturates quickly to a constant value in Eq. (7.34). (Center) For $\sigma \gg 1$ and for $m \ll K^2$, tit grows logarithmically with ℓ_m as in Eq. (7.35). (Left) For $\sigma \gg 1$ and for $m \gg K^2$, it saturates to (7.36).

Here we first take the limit of small K and only after large ℓ: the two limits do not commute. The entanglement entropy saturates for large ℓ to a constant value proportional to $K^2 \ln K$. On the left panels of Figure 7.7, we compare the entanglement entropy in Eq. (7.34) with the one from the recurrence relations (7.33), finding a perfect match of the results.

In the opposite limit $\sigma \gg 1$, i.e. for critical coupling $K \to \infty$, we find two different regimes for large ℓ_m. At fixed ℓ_m, for $K^{-1} \ll \ell_m \ll 2^{K^2}$, the entanglement entropy has the following asymptotic expansion

$$S_{\ell_m} = \ln 2 + \frac{\log_2(\ell_m - 1)}{4K^2}\left\{1 - \ln\left[\frac{\log_2(\ell_m - 1)}{4K^2}\right]\right\} + \mathcal{O}\left(K^{-3}, (\log_2 \ell_m)^2 K^{-4}\right) . \tag{7.35}$$

In this regime, the entanglement entropy grows logarithmically with the length of the interval, but with a very small prefactor proportional to K^{-2}, as it was clear already from the data in Figure 7.6. This prediction is checked against the exact data from the recurrence relations in Figure 7.7 (right panels), finding perfect agreement. Furthermore, the results in Figure 7.6 for $\sigma \gg 1$ show that the same logarithmic growth, numerically with the same prefactor, appears for all other lengths with $p \neq 1$, although we do not have an analytic handle on them. It is worth mentioning that this behavior is reminiscent of the standard one for critical short-range systems [102]. However, the right panels of Figure 7.7, show also that the exact data start deviating from this logarithmic scaling for $\ell_m \sim 2^{K^2}$. Indeed, at this value of ℓ_m, saturation toward the asymptotic value starts taking place and Eq. (7.35) fails: in other words the limits $K \to \infty$ and $m \to \infty$ do not commute. In turn, when $\ell_m \gg 2^{K^2}$, the entanglement entropy saturates to

$$S_{\text{sat}} = 2 \ln 2 - \frac{1}{K^2} + \mathcal{O}(K^{-3}) . \tag{7.36}$$

7.2.3 Entanglement entropy for the partition (3).

We now consider the partition (3) as in Figure 7.2 (bottom). This partition cuts n effective spins, giving rise to a $L \times L$ reduced density matrix. The ground-state

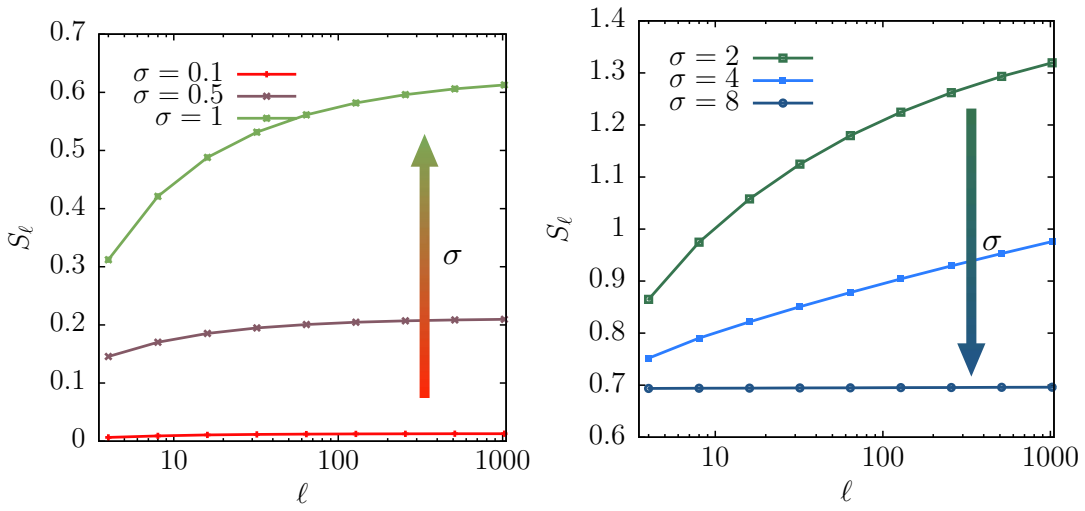

Figure 7.8: Entanglement entropy S_ℓ with the subsystem length ℓ at the critical point with the partition (3). (Left) Results for $\sigma = 0.1, 0.5, 1$. (Right) $\sigma = 2, 4, 8$. For $\sigma \gg 1$, $S_l \sim \ln \ell$ as for the partition (2), as in Figure 7.7.

density matrix can be written as a function of the $(n-1)$-th effective spins as in Eq. (7.17)

$$\hat{\rho}_{\rm GS} = a^2 \, |+\rangle\langle+|_1^{[n-1]} \otimes |+\rangle\langle+|_2^{[n-1]} + b^2 \, |-\rangle\langle-|_1^{[n-1]} \otimes |-\rangle\langle-|_2^{[n-1]} + ab \, |+\rangle\langle-|_1^{[n-1]} \otimes |+\rangle\langle-|_2^{[n-1]} + ab \, |-\rangle\langle+|_1^{[n-1]} \otimes |-\rangle\langle+|_2^{[n-1]} \, , \quad (7.37)$$

where the coefficients a, b are given by Eq. (7.11) We trace away the sub-system A and write the density matrix in the basis represented pictorially by the green circles in Figure 7.2 (bottom-right). This trace over A is relatively simple because it can be performed separately on the first and the second $(n-1)$-th effective spin, see Figure 7.2. On the left, the partial trace is equivalent to the procedure (1) applied to $|\pm\rangle\langle\pm|_1^{[n-1]}$. It results in the 2×2 matrices $\hat{\tau}_i^{[n-1]}$ defined in Eq. (7.20) in the basis $|\pm\rangle_1^{[0]}$ of the first physical spin. On the second block spin, the result obtained from the trace corresponds to Eq. (7.31) with $p = n-2$ in the basis of $|\pm\rangle_{2^{n-1}+2}^{[0]} \otimes |\pm\rangle_{2^{n-2}+2}^{[1]} \otimes \ldots |\pm\rangle_4^{[n-2]}$. Accordingly, the reduced density matrix is

$$\hat{\rho}_A = a^2 \, \hat{\tau}_0^{[n-1]} \otimes \hat{\rho}_0^{[n-2]} + b^2 \, \hat{\tau}_1^{[n-1]} \otimes \hat{\rho}_1^{[n-2]} + ab \, \hat{\tau}_2^{[n-1]} \otimes \hat{\rho}_2^{[n-2]} + ab \, \hat{\tau}_3^{[n-1]} \otimes \hat{\rho}_3^{[n-2]} \, . \quad (7.38)$$

The resulting entanglement entropy reported in Figure 7.8 as a function of $\ell = L/2$ has the same qualitative behavior of the partition (2): it initially grows with the system size and then saturates to a finite value.

For large σ we can make also a more quantitive comparison. We focus on the partition (2) with $m = 1$ and $p = n-2$ in (7.33), i.e. $\ell = L/2 - 1$ which is the choice that scales more similar to the partition of length $\ell = L/2$ considered in this subsection. These two entanglement entropies are compared in Figure 7.9. We have analytic result for partition (2) only for $p = 1$ and in the regime $K^{-1} \ll \ell \ll 2^{K^2}$, when

$$S_\ell = \ln 2 + f(\ell) \, . \quad (7.39)$$

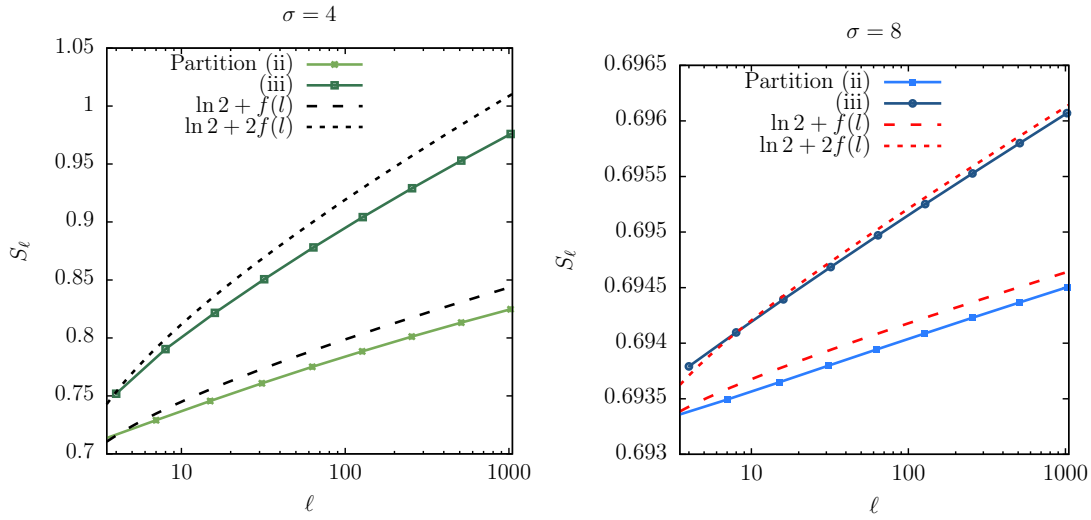

Figure 7.9: Comparison between the entanglement entropy S_ℓ for the partitions (2) and (3), respectively of length $\ell = L/2 - 1$ and $\ell = L/2$, at the critical point for $\sigma \gg 1$. (Left) $\sigma = 4$. (Right) $\sigma = 8$. The full lines are the entanglement entropies obtained from the recursive density matrices (7.33) for $\ell = L/2 - 1$ ($m = 1, p = n - 2$) and (7.38) for $\ell = L/2$. The dashed lines are Eq. (7.39).

with $f(y+1) = (1/4K^2 \ln 2) \ln y \, [1 - \ln(\ln y / 4K^2 \ln 2)]$). We have noticed in Figure 7.6 that the same growth with $f(\ell)$ is approximately valid for all values of p, and indeed also in Figure 7.9 the data for $m = 1$ and $p = n - 2$ are well described by Eq. (7.39). For partition (3), the same form describes very well the data, just multiplying $f(\ell)$ by 2. This factor is likely related to the number of boundaries in the partitions, in analogy to what happens for systems with short-range interaction, also at the critical point [102, 217].

7.2.4 Finite rank reduced density matrix.

We show now by a very elementary argument that the rank of the reduced density matrix is finite. We focus here on the partition (3), but the same reasoning applies to the partition (2) and also others that we did not consider. At criticality the reduced density matrix of partition (3) can always be written from Eq. (7.38) as

$$\hat{\rho}_A = \sum_{i=0}^{3} c_i \, \hat{\tau}_i^{[n-1]} \otimes \hat{\rho}_i^{[n-2]} \, , \tag{7.40}$$

where $\vec{c} = (a^2, b^2, ab, ab)$, $\hat{\tau}_i^{[n-1]}$ are 2×2 matrices, whose coefficients have been determined exactly (cf. Eqs. (7.21-7.23)), and $\hat{\rho}_i^{[n]}$ are defined recursively in Eq. (7.31). The structure of $\hat{\rho}_i^{[n]}$ is such that for all n

$$\text{Rank} \left[\rho_i^{[n]} \right] = 2 \, . \tag{7.41}$$

From the sub-additivity of the rank it follows that $\text{Rank}[\hat{\rho}_A] \leq 16$. For partition (3) this bound can be improved to $\text{Rank}[\hat{\rho}_A] = 8$, but for other partitions is tight. In

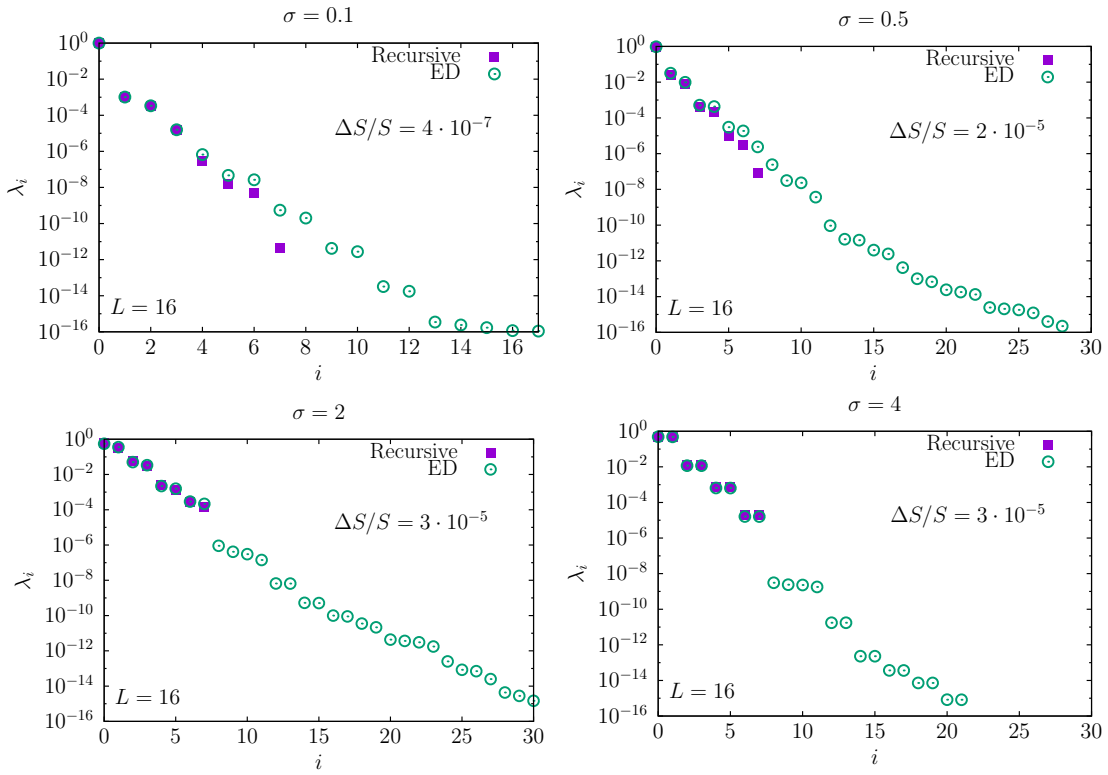

Figure 7.10: Comparison between the entanglement spectrum $\{\lambda_i\}$ obtained by exact diagonalisation and the recursive projection for the partition (3). The data are for $L = 16$. The agreement for the largest eigenvalues is excellent, although the fixed-point RG reduced density matrix has Rank$[\hat{\rho}_A] = 8$ and cannot capture the small one. The relative difference between the exact and RG entanglement entropy is at most of order $\Delta S/S \leq 10^{-5}$.

E.3, we provide a proof of Eq. (7.41) based on linear algebra. An analogous proof might be obtained using tensor networks.

The real-space RG procedure projects the ground state onto a finite entanglement state. In Figure 7.10, we compare the spectrum of the reduced density matrix, i.e. the *entanglement spectrum*, of the fixed-point RG ground state (7.41) to the one computed from the ground state of from exact diagonalization. In the RG procedure, we have only eight non-zero eigenvalues. These match extremely well the largest eigenvalues of the exact reduced density matrix. Consequently, the relative difference between the exact entanglement entropy and the one computed with eight eigenvalues is small for all values of σ and it is at most of order $\Delta S/S \leq 10^{-5}$. This suggests that the portion of the entanglement spectrum not captured by the RG procedure is irrelevant for the exact entanglement entropy in the thermodynamic limit.

7.2.5 Power-law decaying correlation functions.

The most striking and surprising aspect of our result is that we have an area law state which supposedly captures power-law correlation functions. This fact is against many common beliefs in the literature. Such peculiar behavior is due to the

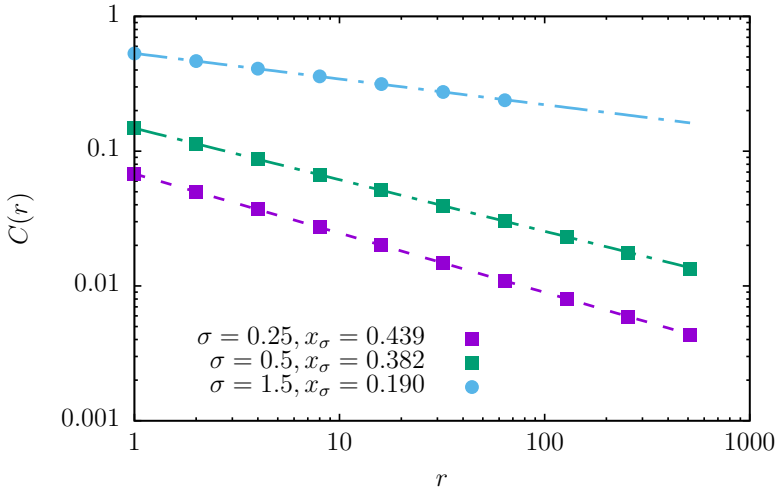

Figure 7.11: Power-law decay of the correlation function for the RG ground state at the critical point. $C(r) \sim r^{-2x_\sigma}$ decays with the critical exponent x_σ predicted by RG (7.19). In the plot, we show $C(r)$ as calculated with the recursive reduced density matrix of the partition (3) and we compare it with the RG algebraic decay (7.19).

hierarchical structure of the ground state and, a fortiori, to the lack of translational invariance. Yet, one can be very suspicious of whether this is really possible. For this reason, from the finite rank reduced density matrix in Eq. (7.40) we reconstruct the two-point correlation function

$$C(r) \equiv \langle \hat{\sigma}^x_{\frac{L}{2}+1} \hat{\sigma}^x_{\frac{L}{2}+1+r} \rangle = \mathrm{Tr}\left[\hat{\rho}_{\frac{L}{2}} \; \hat{\sigma}^x_{\frac{L}{2}+1} \hat{\sigma}^x_{\frac{L}{2}+1+r} \right] \; , \tag{7.42}$$

that at the critical point should scale as $C(r) \sim r^{-2\,x_\sigma}$, with exponent given in Eq. (7.19). We test this behavior numerically on the fixed-point reduced density matrix obtained recursively. The i-th physical spin is equally correlated with all the physical spins belonging to the same block and hence, we evaluate the correlation function between effective spins at distance $r = 2^k$, being the reduced density matrix (7.40) written in the basis of the k-th effective spins. The resulting correlation function is reported in Figure 7.11 and displays the expected power-law decay with exponent x_σ predicted analytically by RG (7.19).

7.3 Conclusions and perspectives

In this chapter, we presented a detailed RG analysis of the ground-state entanglement entropy of a spin-block in the quantum Dyson hierarchical model. Our main goal was to get an analytical insight into the entanglement of long-range interacting spin systems beyond mean-field approximation. We found, surprisingly, that entanglement entropy obeys the area law also at criticality when correlation functions decay algebraically. This peculiar behavior is due to the particular simple structure of the RG ground state: it is a tree tensor network with finite bond dimension and hence it has a finite-rank reduced density matrix. We must mention that unusual scalings of the entanglement in critical (but non-conformal) ground states have been

already observed in other models [402, 407, 507–509], and so our results represent yet another example of anomalous scaling in the absence of conformal invariance. Although it is unlikely that the true long-range ferromagnetic Ising model obeys the area law at criticality, it is desirable to check this expectation from direct numerical simulations.

Because of its simplicity, the Dyson hierarchical Hamiltonian is an interesting playground to explore also other entanglement properties of long-range interacting spin chains. For example, it would be worthy to characterise better the simple structure of this RG state as a tree tensor network, since it undergoes a quantum phase transition with finite entanglement, like those introduced in [510]. It would be interesting also to study the entanglement entropy and negativity between two disjoint blocks (as in [224] for short-range critical systems) to investigate whether there is some form of long-distance entanglement. Finally, the RG approach also gives access to the low-lying excited states and consequently to their entanglement. In the short-range models, the entanglement of low-lying states captures many interesting physical features (see, e.g., [511]) and it is natural to wonder whether the same is true for long-range systems.

Finally, questions about the real-time dynamics of long-range systems can in principle be addressed using this model. As such, we will leave this study for future work.

Chapter 8

Multipartite entanglement structure of chaotic eigenstates

This chapter shows how the multipartite entanglement structure of chaotic eigenstates can shed new light on the eigenstates thermalization hypothesis. By studying the quantum Fisher information of energy eigenstates, we derive a hierarchy in the multipartite entanglement content of thermal states. The analysis is complemented by a numerical example on a non-integrable Hamiltonian.

The most successful framework for understanding thermalization from quantum dynamics is the eigenstate thermalization hypothesis, introduced in detail in Section 1.1.2. As we argued, whenever the ETH is satisfied, it is difficult to contrast the coherence of a pure state with that of a statistical mixture using standard measurements. Therefore, a question that naturally comes to mind is: will pure state dynamics possess detectable features beyond thermal noise? This question posed recently by Kitaev [147] in the context of black-hole physics, lead him to suggest the study of the peculiar out-of-time-order correlations (see Section 1.2.4), originally introduced by Larkin and Ovchinikov [160]. This object, as a result of a nested time structure, detects quantum chaos and correlations beyond thermal ones [56, 512]. As discussed throughout the thesis, despite its promising features, the interpretation of the connection between the OTOC and the underlying quantum state dynamics is, in general, complex.

The purpose of this chapter is to show that the task of discriminating a pure state that "looks" thermal from a true, thermal Gibbs density matrix might be better achieved by a different physical quantity: the quantum Fisher information, introduced in Section 1.2.3. The first observation of this chapter is that the QFI computed in the eigenstates of the Hamiltonian $\mathcal{F}_{\text{ETH}}$ (or in the asymptotic state of a quenched dynamics), and the one computed in the Gibbs state at the corresponding inverse temperature β, $\mathcal{F}_{\text{Gibbs}}$ [132, 220], satisfy the inequality $\mathcal{F}_{\text{ETH}} \geq \mathcal{F}_{\text{Gibbs}}$, where the equality holds at zero temperature. By computing both terms, we quantify the difference. The corresponding multipartite entanglement structure, as obtained from the Fisher information densities $f_Q = \mathcal{F}/N$ are in stark contrast. For example, in systems possessing finite temperature phase transitions, we argue that $\mathcal{F}_{\text{ETH}}$ diverges with system size at critical points (implying extensive multipartiteness of

entanglement in the pure state), while it is only finite in the corresponding Gibbs ensemble [132, 220, 513].

The explicit calculation of $\mathcal{F}_{\rm ETH}$ in a non-integrable model is an arduous task as it involves full diagonalization and data processing of off-diagonal matrix elements which exponentially increase with system size. We use state-of-the-art and highly optimized exact diagonalization and data sorting routines to extract the universal features of these off-diagonal matrix elements, to compute the relevant correlation functions and the corresponding QFI densities. We study both $\mathcal{F}_{\rm ETH}$ and $\mathcal{F}_{\rm Gibbs}$ in the XXZ model with integrability breaking staggered field, unravelling the interesting behavior of these quantities.

The rest of the chapter is organized as follows. In Section 8.1, we describe the general setting for the study of multipartite entanglement out-of-equilibrium. Section 8.2 contains the main results, where we contrast the QFI for a chaotic eigenstate with the one of thermal density matrices. In Section 8.2.2, we discuss the numerical evaluation in the XXZ model, while we present a possible scheme to observe the consequences of our result in atomic experiments in Section 8.2.3. We summarize the results and perspectives in Section 8.3. In the following, we refer to the general out-of-equilibrium approach and notations introduced in Section 1.1.

8.1 QFI out-of-equilibrium

Let us consider the dynamics of thermally isolated quantum systems following a quantum quench, like the one outlined in Section 1.1. The system is initialized in a given (possibly mixed) many-body state and is let free to evolve in time under the action of a Hamiltonian $\hat{H}$. In the thermodynamic limit, local observables and correlation functions are expected to attain a stationary value at long times [cf. Eq.(1.5)].

To characterize multipartite entanglement both in the transient and in the stationary state, we now study the QFI (1.34) in such conditions. As we already discussed, in the special case of thermal equilibrium, the QFI can be expressed in terms of a dynamical response function [cf. Eq.(1.47)] [132]. Hence, it would be highly desirable to have a similar expression for a generic non-equilibrium situation. Below, we generalize the result of Ref. [132] to a many-body system subject to a quantum quench, and show that also in this case the QFI can be expressed in terms of a *generalized* response function of the operator $\hat{O}$ generating the phase shift.

In order to obtain this result, let us start by choosing a basis for the initial state that diagonalizes the density matrix $\hat{\rho} = \sum_\alpha p_\alpha |E^0_\alpha\rangle\langle E^0_\alpha|$. If the initial state is a thermal one relative to the initial Hamiltonian $\hat{H}_0$, then $\hat{H}_0|E^0_\alpha\rangle = E^0_\alpha|E^0_\alpha\rangle$ and $p_\alpha = e^{-\beta E^0_\alpha}/Z$ is the standard Gibbs weight. The state is then time evolved with the final Hamiltonian $\hat{H}$, which leads to

$$\hat{\rho}(t) = \sum_\alpha p_\alpha |E^0_\alpha(t)\rangle\langle E^0_\alpha(t)| = \sum_{nm} a_{nm} e^{-i(E_n - E_m)t} |E_n\rangle\langle E_m| \,, \tag{8.1}$$

where $|E^0_\alpha(t)\rangle = e^{-i\hat{H}t}|\lambda_\alpha\rangle$ and $|E_n\rangle$ and E_n are the eigenvectors and eigenvalues of

$\hat{H}$. In particular, $a_{nm} \equiv \sum_\alpha p_\alpha \langle E_n|\lambda_\alpha\rangle\langle\lambda_\alpha|E_m\rangle$. Using Eq. (1.34) we can write the quantum Fisher information at time t as

$$\mathcal{F}(\hat{O}, \hat{\rho}(t)\,) = 2\sum_{\alpha\beta} \frac{(p_\alpha - p_\beta)^2}{p_\alpha + p_\beta} |\langle E^0_\alpha(t)|\hat{O}|E^0_\beta(t)\rangle|^2 \,. \tag{8.2}$$

Focusing now on thermal initial states and using the identity $(p_\alpha - p_\beta)/(p_\alpha + p_\beta) = \tanh[\beta(E^0_\beta - E^0_\alpha)/2]$ it is easy to show that

$$\mathcal{F}(\hat{O}, \hat{\rho}(t)\,) = \frac{4}{\pi}\int_0^{+\infty} d\omega\ \tanh\left[\frac{\beta\omega}{2}\right]\ \tilde{\chi}''(t,\omega)\,, \tag{8.3}$$

where

$$\tilde{\chi}''(t,\omega) = \pi\sum_{\alpha,\beta}(p_\alpha - p_\beta)|\langle E^0_\alpha(t)|\hat{O}|E^0_\beta(t)\rangle|^2\delta(\omega + E^0_\alpha - E^0_\beta)\,.$$

In particular $\tilde{\chi}''(t,\omega) = -\mathrm{Im}[\tilde{\chi}(t,\omega)]$ where the latter is the Fourier transform with respect to τ of the generalized retarded correlation function

$$\tilde{\chi}(t,\tau) = -i\theta(\tau)\mathrm{Tr}\left[\hat{\rho}\,[\hat{\mathcal{O}}(t,\tau), \hat{\mathcal{O}}(t,0)]\right], \tag{8.4}$$

where $\hat{\mathcal{O}}(t,\tau) = e^{i\hat{H}_0\tau}e^{i\hat{H}t}\hat{\mathcal{O}}e^{-i\hat{H}t}e^{-i\hat{H}_0\tau}$.

The previous equations generalize the equilibrium results of Eq.(1.47) to the case of a quantum quench. In the case of thermal equilibrium ($\hat{H}_0 = \hat{H}$), one straightforwardly retrieves the Kubo response function, i.e. $\tilde{\chi}(\tau,0) = \chi_{\hat{O}}(\tau,0) = -i\theta(\tau)\mathrm{Tr}\left[\hat{\rho}\,[\hat{\mathcal{O}}(\tau), \hat{\mathcal{O}}(0)]\right]$: the QFI comes from the imaginary part of the standard response function associated to the phase-shift operator [132].

In the equilibrium case, the validity of the fluctuation-dissipation theorem is crucial. Out-of-equilibrium, this theorem does not always hold and the QFI cannot be generally written as a dynamical susceptibility. However, as we discussed in Appendix A.2, in the case of the thermalizing systems, ETH ensures the validity of the fluctuation-dissipation theorem. As we will illustrate in the next section, this has important consequences on the multipartite entanglement structure of chaotic eigenstates.

Let us now discuss the QFI dynamics when the system is initialized in a *pure* quantum state $|\psi\rangle$. This corresponds to the standard-setting of the quenched dynamics introduced in Section 1.1. Following from the definition in Eq.(1.35), the quantum Fisher information of the time-evolved state $|\psi(t)\rangle = e^{-i\hat{H}t/\hbar}|\psi\rangle$ reads

$$\mathcal{F}(\hat{O}, |\psi(t)\rangle\,) = 4\langle\,\Delta\hat{O}^2(t)\,\rangle\,, \tag{8.5}$$

where $\langle\Delta\,\hat{O}^2(t)\,\rangle = \langle\psi(t)|\hat{O}^2|\psi(t)\rangle - \langle\psi(t)|\,\hat{O}\,|\psi(t)\rangle^2$. Provided that the QFI attains an asymptotic value at long times, then equilibration immediately implies that the infinite time-average (1.6) of Eq.(8.5) reads

$$\overline{\mathcal{F}(\hat{O}, |\psi(t)\rangle\,)} = 4\,\overline{\langle\psi(t)|\Delta^2\hat{O}|\psi(t)\rangle} = \int_{-\infty}^{+\infty}\frac{d\omega}{\pi}S_{\mathrm{DE}}(\omega) \equiv \mathcal{F}_\infty(\hat{O})\,, \tag{8.6}$$

where $S_{\rm DE}(\omega)$ is the Fourier transform with respect to τ of the symmetrized response function $S_{\hat{O}}(\tau) \equiv \langle\{\hat{O}(\tau), \hat{O}(0)\}\rangle - 2\langle\hat{O}(\tau)\rangle\langle\hat{O}(0)\rangle$ evaluated over the diagonal ensemble

$$\hat{\rho}_{\rm DE} = \sum_n |c_n|^2 |E_n\rangle\langle E_n| \qquad \text{with} \quad c_n = \langle\psi|E_n\rangle \,, \tag{8.7}$$

defined in Eq.(1.8). Notice that the asymptotic QFI of a pure state out-of-equilibrium $\mathcal{F}_\infty(\hat{O})$ in Eq.(8.6) is different from the QFI for the diagonal ensemble $\mathcal{F}(\hat{O}, \hat{\rho}_{\rm DE})$, which should be computed from the definition (1.34) for mixed states.

The discussion so far has been general and we only assumed absence of degeneracies. Anyhow, we can now apply the considerations of Section 1.1.1. For a sufficiently chaotic Hamiltonian, typical initial states $|\psi\rangle$ are be such that $|c_n|^2$ can be taken as a narrow distribution around an average energy E, with small fluctuations $\delta E^2/E^2 \sim 1/N$, see also Eq.(1.9). This allows to re-write the QFI of the asymptotic state (8.6) as

$$\mathcal{F}_\infty(\hat{O}) = \mathcal{F}(\hat{O}, |E\rangle) + 4 \left(\frac{\partial \mathcal{O}(E_n)}{\partial E_n}\bigg|_E \right)^2 \delta E^2 \,, \tag{8.8}$$

where $\hat{O}(E_n)$ refers to the microcanonical value of the operator. In this equation, $\mathcal{F}(\hat{O}, |E\rangle) = 4\langle E|\Delta^2\hat{O}|E\rangle$ is the QFI of the eigenstate $|E\rangle$ corresponding to the mean energy E. Therefore, one has that the multipartite entanglement of the asymptotic state for quenched dynamics is always bounded by the contribution of the single eigenstate corresponding to the initial energy.

Eq.(8.8) is derived by evaluating the fluctuations of the operator $\hat{O}$ over the diagonal ensemble

$$\langle\Delta^2\hat{O}\rangle_{\rm DE} = \sum_n |c_n|^2 \, (O_{nn})^2 - \left(\sum_n |c_n|^2 \, O_{nn} \right)^2 \,, \tag{8.9}$$

with a Taylor expansion of diagonal smooth function of the ETH around the mean energy, see e.g. Note 3 in the Appendix A. Substituting back, keeping terms up to $\mathcal{O}(\delta E^2)$ one obtains [17]

$$\langle\Delta^2\hat{O}\rangle_{\rm DE} = \langle E_n|\Delta^2\hat{O}|E_n\rangle + \left(\frac{\partial O}{\partial E_n} \right)^2 \delta^2 E + O(\delta E^4/E^4) \,, \tag{8.10}$$

where $|E_n\rangle$ is the eigenstate corresponding to the mean energy $E = E_n$. The fluctuations of any observable in the diagonal ensemble have essentially two independent contributions, the first coming from fluctuations within each eigenstate and the second from the energy fluctuations. For intensive observables, the second contribution becomes subleading (since $\langle E_n|\Delta^2\hat{O}|E_n\rangle \sim 1$, $\delta^2 E/E^2 \sim 1/N$ and $O' \sim 1$). For extensive observables – relevant for the QFI – these two contributions are of the same order (since $\langle E_n|\Delta^2\hat{O}|E_n\rangle \sim N$, $\delta^2 E/E^2 \sim 1/N$ and $O' \sim N$) and fluctuations between different eigenstates might become relevant.

8.2 QFI within ETH

Let us now contrast the QFI computed on a thermodynamic ensemble with the one of a single energy eigenstate for an operator satisfying ETH. As discussed in Section 1.3, when computed on a canonical Gibbs state with $p_n = e^{-\beta E_n}/Z$, it can be shown that [132]

$$\mathcal{F}_{\text{Gibbs}}(\hat{O}) \equiv \mathcal{F}(\hat{O}, \hat{\rho}_{\text{Gibbs}}) = \frac{2}{\pi}\int_{-\infty}^{+\infty} d\omega \, \tanh\left(\frac{\beta\omega}{2}\right) \chi''_{\hat{O}}(\omega) \, . \tag{8.11}$$

The same result holds in the microcanonical ensemble [1]. If, by contrast, one considers a pure eigenstate at the same temperature, i.e. with energy $E = \text{Tr}(\hat{H}e^{-\beta\hat{H}}/Z)$ compatible with the average energy of a canonical state in the system, the QFI is

$$\mathcal{F}_{\text{ETH}}(\hat{O}) \equiv \mathcal{F}(\hat{O}, |E\rangle) = \frac{2}{\pi}\int_{-\infty}^{+\infty} d\omega \, \coth\left(\frac{\beta\omega}{2}\right) \chi''_{\hat{O}}(\omega) \, , \tag{8.12}$$

where $S_{\hat{O}}(\omega)$ in the previous equation is determined by the function $f_{\hat{O}}(E,\omega)$ appearing in the ETH fluctuation dissipation relations Eq. (1.15) as described. Since $S_{\hat{O}}(\omega)$ evaluated explicitly from ETH is equivalent to its canonical counterpart, then the following result holds

$$\mathcal{F}_{\text{ETH}}(\hat{O}) \geq \mathcal{F}_{\text{Gibbs}}(\hat{O}) \, . \tag{8.13}$$

Notice that the variance over the Gibbs ensemble, that already bounds the corresponding QFI through Eq.(1.38), also bounds from above $\mathcal{F}_{\text{ETH}}$, as discussed below.

This analysis has immediate consequences for the QFI and the entanglement structure, of asymptotic states in out-of-equilibrium unitary dynamics.
As shown in the previous section, the asymptotic value of the QFI out-of-equilibrium is given by the variance of $\hat{O}$ over the diagonal ensemble which is different from the QFI computed on the state $\hat{\rho}_{\text{DE}}$, i.e. Eq.(1.34). Furthermore, using the expression for generic chaotic states, we found Eq.(8.8), namely that the asymptotic QFI is bounded by the ETH result. This observation, together with the bound (8.13), leads to

$$\mathcal{F}_{\infty}(\hat{O}) \geq \mathcal{F}_{\text{ETH}}(\hat{O}) \geq \mathcal{F}_{\text{Gibbs}}(\hat{O}) \, , \tag{8.14}$$

where the equality holds in the low temperature limit $T \to 0$. This also implies that $4\langle\Delta\hat{O}^2\rangle_{\text{Gibbs}} \geq \mathcal{F}_{\text{ETH}}(\hat{O})$ [2]. These expressions set a hierarchy in the entanglement content of "thermal states" at the same temperature, yet of different nature

[1] Since the definition (1.38) applies to both the microcanonical (MC) and the canonical Gibbs ensembles, if the energy width of the two coincides, then the QFI's are the same and given exactly by Eq.(8.11). This can be easily seen using ETH. From now on we assume equivalence of ensembles, otherwise only the microcanonical result should be considered.

[2] Since in standard thermodynamics energy fluctuations are small $\delta E^2_{\text{Gibbs}}/E^2_{\text{Gibbs}} \sim 1/N$, the same expansion around the average energy $E = \text{Tr}(\hat{\rho}_{\text{Gibbs}}\hat{O})$ done for the diagonal ensemble can be performed for $\langle\Delta\hat{O}^2\rangle_{\text{Gibbs}} = \text{Tr}(\hat{\rho}_{\text{Gibbs}}\hat{O}^2) - \text{Tr}(\hat{\rho}_{\text{Gibbs}}\hat{O})^2$, therefore $\langle\Delta\hat{O}^2\rangle_{\text{Gibbs}} \geq \langle E|\Delta\hat{O}^2|E\rangle$.

(mixed/pure). Although expectation values and fluctuations of an observable computed in the context of ETH are indistinguishable from the canonical predictions, the entanglement structure in the two ensembles is strongly different. Furthermore, we can state that the quantum Fisher information, evaluated in the context of ETH, is a quantity that can distinguish correlations beyond thermal noise by local measurements. As mentioned in the introduction, this was a motivating factor for Kitaev to introduce the OTOC correlation function [147]. Furthermore, via Eqs. (8.11)-(8.12), one can quantify this difference via

$$\Delta\mathcal{F} = \mathcal{F}_{\text{ETH}} - \mathcal{F}_{\text{Gibbs}} = \frac{1}{\pi}\int d\omega \frac{S_{\hat{O}}(\omega)}{\cosh^2(\beta\omega/2)} \,. \tag{8.15}$$

8.2.1 Multipartite entanglement at thermal criticality

The major difference between the ETH and Gibbs multipartite entanglement can be appreciated at critical points of thermal phase transitions, where $\hat{O}$ in (1.38) is the order parameter of the theory. While it is well known that the QFI does not witness divergence of multipartiteness at thermal criticality, i.e. $\mathcal{F}_{\text{Gibbs}}/N \sim$ const. [132, 220], on the other hand, the ETH result obeys the following critical scaling with the system size N

$$f_Q^{\text{ETH}} \sim \frac{\mathcal{F}_{\text{ETH}}}{N} \sim N^{\gamma/(\nu\, d)} \,, \tag{8.16}$$

where γ and ν are the critical exponents of susceptibility and correlation length of the thermal phase transition respectively and d is the dimensionality of the system [219].

8.2.2 Numerical example

We now turn to the numerical evaluation of Eq.(8.14) in the context of a physical system with a microscopic Hamiltonian description. Consider the anisotropic spin-1/2 Heisenberg chain, also known as the spin-1/2 XXZ chain, with the Hamiltonian given by ($\hbar = 1$)

$$\hat{H}_{\text{XXZ}} = \sum_{i=1}^{N-1} \left[\left(\hat{\sigma}_i^x \hat{\sigma}_{i+1}^x + \hat{\sigma}_i^y \hat{\sigma}_{i+1}^y \right) + \Delta\, \hat{\sigma}_i^z \hat{\sigma}_{i+1}^z \right] , \tag{8.17}$$

where $\hat{\sigma}_i^\nu$, $\nu = x, y, z$, correspond to Pauli matrices in the ν direction at site i in a one-dimensional lattice with N sites defined with open boundary conditions (OBCs). In Eq. (8.17), Δ corresponds to the anisotropy parameter. The spin-$\frac{1}{2}$ XXZ chain corresponds to one of the canonical integrable models. We now add a strong integrability breaking perturbation in the form of a staggered magnetic field across the chain, with the Hamiltonian defined as

$$\hat{H}_{\text{SF}} = \hat{H}_{\text{XXZ}} + b \sum_{i\ \text{even}} \hat{\sigma}_i^z, \tag{8.18}$$

where b is the strength of the staggered magnetic field. Eq. (8.18) is the Hamiltonian of the *staggered field* model. This model is quantum chaotic with Wigner-Dyson

level spacing statistics and diffusive transport [514]. The models described before commute with the total magnetization operator in the z direction, $[\hat{H}_{\mathrm{XXZ}}, \sum_i \hat{\sigma}_i^z] = [\hat{H}_{\mathrm{SF}}, \sum_i \hat{\sigma}_i^z] = 0$ and are, therefore, $U(1)$-symmetric. Even with OBCs, parity symmetry is present in the system. We break this symmetry by adding a small perturbation $\delta\hat{\sigma}_1^z$ on the first site. To evaluate our results in the canonical ensemble and in the context of ETH, we proceed with the full diagonalization of $\hat{H}_{\mathrm{SF}}$ in the largest $U(1)$ sector, in which $\sum_i \langle\hat{\sigma}_i^z\rangle = 0$. We focus on the total staggered magnetization $\hat{O} = \sum_i (-1)^i \hat{\sigma}_i^z$ as our extensive observable, and compute all the matrix elements of $\hat{O}$ in the eigenbasis of the Hamiltonian $\hat{H}_{\mathrm{SF}}$ (see Figure A.1 (left) in the Appendix A.1 for an evaluation on a local, non-extensive observable).

Our starting point is to evaluate the expectation value of $\hat{O}$ in the canonical ensemble and compare it with the ETH prediction. In the thermodynamic limit, a single eigenstate $|E\rangle$ with energy E suffices to obtain the canonical prediction: $\langle\hat{O}\rangle = \langle E|\hat{O}|E\rangle = \mathrm{Tr}(\hat{O}\, e^{-\beta\hat{H}})/Z$, with an inverse temperature β that yields an average energy E. For finite-size systems, we instead focus on a small energy window centred around E of width 0.1ϵ to average eigenstate fluctuations, where ϵ is the bandwidth of the Hamiltonian for a given N. The results are illustrated in Figure A.1 (right) of the Appendix A.1, showing $\langle\hat{O}\rangle$ as a function of temperature for two different system sizes, including $N = 20$, the largest system we have access to (Hilbert space dimension $\mathcal{D} = N!/[(N/2)!(N/2)!] = 184\ 756$). The results exhibit the expected behavior predicted from ETH for finite-size systems: the thermal expectation value is well approximated away from the edges of the spectrum (low temperature, section highlighted in grey on Fig. A.1), and the canonical expectation value is better approximated as the system size increases.

We now turn to the evaluation of $\mathcal{F}_{\mathrm{ETH}}$ and $\mathcal{F}_{\mathrm{Gibbs}}$. The task requires to either compute $S_{\hat{O}}(E,\omega)$ or $\chi''_{\hat{O}}(E,\omega)$ in each respective framework. For the former, in the context of ETH, we can employ the ETH result for the response functions [cf. Eq. (1.15)], i.e.

$$\chi''_{\hat{O}}(\omega) \approx 2\pi \sinh(\beta\omega/2)\, |f_{\hat{O}}(E,\omega)|^2 ,$$
$$S_{\hat{O}}(\omega) \approx 4\pi \cosh(\beta\omega/2)\, |f_{\hat{O}}(E,\omega)|^2 .$$

As before, we focus on a small window of energies and extract all the relevant off-diagonal elements of $\hat{O}$ in the eigenbasis of $\hat{H}_{\mathrm{SF}}$. Fluctuations are then accounted for by computing a bin average over small windows $\delta\omega$, chosen such that the resulting average produces a smooth curve.

Let us now describe how to extract numerically $e^{-S(E)/2} f_{\hat{O}}(E,\omega)$ [66, 515]. This is done by computing the binned average of the samples, using small frequency windows $\delta\omega$. The size of these windows is selected such that a smooth curve is obtained from the average and the resulting function is not sensitive to the particular choice of $\delta\omega$. This window of frequencies typically changes depending on the dimension of the magnetization subsector studied in our spin model [515]. In Figure 8.1, we present the absolute value of the off-diagonal elements of both the local magnetization operator in the middle of the chain and the total staggered magnetization. These matrix elements were computed for $T = 5$, $N = 18$ and an energy window of width 0.1ϵ. The smooth black lines shown are binned averages for each

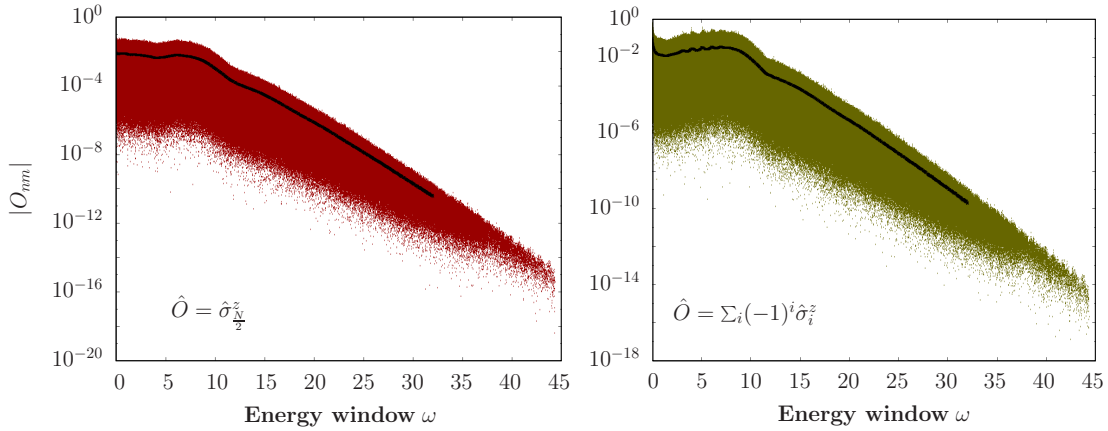

Figure 8.1: Absolute value of the off-diagonal elements in the energy eigenbasis of the local magnetization in the middle of the chain (left) and the total staggered magnetization (right) as a function of ω for $T = 5$ and $N = 18$. The black lines correspond to binned averages.

corresponding observable. This average corresponds to $e^{-S(\bar{E})/2} f_{\hat{O}}(\bar{E}, \omega)$ up to a constant factor that can, in principle, be determined from finite-size scaling. Both this constant factor, however, as well as the entropy term, can be left undetermined in our calculations as they only affect the approximations on correlation functions on only constant values of ω. These correlation functions are defined under physical normalization conditions, allowing us to focus on the main ω dependence of $f_{\hat{O}}(\bar{E}, \omega)$. The binned average of the local observables from Figure 8.1 exhibits the expected exponential decay behavior at high frequencies, which has been observed in previous works [17, 515, 516] and is related to the universal exponential decay of two-point correlation functions in time for chaotic systems with a bounded spectrum [474, 517]. On the opposite side of the spectrum, at low frequencies, $f_{\hat{O}}(\bar{E}, \omega)$ contains important features relevant to the long-time behavior of correlation functions. These frequencies are the most relevant for the response functions used in this work to evaluate the quantum Fisher information in the context of ETH.

The procedure leads to a smooth function $e^{-S(E)/2} f_{\hat{O}}(E, \omega)$, in which the first factor is a constant value with respect to ω. The entropy factor can be left undetermined in our calculations if we normalize the curve by the sum rule shown in Eq. (8.12), computed in this case from the ETH prediction of the expectation value of $\langle \Delta \hat{O}^2 \rangle$. Once the $f_{\hat{O}}(E, \omega)$ is calculated numerically, one can compare the ETH prediction for the response functions and the resulting fluctuations dissipation theorems.

In Figure A.2 of the Appendix, we show $S_{\hat{O}}(\omega)$ for both the canonical ensemble for $T = 5$ and the corresponding ETH prediction normalized by the sum rule mentioned before. The sum rule is evaluated from the expectation values computed within both the canonical ensemble and ETH, correspondingly. It can be observed that the main features of the response function can be well approximated from the corresponding ETH calculation. For this particular case, however, the approximation is only marginally improved by increasing the system size. This behavior is expected given that overall fluctuations for extensive observables carry an extensive

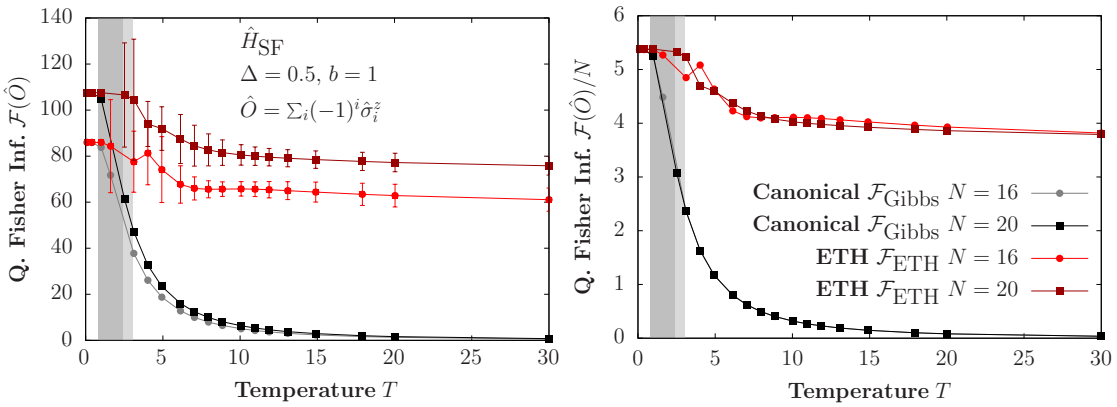

Figure 8.2: The quantum Fisher information and the corresponding density for different system sizes as a function of temperature in both the canonical ensemble ($\mathcal{F}_{\mathrm{Gibbs}}$) and corresponding ETH prediction ($\mathcal{F}_{\mathrm{ETH}}$). At infinite temperature, ETH predicts the presence of multipartite entanglement while there is none in the canonical ensemble.

energy fluctuation contribution, as mentioned before [17]. The previous analysis unravels the agreement between the thermal expectation values of non-equal correlation functions in time and those predicted by ETH. From these results, as $S_{\hat{O}}(\omega)$ (and, consequently, $\chi''_{\hat{O}}(\omega)$ from the FDT) is well approximated by means of ETH, the inequality in Eq. (8.13) is satisfied.

Finally, we compute the QFI for $\hat{O}$ in our model within both contexts: $\mathcal{F}_{\mathrm{ETH}}$ and $\mathcal{F}_{\mathrm{Gibbs}}$. The results are shown in Figure 8.2. The fluctuations in the ETH calculation of $\mathcal{F}_{\mathrm{ETH}}$ are inherited from the fluctuations of the predicted expectation value of $\langle \Delta \hat{O}^2 \rangle$, which, as expected for finite-size systems, decrease away from the edges of the spectrum. Both predictions for the QFI, canonical and ETH, are equivalent at vanishing temperatures. Remarkably, the QFI predicted from ETH is finite at infinite temperature, while the QFI from the canonical ensemble in this regime vanishes.

8.2.3 Experimental consequences

In the following, we discuss a possible scheme to appreciate the consequences of our result experimentally. Since ETH applies to chaotic quantum systems undergoing unitary evolution, then the type of experimental setup would have to be extremely well isolated from the laboratory environment. Specifically one needs the thermalization time $\tau_{th} \ll \tau_\phi$, where τ_ϕ is the coherence time, this condition is routinely achieved in ultra-cold atomic physics. In these experiments, one would prepare a pure state, which could be the ground state of some simulated Hamiltonian. Such a pure state preparation is routinely performed in these setups. A quench is then performed and the state of the system – represented by a density matrix $\rho(t)$ – is a superposition of energy eigenstates with an energy which is conserved in the subsequent evolution. To extract the correct QFI one could try to certify the purity of the state during time evolution following a quench. Performing this procedure beyond full state tomography is challenging. Under these assumptions, the correct

ETH value of the QFI could be obtained by just measuring the fluctuations of observables such as the density.

However, a possible experimental signature could be obtained by an alternative procedure. Consider the time evolution of a generic ergodic many-body system with $\tau_{th} \ll \tau_\phi$. If we let the system evolve up to time t and use $\hat{\rho}(t)$ for *phase estimation purposes* [122], i.e. to estimate an unknown phase ϕ. The accuracy of this protocol $\Delta\phi(t)$ is related to the time-dependent QFI via the quantum Cramer-Rao bound [cf. Eq.(1.32)], i.e. $\Delta\phi(t) \geq 1/\sqrt{M\mathcal{F}(\hat{O}, \hat{\rho}(t))}$, where M is the number of measurements [518]. Our result has direct consequences for $\Delta\phi(t)$ for $t > \tau_{th}$. As long as the state is pure, $\Delta\phi(t)$ will reach a constant value, which is bounded by the ETH result.
In turn, as time t gets beyond τ_ϕ, the maximum accuracy will increasingly degrade, since the state will get progressively mixed and the Gibbs result will hold. It is natural to suspect that in certain conditions, this degradation could be studied in detail. This follows from the fact that, e.g., close to thermal transitions the ETH QFI is diverging while the other stays finite. This might be hard to check experimentally, but a priori it is possible and it would yield a very interesting proof of principle.

8.3 Conclusions

We have shown that the QFI detects the difference between a pure state satisfying ETH and the Gibbs ensemble at the corresponding temperature. It would be interesting to extend these results to integrable systems, described by the generalized Gibbs ensemble. Even though it is expected that global observables could be sensitive to the difference between pure states and the Gibbs ensemble [519], several operators including the sum of local ones and the non-local entanglement entropy appear to coincide at the leading order with the thermodynamic values when ETH is applied [225, 248, 249, 519, 520], as discussed in Section 1.3.2. Here, the difference between ETH/Gibbs multipartite entanglement, which can be macroscopic in the proximity of a thermal phase transition, is observed numerically in an XXZ chain with integrability breaking term, when the temperature grows toward infinity. The consequences of this could be observed in an ion trap and cold-atom experiments via phase estimation protocols on pure state preparations evolved beyond the coherence time. Our result suggests that although at a local level all thermal states look the same, a quantum information perspective indicates that there are many ways to be thermal.

Chapter 9

Future directions

The research of the present thesis leads to a number of problems that one may be interested in pursuing.

The first question concerns the fate of the dynamics of long-range interacting systems (with $\alpha \leq d$) at infinite times. One of the main results of the thesis is the existence of a long-time regime where such systems remain trapped close to the Dicke manifold. Therefore, it is natural to wonder whether this is just an intermediate regime or if it is reflected in the system spectral properties. In particular, one might expect a quantum scars picture underlying the slow dynamics of long-range systems.

Secondly, a new and exciting chapter is opening in the study of thermalization, focused on the distribution of the non-diagonal matrix elements of physical operators. On one side, recent numerical studies have shown that single matrix elements are compatible with a gaussian distribution [514, 521, 522]. Nevertheless, more refined indicators show important deviations from random matrix theory [55], consistent with the existence of sensible correlations between the matrix elements [56]. Accordingly, it is important to understand the diverse physical implications of such deviations. These first two issues are the subject of current investigations.

At the same time, we believe that many relevant recent questions in many-body dynamics could be addressed employing the *lovely theory* of semiclassical physics [1].

To begin with, it would be interesting to understand the relation between quantum scarred eigenstates and the large-S limit of their Hamiltonians. Likewise, various recent works have applied classical approaches to the TDVP/MPS manifold at fixed bond dimension [335, 379, 380]. Yet, it is still not clear how to interpret quantum fluctuations on top of the reduced MPS states, hence their *semi*-classics.

One of the most intriguing puzzles of recent years regards the low-temperature physics of the SYK model. One may try to interpret the bound to chaos with semiclassical approaches, as a cutoff to the Lyapunov spectrum imposed by the quantum fluctuations.

[1] See Chapter 2.

Acknowledgments

I would like to conclude this thesis trying to express my gratitude to the people that have accompanied me in the last four years.

First of all, I wish to thank my supervisors for making my PhD an incredibly rich experience from the scientific and human point of view, providing me with continuous supervision, support, and freedom. I thank professor Alessandro Silva for sharing the genuine excitement about physics discoveries and for his positivity and constant trust. A big part of the confidence and optimism I learned during these years I owe to him. I deeply thank professor Rosario Fazio for being present whenever I needed a word or suggestion, both when it came to science or about the future. More importantly, he has taught me how to follow my inclinations and thoughts, yet always emphasizing the importance of depth, rigor, and focus. I think I started to understand many of the conversations we have had only recently, and for those, I am truly grateful to him.

Secondly, I should thank all the collaborators with whom I had the pleasure to work with. I owe a huge part of the knowledge I acquired during these years to professor Anatoli Polkovnikov, who I thank for hosting me during my research stay in Boston and, more broadly, for his generosity in science and beyond. I would like to thank professor Giorgio Parisi, for his inestimable continuous mentorship over the past years and for revealing me that "science is a nocturnal fire on an undiscovered island". It has been a privilege to learn from professor Pasquale Calabrese, who I thank for teaching me that discipline and respect for others are compulsory ingredients in science. I would also like to thank professor John Goold, a real friend before being a collaborator, whose enthusiasm and intuitions have been a guide since our first chat four years ago. I conclude this list by thanking Alessio Lerose, with whom I shared the most fulfilling work, the adventures, the mistakes, and the thrill.

More generally, I am sincerely grateful to all the colleagues spread around the world with whom I had the chance to share stimulating and valuable discussions, and to the Condensed Matter and Statistical Physics groups in SISSA and ICTP, who have contributed to creating such a lively and inspiring workplace in Trieste, most probably unique.

Work never comes by itself. I am truly grateful to my parents Claudia and Francesco, to my brother Giovanni and all my friends who have been preciously close to me during these years. My final thank goes to Xhek, è *la voce a te dovuta*.

This thesis is dedicated to Serena, whose love, bravery and sincerity have been, and will be, the greatest example to follow.

Bibliography

[1] S. Pappalardi, A. Russomanno, A. Silva, and R. Fazio*Multipartite entanglement after a quantum quench*, Journal of Statistical Mechanics: Theory and Experiment **2017**, 053104 (2017).

[2] S. Pappalardi, A. Russomanno, B. Žunkovič, F. Iemini, A. Silva, and R. Fazio, *Scrambling and entanglement spreading in long-range spin chains*, Phys. Rev. B **98**, 134303 (2018).

[3] S. Pappalardi, P. Calabrese, and G. Parisi, *Entanglement entropy of the long-range Dyson hierarchical model*, Journal of Statistical Mechanics: Theory and Experiment **2019**, 073102 (2019).

[4] A. Lerose and S. Pappalardi, *Origin of the slow growth of entanglement entropy in long-range interacting spin systems*, Phys. Rev. Res. **2** (2020).

[5] M. Brenes, S. Pappalardi, J. Goold, and A. Silva, *Multipartite Entanglement Structure in the Eigenstate Thermalization Hypothesis*, Phys. Rev. Lett. **124** (2020).

[6] S. Pappalardi, A. Polkovnikov, and A. Silva, *Quantum echo dynamics in the Sherrington-Kirkpatrick model*, SciPost Physics **9** (2020).

[7] A. Lerose and S. Pappalardi, *Bridging entanglement dynamics and chaos in semiclassical systems*, Phys. Rev. A **102**, 032404 (2020).

[8] L. Boltzmann, *Weitere studien über das wärmegleichgewicht unter gasmolekülen. Sitzungsberichte der Akademie der Wissenschaften 66 (1872), 275–370. Translation: Further studies on the thermal equilibrium of gas molecules*, Kinetic Theory **2**, 88174 (1964).

[9] M. J. Klein, *The development of Boltzmann's statistical ideas* (Springer, 1973).

[10] T. Kinoshita, T. Wenger, and D. S. Weiss, *A quantum Newton's cradle*, Nature **440**, 900 (2006).

[11] M. Lewenstein, A. Sanpera, V. Ahufinger, B. Damski, A. Sen(De), and U. Sen, *Ultracold atomic gases in optical lattices: mimicking condensed matter physics and beyond*, Advances in Physics **56**, 243 (2007).

[12] I. Bloch, J. Dalibard, and S. Nascimbène, *Quantum simulations with ultracold quantum gases*, Nature Physics **8**, 267 (2012).

[13] A. Polkovnikov, K. Sengupta, A. Silva, and M. Vengalattore, *Colloquium: Nonequilibrium dynamics of closed interacting quantum systems*, Rev. Mod. Phys. **83**, 863 (2011).

[14] J. Eisert, M. Friesdorf, and C. Gogolin, *Quantum many-body systems out of equilibrium*, Nature Physics **11**, 124 (2015).

[15] C. Gogolin and J. Eisert, *Equilibration, thermalisation, and the emergence of statistical mechanics in closed quantum systems*, Reports on Progress in Physics **79**, 056001 (2016).

[16] F. Borgonovi, F. Izrailev, L. Santos, and V. Zelevinsky, *Quantum chaos and thermalization in isolated systems of interacting particles*, Physics Reports **626**, 1 (2016).

[17] L. D'Alessio, Y. Kafri, A. Polkovnikov, and M. Rigol, *From quantum chaos and eigenstate thermalization to statistical mechanics and thermodynamics*, Advances in Physics **65**, 239 (2016).

[18] S. Goldstein, D. A. Huse, J. L. Lebowitz, and R. Tumulka, *Thermal Equilibrium of a Macroscopic Quantum System in a Pure State*, Phys. Rev. Lett. **115**, 100402 (2015).

[19] A. Lerose, *Nonequilibrium phenomena in quantum many-body systems with long-range interactions* (SISSA, 2019).

[20] A. del Campo and W. H. Zurek, *Universality of phase transition dynamics: Topological defects from symmetry breaking*, International Journal of Modern Physics A **29**, 1430018 (2014).

[21] A. Chandran, A. Erez, S. S. Gubser, and S. L. Sondhi, *Kibble-Zurek problem: Universality and the scaling limit*, Phys. Rev. B **86** (2012).

[22] M. Grifoni and P. Hänggi, *Driven quantum tunneling*, Physics Reports **304**, 229 (1998).

[23] M. Bukov, L. D'Alessio, and A. Polkovnikov, *Universal high-frequency behavior of periodically driven systems: from dynamical stabilization to Floquet engineering*, Advances in Physics **64**, 139 (2015).

[24] M. Holthaus, *Floquet engineering with quasienergy bands of periodically driven optical lattices*, Journal of Physics B: Atomic, Molecular and Optical Physics **49**, 013001 (2015).

[25] K. Sacha and J. Zakrzewski, *Time crystals: a review*, Reports on Progress in Physics **81**, 016401 (2017).

[26] U. Schneider, L. Hackermüller, J. P. Ronzheimer, S. Will, S. Braun, T. Best, I. Bloch, E. Demler, S. Mandt, D. Rasch, and A. Rosch, *Fermionic transport and out-of-equilibrium dynamics in a homogeneous Hubbard model with ultracold atoms*, Nature Physics **8**, 213 (2012).

[27] S. Langer, F. Heidrich-Meisner, J. Gemmer, I. P. McCulloch, and U. Schollwöck, *Real-time study of diffusive and ballistic transport in spin-12chains using the adaptive time-dependent density matrix renormalization group method*, Phys. Rev. B **79** (2009).

[28] L. F. Santos, *Transport and control in one-dimensional systems*, Journal of Mathematical Physics **50**, 095211 (2009).

[29] E. A. Yuzbashyan, O. Tsyplyatyev, and B. L. Altshuler, *Relaxation and Persistent Oscillations of the Order Parameter in Fermionic Condensates*, Phys. Rev. Lett. **96** (2006).

[30] P. Barmettler, M. Punk, V. Gritsev, E. Demler, and E. Altman, *Relaxation of Antiferromagnetic Order in Spin-1/2Chains Following a Quantum Quench*, Phys. Rev. Lett. **102** (2009).

[31] S. Diehl, A. Tomadin, A. Micheli, R. Fazio, and P. Zoller, *Dynamical Phase Transitions and Instabilities in Open Atomic Many-Body Systems*, Phys. Rev. Lett. **105** (2010).

[32] B. Sciolla and G. Biroli, *Quantum Quenches and Off-Equilibrium Dynamical Transition in the Infinite-Dimensional Bose-Hubbard Model*, Phys. Rev. Lett. **105** (2010).

[33] A. Mitra, *Time Evolution and Dynamical Phase Transitions at a Critical Time in a System of One-Dimensional Bosons after a Quantum Quench*, Phys. Rev. Lett. **109** (2012).

[34] M. Heyl, A. Polkovnikov, and S. Kehrein, *Dynamical Quantum Phase Transitions in the Transverse-Field Ising Model*, Phys. Rev. Lett. **110** (2013).

[35] M. Heyl, *Dynamical quantum phase transitions: a review*, Reports on Progress in Physics **81**, 054001 (2018).

[36] E. H. Lieb and D. W. Robinson, *The finite group velocity of quantum spin systems*, Communications in Mathematical Physics **28**, 251 (1972).

[37] M. L. Mehta, *Random matrices* (Elsevier, 2004).

[38] G. Livan, M. Novaes, and P. Vivo, *Introduction to Random Matrices* (Springer International Publishing, 2018).

[39] L. F. Santos and M. Rigol, *Onset of quantum chaos in one-dimensional bosonic and fermionic systems and its relation to thermalization*, Phys. Rev. E **81** (2010).

[40] L. F. Santos and M. Rigol, *Localization and the effects of symmetries in the thermalization properties of one-dimensional quantum systems*, Phys. Rev. E **82** (2010).

[41] P. Kos, M. Ljubotina, and T. Prosen, *Many-Body Quantum Chaos: Analytic Connection to Random Matrix Theory*, Phys. Rev. X **8**, 021062 (2018).

[42] A. Chan, A. De Luca, and J. T. Chalker, *Solution of a Minimal Model for Many-Body Quantum Chaos*, Phys. Rev. X **8**, 041019 (2018).

[43] J. v. Neumann, *Beweis des Ergodensatzes und desH-Theorems in der neuen Mechanik*, 1, Zeitschrift für Physik , 30 (1929), Translated to English in "European Phys. J. H **35**, 201 (2010)".

[44] M. Srednicki, *The approach to thermal equilibrium in quantized chaotic systems*, Journal of Physics A: Mathematical and General **32**, 1163 (1999).

[45] D. Ruelle, *Statistical mechanics of a one-dimensional lattice gas*, Communications in Mathematical Physics **9**, 267 (1968).

[46] K. Huang, *Statistical physics, 2 ed.* (Wiley, 1987).

[47] A. Campa, T. Dauxois, D. Fanelli, and S. Ruffo, *Physics of long-range interacting systems* (OUP Oxford, 2014).

[48] F. H. L. Essler and M. Fagotti, *Quench dynamics and relaxation in isolated integrable quantum spin chains*, Journal of Statistical Mechanics: Theory and Experiment **2016**, 064002 (2016).

[49] M. Berry and M. Tabor, *Level Clustering in the Regular Spectrum*, Proceedings of the Royal Society of London A: Mathematical, Physical and Engineering Sciences **356**, 375 (1977).

[50] M. V. Berry, *Regular and irregular semiclassical wavefunctions*, Journal of Physics A: Mathematical and General **10**, 2083 (1977).

[51] J. M. Deutsch, *Quantum statistical mechanics in a closed system*, Phys. Rev. A **43**, 2046 (1991).

[52] M. Srednicki, *Chaos and quantum thermalization*, Phys. Rev. E **50**, 888 (1994).

[53] M. Srednicki, *Thermal fluctuations in quantized chaotic systems*, Journal of Physics A: Mathematical and General **29**, L75 (1996).

[54] D. J. Luitz and Y. B. Lev, *Anomalous Thermalization in Ergodic Systems*, Phys. Rev. Lett. **117** (2016).

[55] J. Richter, A. Dymarsky, R. Steinigeweg, and J. Gemmer, *The eigenstate thermalization hypothesis beyond standard indicators: emergence of random-matrix behavior at small frequencies*, arXiv:2007.15070 (2020).

[56] L. Foini and J. Kurchan, *Eigenstate thermalization hypothesis and out of time order correlators*, Phys. Rev. E **99** (2019).

[57] H. Kim, T. N. Ikeda, and D. A. Huse, *Testing whether all eigenstates obey the eigenstate thermalization hypothesis*, Phys. Rev. E **90** (2014), 10.1103/physreve.90.052105.

[58] M. Rigol, V. Dunjko, and M. Olshanii, *Thermalization and its mechanism for generic isolated quantum systems*, Nature **452**, 854 (2008).

[59] H. Bernien, S. Schwartz, A. Keesling, H. Levine, A. Omran, H. Pichler, S. Choi, A. S. Zibrov, M. Endres, M. Greiner, V. Vuletic, and M. D. Lukin, *Probing many-body dynamics on a 51-atom quantum simulator*, Nature **551**, 579 (2017).

[60] C. J. Turner, A. A. Michailidis, D. A. Abanin, M. Serbyn, and Z. Papić, *Weak ergodicity breaking from quantum many-body scars*, Nature Physics **14**, 745 (2018).

[61] S. Moudgalya, N. Regnault, and B. A. Bernevig, *Entanglement of exact excited states of Affleck-Kennedy-Lieb-Tasaki models: Exact results, many-body scars, and violation of the strong eigenstate thermalization hypothesis*, Phys. Rev. B **98** (2018).

[62] M. Schecter and T. Iadecola, *Weak Ergodicity Breaking and Quantum Many-Body Scars in Spin-1 X Y Magnets*, Phys. Rev. Lett. **123**, 147201 (2019).

[63] T. Iadecola and M. Schecter, *Quantum many-body scar states with emergent kinetic constraints and finite-entanglement revivals*, Phys. Rev. B **101** (2020).

[64] K. Lee, R. Melendrez, A. Pal, and H. J. Changlani, *Exact three-colored quantum scars from geometric frustration*, Phys. Rev. B **101** (2020).

[65] D. K. Mark, C.-J. Lin, and O. I. Motrunich, *Unified structure for exact towers of scar states in the AKLT and other models*, arXiv:2001.03839 [cond-mat] (2020).

[66] E. Khatami, G. Pupillo, M. Srednicki, and M. Rigol, *Fluctuation-Dissipation Theorem in an Isolated System of Quantum Dipolar Bosons after a Quench*, Phys. Rev. Lett. **111**, 050403 (2013).

[67] M. Rigol, V. Dunjko, V. Yurovsky, and M. Olshanii, *Relaxation in a Completely Integrable Many-Body Quantum System: AnAb InitioStudy of the Dynamics of the Highly Excited States of 1D Lattice Hard-Core Bosons*, Phys. Rev. Lett. **98** (2007).

[68] J. S. Caux and J. Mossel, *Remarks on the notion of quantum integrability*, Journal of Statistical Mechanics: Theory and Experiment **2011**, P02023 (2011).

[69] S. Sachdev, *Quantum Phase Transitions* (Cambridge University Press, 2009).

[70] B. Sutherland, *Beautiful Models* (World scientific, 2004).

[71] D. A. Abanin, E. Altman, I. Bloch, and M. Serbyn, *Colloquium: Many-body localization, thermalization, and entanglement*, Rev. Mod. Phys. **91** (2019).

[72] P. W. Anderson, *Absence of Diffusion in Certain Random Lattices*, Phys. Rev. **109**, 1492 (1958).

[73] V. Ros, M. Müller, and A. Scardicchio, *Integrals of motion in the many-body localized phase*, Nuclear Physics B **891**, 420 (2015).

[74] D. A. Huse, R. Nandkishore, and V. Oganesyan, *Phenomenology of fully many-body-localized systems*, Phys. Rev. B **90** (2014).

[75] W. D. Roeck and F. Huveneers, *Stability and instability towards delocalization in many-body localization systems*, Phys. Rev. B **95** (2017).

[76] A. Goremykina, R. Vasseur, and M. Serbyn, *Analytically Solvable Renormalization Group for the Many-Body Localization Transition*, Phys. Rev. Lett. **122** (2019).

[77] A. Pal and D. A. Huse, *Many-body localization phase transition*, Phys. Rev. B **82** (2010).

[78] D. J. Luitz, N. Laflorencie, and F. Alet, *Many-body localization edge in the random-field Heisenberg chain*, Phys. Rev. B **91** (2015).

[79] P. Sierant, D. Delande, and J. Zakrzewski, *Thouless Time Analysis of Anderson and Many-Body Localization Transitions*, Phys. Rev. Lett. **124** (2020).

[80] M. Schreiber, S. S. Hodgman, P. Bordia, H. P. Luschen, M. H. Fischer, R. Vosk, E. Altman, U. Schneider, and I. Bloch, *Observation of many-body localization of interacting fermions in a quasirandom optical lattice*, Science **349**, 842 (2015).

[81] J. y. Choi, S. Hild, J. Zeiher, P. Schauss, A. Rubio-Abadal, T. Yefsah, V. Khemani, D. A. Huse, I. Bloch, and C. Gross, *Exploring the many-body localization transition in two dimensions*, Science **352**, 1547 (2016).

[82] J. Smith, A. Lee, P. Richerme, B. Neyenhuis, P. W. Hess, P. Hauke, M. Heyl, D. A. Huse, and C. Monroe, *Many-body localization in a quantum simulator with programmable random disorder*, Nature Physics **12**, 907 (2016).

[83] B. M. McCoy and T. T. Wu, *Two-dimensional Ising field theory in a magnetic field: Breakup of the cut in the two-point function*, Phys. Rev. D **18**, 1259 (1978).

[84] M. Kormos, M. Collura, G. Takács, and P. Calabrese, *Real-time confinement following a quantum quench to a non-integrable model*, Nature Physics **13**, 246 (2016).

[85] F. M. Surace, P. P. Mazza, G. Giudici, A. Lerose, A. Gambassi, and M. Dalmonte, *Lattice Gauge Theories and String Dynamics in Rydberg Atom Quantum Simulators*, Phys. Rev. X **10** (2020).

[86] P. Sala, T. Rakovszky, R. Verresen, M. Knap, and F. Pollmann, *Ergodicity Breaking Arising from Hilbert Space Fragmentation in Dipole-Conserving Hamiltonians*, Phys. Rev. X **10** (2020).

[87] V. Khemani, M. Hermele, and R. Nandkishore, *Localization from Hilbert space shattering: From theory to physical realizations*, Phys. Rev. B **101** (2020).

[88] J. Berges, S. Borsányi, and C. Wetterich, *Prethermalization*, Phys. Rev. Lett. **93** (2004).

[89] C. Kollath, A. M. Läuchli, and E. Altman, *Quench Dynamics and Nonequilibrium Phase Diagram of the Bose-Hubbard Model*, Phys. Rev. Lett. **98** (2007).

[90] M. Marcuzzi, J. Marino, A. Gambassi, and A. Silva, *Prethermalization in a Nonintegrable Quantum Spin Chain after a Quench*, Phys. Rev. Lett. **111** (2013).

[91] B. Bertini, F. H. Essler, S. Groha, and N. J. Robinson, *Prethermalization and Thermalization in Models with Weak Integrability Breaking*, Phys. Rev. Lett. **115** (2015).

[92] D. Abanin, W. D. Roeck, W. W. Ho, and F. Huveneers, *A Rigorous Theory of Many-Body Prethermalization for Periodically Driven and Closed Quantum Systems*, Communications in Mathematical Physics **354**, 809 (2017).

[93] C.-J. Lin and O. I. Motrunich, *Explicit construction of quasiconserved local operator of translationally invariant nonintegrable quantum spin chain in prethermalization*, Phys. Rev. B **96**, 214301 (2017).

[94] T. Mori, T. N. Ikeda, E. Kaminishi, and M. Ueda, *Thermalization and prethermalization in isolated quantum systems: a theoretical overview*, Journal of Physics B: Atomic, Molecular and Optical Physics **51**, 112001 (2018).

[95] A. Michailidis, C. Turner, Z. PapiÄ⊠, D. Abanin, and M. Serbyn, *Slow Quantum Thermalization and Many-Body Revivals from Mixed Phase Space*, Phys. Rev. X **10**, 011055 (2020).

[96] S. Choi, C. J. Turner, H. Pichler, W. W. Ho, A. A. Michailidis, Z. Papić, M. Serbyn, M. D. Lukin, and D. A. Abanin, *Emergent SU(2) Dynamics and Perfect Quantum Many-Body Scars*, Phys. Rev. Lett. **122**, 220603 (2019).

[97] N. Shiraishi and T. Mori, *Systematic Construction of Counterexamples to the Eigenstate Thermalization Hypothesis*, Phys. Rev. Lett. **119**, 030601 (2017).

[98] E. Schrödinger, *Discussion of Probability Relations between Separated Systems*, Mathematical Proceedings of the Cambridge Philosophical Society **31**, 555 (1935).

[99] A. Aspect, P. Grangier, and G. Roger, *Experimental Tests of Realistic Local Theories via Bell's Theorem*, Phys. Rev. Lett. **47**, 460 (1981).

[100] J. S. Bell, *On the einstein podolsky rosen paradox*, Physics Physique Fizika **1**, 195 (1964).

[101] M. Nielsen and I. Chuang, *Quantum computation and quantum information* (2010).

[102] P. Calabrese and J. Cardy, *Evolution of entanglement entropy in one-dimensional systems*, Journal of Statistical Mechanics: Theory and Experiment **2005**, P04010 (2005).

[103] J. I. Latorre, R. Orús, E. Rico, and J. Vidal, *Entanglement entropy in the Lipkin-Meshkov-Glick model*, Phys. Rev. A **71** (2005).

[104] L. Amico, R. Fazio, A. Osterloh, and V. Vedral, *Entanglement in many-body systems*, Rev. Mod. Phys. **80**, 517 (2008).

[105] R. Horodecki, P. Horodecki, M. Horodecki, and K. Horodecki, *Quantum entanglement*, Rev. Mod. Phys. **81**, 865 (2009).

[106] E. Witten, *APS Medal for Exceptional Achievement in Research: Invited article on entanglement properties of quantum field theory*, Rev. Mod. Phys. **90**, 045003 (2018).

[107] S. Ryu and T. Takayanagi, *Aspects of holographic entanglement entropy*, Journal of High Energy Physics **2006**, 045 (2006).

[108] P. Calabrese, J. Cardy, and B. Doyon, *Entanglement entropy in extended quantum systems*, Journal of Physics A: Mathematical and Theoretical **42**, 500301 (2009).

[109] J. Eisert, M. Cramer, and M. B. Plenio, *Colloquium: Area laws for the entanglement entropy*, Rev. Mod. Phys. **82**, 277 (2010).

[110] N. Laflorencie, *Quantum entanglement in condensed matter systems*, Physics Reports **646**, 1 (2016).

[111] R. Horodecki, P. Horodecki, M. Horodecki, and K. Horodecki, *Quantum entanglement*, Rev. Mod. Phys. **81**, 865 (2009).

[112] B. Groisman, S. Popescu, and A. Winter, *Quantum, classical, and total amount of correlations in a quantum state*, Phys. Rev. A **72** (2005).

[113] C. T. Asplund and A. Bernamonti, *Mutual information after a local quench in conformal field theory*, Phys. Rev. D **89** (2014).

[114] V. Alba and P. Calabrese, *Quantum information scrambling after a quantum quench*, Phys. Rev. B **100** (2019).

[115] G. Vidal and R. F. Werner, *Computable measure of entanglement*, Phys. Rev. A **65** (2002).

[116] P. Hosur, X.-L. Qi, D. A. Roberts, and B. Yoshida, *Chaos in quantum channels*, Journal of High Energy Physics (2016), 10.1007/JHEP02(2016)004.

[117] D. Ding, P. Hayden, and M. Walter, *Conditional mutual information of bipartite unitaries and scrambling*, Journal of High Energy Physics **2016** (2016).

[118] C. Sünderhauf, L. Piroli, X.-L. Qi, N. Schuch, and J. I. Cirac, *Quantum chaos in the Brownian SYK model with large finite N : OTOCs and tripartite information*, Journal of High Energy Physics **2019** (2019).

[119] C. W. Helstrom, *Quantum detection and estimation theory*, Journal of Statistical Physics **1**, 231 (1969).

[120] G. Tóth and I. Apellaniz, *Quantum metrology from a quantum information science perspective*, Journal of Physics A: Mathematical and Theoretical **47**, 424006 (2014).

[121] L. Pezze and A. Smerzi, *Quantum theory of phase estimation*, arXiv:1411.5164 (2014).

[122] L. Pezzè, A. Smerzi, M. K. Oberthaler, R. Schmied, and P. Treutlein, *Quantum metrology with nonclassical states of atomic ensembles*, Rev. Mod. Phys. **90** (2018).

[123] S. L. Braunstein and C. M. Caves, *Statistical distance and the geometry of quantum states*, Phys. Rev. Lett. **72**, 3439 (1994).

[124] D. Petz and C. Ghinea, in *Quantum Probability and Related Topics* (World Scientific, 2011).

[125] P. Hyllus, W. Laskowski, R. Krischek, C. Schwemmer, W. Wieczorek, H. Weinfurter, L. Pezzé, and A. Smerzi, *Fisher information and multiparticle entanglement*, Phys. Rev. A **85**, 022321 (2012).

[126] G. Tóth, *Multipartite entanglement and high-precision metrology*, Phys. Rev. A **85**, 022322 (2012).

[127] D. J. Wineland, J. J. Bollinger, W. M. Itano, F. L. Moore, and D. J. Heinzen, *Spin squeezing and reduced quantum noise in spectroscopy*, Phys. Rev. A **46**, R6797 (1992).

[128] D. J. Wineland, J. J. Bollinger, W. M. Itano, and D. J. Heinzen, *Squeezed atomic states and projection noise in spectroscopy*, Phys. Rev. A **50**, 67 (1994).

[129] A. Sorensen, L.-M. Duan, J. I. Cirac, and P. Zoller, *Many-particle entanglement with Bose–Einstein condensates*, Nature **409**, 63 (2001).

[130] J. Ma, X. Wang, C. Sun, and F. Nori, *Quantum spin squeezing*, Physics Reports **509**, 89 (2011).

[131] H. Strobel, W. Muessel, D. Linnemann, T. Zibold, D. B. Hume, L. Pezzè, A. Smerzi, and M. K. Oberthaler, *Fisher information and entanglement of non-Gaussian spin states*, Science **345**, 424 (2014).

[132] P. Hauke, M. Heyl, L. Tagliacozzo, and P. Zoller, *Measuring multipartite entanglement through dynamic susceptibilities*, Nature Physics **12**, 778 (2016).

[133] R. C. de Almeida and P. Hauke, *From entanglement certification with quench dynamics to multipartite entanglement of interacting fermions*, arXiv preprint arXiv:2005.03049 (2020).

[134] A. Holevo, *Probabilistic and statistical aspects of quantum theory*, Vol. 1 (Springer Science & Business Media, 2011).

[135] A. D. Cronin, J. Schmiedmayer, and D. E. Pritchard, *Optics and interferometry with atoms and molecules*, Rev. Mod. Phys. **81**, 1051 (2009).

[136] D. Bures, *An Extension of Kakutani's Theorem on Infinite Product Measures to the Tensor Product of Semifinite w ∗ -Algebras*, Transactions of the American Mathematical Society **135**, 199 (1969).

[137] P. Hyllus, W. Laskowski, R. Krischek, C. Schwemmer, W. Wieczorek, H. Weinfurter, L. Pezzé, and A. Smerzi, *Fisher information and multiparticle entanglement*, Phys. Rev. A **85**, 022321 (2012).

[138] V. Giovannetti, S. Lloyd, and L. Maccone, *Advances in quantum metrology*, Nature Photonics **5**, 222 (2011).

[139] L. Pezzé and A. Smerzi, *Entanglement, Nonlinear Dynamics, and the Heisenberg Limit*, Phys. Rev. Lett. **102**, 100401 (2009).

[140] O. Gühne, G. Tóth, and H. Briegel, *Multipartite entanglement in spin chains*, New Journal of Physics 7, 229 (2005).

[141] L. Pezzè, Y. Li, W. Li, and A. Smerzi, *Witnessing entanglement without entanglement witness operators*, Proceedings of the National Academy of Sciences **113**, 11459 (2016).

[142] L. Pezzè, M. Gabbrielli, L. Lepori, and A. Smerzi, *Multipartite Entanglement in Topological Quantum Phases*, Phys. Rev. Lett. **119** (2017).

[143] L. Pezzè, M. Gabbrielli, L. Lepori, and A. Smerzi, *Multipartite Entanglement in Topological Quantum Phases*, Phys. Rev. Lett. **119**, 250401 (2017).

[144] K. Gietka, J. Chwedeńczuk, T. Wasak, and F. Piazza, *Multipartite entanglement dynamics in a regular-to-ergodic transition: Quantum Fisher information approach*, Phys. Rev. B **99** (2019).

[145] T. Hiroshima, *Decoherence and entanglement in two-mode squeezed vacuum states*, Phys. Rev. A **63**, 022305 (2001).

[146] A. S. Sorensen and K. Molmer, *Entanglement and Extreme Spin Squeezing*, Phys. Rev. Lett. **86**, 4431 (2001).

[147] A. Kitaev, "A simple model of quantum holography," http://online.kitp.ucsb.edu/online/entangled15/kitaev/ (2015).

[148] I. L. Aleiner, L. Faoro, and L. B. Ioffe, *Microscopic model of quantum butterfly effect: out-of-time-order correlators and traveling combustion waves*, Annals of Physics **375**, 378 (2016).

[149] D. A. Roberts and B. Yoshida, *Chaos and complexity by design*, Journal of High Energy Physics **2017** (2017).

[150] Y. Sekino and L. Susskind, *Fast scramblers*, Journal of High Energy Physics **2008**, 065 (2008).

[151] J. Maldacena, S. H. Shenker, and D. Stanford, *A bound on chaos*, Journal of High Energy Physics **2016**, 106 (2016).

[152] M. Campisi and J. Goold, *Thermodynamics of quantum information scrambling*, Phys. Rev. E **95** (2017).

[153] A. Chenu, J. Molina-Vilaplana, and A. del Campo, *Work Statistics, Loschmidt Echo and Information Scrambling in Chaotic Quantum Systems*, Quantum **3**, 127 (2019).

[154] M. Blake, R. A. Davison, and S. Sachdev, *Thermal diffusivity and chaos in metals without quasiparticles*, Phys. Rev. D **96** (2017).

[155] S. Banerjee and E. Altman, *Solvable model for a dynamical quantum phase transition from fast to slow scrambling*, Phys. Rev. B **95** (2017).

[156] A. Bohrdt, C. B. Mendl, M. Endres, and M. Knap, *Scrambling and thermalization in a diffusive quantum many-body system*, New Journal of Physics **19**, 063001 (2017).

[157] J. Li, R. Fan, H. Wang, B. Ye, B. Zeng, H. Zhai, X. Peng, and J. Du, *Measuring Out-of-Time-Order Correlators on a Nuclear Magnetic Resonance Quantum Simulator*, Phys. Rev. X 7, 031011 (2017).

[158] M. Gärttner, J. G. Bohnet, A. Safavi-Naini, M. L. Wall, J. J. Bollinger, and A. M. Rey, *Measuring out-of-time-order correlations and multiple quantum spectra in a trapped-ion quantum magnet*, Nature Physics **13**, 781 (2017).

[159] K. A. Landsman, C. Figgatt, T. Schuster, N. M. Linke, B. Yoshida, N. Y. Yao, and C. Monroe, *Verified quantum information scrambling*, Nature **567**, 61 (2019).

[160] A. Larkin and Y. N. Ovchinnikov, *Quasiclassical method in the theory of superconductivity*, Sov Phys JETP **28**, 1200 (1969).

[161] J. S. Cotler, D. Ding, and G. R. Penington, *Out-of-time-order operators and the butterfly effect*, Annals of Physics **396**, 318 (2018).

[162] R. A. Jalabert, I. García-Mata, and D. A. Wisniacki, *Semiclassical theory of out-of-time-order correlators for low-dimensional classically chaotic systems*, Phys. Rev. E **98**, 062218 (2018).

[163] B. Yan, L. Cincio, and W. H. Zurek, *Information Scrambling and Loschmidt Echo*, Phys. Rev. Lett. **124** (2020).

[164] L. Boltzmann, in *Kinetische Theorie II* (Springer, 1970) pp. 115–225.

[165] J. Loschmidt, *Sitzungsberichte der akademie der wissenschaften*, Wien, II **73**, 128 (1876).

[166] W. Thomson, *9. The Kinetic Theory of the Dissipation of Energy*, Proceedings of the Royal Society of Edinburgh **8**, 325 (1875).

[167] A. Peres, *Stability of quantum motion in chaotic and regular systems*, Phys. Rev. A **30**, 1610 (1984).

[168] R. A. Jalabert and H. M. Pastawski, *Environment-Independent Decoherence Rate in Classically Chaotic Systems*, Phys. Rev. Lett. **86**, 2490 (2001).

[169] P. Jacquod, P. Silvestrov, and C. Beenakker, *Golden rule decay versus Lyapunov decay of the quantum Loschmidt echo*, Phys. Rev. E **64**, 055203 (2001).

[170] T. Gorin, T. Prosen, T. H. Seligman, and M. Zinidaric, *Dynamics of Loschmidt echoes and fidelity decay*, Physics Reports **435**, 33 (2006).

[171] A. Goussev, R. A. Jalabert, H. M. Pastawski, and D. Wisniacki, *Loschmidt echo*, arXiv:1206.6348 (2012).

[172] H. M. Pastawski, P. R. Levstein, G. Usaj, J. Raya, and J. Hirschinger, *A nuclear magnetic resonance answer to the Boltzmann–Loschmidt controversy?*, Physica A: Statistical Mechanics and its Applications **283**, 166 (2000).

[173] P. Jacquod and C. Petitjean, *Decoherence, entanglement and irreversibility in quantum dynamical systems with few degrees of freedom*, Advances in Physics **58**, 67 (2009).

[174] P. R. Levstein, G. Usaj, and H. M. Pastawski, *Attenuation of polarization echoes in nuclear magnetic resonance: A study of the emergence of dynamical irreversibility in many-body quantum systems*, The Journal of chemical physics **108**, 2718 (1998).

[175] G. Veble and T. Prosen, *Classical Loschmidt echo in chaotic many-body systems*, Phys. Rev. E **72**, 025202 (2005).

[176] B. V. Fine, *Long-Time Behavior of Spin Echo*, Phys. Rev. Lett. **94**, 247601 (2005).

[177] S. W. Morgan, V. Oganesyan, and G. S. Boutis, *Multispin correlations and pseudothermalization of the transient density matrix in solid-state NMR: Free induction decay and magic echo*, Phys. Rev. B **86**, 214410 (2012).

[178] E. G. Sorte, B. V. Fine, and B. Saam, *Long-time behavior of nuclear spin decays in various lattices*, Phys. Rev. B **83**, 064302 (2011).

[179] G. Boutis, P. Cappellaro, H. Cho, C. Ramanathan, and D. Cory, *Pulse error compensating symmetric magic-echo trains*, Journal of Magnetic Resonance **161**, 132 (2003).

[180] W.-K. Rhim, A. Pines, and J. S. Waugh, *Time-Reversal Experiments in Dipolar-Coupled Spin Systems*, Phys. Rev. B **3**, 684 (1971).

[181] B. V. Fine, T. A. Elsayed, C. M. Kropf, and A. S. de Wijn, *Absence of exponential sensitivity to small perturbations in nonintegrable systems of spins 1/2*, Phys. Rev. E **89**, 012923 (2014).

[182] J. Kurchan, *Quantum bound to chaos and the semiclassical limit*, Journal of Statistical Physics **171**, 965 (2018).

[183] M. Schmitt, D. Sels, S. Kehrein, and A. Polkovnikov, *Semiclassical echo dynamics in the Sachdev-Ye-Kitaev model*, Phys. Rev. B **99**, 134301 (2019).

[184] E. B. Rozenbaum, S. Ganeshan, and V. Galitski, *Lyapunov Exponent and Out-of-Time-Ordered Correlator's Growth Rate in a Chaotic System*, Phys. Rev. Lett. **118**, 086801 (2017).

[185] J. Chávez-Carlos, B. López-del Carpio, M. A. Bastarrachea-Magnani, P. Stránský, S. Lerma-Hernández, L. F. Santos, and J. G. Hirsch, *Quantum and Classical Lyapunov Exponents in Atom-Field Interaction Systems*, Phys. Rev. Lett. **122**, 024101 (2019).

[186] R. Lewis-Swan, A. Safavi-Naini, J. Bollinger, and A. Rey, *Unifying scrambling, thermalization and entanglement through measurement of fidelity out-of-time-order correlators in the Dicke model*, Nature communications **10**, 1581 (2019).

[187] B. Craps, M. De Clerck, D. Janssens, V. Luyten, and R. Charles, *Lyapunov growth in quantum spin chains*, arXiv:1908.08059 (2019).

[188] E. B. Rozenbaum, L. A. Bunimovich, and V. Galitski, *Quantum chaos in classically non-chaotic systems*, arXiv:1902.05466 (2019).

[189] J. Rammensee, J. D. Urbina, and K. Richter, *Many-Body Quantum Interference and the Saturation of Out-of-Time-Order Correlators*, Phys. Rev. Lett. **121** (2018), 10.1103/physrevlett.121.124101.

[190] M. Rautenberg and M. Gärttner, *Classical and quantum chaos in a three-mode bosonic system*, arXiv:1907.04094 (2019).

[191] R. Prakash and A. Lakshminarayan, *Scrambling in strongly chaotic weakly coupled bipartite systems: Universality beyond the Ehrenfest time-scale*, arXiv:1904.06482 (2019).

[192] J. Wang, G. Benenti, G. Casati, and W. Wang, *Complexity of quantum motion and quantum-classical correspondence: A phase-space approach*, arXiv:1912.07043 (2019).

[193] S. Sachdev and J. Ye, *Gapless spin-fluid ground state in a random quantum Heisenberg magnet*, Phys. Rev. Lett. **70**, 3339 (1993).

[194] I. Kukuljan, S. Grozdanov, and T. Prosen, *Weak quantum chaos*, Phys. Rev. B **96**, 060301 (2017).

[195] A. Polkovnikov, *Phase space representation of quantum dynamics*, Annals of Physics **325**, 1790 (2010).

[196] A. Nahum, S. Vijay, and J. Haah, *Operator Spreading in Random Unitary Circuits*, Phys. Rev. X **8** (2018).

[197] C. von Keyserlingk, T. Rakovszky, F. Pollmann, and S. Sondhi, *Operator Hydrodynamics, OTOCs, and Entanglement Growth in Systems without Conservation Laws*, Phys. Rev. X **8** (2018).

[198] V. Khemani, A. Vishwanath, and D. A. Huse, *Operator Spreading and the Emergence of Dissipative Hydrodynamics under Unitary Evolution with Conservation Laws*, Phys. Rev. X **8** (2018).

[199] T. Rakovszky, F. Pollmann, and C. von Keyserlingk, *Diffusive Hydrodynamics of Out-of-Time-Ordered Correlators with Charge Conservation*, Phys. Rev. X **8** (2018).

[200] P. Zanardi, C. Zalka, and L. Faoro, *Entangling power of quantum evolutions*, Phys. Rev. A **62**, 030301 (2000).

[201] J. N. Bandyopadhyay and A. Lakshminarayan, *Entangling power of quantum chaotic evolutions via operator entanglement*, arXiv:quant-ph/0504052 (2005), arXiv: quant-ph/0504052.

[202] T. Prosen and I. Pizorn, *Operator space entanglement entropy in transverse Ising chain*, Phys. Rev. A **76**, 032316 (2007), arXiv: 0706.2480.

[203] M. Znidaric, T. Prosen, and I. Pizorn, *Complexity of thermal states in quantum spin chains*, Phys. Rev. A **78**, 022103 (2008), arXiv: 0805.4149.

[204] T. Zhou and D. J. Luitz, *Operator entanglement entropy of the time evolution operator in chaotic systems*, Phys. Rev. B **95**, 094206 (2017).

[205] D. E. Parker, X. Cao, A. Avdoshkin, T. Scaffidi, and E. Altman, *A Universal Operator Growth Hypothesis*, Phys. Rev. X **9** (2019).

[206] U. Schollwöck, *The density-matrix renormalization group*, Rev. Mod. Phys. 77, 259 (2005).

[207] D. Perez-Garcia, F. Verstraete, M. M. Wolf, and J. I. Cirac, *Matrix product state representations*, arXiv preprint quant-ph/0608197 (2006).

[208] F. Verstraete, V. Murg, and J. Cirac, *Matrix product states, projected entangled pair states, and variational renormalization group methods for quantum spin systems*, Advances in Physics **57**, 143 (2008).

[209] J. I. Cirac and F. Verstraete, *Renormalization and tensor product states in spin chains and lattices*, Journal of Physics A: Mathematical and Theoretical **42**, 504004 (2009).

[210] A. J. Daley, C. Kollath, U. Schollwöck, and G. Vidal, *Time-dependent density-matrix renormalization-group using adaptive effective Hilbert spaces*, Journal of Statistical Mechanics: Theory and Experiment **2004**, P04005 (2004).

[211] S. R. White and A. E. Feiguin, *Real-Time Evolution Using the Density Matrix Renormalization Group*, Phys. Rev. Lett. **93** (2004).

[212] J. Haegeman, C. Lubich, I. Oseledets, B. Vandereycken, and F. Verstraete, *Unifying time evolution and optimization with matrix product states*, Phys. Rev. B **94**, 165116 (2016).

[213] J. Haegeman, J. I. Cirac, T. J. Osborne, I. Pizorn, H. Verschelde, and F. Verstraete, *Time-Dependent Variational Principle for Quantum Lattices*, Phys. Rev. Lett. **107**, 070601 (2011).

[214] M. B. Hastings, *An area law for one-dimensional quantum systems*, J. Stat. Mech. **2007**, P08024 (2007).

[215] G. Vidal, J. I. Latorre, E. Rico, and A. Kitaev, *Entanglement in Quantum Critical Phenomena*, Phys. Rev. Lett. **90** (2003).

[216] P. Calabrese and J. Cardy, *Entanglement entropy and quantum field theory*, Journal of Statistical Mechanics: Theory and Experiment **2004**, P06002 (2004).

[217] P. Calabrese and J. Cardy, *Entanglement entropy and conformal field theory*, Journal of Physics A: Mathematical and Theoretical **42**, 504005 (2009).

[218] M. Gabbrielli, L. Lepori, and L. Pezzè, *Multipartite-Entanglement Tomography of a Quantum Simulator*, arXiv:1809.01091 (2018).

[219] J. Cardy, *Finite-size scaling*, Vol. 2 (Elsevier, 2012).

[220] M. Gabbrielli, A. Smerzi, and L. Pezzè, *Multipartite Entanglement at Finite Temperature*, Scientific Reports **8** (2018).

[221] J. M. Deutsch, H. Li, and A. Sharma, *Microscopic origin of thermodynamic entropy in isolated systems*, Phys. Rev. E **87** (2013).

[222] L. Vidmar and M. Rigol, *Entanglement Entropy of Eigenstates of Quantum Chaotic Hamiltonians*, Phys. Rev. **119**, 220603 (2017).

[223] C. Murthy and M. Srednicki, *Structure of chaotic eigenstates and their entanglement entropy*, Phys. Rev. E **100**, 022131 (2019).

[224] M. Fagotti and P. Calabrese, *Evolution of entanglement entropy following a quantum quench: Analytic results for the XY chain in a transverse magnetic field*, Phys. Rev. A **78**, 010306 (2008).

[225] V. Alba and P. Calabrese, *Entanglement and thermodynamics after a quantum quench in integrable systems*, Proceedings of the National Academy of Sciences **114**, 7947 (2017).

[226] D. N. Page, *Average entropy of a subsystem*, Phys. Rev. Lett. **71**, 1291 (1993).

[227] B. Bauer and C. Nayak, *Area laws in a many-body localized state and its implications for topological order*, Journal of Statistical Mechanics: Theory and Experiment **2013**, P09005 (2013).

[228] M. Serbyn, Z. Papić, and D. A. Abanin, *Local Conservation Laws and the Structure of the Many-Body Localized States*, Phys. Rev. Lett. **111** (2013).

[229] J. H. Bardarson, F. Pollmann, and J. E. Moore, *Unbounded Growth of Entanglement in Models of Many-Body Localization*, Phys. Rev. Lett. **109**, 017202 (2012).

[230] A. M. Läuchli and C. Kollath, *Spreading of correlations and entanglement after a quench in the one-dimensional Bose–Hubbard model*, Journal of Statistical Mechanics: Theory and Experiment **2008**, P05018 (2008).

[231] H. Kim and D. A. Huse, *Ballistic Spreading of Entanglement in a Diffusive Nonintegrable System*, Phys. Rev. Lett. **111**, 127205 (2013).

[232] M. Mezei and D. Stanford, *On entanglement spreading in chaotic systems*, Journal of High Energy Physics **2017** (2017).

[233] A. Nahum, J. Ruhman, S. Vijay, and J. Haah, *Quantum Entanglement Growth under Random Unitary Dynamics*, Phys. Rev. X 7, 031016 (2017).

[234] V. Alba and P. Calabrese, *Entanglement dynamics after quantum quenches in generic integrable systems*, SciPost Physics 4, 017 (2018).

[235] P. Calabrese, *Entanglement spreading in non-equilibrium integrable systems*, arXiv:2008.11080 (2020).

[236] G. D. Chiara, S. Montangero, P. Calabrese, and R. Fazio, *Entanglement entropy dynamics of Heisenberg chains*, Journal of Statistical Mechanics: Theory and Experiment **2006**, P03001 (2006).

[237] M. Žnidarič, T. Prosen, and P. Prelovšek, *Many-body localization in the HeisenbergXXZmagnet in a random field*, Phys. Rev. B 77 (2008).

[238] M. Serbyn, Z. Papić, and D. A. Abanin, *Universal Slow Growth of Entanglement in Interacting Strongly Disordered Systems*, Phys. Rev. Lett. **110**, 260601 (2013).

[239] X. Cao, A. Tilloy, and A. De Luca, *Entanglement in a fermion chain under continuous monitoring*, SciPost Physics 7, 024 (2019).

[240] A. Chan, R. M. Nandkishore, M. Pretko, and G. Smith, *Unitary-projective entanglement dynamics*, Phys. Rev. B **99**, 224307 (2019).

[241] B. Skinner, J. Ruhman, and A. Nahum, *Measurement-Induced Phase Transitions in the Dynamics of Entanglement*, Phys. Rev. X **9**, 031009 (2019).

[242] Y. Li, X. Chen, and M. P. A. Fisher, *Quantum Zeno effect and the many-body entanglement transition*, Phys. Rev. B **98**, 205136 (2018).

[243] Y. Li, X. Chen, and M. P. A. Fisher, *Measurement-driven entanglement transition in hybrid quantum circuits*, Phys. Rev. B **100**, 134306 (2019).

[244] S. Choi, Y. Bao, X.-L. Qi, and E. Altman, *Quantum Error Correction in Scrambling Dynamics and Measurement-Induced Phase Transition*, Phys. Rev. Lett. **125**, 030505 (2020).

[245] X. Turkeshi, R. Fazio, and M. Dalmonte, *Measurement-induced criticality in (2 + 1) -dimensional hybrid quantum circuits*, Phys. Rev. B **102**, 014315 (2020).

[246] M. G. Nezhadhaghighi and M. A. Rajabpour, *Entanglement dynamics in short- and long-range harmonic oscillators*, Phys. Rev. B **90** (2014).

[247] H. Kim and D. A. Huse, *Ballistic Spreading of Entanglement in a Diffusive Nonintegrable System*, Phys. Rev. Lett. **111**, 127205 (2013).

[248] A. Polkovnikov, *Microscopic diagonal entropy and its connection to basic thermodynamic relations*, Annals of Physics **326**, 486 (2011).

[249] L. F. Santos, A. Polkovnikov, and M. Rigol, *Entropy of Isolated Quantum Systems after a Quench*, Phys. Rev. Lett. **107**, 040601 (2011).

[250] N. Y. Yao, C. R. Laumann, J. I. Cirac, M. D. Lukin, and J. E. Moore, *Quasi-Many-Body Localization in Translation-Invariant Systems*, Phys. Rev. Lett. **117**, 240601 (2016).

[251] A. A. Michailidis, M. Zidnaric, M. Medvedyeva, D. A. Abanin, T. Prosen, and Z. Papic, *Slow dynamics in translation-invariant quantum lattice models*, Phys. Rev. B **97**, 104307 (2018).

[252] A. Smith, J. Knolle, R. Moessner, and D. L. Kovrizhin, *Absence of Ergodicity without Quenched Disorder: From Quantum Disentangled Liquids to Many-Body Localization*, Phys. Rev. Lett. **119**, 176601 (2017).

[253] A. Smith, J. Knolle, R. Moessner, and D. L. Kovrizhin, *Dynamical localization in $\mathbb{Z}_2$ lattice gauge theories*, Phys. Rev. B **97**, 245137 (2018).

[254] M. Brenes, M. Dalmonte, M. Heyl, and A. Scardicchio, *Many-Body Localization Dynamics from Gauge Invariance*, Phys. Rev. Lett. **120**, 030601 (2018).

[255] N. Wheeler, *Remarks concerning the status & some ramifications of Ehrenfest's theorem* (1998).

[256] C. M. Bender and S. A. Orszag, *Advanced Mathematical Methods for Scientists and Engineers I* (Springer New York, 1999).

[257] M. C. Gutzwiller, *Chaos is classical and quantum mechanics* (Springer, 1990).

[258] M. Albiez, R. Gati, J. Fölling, S. Hunsmann, M. Cristiani, and M. K. Oberthaler, *Direct Observation of Tunneling and Nonlinear Self-Trapping in a Single Bosonic Josephson Junction*, Phys. Rev. Lett. **95**, 010402 (2005).

[259] I. D. Leroux, M. H. Schleier-Smith, and V. Vuletić, *Implementation of Cavity Squeezing of a Collective Atomic Spin*, Phys. Rev. Lett. **104**, 073602 (2010).

[260] E. J. Davis, G. Bentsen, L. Homeier, T. Li, and M. H. Schleier-Smith, *Photon-Mediated Spin-Exchange Dynamics of Spin-1 Atoms*, Phys. Rev. Lett. **122**, 010405 (2019).

[261] J. G. Bohnet, B. C. Sawyer, J. W. Britton, M. L. Wall, A. M. Rey, M. Foss-Feig, and J. J. Bollinger, *Quantum spin dynamics and entanglement generation with hundreds of trapped ions*, Science **352**, 1297 (2016).

[262] B. Sciolla and G. Biroli, *Dynamical transitions and quantum quenches in mean-field models*, Journal of Statistical Mechanics: Theory and Experiment **2011**, P11003 (2011).

[263] R. G. Littlejohn, *The semiclassical evolution of wave packets*, Phys. Rep. **138**, 193 (1986).

[264] M. Brack and R. K. Bhaduri, *Semiclassical Physics* (Addison-Wesley, 1997).

[265] A. Polkovnikov, *Quantum mechanics in phase space*, Ann. Phys. **325**, 1790 (2010).

[266] J. Vidal, R. Mosseri, and J. Dukelsky, *Entanglement in a first-order quantum phase transition*, Phys. Rev. A **69**, 054101 (2004).

[267] P. A. Miller and S. Sarkar, *Signatures of chaos in the entanglement of two coupled quantum kicked tops*, Phys. Rev. E **60**, 1542 (1999).

[268] T. L. Curtright, D. B. Fairlie, and C. K. Zachos, *A Concise Treatise on Quantum Mechanics in Phase Space* (World Scientific, 2014).

[269] D. Leibfried, T. Pfau, and C. Monroe, *Shadows and Mirrors: Reconstructing Quantum States of Atom Motion*, Physics Today **51**, 22 (1998).

[270] E. Wigner, *On the Quantum Correction For Thermodynamic Equilibrium*, Phys. Rev. **40**, 749 (1932).

[271] H. Weyl, *The theory of groups and quantum mechanics* (Courier Corporation, 1950).

[272] H. Groenewold, *On the principles of elementary quantum mechanics*, Physica **12**, 405 (1946).

[273] J. E. Moyal, *Quantum mechanics as a statistical theory*, Mathematical Proceedings of the Cambridge Philosophical Society **45**, 99 (1949).

[274] C. Gardiner, P. Zoller, and P. Zoller, *Quantum noise: a handbook of Markovian and non-Markovian quantum stochastic methods with applications to quantum optics* (Springer Science & Business Media, 2004).

[275] S. Haroche and J.-M. Raimond, *Exploring the Quantum* (Oxford University Press, 2006).

[276] A. Sinatra, C. Lobo, and Y. Castin, *The truncated Wigner method for Bose-condensed gases: limits of validity and applications*, Journal of Physics B: Atomic, Molecular and Optical Physics **35**, 3599 (2002).

[277] P. Blakie, A. Bradley, M. Davis, R. Ballagh, and C. Gardiner, *Dynamics and statistical mechanics of ultra-cold Bose gases using c-field techniques*, Advances in Physics **57**, 363 (2008).

[278] W. K. Wootters, *A Wigner-function formulation of finite-state quantum mechanics*, Annals of Physics **176**, 1 (1987).

[279] T. L. Curtright, D. B. Fairlie, and C. K. Zachos, *A concise treatise on quantum mechanics in phase space* (World Scientific Publishing Company, 2013).

[280] A. Polkovnikov, *Quantum corrections to the dynamics of interacting bosons: Beyond the truncated Wigner approximation*, Phys. Rev. A **68** (2003).

[281] A. Auerbach, *Interacting Electrons and Quantum Magnetism* (Springer New York, 1994).

[282] M. Hillery, R. F. O'Connell, M. O. Scully, and E. P. Wigner, *Distribution functions in physics: fundamentals*, Physics reports **106**, 121 (1984).

[283] M. J. Steel, M. K. Olsen, L. I. Plimak, P. D. Drummond, S. M. Tan, M. J. Collett, D. F. Walls, and R. Graham, *Dynamical quantum noise in trapped Bose-Einstein condensates*, Phys. Rev. A **58**, 4824 (1998).

[284] J. Schachenmayer, A. Pikovski, and A. M. Rey, *Many-body quantum spin dynamics with Monte Carlo trajectories on a discrete phase space*, Phys. Rev. X **5**, 011022 (2015).

[285] J. Wurtz, A. Polkovnikov, and D. Sels, *Cluster truncated Wigner approximation in strongly interacting systems*, Annals of Physics **395**, 341 (2018).

[286] P. Kramer and M. Saraceno, *Geometry of the Time Dependent Vacational Principle in Quantum Mechanics* (Springer-Verlag, Berlin, 1981).

[287] A. Kamenev and A. Levchenko, *Keldysh technique and non-linear σ-model: basic principles and applications*, Advances in Physics **58**, 197 (2009).

[288] B. Berg, L. Plimak, A. Polkovnikov, M. Olsen, M. Fleischhauer, and W. Schleich, *Commuting Heisenberg operators as the quantum response problem: Time-normal averages in the truncated Wigner representation*, Phys. Rev. A **80**, 033624 (2009).

[289] T. Mori, *Prethermalization in the transverse-field Ising chain with long-range interactions*, Journal of Physics A: Mathematical and Theoretical **52**, 054001 (2019).

[290] R. Khasseh, A. Russomanno, M. Schmitt, M. Heyl, and R. Fazio, *Discrete truncated Wigner approach to dynamical phase transitions in Ising models after a quantum quench*, Phys. Rev. B **102**, 014303 (2020).

[291] J. Wurtz and A. Polkovnikov, *Quantum hydrodynamics in spin chains with phase space methods*, arXiv:1808.08977 (2018).

[292] H. J. Lipkin, N. Meshkov, and A. Glick, *Validity of many-body approximation methods for a solvable model:(I)-(II), (III).*, Nuclear Physics **62**, 188 (1965).

[293] A. Lerose, J. Marino, B. Žunkovič, A. Gambassi, and A. Silva, *Chaotic Dynamical Ferromagnetic Phase Induced by Nonequilibrium Quantum Fluctuations*, Phys. Rev. Lett. **120**, 130603 (2018).

[294] A. Lerose, B. Žunkovič, J. Marino, A. Gambassi, and A. Silva, *Impact of nonequilibrium fluctuations on prethermal dynamical phase transitions in long-range interacting spin chains*, Phys. Rev. B **99**, 045128 (2019).

[295] G. H. Wannier, *Statistical Physics* (Dover, 1966).

[296] S. Dusuel and J. Vidal, *Continuous unitary transformations and finite-size scaling exponents in the Lipkin-Meshkov-Glick model*, Phys. Rev. B **71**, 224420 (2005).

[297] S. Dusuel and J. Vidal, *Finite-Size Scaling Exponents of the Lipkin-Meshkov-Glick Model*, Phys. Rev. Lett. **93**, 237204 (2004).

[298] W. H. Zurek and J. P. Paz, *Decoherence, chaos, and the second law*, Phys. Rev. Lett. **72**, 2508 (1994).

[299] W. H. Zurek and J. P. Paz, *Quantum chaos: a decoherent definition*, Physica D: Nonlinear Phenomena **83**, 300 (1995).

[300] A. N. Kolmogorov, *New Metric Invariant of Transitive Dynamical Systems and Endomorphisms of Lebesgue Spaces*, Doklady of Russian Academy of Sciences **119**, 861 (1958).

[301] Y. G. Sinai, *On the Notion of Entropy of a Dynamical System*, Doklady of Russian Academy of Sciences **124**, 768 (1959).

[302] J. B. Pesin, *Characteristic Lyapunov exponents and smooth ergodic theory.*, Russ. Math. Surv. **32**, 55 (1977).

[303] R. Zarum and S. Sarkar, *Quantum-classical correspondence of entropy contours in the transition to chaos*, Phys. Rev. E **57**, 5467 (1998).

[304] K. Furuya, M. C. Nemes, and G. Q. Pellegrino, *Quantum Dynamical Manifestation of Chaotic Behavior in the Process of Entanglement*, Phys. Rev. Lett. **80**, 5524 (1998).

[305] P. A. Miller and S. Sarkar, *Entropy production, dynamical localization and criteria for quantum chaos in the open quantum kicked rotor*, Nonlinearity **12**, 419 (1999).

[306] A. K. Pattanayak, *Lyapunov Exponents, Entropy Production, and Decoherence*, Phys. Rev. Lett. **83**, 4526 (1999).

[307] D. Monteoliva and J. P. Paz, *Decoherence and the Rate of Entropy Production in Chaotic Quantum Systems*, Phys. Rev. Lett. **85**, 3373–3376 (2000).

[308] J. Gong and P. Brumer, *Intrinsic decoherence dynamics in smooth Hamiltonian systems: Quantum-classical correspondence*, Phys. Rev. A **68** (2003).

[309] J. Gong and P. Brumer, *When is Quantum Decoherence Dynamics Classical?*, Phys. Rev. Lett. **90** (2003).

[310] R. Alicki, A. Łoziński, P. Pakoński, and K. Życzkowski, *Quantum dynamical entropy and decoherence rate*, Journal of Physics A: Mathematical and General **37**, 5157–5172 (2004).

[311] R. M. Angelo and K. Furuya, *Semiclassical limit of the entanglement in closed pure systems*, Phys. Rev. A **71** (2005).

[312] C. Petitjean and P. Jacquod, *Lyapunov Generation of Entanglement and the Correspondence Principle*, Phys. Rev. Lett. **97**, 194103 (2006).

[313] A. D. Ribeiro and R. M. Angelo, *Entanglement dynamics via coherent-state propagators*, Phys. Rev. A **82** (2010).

[314] K. M. F. Romero, J. E. Parreira, L. A. M. Souza, M. C. Nemes, and W. Wreszinski, *An analytical relation between entropy production and quantum Lyapunov exponents for Gaussian bipartite systems*, Journal of Physics A: Mathematical and Theoretical **41**, 115303 (2008).

[315] G. Casati, I. Guarneri, and J. Reslen, *Classical dynamics of quantum entanglement*, Phys. Rev. E **85** (2012).

[316] M. V. S. Bonança, *Lyapunov decoherence rate in classically chaotic systems*, Phys. Rev. E **83**, 046214 (2011).

[317] L. Souza, J. Faria, and M. Nemes, *Parametric competition in non-autonomous Hamiltonian systems*, Optics Communications **331**, 148–153 (2014).

[318] M. Znidaric and T. Prosen, *Fidelity and purity decay in weakly coupled composite systems*, Journal of Physics A: Mathematical and General **36**, 2463 (2003).

[319] P. Jacquod, *Semiclassical Time Evolution of the Reduced Density Matrix and Dynamically Assisted Generation of Entanglement for Bipartite Quantum Systems*, Phys. Rev. Lett. **92**, 150403 (2004).

[320] E. Bianchi, L. Hackl, and N. Yokomizo, *Linear growth of the entanglement entropy and the Kolmogorov-Sinai rate*, Journal of High Energy Physics **2018**, 25 (2018).

[321] C. T. Asplund and D. Berenstein, *Entanglement entropy converges to classical entropy around periodic orbits*, Annals of Physics **366**, 113 (2016).

[322] L. Hackl, E. Bianchi, R. Modak, and M. Rigol, *Entanglement production in bosonic systems: Linear and logarithmic growth*, Phys. Rev. A **97**, 032321 (2018).

[323] F. Haake, M. Kuś, and R. Scharf, *Classical and quantum chaos for a kicked top*, Zeitschrift für Physik B Condensed Matter **65**, 381 (1987).

[324] F. Haake, *Quantum Signatures of Chaos* (Springer Berlin Heidelberg, 2010).

[325] R. H. Dicke, *Coherence in Spontaneous Radiation Processes*, Phys. Rev. **93**, 99 (1954).

[326] M. de Aguiar, K. Furuya, C. Lewenkopf, and M. Nemes, *Chaos in a spin-boson system: Classical analysis*, Annals of Physics **216**, 291 (1992).

[327] M. Cencini, F. Cecconi, and A. Vulpiani, *Chaos: from simple models to complex systems* (World Scientific, 2010).

[328] V. I. Oseledets, *A multiplicative ergodic theorem. Liapunov characteristic number for dynamical systems*, Trans. Moscow Math. Soc. **19**, 197 (1968).

[329] G. Benettin, L. Galgani, and J.-M. Strelcyn, *Kolmogorov entropy and numerical experiments*, Phys. Rev. A **14**, 2338 (1976).

[330] G. Benettin, L. Galgani, A. Giorgilli, and J.-M. Strelcyn, *Lyapunov Characteristic Exponents for smooth dynamical systems and for hamiltonian systems. A method for computing all of them. Part 1 Theory*, Meccanica **15**, 9 (1980).

[331] G. Benettin, L. Galgani, A. Giorgilli, and J.-M. Strelcyn, *Lyapunov Characteristic Exponents for smooth dynamical systems and for hamiltonian systems. A method for computing all of them. Part 2 Numerical application*, Meccanica **15**, 21 (1980).

[332] F. Benatti, F. Carollo, R. Floreanini, and H. Narnhofer, *Quantum fluctuations in mesoscopic systems*, Journal of Physics A: Mathematical and Theoretical **50**, 423001 (2017).

[333] D. S. Vidal J. and T. Barthel, *Entanglement entropy in collective models*, Journal of Statistical Mechanics: Theory and Experiment **2007**, P01015 (2007).

[334] J. Pöschel, *A lecture on the classical KAM theorem*, arXiv:0908.2234 (2009).

[335] W. W. Ho, S. Choi, H. Pichler, and M. D. Lukin, *Periodic Orbits, Entanglement, and Quantum Many-Body Scars in Constrained Models: Matrix Product State Approach*, Phys. Rev. Lett. **122** (2019).

[336] G. J. Milburn, J. Corney, E. M. Wright, and D. F. Walls, *Quantum dynamics of an atomic Bose-Einstein condensate in a double-well potential*, Phys. Rev. A **55**, 4318 (1997).

[337] J. I. Cirac, M. Lewenstein, K. Molmer, and P. Zoller, *Quantum superposition states of Bose-Einstein condensates*, Phys. Rev. A **57**, 1208 (1998).

[338] V. Bapst and G. Semerjian, *On quantum mean-field models and their quantum annealing*, Journal of Statistical Mechanics: Theory and Experiment **2012**, P06007 (2012).

[339] A. Russomanno, R. Fazio, and G. E. Santoro, *Thermalization in a periodically driven fully connected quantum Ising ferromagnet*, EPL (Europhysics Letters) **110**, 37005 (2015).

[340] I. Homrighausen, N. O. Abeling, V. Zauner-Stauber, and J. C. Halimeh, *Anomalous dynamical phase in quantum spin chains with long-range interactions*, Phys. Rev. B **96**, 104436 (2017).

[341] J. Schachenmayer, B. P. Lanyon, C. F. Roos, and A. J. Daley, *Entanglement Growth in Quench Dynamics with Variable Range Interactions*, Phys. Rev. X **3**, 031015 (2013).

[342] A. S. Buyskikh, M. Fagotti, J. Schachenmayer, F. Essler, and A. J. Daley, *Entanglement growth and correlation spreading with variable-range interactions in spin and fermionic tunneling models*, Phys. Rev. A **93**, 053620 (2016).

[343] M. Gabbrielli, L. Lepori, and L. Pezzè, *Multipartite-entanglement tomography of a quantum simulator*, New Journal of Physics **21**, 033039 (2019).

[344] M. Kitagawa and M. Ueda, *Squeezed spin states*, Phys. Rev. A **47**, 5138 (1993).

[345] G. Sorelli, M. Gessner, A. Smerzi, and L. Pezzè, *Fast and optimal generation of entanglement in bosonic Josephson junctions*, Phys. Rev. A **99** (2019).

[346] S. Chaudhury, A. Smith, B. E. Anderson, S. Ghose, and P. S. Jessen, *Quantum signatures of chaos in a kicked top*, Nature **461**, 768 (2009).

[347] S. Ghose and B. Sanders, *Entanglement dynamics in chaotic systems*, Phys. Rev. A **70**, 062315 (2004).

[348] A. Piga, M. Lewenstein, and J. Q. Quach, *Quantum chaos and entanglement in ergodic and nonergodic systems*, Phys. Rev. E **99**, 032213 (2019).

[349] X. Wang, S. Ghose, B. C. Sanders, and B. Hu, *Entanglement as a signature of quantum chaos*, Phys. Rev. E **70**, 016217 (2004).

[350] C. M. Trail, V. Madhok, and I. H. Deutsch, *Entanglement and the generation of random states in the quantum chaotic dynamics of kicked coupled tops*, Phys. Rev. E **78**, 046211 (2008).

[351] S. Ghose, R. Stock, P. Jessen, R. Lal, and A. Silberfarb, *Chaos, entanglement, and decoherence in the quantum kicked top*, Phys. Rev. A **78**, 042318 (2008).

[352] M. Kumari and S. Ghose, *Untangling entanglement and chaos*, Phys. Rev. A **99**, 042311 (2019).

[353] M. Lombardi and A. Matzkin, *Entanglement and chaos in the kicked top*, Phys. Rev. E **83**, 016207 (2011).

[354] G. Stamatiou and D. P. Ghikas, *Quantum entanglement dependence on bifurcations and scars in non-autonomous systems. The case of quantum kicked top*, Physics Letters A **368**, 206 (2007).

[355] V. Madhok, C. A. Riofrío, S. Ghose, and I. H. Deutsch, *Information Gain in Tomography–A Quantum Signature of Chaos*, Phys. Rev. Lett. **112** (2014).

[356] L. J. Fiderer and D. Braun, *Quantum metrology with quantum-chaotic sensors*, Nature Communications **9** (2018).

[357] S. Pappalardi, A. Russomanno, B. Žunkovič, F. Iemini, A. Silva, and R. Fazio, *Scrambling and entanglement spreading in long-range spin chains*, Phys. Rev. B **98**, 134303 (2018).

[358] L. M. Sieberer, T. Olsacher, A. Elben, M. Heyl, P. Hauke, F. Haake, and P. Zoller, *Digital quantum simulation, Trotter errors, and quantum chaos of the kicked top*, npj Quantum Information **5**, 78 (2019).

[359] S. Pilatowsky-Cameo, J. Chávez-Carlos, M. A. Bastarrachea-Magnani, P. Stránský, S. Lerma-Hernández, L. F. Santos, and J. G. Hirsch, *Positive quantum Lyapunov exponents in experimental systems with a regular classical limit*, Phys. Rev. E **101** (2020).

[360] Y. L. Loh and M. Kim, *Visualizing spin states using the spin coherent state representation*, American Journal of Physics **83**, 30 (2015).

[361] F. Johansson *et al.*, *mpmath: a Python library for arbitrary-precision floating-point arithmetic (version 1.1.0)* (2013), `http://mpmath.org/`.

[362] C. Emary and T. Brandes, *Chaos and the quantum phase transition in the Dicke model*, Phys. Rev. E **67**, 066203 (2003).

[363] N. Lambert, C. Emary, and T. Brandes, *Entanglement and the Phase Transition in Single-Mode Superradiance*, Phys. Rev. Lett. **92**, 073602 (2004).

[364] C. Lóbez and A. Relaño, *Entropy, chaos and excited-state quantum phase transitions in the Dicke model*, Phys. Rev. E **94**, 012140 (2016), arXiv: 1604.06334.

[365] S. Sinha and S. Sinha, *Chaos, non-ergodic states and quantum scars in Bose-Josephson junction coupled to a bosonic mode*, arXiv:1912.06593 (2019).

[366] L. Song, J. Ma, D. Yan, and X. Wang, *Quantum Fisher information and chaos in the Dicke model*, The European Physical Journal D **66**, 201 (2012).

[367] T.-L. Wang, L.-N. Wu, W. Yang, G.-R. Jin, N. Lambert, and F. Nori, *Quantum Fisher information as a signature of the superradiant quantum phase transition*, New Journal of Physics **16**, 063039 (2014).

[368] Y.-Y. Zhang and X.-Y. Chen, *Large-N scaling behavior of the quantum fisher information in the Dicke model*, The European Physical Journal D **69**, 241 (2015), arXiv: 1503.03953.

[369] S. S. Mirkhalaf and A. Smerzi, *Entanglement detection in a coupled atom-field system via quantum Fisher information*, Phys. Rev. A **95**, 022302 (2017).

[370] K. Gietka, J. Chwedeńczuk, T. Wasak, and F. Piazza, *Multipartite-Entanglement Dynamics in Regular-to-Ergodic Transition: a Quantum-Fisher-Information approach*, Phys. Rev. B **99**, 064303 (2019), arXiv: 1812.01013.

[371] A. B. Bhattacherjee and D. Sharma, *Spin squeezing and Quantum Fisher Information in the Jaynes-Cummings Dicke Model*, arXiv:1607.01930 (2016).

[372] W. Buijsman, V. Gritsev, and R. Sprik, *Nonergodicity in the Anisotropic Dicke Model*, Phys. Rev. Lett. **118**, 080601 (2017).

[373] Y. Alavirad and A. Lavasani, *Scrambling in the Dicke model*, Phys. Rev. A **99**, 043602 (2019).

[374] J. Johansson, P. Nation, and F. Nori, *QuTiP: An open-source Python framework for the dynamics of open quantum systems*, Computer Physics Communications **183**, 1760 (2012).

[375] J. Johansson, P. Nation, and F. Nori, *QuTiP 2: A Python framework for the dynamics of open quantum systems*, Computer Physics Communications **184**, 1234 (2013).

[376] Q. Zhuang, T. Schuster, B. Yoshida, and N. Y. Yao, *Scrambling and complexity in phase space*, Phys. Rev. A **99** (2019).

[377] A. Safavi-Naini, R. Lewis-Swan, J. G. Bohnet, M. Gärttner, K. A. Gilmore, J. E. Jordan, J. Cohn, J. K. Freericks, A. M. Rey, and J. J. Bollinger, *Verification of a Many-Ion Simulator of the Dicke Model Through Slow Quenches across a Phase Transition*, Phys. Rev. Lett. **121**, 040503 (2018).

[378] J. Rammensee, J. D. Urbina, and K. Richter, *Many-Body Quantum Interference and the Saturation of Out-of-Time-Order Correlators*, Phys. Rev. Lett. **121**, 124101 (2018).

[379] A. Hallam, J. G. Morley, and A. G. Green, *The Lyapunov spectra of quantum thermalisation*, Nature Communications **10** (2019).

[380] A. Michailidis, C. Turner, Z. Papić, D. Abanin, and M. Serbyn, *Slow Quantum Thermalization and Many-Body Revivals from Mixed Phase Space*, Phys. Rev. X **10** (2020).

[381] S. Ghose, R. Stock, P. Jessen, R. Lal, and A. Silberfarb, *Chaos, entanglement, and decoherence in the quantum kicked top*, Phys. Rev. A **78** (2008).

[382] R. Blatt and C. F. Roos, *Quantum simulations with trapped ions*, Nature Physics **8**, 277 (2012).

[383] B. Neyenhuis, J. Zhang, P. W. Hess, J. Smith, A. C. Lee, P. Richerme, Z. Gong, A. V. Gorshkov, and C. Monroe, *Observation of prethermalization in long-range interacting spin chains*, Science advances **3**, e1700672 (2017).

[384] P. Jurcevic, H. Shen, P. Hauke, C. Maier, T. Brydges, C. Hempel, B. P. Lanyon, M. Heyl, R. Blatt, and C. F. Roos, *Direct Observation of Dynamical Quantum Phase Transitions in an Interacting Many-Body System*, Phys. Rev. Lett. **119**, 080501 (2017).

[385] B. Žunkovič, M. Heyl, M. Knap, and A. Silva, *Dynamical Quantum Phase Transitions in Spin Chains with Long-Range Interactions: Merging Different Concepts of Nonequilibrium Criticality*, Phys. Rev. Lett. **120**, 130601 (2018).

[386] G. Piccitto, B. Žunkovič, and A. Silva, *Dynamical phase diagram of a quantum Ising chain with long-range interactions*, Phys. Rev. B **100** (2019).

[387] G. Piccitto and A. Silva, *Crossover from fast to slow dynamics in a long range interacting Ising chain*, Journal of Statistical Mechanics: Theory and Experiment **2019**, 094017 (2019).

[388] Z.-X. Gong, M. Foss-Feig, S. Michalakis, and A. V. Gorshkov, *Persistence of Locality in Systems with Power-Law Interactions*, Phys. Rev. Lett. **113**, 030602 (2014).

[389] M. Foss-Feig, Z.-X. Gong, C. W. Clark, and A. V. Gorshkov, *Nearly Linear Light Cones in Long-Range Interacting Quantum Systems*, Phys. Rev. Lett. **114**, 157201 (2015).

[390] P. Hauke and L. Tagliacozzo, *Spread of Correlations in Long-Range Interacting Quantum Systems*, Phys. Rev. Lett. **111**, 207202 (2013).

[391] J. Eisert, M. van den Worm, S. R. Manmana, and M. Kastner, *Breakdown of quasilocality in long-range quantum lattice models*, Phys. Rev. Lett. **111**, 260401 (2013).

[392] L. Lepori, A. Trombettoni, and D. Vodola, *Singular dynamics and emergence of nonlocality in long-range quantum models*, Journal of Statistical Mechanics: Theory and Experiment **2017**, 033102 (2017).

[393] L. Cevolani, G. Carleo, and L. Sanchez-Palencia, *Protected quasilocality in quantum systems with long-range interactions*, Phys. Rev. A **92**, 041603 (2015).

[394] L. Cevolani, G. Carleo, and L. Sanchez-Palencia, *Spreading of correlations in exactly solvable quantum models with long-range interactions in arbitrary dimensions*, New Journal of Physics **18**, 093002 (2016).

[395] M. Van Regemortel, D. Sels, and M. Wouters, *Information propagation and equilibration in long-range Kitaev chains*, Phys. Rev. A **93**, 032311 (2016).

[396] M. C. Tran, C.-F. Chen, A. Ehrenberg, A. Y. Guo, A. Deshpande, Y. Hong, Z.-X. Gong, A. V. Gorshkov, and A. Lucas, *Hierarchy of Linear Light Cones with Long-Range Interactions*, Phys. Rev. X **10** (2020).

[397] D. V. Else, F. Machado, C. Nayak, and N. Y. Yao, *An improved Lieb-Robinson bound for many-body Hamiltonians with power-law interactions*, arXiv:1809.06369 (2018).

[398] T. Matsuta, T. Koma, and S. Nakamura, *Improving the Lieb–Robinson Bound for Long-Range Interactions*, Annales Henri Poincaré **18**, 519 (2017).

[399] M. B. Hastings and T. Koma, *Spectral Gap and Exponential Decay of Correlations*, Communications in Mathematical Physics **265**, 781 (2006).

[400] T. Koffel, M. Lewenstein, and L. Tagliacozzo, *Entanglement Entropy for the Long-Range Ising Chain in a Transverse Field*, Phys. Rev. Lett. **109**, 267203 (2012).

[401] G. Gori, S. Paganelli, A. Sharma, P. Sodano, and A. Trombettoni, *Explicit Hamiltonians inducing volume law for entanglement entropy in fermionic lattices*, Phys. Rev. B **91** (2015).

[402] I. Frérot, P. Naldesi, and T. Roscilde, *Entanglement and fluctuations in the XXZ model with power-law interactions*, Phys. Rev. B **95**, 245111 (2017).

[403] Z.-X. Gong, M. Foss-Feig, F. G. S. L. Brandão, and A. V. Gorshkov, *Entanglement Area Laws for Long-Range Interacting Systems*, Phys. Rev. Lett. **119**, 050501 (2017).

[404] F. Ares, J. G. Esteve, F. Falceto, and A. R. de Queiroz, *Entanglement entropy in the long-range Kitaev chain*, Phys. Rev. A **97**, 062301 (2018).

[405] M. G. Nezhadhaghighi and M. A. Rajabpour, *Entanglement entropy in long-range harmonic oscillators*, EPL **100**, 60011 (2012).

[406] M. G. Nezhadhaghighi and M. A. Rajabpour, *Quantum entanglement entropy and classical mutual information in long-range harmonic oscillators*, Phys. Rev. B **88** (2013).

[407] F. Ares, J. G. Esteve, F. Falceto, and Z. Zimborás, *Sublogarithmic behaviour of the entanglement entropy in fermionic chains*, Journal of Statistical Mechanics: Theory and Experiment **2019**, 093105 (2019).

[408] D. Vodola, L. Lepori, E. Ercolessi, A. V. Gorshkov, and G. Pupillo, *Kitaev Chains with Long-Range Pairing*, Phys. Rev. Lett. **113**, 156402 (2014).

[409] M. G. Nezhadhaghighi and M. A. Rajabpour, *Entanglement dynamics in short- and long-range harmonic oscillators*, Phys. Rev. B **90**, 205438 (2014).

[410] I. Frérot, P. Naldesi, and T. Roscilde, *Multispeed Prethermalization in Quantum Spin Models with Power-Law Decaying Interactions*, Phys. Rev. Lett. **120**, 050401 (2018).

[411] T. Kuwahara and K. Saito, *Strictly Linear Light Cones in Long-Range Interacting Systems of Arbitrary Dimensions*, Phys. Rev. X **10** (2020).

[412] D. J. Luitz and Y. B. Lev, *Emergent locality in systems with power-law interactions*, Phys. Rev. A **99** (2019).

[413] C.-J. Lin and O. I. Motrunich, *Out-of-time-ordered correlators in short-range and long-range hard-core boson models and in the Luttinger-liquid model*, Phys. Rev. B **98**, 134305 (2018).

[414] X. Chen and T. Zhou, *Quantum chaos dynamics in long-range power law interaction systems*, Phys. Rev. B **100**, 064305 (2019).

[415] C.-F. Chen and A. Lucas, *Finite Speed of Quantum Scrambling with Long Range Interactions*, Phys. Rev. Lett. **123**, 250605 (2019).

[416] L. Colmenarez and D. J. Luitz, *Lieb Robinson bounds and out of time order correlators in a long range spin chain*, arXiv:2005.10257 [cond-mat, physics:quant-ph] (2020).

[417] A. Y. Guo, M. C. Tran, A. M. Childs, A. V. Gorshkov, and Z.-X. Gong, *Signaling and scrambling with strongly long-range interactions*, Phys. Rev. A **102**, 010401 (2020).

[418] M. K. Joshi, A. Elben, B. Vermersch, T. Brydges, C. Maier, P. Zoller, R. Blatt, and C. F. Roos, *Quantum Information Scrambling in a Trapped-Ion Quantum Simulator with Tunable Range Interactions*, Phys. Rev. Lett. **124** (2020).

[419] M. Heyl, F. Pollmann, and B. Dóra, *Detecting Equilibrium and Dynamical Quantum Phase Transitions in Ising Chains via Out-of-Time-Ordered Correlators*, Phys. Rev. Lett. **121**, 016801 (2018).

[420] M. Saffman, T. G. Walker, and K. Molmer, *Quantum information with Rydberg atoms*, Rev. Mod. Phys. **82**, 2313 (2010).

[421] P. Schauß, M. Cheneau, M. Endres, T. Fukuhara, S. Hild, A. Omran, T. Pohl, C. Gross, S. Kuhr, and I. Bloch, *Observation of spatially ordered structures in a two-dimensional Rydberg gas*, Nature **491**, 87 (2012).

[422] B. Yan, S. A. Moses, B. Gadway, J. P. Covey, K. R. Hazzard, A. M. Rey, D. S. Jin, and J. Ye, *Observation of dipolar spin-exchange interactions with lattice-confined polar molecules*, Nature **501**, 521 (2013).

[423] M. Lu, N. Q. Burdick, and B. L. Lev, *Quantum degenerate dipolar Fermi gas*, Phys. Rev. Lett. **108**, 215301 (2012).

[424] P. Jurcevic, B. P. Lanyon, P. Hauke, C. Hempel, P. Zoller, R. Blatt, and C. F. Roos, *Quasiparticle engineering and entanglement propagation in a quantum many-body system*, Nature **511**, 202 (2014).

[425] H. Häffner, C. F. Roos, and R. Blatt, *Quantum computing with trapped ions*, Physics reports **469**, 155 (2008).

[426] G. Pagano, P. W. Hess, H. B. Kaplan, W. L. Tan, P. Richerme, P. Becker, A. Kyprianidis, J. Zhang, E. Birckelbaw, M. R. Hernandez, Y. Wu, and C. Monroe, *Cryogenic trapped-ion system for large scale quantum simulation*, Quantum Science and Technology **4**, 014004 (2018).

[427] M. F. Maghrebi, Z.-X. Gong, M. Foss-Feig, and A. V. Gorshkov, *Causality and quantum criticality in long-range lattice models*, Phys. Rev. B **93**, 125128 (2016).

[428] A. Dutta and J. Bhattacharjee, *Phase transitions in the quantum Ising and rotor models with a long-range interaction*, Phys. Rev. B **64**, 184106 (2001).

[429] N. Defenu, A. Trombettoni, and S. Ruffo, *Criticality and phase diagram of quantum long-range O(N) models*, Phys. Rev. B **96**, 104432 (2017).

[430] S. Fey and K. P. Schmidt, *Critical behavior of quantum magnets with long-range interactions in the thermodynamic limit*, Phys. Rev. B **94**, 075156 (2016).

[431] R. Juhász, I. A. Kovács, and F. Iglói, *Random transverse-field Ising chain with long-range interactions*, EPL (Europhysics Letters) **107**, 47008 (2014).

[432] L. Lepori, D. Vodola, G. Pupillo, G. Gori, and A. Trombettoni, *Effective theory and breakdown of conformal symmetry in a long-range quantum chain*, Annals of Physics **374**, 35 (2016).

[433] L. Vanderstraeten, M. Van Damme, H. P. Buchler, and F. Verstraete, *Quasiparticles in Quantum Spin Chains with Long-Range Interactions*, Phys. Rev. Lett. **121**, 090603 (2018).

[434] S. Hernández-Santana, C. Gogolin, J. I. Cirac, and A. Acín, *Correlation Decay in Fermionic Lattice Systems with Power-Law Interactions at Nonzero Temperature*, Phys. Rev. Lett. **119** (2017).

[435] T. Vojta, *Quantum version of a spherical model: Crossover from quantum to classical critical behavior*, Phys. Rev. B **53**, 710 (1996).

[436] N. Laflorencie, I. Affleck, and M. Berciu, *Critical phenomena and quantum phase transition in long range Heisenberg antiferromagnetic chains*, Journal of Statistical Mechanics: Theory and Experiment **2005**, P12001 (2005).

[437] M. Tezuka, A. M. García-García, and M. A. Cazalilla, *Destruction of long-range order by quenching of the hopping range in one dimension*, Phys. Rev. A **90** (2014).

[438] A. Lerose, B. Žunkovič, A. Silva, and A. Gambassi, *Quasilocalized excitations induced by long-range interactions in translationally invariant quantum spin chains*, Phys. Rev. B **99**, 121112 (2019).

[439] D. Jaschke, K. Maeda, J. D. Whalen, M. L. Wall, and L. D. Carr, *Critical phenomena and Kibble–Zurek scaling in the long-range quantum Ising chain*, New Journal of Physics **19**, 033032 (2017).

[440] M. P. Zaletel, R. S. K. Mong, C. Karrasch, J. E. Moore, and F. Pollmann, *Time-evolving a matrix product state with long-ranged interactions*, Phys. Rev. B **91** (2015).

[441] M. A. Rajabpour and S. Sotiriadis, *Quantum quench in long-range field theories*, Phys. Rev. B **91** (2015).

[442] P. Hauke and M. Heyl, *Many-body localization and quantum ergodicity in disordered long-range Ising models*, Phys. Rev. B **92**, 134204 (2015).

[443] A. Bermudez, L. Tagliacozzo, G. Sierra, and P. Richerme, *Long-range Heisenberg models in quasiperiodically driven crystals of trapped ions*, Phys. Rev. B **95** (2017).

[444] R. M. Nandkishore and S. L. Sondhi, *Many-Body Localization with Long-Range Interactions*, Phys. Rev. X 7, 041021 (2017).

[445] R. Singh, R. Moessner, and D. Roy, *Effect of long-range hopping and interactions on entanglement dynamics and many-body localization*, Phys. Rev. B **95**, 094205 (2017).

[446] K. R. A. Hazzard, M. van den Worm, M. Foss-Feig, S. R. Manmana, E. G. Dalla Torre, T. Pfau, M. Kastner, and A. M. Rey, *Quantum correlations and entanglement in far-from-equilibrium spin systems*, Phys. Rev. A **90**, 063622 (2014).

[447] A. González-Tudela and J. I. Cirac, *Exotic quantum dynamics and purely long-range coherent interactions in Dirac conelike baths*, Phys. Rev. A **97** (2018).

[448] J. C. Halimeh and V. Zauner-Stauber, *Dynamical phase diagram of quantum spin chains with long-range interactions*, Phys. Rev. B **96**, 134427 (2017).

[449] N. Defenu, T. Enss, M. Kastner, and G. Morigi, *Dynamical Critical Scaling of Long-Range Interacting Quantum Magnets*, Phys. Rev. Lett. **121**, 240403 (2018).

[450] L. Cevolani, J. Despres, G. Carleo, L. Tagliacozzo, and L. Sanchez-Palencia, *Universal scaling laws for correlation spreading in quantum systems with short- and long-range interactions*, Phys. Rev. B **98** (2018).

[451] M. C. Tran, A. Y. Guo, Y. Su, J. R. Garrison, Z. Eldredge, M. Foss-Feig, A. M. Childs, and A. V. Gorshkov, *Locality and digital quantum simulation of power-law interactions*, arXiv:1808.05225 (2018).

[452] B. Žunkovič, M. Heyl, M. Knap, and A. Silva, *Dynamical Quantum Phase Transitions in Spin Chains with Long-Range Interactions: Merging Different Concepts of Nonequilibrium Criticality*, Phys. Rev. Lett. **120**, 130601 (2018).

[453] L. F. Santos, F. Borgonovi, and G. L. Celardo, *Cooperative Shielding in Many-Body Systems with Long-Range Interaction*, Phys. Rev. Lett. **116**, 250402 (2016).

[454] M. Kač and C. J. Thompson, *Critical behavior of several lattice models with long-range interaction*, J. Math. Phys. **10**, 1373 (1969).

[455] F. J. Dyson, *Existence of a phase-transition in a one-dimensional Ising ferromagnet*, , Communications in Mathematical Physics **12**, 91 (1969).

[456] F. J. Dyson, *An Ising ferromagnet with discontinuous long-range order*, Communications in Mathematical Physics **21**, 269 (1971).

[457] M. E. Fisher, S.-k. Ma, and B. G. Nickel, *Critical Exponents for Long-Range Interactions*, Phys. Rev. Lett. **29**, 917 (1972).

[458] N. Defenu, A. Codello, S. Ruffo, and A. Trombettoni, *Criticality of spin systems with weak long-range interactions*, Journal of Physics A: Mathematical and Theoretical **53**, 143001 (2020).

[459] K. R. Fratus and M. Srednicki, *Eigenstate Thermalization and Spontaneous Symmetry Breaking in the One-Dimensional Transverse-Field Ising Model with Power-Law Interactions*, arXiv:1611.03992 (2016).

[460] A. Lerose, J. Marino, A. Gambassi, and A. Silva, *Prethermal quantum many-body Kapitza phases of periodically driven spin systems*, Phys. Rev. B **100**, 104306 (2019).

[461] F. Liu, R. Lundgren, P. Titum, G. Pagano, J. Zhang, C. Monroe, and A. V. Gorshkov, *Confined Quasiparticle Dynamics in Long-Range Interacting Quantum Spin Chains*, Phys. Rev. Lett. **122**, 150601 (2019).

[462] D. Mukamel, S. Ruffo, and N. Schreiber, *Breaking of Ergodicity and Long Relaxation Times in Systems with Long-Range Interactions*, Phys. Rev. Lett. **95**, 240604 (2005).

[463] Z.-X. Gong and L.-M. Duan, *Prethermalization and dynamic phase transition in an isolated trapped ion spin chain*, New Journal of Physics **15**, 113051 (2013).

[464] L. D. Landau and E. M. Lifsits, *Mechanics* (Butterworth-Heinemann, 1976).

[465] S. Blanes, F. Casas, J. Oteo, and J. Ros, *The Magnus expansion and some of its applications*, Physics Reports **470**, 151 (2009).

[466] T. Barthel, M.-C. Chung, and U. Schollwöck, *Entanglement scaling in critical two-dimensional fermionic and bosonic systems*, Phys. Rev. A **74**, 022329 (2006).

[467] C. Weedbrook, S. Pirandola, R. García-Patrón, N. J. Cerf, T. C. Ralph, J. H. Shapiro, and S. Lloyd, *Gaussian quantum information*, Rev. Mod. Phys. **84**, 621 (2012).

[468] A. Chan, A. De Luca, and J. T. Chalker, *Solution of a Minimal Model for Many-Body Quantum Chaos*, Phys. Rev. X **8**, 041019 (2018).

[469] P. Ray, B. K. Chakrabarti, and A. Chakrabarti, *Sherrington-Kirkpatrick model in a transverse field: Absence of replica symmetry breaking due to quantum fluctuations*, Phys. Rev. B **39**, 11828 (1989).

[470] J. Miller and D. A. Huse, *Zero-temperature critical behavior of the infinite-range quantum Ising spin glass*, Phys. Rev. Lett. **70**, 3147 (1993).

[471] A. Andreanov and M. Müller, *Long-Range Quantum Ising Spin Glasses at $T=0$: Gapless Collective Excitations and Universality*, Phys. Rev. Lett. **109**, 177201 (2012).

[472] E. B. Rozenbaum, S. Ganeshan, and V. Galitski, *Universal level statistics of the out-of-time-ordered operator*, Physical Review B **100** (2019).

[473] T. Scaffidi and E. Altman, *Chaos in a classical limit of the Sachdev-Ye-Kitaev model*, Physical Review B **100** (2019), 10.1103/physrevb.100.155128.

[474] C. Murthy and M. Srednicki, *Bounds on Chaos from the Eigenstate Thermalization Hypothesis*, Phys. Rev. Lett. **123** (2019).

[475] D. Sherrington and S. Kirkpatrick, *Solvable Model of a Spin-Glass*, Phys. Rev. Lett. **35**, 1792 (1975).

[476] G. Parisi, *Infinite Number of Order Parameters for Spin-Glasses*, Phys. Rev. Lett. **43**, 1754 (1979).

[477] L. F. Cugliandolo, D. R. Grempel, G. Lozano, and H. Lozza, *Effects of dissipation on disordered quantum spin models*, Phys. Rev. B **70** (2004), 10.1103/physrevb.70.024422.

[478] C. Laumann, A. Pal, and A. Scardicchio, *Many-Body Mobility Edge in a Mean-Field Quantum Spin Glass*, Phys. Rev. Lett. **113** (2014).

[479] C. Baldwin, C. Laumann, A. Pal, and A. Scardicchio, *Clustering of nonergodic eigenstates in quantum spin glasses*, Phys. Rev, Lett. **118**, 127201 (2017).

[480] C. L. Baldwin and C. R. Laumann, *Quantum algorithm for energy matching in hard optimization problems*, Phys. Rev. B **97** (2018), 10.1103/physrevb.97.224201.

[481] R. B. Sidje, *Expokit: A software package for computing matrix exponentials*, ACM Transactions on Mathematical Software (TOMS) **24**, 130 (1998).

[482] H. Fujisaka, *Statistical dynamics generated by fluctuations of local Lyapunov exponents*, Progress of theoretical physics **70**, 1264 (1983).

[483] R. Benzi, G. Paladin, G. Parisi, and A. Vulpiani, *Characterisation of intermittency in chaotic systems*, Journal of Physics A: Mathematical and General **18**, 2157 (1985).

[484] A. E. Tarkhov and B. V. Fine, *Estimating ergodization time of a chaotic many-particle system from a time reversal of equilibrium noise*, New Journal of Physics **20**, 123021 (2018).

[485] N. Defenu, A. Trombettoni, and S. Ruffo, *Anisotropic long-range spin systems*, Phys. Rev. B **94** (2016).

[486] J. Vidal, S. Dusuel, and T. B., *Entanglement entropy in collective models*, J. Stat. Mech. **2007**, P01015 (2007).

[487] C. Monthus, *Dyson hierarchical quantum ferromagnetic Ising chain with pure or random transverse fields*, J. Stat. Mech. **2015**, P05026 (2015).

[488] C. Monthus, *Dyson hierarchical long-ranged quantum spin-glass via real-space renormalization*, J. Stat. Mech. **2015**, P10024 (2015).

[489] L. Tagliacozzo, G. Evenbly, and G. Vidal, *Simulation of two-dimensional quantum systems using a tree tensor network that exploits the entropic area law*, Phys. Rev. B **80**, 235127 (2009).

[490] V. Murg, F. Verstraete, O. Legeza, and R. M. Noack, *Simulating strongly correlated quantum systems with tree tensor networks*, Phys. Rev. B **82** (2010).

[491] V. Alba, L. Tagliacozzo, and P. Calabrese, *Entanglement entropy of two disjoint intervals in c= 1 theories*, J. Stat. Mech. **2011**, P06012 (2011).

[492] L. Tagliacozzo, In preparation.

[493] G. Parisi and R. Shankar, *Statistical Field Theory*, Physics Today **41**, 110 (1988).

[494] P. Collet and J. P. Eckmann, *A Renormalization Group Analysis of the Hierarchical Model in Statistical Mechanics* (Springer-Verlag, 1978).

[495] P. Werner, M. Völker, K.and Troyer, and S. Chakravarty, *Phase diagram and critical exponents of a dissipative Ising spin chain in a transverse magnetic field*, Phys. Rev. Lett. **94**, 047201 (2005).

[496] P. Werner, M. Troyer, and S. Sachdev, *Quantum spin chains with site dissipation*, Journal of the Physical Society of Japan **74**, 67 (2005).

[497] I. B. Sperstad, E. B. Stiansen, and A. Sudbo, *Quantum criticality in spin chains with non-Ohmic dissipation*, Physical Review B **85** (2012).

[498] G. Refael and J. E. Moore, *Entanglement Entropy of Random Quantum Critical Points in One Dimension*, Phys. Rev. Lett. **93** (2004).

[499] G. Refael and J. E. Moore, *Criticality and entanglement in random quantum systems*, Journal of Physics A: Mathematical and Theoretical **42**, 504010 (2009).

[500] R. Santachiara, *Increasing of entanglement entropy from pure to random quantum critical chains*, Journal of Statistical Mechanics: Theory and Experiment **2006**, L06002 (2006).

[501] M. Fagotti, P. Calabrese, and J. E. Moore, *Entanglement spectrum of random-singlet quantum critical points*, Phys. Rev. B **83** (2011).

[502] Y.-C. Lin, F. Iglói, and H. Rieger, *Entanglement Entropy at Infinite-Randomness Fixed Points in Higher Dimensions*, Phys. Rev. Lett. **99** (2007).

[503] F. Iglói and Y.-C. Lin, *Finite-size scaling of the entanglement entropy of the quantum Ising chain with homogeneous, periodically modulated and random couplings*, Journal of Statistical Mechanics: Theory and Experiment **2008**, P06004 (2008).

[504] F. Iglói and C. Monthus, *Strong disorder RG approach – a short review of recent developments*, The European Physical Journal B **91** (2018).

[505] X. Turkeshi, P. Ruggiero, and P. Calabrese, *Negativity spectrum in the random singlet phase*, Phys. Rev. B **101**, 064207 (2020).

[506] X. Turkeshi, P. Ruggiero, V. Alba, and P. Calabrese, *Entanglement equipartition in critical random spin chains*, Phys. Rev. B **102**, 014455 (2020).

[507] B. Swingle and J. McGreevy, *Area law for gapless states from local entanglement thermodynamics*, Phys. Rev. B **93**, 205120 (2016).

[508] A. Cadarso, M. Sanz, M. M. Wolf, J. I. Cirac, and D. Pérez-García, *Entanglement, fractional magnetization, and long-range interactions*, Phys. Rev. B **87** (2013).

[509] R. Movassagh and P. W. Shor, *Supercritical entanglement in local systems: Counterexample to the area law for quantum matter*, Proceedings of the National Academy of Sciences **113**, 13278 (2016).

[510] M. M. Wolf, G. Ortiz, F. Verstraete, and J. I. Cirac, *Quantum phase transitions in matrix product systems*, Phys. Rev. Lett. **97**, 110403 (2006).

[511] V. Alba, M. Fagotti, and P. Calabrese, *Entanglement entropy of excited states*, Journal of Statistical Mechanics: Theory and Experiment **2009**, P10020 (2009).

[512] A. Chan, A. De Luca, and J. T. Chalker, *Eigenstate Correlations, Thermalization, and the Butterfly Effect*, Phys. Rev. Lett. **122**, 220601 (2019).

[513] I. Frérot and T. Roscilde, *Quantum Critical Metrology*, Phys. Rev. Lett. **121**, 020402 (2018).

[514] M. Brenes, E. Mascarenhas, M. Rigol, and J. Goold, *High-temperature coherent transport in the XXZ chain in the presence of an impurity*, Phys. Rev. B **98**, 235128 (2018).

[515] R. Mondaini and M. Rigol, *Eigenstate thermalization in the two-dimensional transverse field Ising model. II. Off-diagonal matrix elements of observables*, Phys. Rev. E **96**, 012157 (2017).

[516] W. Beugeling, R. Moessner, and M. Haque, *Off-diagonal matrix elements of local operators in many-body quantum systems*, Phys. Rev. E **91**, 012144 (2015).

[517] S. Mukerjee, V. Oganesyan, and D. Huse, *Statistical theory of transport by strongly interacting lattice fermions*, Phys. Rev. B **73**, 035113 (2006).

[518] M. G. Paris, *Quantum estimation for quantum technology*, International Journal of Quantum Information 7, 125 (2009).

[519] J. R. Garrison and T. Grover, *Does a Single Eigenstate Encode the Full Hamiltonian?*, Phys. Rev. X **8** (2018).

[520] V. Gurarie, *Global large time dynamics and the generalized Gibbs ensemble*, Journal of Statistical Mechanics: Theory and Experiment **2013**, P02014 (2013).

[521] T. LeBlond, K. Mallayya, L. Vidmar, and M. Rigol, *Entanglement and matrix elements of observables in interacting integrable systems*, Phys. Rev. E **100**, 062134 (2019).

[522] E. J. Torres-Herrera, I. Vallejo-Fabila, A. J. Martínez-Mendoza, and L. F. Santos, *Self-averaging in many-body quantum systems out of equilibrium: Time dependence of distributions*, arXiv:2005.14188 (2020).

[523] E. P. Wigner, *Characteristics Vectors of Bordered Matrices with Infinite Dimensions II*, The Annals of Mathematics **65**, 203 (1957).

[524] E. P. Wigner, *On the Distribution of the Roots of Certain Symmetric Matrices*, The Annals of Mathematics **67**, 325 (1958).

[525] F. J. Dyson, *Statistical Theory of the Energy Levels of Complex Systems. I*, Journal of Mathematical Physics **3**, 140 (1962).

[526] D. Rossini, R. Fazio, V. Giovannetti, and A. Silva, *Quantum quenches, linear response and superfluidity out of equilibrium*, EPL (Europhysics Letters) **107**, 30002 (2014).

[527] R. Shankar, *Principles of quantum mechanics* (Springer Science & Business Media, 2012).

[528] A. Kamenev, *Field theory of non-equilibrium systems* (Cambridge University Press, 2011).

Chapter A

A pedagogical inroduction to ETH

In this appendix we review the basic framework of eigenstate-thermalization-hypothesis, focusing on the consequences on physical observables and fluctuations. The relevant steps of the derivations are worked out.

Since the beginning of quantum mechanics [43], continuous efforts have been made to identify the minimal set of conditions for the validity of quantum thermalization. The first crucial insight, based on early works by Wigner and Dyson [523–525], goes under the name of *random matrix theory*, see, e.g., Refs. [17, 38]. It predicts that a sufficiently complex Hamiltonian, when focusing on an appropriately small energy window (where the density of states is constant), essentially behaves like a random matrix. The importance of the random matrix theory for thermalization was discussed by Deutsch in 1991 in Ref.[51]. There, he extended the studies of Berry on single-particle quantum systems [49, 50] to generic complex quantum Hamiltonians. Ultimately, the quantitative and predictive framework for understanding thermalization was fully established by Srednicki in a series of papers in the early 1990's [44, 52, 53]. His ansatz is now known as *eigenstate thermalization hypothesis* (ETH). Srednicki was able to complement random matrix theory with the structure given by the energy dependence, in such a way for all statistical mechanics to naturally follow. ETH not only solves the issue of the relaxation of observables to the microcanonical predictions, but it also explains why they remain close to it almost all large times.

ETH is usually formulated as an ansatz for the matrix elements of observables on the basis of the eigenstates of a Hamiltonian $\hat{H}$ ($\hat{H}|E_n\rangle = E_n|E_n\rangle$). For a generic operator $\hat{O}$, it reads [44]

$$O_{nm} \equiv \langle E_n|\hat{O}|E_m\rangle = \mathcal{O}(\bar{E})\,\delta_{nm} + e^{-S(\bar{E})/2}\, f_{\hat{O}}(\bar{E},\omega)\, R_{nm}\ , \tag{A.1}$$

where $\bar{E} = (E_n + E_m)/2$ is the average energy of the two eigenstates, $\omega = E_n - E_m$ is the energy difference, $\mathcal{O}(\bar{E})$ is the micro-canonical value at energy $\bar{E}$, $S(\bar{E})$ is the thermodynamic entropy (logarithm of the density of states) and $f_{\hat{O}}(\bar{E},\omega) = f_{\hat{O}}(\bar{E},-\omega)$ is a real smooth functions of its two arguments. The numbers R_{nm} are erratically fluctuating variables, that can be seen as are random real or complex numbers with zero mean and unit variance ($\overline{R_{nm}^2} = 1$ or $\overline{|R_{nm}|^2} = 1$ respectively).

At this level, no assumption has been made on the distribution of the R_{nm} (besides its mean and variance). However, focusing on a small energy window where $f_{\hat{O}}(\bar{E},\omega) \sim$ const., one should retrieve the random matrix theory prediction in which non-diagonal elements are Gaussian random variables. Recent numerical studies have shown that single matrix elements are compatible with a gaussian distribution [514, 521, 522]. Nevertheless, more refined indicators show important deviations from random matrix theory [55], consistent with the existence of sensible correlations between the matrix elements [56]. Accordingly, it is important to understand the diverse physical implications of such deviations.

The validity of ETH is restricted to states which have a finite energy density, away from the edges of the spectrum. This excludes the ground state and low-lying excited states or states with the highest energies, where the spectrum is more sparse. ETH is said to hold in a *strong* (weak) sense, if all (almost all) the eigenstates at the center of the spectrum obey Eq.(1.12) [57]. Recent numerical and analytical studies have demonstrated a violation of strong ETH in several classes of spin chains, due to the existence of athermal eigenstates in the center of the spectrum [60–65]. This is discussed in the context of ergodicity breaking in Sec.1.1.3.
Notice that there is no rigorous proof of what observables satisfy Eq.(1.12). While ETH has been demonstrated numerically for several spin chains in the case of local observables [1] (or sum of local ones) [17] , it clearly fails for very non-local operators, e.g. eigenstate projectors $P_n = |E_n\rangle\langle E_n|$.
As already mentioned, understanding the range of validity of ETH in physical Hamiltonians has motivated a considerable body of numerical work over the past decade [17, 40, 58].

The ETH framework is enough to deduce thermalization in isolated quantum systems. To fully appreciate the impact of Eq.(1.12), let us analyze one by one of the relevant consequences. As the main outcome, we will see that pure energy eigenstates are indistinguishable from thermal states using local probes, fluctuation dissipation's relations, or for their entropic content (see Section 1.3.2).

A.1 ETH and local observables

Let us first show how ETH implies quantum thermalization in Eq.(1.10). The infinite time-average of a local operator $\hat{O}$ [2], by virtue of Eq.(1.7), is given by

$$\begin{aligned} \overline{O} &= \sum_n |c_n|^2 O_{nn} = \sum_n |c_n|^2 \mathcal{O}(E_n) + O(e^{-S/2}) \\ &\simeq \mathcal{O}(E) + \frac{1}{2}\left(\frac{\partial^2 \mathcal{O}}{\partial E^2}\right) \delta E^2 = \langle E|\hat{O}|E\rangle + O(1/N) \ , \end{aligned} \tag{A.2}$$

[1] For example in Ref.[519], Garrison and Grover conjecture that Eq.(1.12) holds for all operators within a subsystem A when the volume V_A of subsystem A is such that $V_A/V \to 0$ when the total volume $V \to \infty$. Furthermore, they discuss the case in which the support of the operator scales like a fraction $f = V_A/V$ of the total value and argue that Eq.(1.12) holds up to $f = 1/2$.

[2] We now neglect the superscript A used in the Section 1.1.2, but still consider a local operator with finite support.

where δE^2 is the energy variance of the initial state [cf. Eq.(1.9)]. On the right end side of the first line we have substituted the ETH ansatz (1.12) and considered the extensivity of the entropy $S(E,N) = Ns(E/N)$. On the second line, we first have used the fact that generic initial states have a narrow distribution around an average energy E with small energy variance [3] [cf. Eq.(1.9) and the discussion of Sec.1.1.1]. Secondly, one notices that the correction to the microcanonical result is subleading, because of Eq.(1.9) again.
On the other hand, $\mathcal{O}(E)$ is related, in the presence of equivalence of statistical ensembles (see Note 2), to the equilibrium thermal value of $\hat{O}$, i.e. $\langle\hat{O}\rangle_{\text{Gibbs}}$. By expanding in the energy eigenbasis, using Eq.(1.12) and passing to the continuum ($\sum_n \to \int dE e^{S(E)}$), one obtains [44]

$$\langle\hat{O}\rangle_{\text{Gibbs}} \equiv \text{Tr}\left(\hat{O}\frac{e^{-\beta H}}{Z}\right) = \frac{1}{Z}\int dE e^{S(E)-\beta E}\mathcal{O}(E) + O(e^{-S/2}) \,. \tag{A.4}$$

The energy integral is then performed via the saddle point technique, by noticing that both the arguments appearing in the exponent are extensive. This fixes the energy and the temperature according to the standard thermodynamic prescription $\beta = \partial S/\partial E$. The result with the proper normalization yields $\langle\hat{O}\rangle_{\text{Gibbs}} = \mathcal{O}(E) + O(1/N)$. Putting together the integral in Eq.(A.4) with Eq.(A.2), one obtains, at the leading order in N,

$$\overline{O} \simeq \langle\hat{O}\rangle_{\text{Gibbs}} \simeq \mathcal{O}(E) \simeq \langle E|\hat{O}|E\rangle \,. \tag{A.5}$$

Namely, the equilibrium values of observables after a quenched dynamics correspond to their thermal expectation values which can in turn and be calculated on single eigenstates corresponding to the average energy. This is the essence of the eigenstate thermalization hypothesis. See Figure A.1 for an illustrative example.

As mentioned above, ETH not only describes the relaxation to the microcanonical prediction, but it also explains why instantaneous observables remain close to it at most later times. In fact, one can compute the time fluctuations of the expectation values of the observable $\hat{O}$ as

$$\sigma^2_{\hat{O}} \equiv \overline{O^2} - \overline{O}^2 = \sum_{mn, m\neq n} |c_n|^2|c_m|^2\,|O_{nm}|^2 \leq \max|O_{nm}|^2 \propto e^{-S(\overline{E})} \,, \tag{A.6}$$

where one first inserts the energy eigenbasis in the definition (1.6), then one computes the infinite-time average and lastly one estimates the maximum with the ETH ansatz in Eq.(1.12). Thus, the time fluctuations of the expectation values of the observable are exponentially small in the system size. This implies the existence of the limit in Eq.(1.10), without the need for infinite time-averaging.

[3] In this case, one can perform a Taylor expansion around that energy

$$\mathcal{O}(E_n) = \mathcal{O}(E) + (E_n - E)\,\mathcal{O}'(E) + \frac{1}{2}(E_n - E)^2\,\mathcal{O}''(E) + \dots \tag{A.3}$$

where $\mathcal{O}'(E)$, $\mathcal{O}''(E)$ are the first and second partial derivatives of the micro canonical function $\mathcal{O}(x)$ evaluated at $x = E$. Substituting back, at $o(\delta E^3)$ we obtain Eq.(A.2).

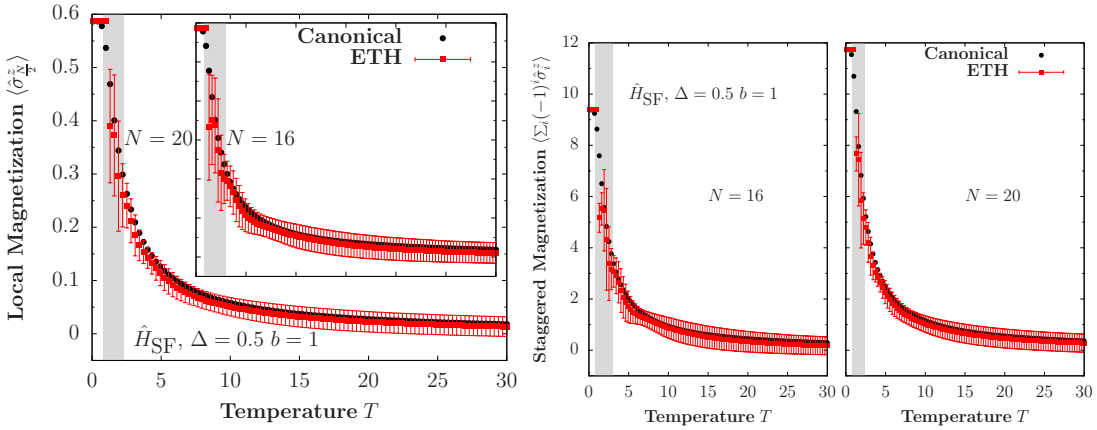

Figure A.1: Illustrative example of the validity of the eigenstate thermalization hypothesis (A.5), in a chaotic spin chain, taken from Ref.[5]. The plots show the expectation value of a local operator (left) and the sum of local operators (right) as a function of temperature in both the canonical ensemble and the corresponding ETH prediction. The gray area highlights the low-temperature regime, close to the edges of the spectrum where the ETH prediction gives the largest fluctuations. By increasing the system size the fluctuations of the ETH prediction's decrease.

A.2 ETH and fluctuation dissipation relations

The smooth function $f_{\hat{O}}(\bar{E}, \omega)$ in the ETH ansatz completely determines also two-point correlation functions. Through that, it allows deriving what is sometimes taken as the definition of equilibrium: the fluctuation dissipation theorem (FDT) [17, 66]. The latter holds both for single energy eigenstates or for asymptotic states of a quenched dynamics.

Let us recall briefly the derivation, following Ref.[17]. The two-point function at energy E_α is defined by

$$F_2(t) = \langle E_\alpha | \hat{O}(t)\, \hat{O} | E_\alpha \rangle - \langle E_\alpha | \hat{O}(t) | E_\alpha \rangle \langle E_\alpha | \hat{O} | E_\alpha \rangle \ . \tag{A.7}$$

Substituting the Eq.(1.12) and the average over the R_{nm} it is easy to see that

$$\begin{aligned} F_2(t) &= \sum_{\beta \neq \alpha} e^{i\omega_{\alpha\beta} t} \, |f_{\alpha\beta}|^2 \, e^{-S_{\alpha\beta}} = \int dE_\beta \, e^{i\omega_{\alpha\beta}} \, |f_{\hat{O}}(E_{\alpha\beta}, \omega_{\alpha\beta})|^2 e^{S(E_\beta) - S(E_{\alpha\beta})} \\ &= \int d\omega \, e^{i\omega t} \, e^{-\beta\omega/2} \, e^{-3\omega^2/8C} |f_{\hat{O}}(E_\alpha - \omega/2, \omega)|^2 + \mathcal{O}(\omega^3) \ , \end{aligned} \tag{A.8}$$

where on the right-hand side of the first line we have substituted sums with integrals $\sum_\beta \to \int dE_\beta e^{S(E_\beta)}$. In the second line, we have changed variable to $\omega = E_\alpha - E_\beta$ and we considered an expansion for small frequencies [4] for the entropies as

$$S(E_\beta) - S(E_{\alpha\beta}) = S(E_\alpha - \omega) - S(E_\alpha - \omega/2) = -\frac{\beta\omega}{2} - \frac{3}{8}\frac{\beta^2\omega^2}{C} + \mathcal{O}(\omega^3) \ , \tag{A.9}$$

[4] This expansion is justified since, for physical operators, $f_{\hat{O}}(E, \omega)$ decays exponentially fast in ω, see Ref.[474] for a rigorous proof.

where we used the thermodynamic definition of inverse temperature $\beta = \frac{\partial S}{\partial E}$ and of heat capacity $\beta^2/C = \frac{\partial^2 S}{\partial E^2}$. By taking the thermodynamic limit $C \sim N \gg 1$, the Fourier transform of Eq.(A.7) is then given by

$$F_2(\omega) = 2\pi\, e^{\beta\omega/2}\, |f_{\hat{O}}(E_\alpha{+}\omega/2,\omega)|^2 \simeq 2\pi\, e^{\beta\omega/2} \left(|f_{\hat{O}}(E_\alpha,\omega)|^2 + \frac{\omega}{2}\frac{\partial |f_{\hat{O}}(E,\omega)|^2}{\partial E}|_{E_\alpha} \right) , \tag{A.10}$$

where on the right hand side we expanded for small frequencies the smooth function $f_{\hat{O}}$. We would like to emphasise that this expression is neglecting terms $\mathcal{O}(\omega^2/N)$. Eq.(A.10) immediately yields the Fourier transform of the *symmetrized response function* $S_{\hat{O}}(t_1) := \langle\{\hat{O}(t_1),\hat{O}(0)\}\rangle - 2\langle\hat{O}(t_1)\rangle\langle\hat{O}(0)\rangle$ and the *imaginary part of the Kubo susceptibility* $\chi_{\hat{O}}(t_1) := -i\theta(t_1)\langle[\hat{O}(t_1),\hat{O}(0)]\rangle$, as

$$\begin{aligned} S_{\hat{O}}(E_\alpha,\omega) &= F_2(\omega) + F_2(-\omega) \qquad\qquad (A.11a)\\ &= 4\pi \left[\cosh(\beta\omega/2) |f_{\hat{O}}(E_\alpha,\omega)|^2 + \frac{\omega}{2}\sinh(\beta\omega/2)\frac{\partial |f_{\hat{O}}(E,\omega)|^2}{\partial E}|_{E_\alpha} \right] \end{aligned}$$

$$\begin{aligned} \chi''_{\hat{O}}(E_\alpha,\omega) &= \frac{F_2(\omega) - F_2(-\omega)}{2} \qquad\qquad (A.11b)\\ &= 2\pi \left[\sinh(\beta\omega/2) |f_{\hat{O}}(E_\alpha,\omega)|^2 + \frac{\omega}{2}\cosh(\beta\omega/2)\frac{\partial |f_{\hat{O}}(E,\omega)|^2}{\partial E}|_{E_\alpha} \right] . \end{aligned}$$

In Eqs.(A.11), the derivatives $\frac{\partial |f_{\hat{O}}(E,\omega)|^2}{\partial E}$ are sub-leading to respect of the first term, for both local or extensive operators [5]. By neglecting them, one obtains the standard expression of the fluctuation dissipation theorem

$$\chi''_{\hat{O}}(E_\alpha,\omega) = \frac{1}{2}\tanh(\beta\omega/2)\, S_{\hat{O}}(E_\alpha,\omega) \, . \tag{A.12}$$

See Figure A.2 for an illustrative example.

Let us now study the two-times correlation functions out-of-equilibrium, with the protocol of quenched dynamics outlined in Section 1.1.1. We define the two-times Kubo response function and symmetric correlation function as

$$\chi_{\hat{O}}(t_1,t_2) = -i\theta(t_1-t_2)\,\langle[\hat{O}(t_1),\hat{O}(t_2)]\rangle \, , \tag{A.13a}$$

$$S_{\hat{O}}(t_1,t_2) = \langle\{\hat{O}(t_1),\hat{O}(t_2)\}\rangle - 2\langle\hat{O}(t_1)\rangle\,\langle\hat{O}(t_2)\rangle, \tag{A.13b}$$

where the average is computed to respect to an initial pure state $|\psi_0\rangle$, which is not an eigenstate of the Hamiltonian $\hat{H}$. Out-of-equilibrium, these quantities do not depend in general on the time-difference $t_1 - t_2$. However, one may still effectively analyse the dynamics with the new variables $t_{1,2} = T \pm \tau/2$ (also know as Wigner coordinates) and Fourier transforming with respect to τ, restricted to $|\tau| \leq 2T$. In particular, one can obtain information about the stationary state attained at a long

[5] If $\hat{O}$ is local $|f|^2 = O(1)$ hence $\partial|f|^2/\partial E = O(1/N)$. On the other hand if $\hat{O}$ is a sum of local operators $|f|^2 = O(N)$ hence $\partial|f|^2/\partial E = O(1)$

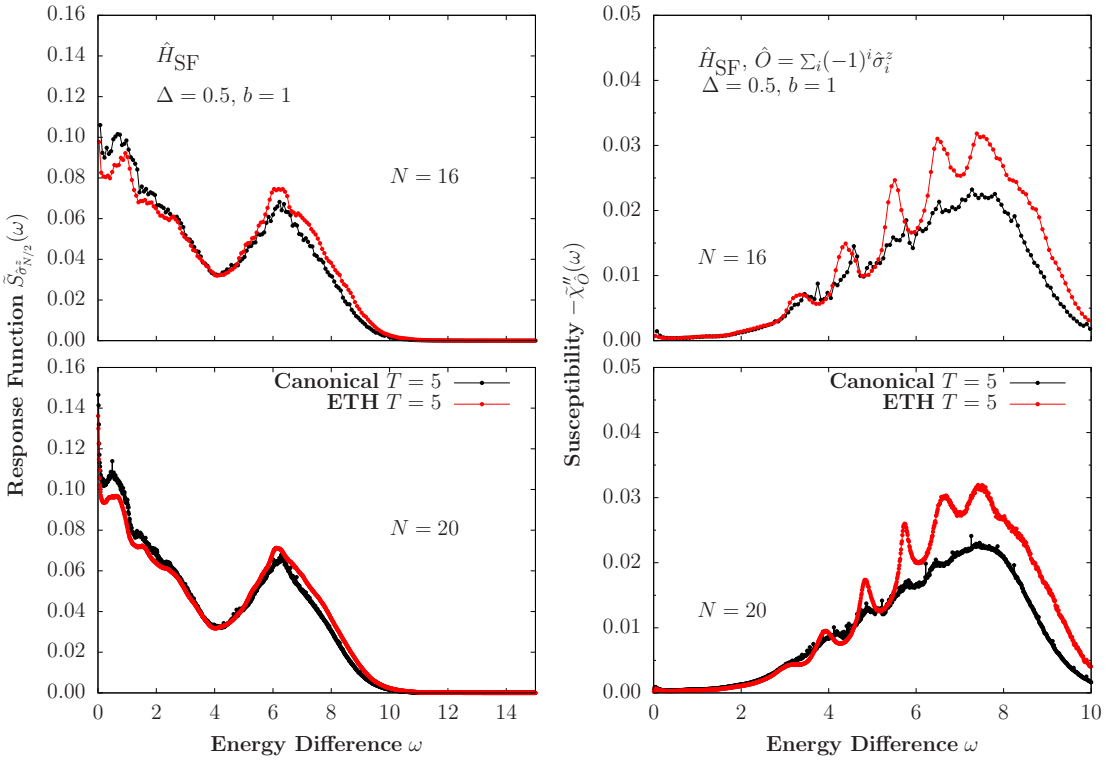

Figure A.2: Illustrative example of the validity of the FDT with ETH (A.11), in a chaotic spin chain taken from Ref.[5]. The plots show the symmetric response function of a local operator (left) and the immaginary Kubo response function of sum of local operators (right) as a function of the energy difference ω at $T = 5$. The ETH predictions (A.11) (red) are compared with the standard expressions obtained in Lehmann representation (black). By increasing the system size the difference between the two results decreases.

time. Indeed, by performing the infinite-time average (1.6) to respect to the average time T, one gets

$$\overline{\chi_{\hat{O}}(T,\tau)} = \chi^{\rm DE}_{\hat{O}}(\tau) = -i\theta(\tau)\,\langle[\hat{O}(\tau),\hat{O}(0)]\rangle_{\rm DE}\,, \tag{A.14a}$$

$$\overline{S_{\hat{O}}(T,\tau)} = S^{\rm DE}_{\hat{O}}(\tau) = \langle\{\hat{O}(\tau),\hat{O}(0)\}\rangle_{\rm DE} - 2\langle\hat{O}(\tau)\rangle_{\rm DE}\,\langle\hat{O}(0)\rangle_{\rm DE}\,, \tag{A.14b}$$

where the expectation value (1.8) is taken over the diagonal ensemble [cf. Eq.(1.7)]. After a quenched dynamics, the stationary two-times response functions are given by the equilibrium result evaluated over the diagonal ensemble depending on the time difference. The result for the Kubo Response function has been derived in Ref.[526].

If we consider an initial generic state $|\psi_0\rangle$ with extensive energy E and sub-extensive energy fluctuations δE^2 [cf. Eq.(1.9)], we can perform again a Taylor expansion

around E and obtain the following

$$S^{\mathrm{DE}}_{\hat{O}}(\omega) = S_{\hat{O}}(E,\omega) + \delta E^2 \left[\frac{\partial^2 S_{\hat{O}}(E_\alpha, t)}{\partial E^2} + \left(\frac{\partial \mathcal{O}}{\partial E} \right)^2 \right] \tag{A.15a}$$

$$\chi''^{\mathrm{DE}}_{\hat{O}}(\omega) = \chi''_{\hat{O}}(E,\omega) + \delta E^2 \left[\frac{\partial^2 \chi''_{\hat{O}}(E,\omega)}{\partial E^2} \right] , \tag{A.15b}$$

where $S_{\hat{O}}(E,\omega)$ and $\chi''_{\hat{O}}(E,\omega)$ are the single energy correlation functions of Eqs.(A.11) and all the partial derivatives are evaluated at energy E. Corrections of the order of the energy variance are usually subleading, except for the case of collective operators, where it can become of the same order. Hence, FDT theorem for ETH in Eqs.(A.11-A.12) is valid not only for single energy eigenstates, but also in the case of the diagonal ensemble.

Chapter B

Out-of-time ordered correlators and phase-space methods

In this Appendix, we show an interesting application of phase-space methods for the study of quantum information spreading and, in particular, of semiclassical scrambling.

We first derive the semiclassical expression for the echo observable and the square-commutator [cf. Section 1.2.4] using Bopp formalism (2.54) and show that in the semiclassical limit both quantities contain the square of the derivatives of the classical trajectories with respect to the initial conditions. This implies that both the echo observable and the square commutator encode the classical Lyapunov exponent.

As discussed above, the Bopp formalism can be used in constructing Weyl symbols for various time-dependent expectation values [195, 288] and, in particular, to compute out-of-time ordered correlators. To do so, we consider the Bopp representation of $\hat{B}(t)$ (2.54) and the corresponding one for $\hat{A}(0)$

$$\hat{A}(0) \to A_0 + \hbar D^{(1)}_{A_0} + \hbar^2 D^{(2)}_{A_0} + O(\hbar^3) \, .$$

To derive the semiclassical limit of OTOC at order $\hbar^2$, it is enough to keep at most the second-order expansion in $\hbar$ of the Bopp operator. We compute the semiclassical limit the OTOC discussed in Section 1.2.4, by evaluating the Weyl symbol of several correlation functions, e.g.

$$\left(\hat{B}(t)\,\hat{A}\,\hat{B}(t)\right)^{\mathrm{w}} = (B_t + D^{(1)}_{B_t} + D^{(2)}_{B_t})\,(A_0 + D^{(1)}_{A_0} + D^{(2)}_{A_0})\,B_t \, ,$$

and we simplify the resulting expressions. After a tedious calculation, the Weyl symbol of the echo observable (1.44) reads

$$\left([\hat{B}(t),[\hat{B}(t),\hat{A}(0)]\,]\right)^{\mathrm{w}} = \hbar^2 \left[3\left(D^{(1)}_{B_t}\right)^2 A_0 - D^{(2)}_{B_t}\,B_t A_0 + D^{(2)}_{A_0} B_t^2 + A_0\,D^{(2)}_{B_t} B_t\right] \, , \tag{B.1}$$

while for the square commutator (1.45) one finds

$$-\left([\hat{B}(t),\hat{A}(0)]\,]^2\right)^{\mathrm{w}} = -4\hbar^2\left(D^{(1)}_{A_0} B_t\right)^2 = \hbar^2\{A_0,B_t\}^2 \, . \tag{B.2}$$

To check Eqs.(B.1-B.2) let us consider as simple example $\hat{A}(0) = \hat{a}^2$ and $\hat{B}(t) = a^\dagger(t)$ and compute the equal time result at $t = 0$. One one side, the exact commutation relation for the bosonic operators immediately gives $-[\hat{a}^\dagger, \hat{a}^2]^2 = -4\hat{a}^2$ and $[\hat{a}^\dagger, [\hat{a}^\dagger, \hat{a}^2]] = 2$. On the other hand, it is straightforward to check that Eqs.(B.1-B.2) lead to $-([\hat{a}^\dagger, \hat{a}^2]^2)^{\rm w} = -4\alpha^2$ and $([\hat{a}^\dagger, [\hat{a}^\dagger, \hat{a}^2]])^{\rm w} = 2$. In fact, the Bopp representation (2.50b) for $\hat{B} = \hat{a}^\dagger$ gives $B = \alpha^*$, $D_B^{(1)} = -\frac{1}{2\hbar}\,\partial/\partial\alpha$, $D_B^{(2)} = 0$, while for $\hat{A} = \hat{a}^2$ one has $A = \alpha^2$, $D_A^{(1)} = \alpha/\hbar\,\partial/\partial\alpha^*$, $D_A^{(2)} = \frac{1}{4\hbar^2}\partial^2/\partial\alpha^{*\,2}$.

It is well known that the classical limit of the square commutator (B.2) encodes the square of the derivatives of the classical trajectory to respect to the initial conditions [160–162]. This means that, whenever the classical limit is chaotic, $c(t)$ is expected to grow exponentially, with a rate given by twice the largest Lyapunov exponent. This can be directly seen also in the example discussed above with $\hat{A}(0) = \hat{a}^2(0)$ and $\hat{B}(t) = \hat{a}^\dagger(t)$, where Eq.(B.2) simply gives

$$\left([\hat{a}^\dagger(t), \hat{a}^2(0)]\right)^{\rm w} = 4\alpha^2(0)\left(\frac{\partial\alpha^*(t)}{\partial\alpha^*(0)}\right)^2 . \tag{B.3}$$

We now show that the same result applies to the semiclassical limit of the echo observable (B.1). This has been already discussed in Ref.[183], but, for the sake of completeness, we illustrate it here within our notations. Let us first analyze the previous simple example. Substituting the Bopp representation for $\hat{A}(0) = \hat{a}^2(0)$ and $\hat{B}(t) = \hat{a}^\dagger(t)$ into Eq.(B.1), and using the chain rule for the second-order derivatives, one gets

$$\left([\hat{a}^\dagger(t), [\hat{a}^\dagger(t), \hat{a}^2(0)]\,]\right)^{\rm w} = \frac{1}{2}\left[3\left(\frac{\partial\alpha(0)}{\partial\alpha(t)}\right)^2 + \left(\frac{\partial\alpha^*(t)}{\partial\alpha^*(0)}\right)^2 + 3\alpha(0)\frac{\partial^2\alpha(0)}{\partial\alpha^2(t)} + \alpha^*(t)\frac{\partial^2\alpha^*(t)}{\partial\alpha^{*\,2}(0)}\right] ,$$

which, exactly as the square commutator, is dominated by the square of the derivatives of the classical trajectory to respect to the initial conditions.
Let us now prove it for spin operators, which are mostly the subject of the present thesis. In this case the Bopp operators are given by Eq.(2.55-2.56). We fix for definiteness $\hat{A}(0) = \hat{S}^z$ and $\hat{B}(t) = \hat{S}^z(t)$, where $\hat{S}^z$ is the spin operator along the z direction. Ignoring factors of the order of the unity and keeping only the second order derivatives in Eq.(2.56), a straightforward calculation yields

$$-\left(\left[\hat{S}^z(t), \hat{S}^z(0)\right]^2\right)^{\rm w} = -\hbar^2\left(D^{(1)}_{S_0^z}\,S_t^z\right)^2 \sim \hbar^2\left[\left(\frac{\partial S_t^z}{\partial S_0^\beta}\right)\left(\frac{\partial S_t^z}{\partial S_0^\gamma}\right)\right] , \tag{B.4a}$$

$$\left([\hat{S}^z(t), [\hat{S}^z(t), \hat{S}^z(0)]\,]\right)^{\rm w} \propto \hbar^2\,D^{(2)}_{S_0^z}\,S_t^{z\,2} \sim \hbar^2\left[\left(\frac{\partial S_t^z}{\partial S_0^\beta}\right)\left(\frac{\partial S_t^z}{\partial S_0^\gamma}\right) + S_t^z\,\frac{\partial^2 S_t^z}{\partial S_0^\beta \partial S_0^\gamma}\right] , \tag{B.4b}$$

where one should sum upon the indices $\beta\,\gamma = x, y, z$. In Eq.(B.4b), we kept only the third term appearing in Eq.(B.1), as the calculation of the other terms is analogous. Eq.(B.4) shows that the semiclassical limit of the square commutator *and* of the

echo observable is proportional to the square of the derivatives of the classical spin trajectory S_t^z to respect to the initial conditions $S_0^{x,y,z}$. Thus, exactly as the square-commutator, also the semiclassical $\mu(t)$ encodes twice the Lyapunov exponent in the presence of classical chaos.

Chapter C

Details on the semiclassical approach to entanglement dynamics and chaos

In this appendix we report the technical details the results of Chapter 3. First, in Appendix C.1 and C.2, we derive the equation of motion for the classical limit and the quantum fluctuations of the Kicked Top and the Dicke model respectively. Then in Appendix C.3 we recall the Benettin et al. algorithm for the computation of the Lyapunov spectrum, which we later apply in Appendix C.4 to the above models. We conclude with Appendix C.5, where we test our analytical results for the entanglement dynamics [cf. Section 3.2.2] with the early time perturbative expansion of the QFI and spin squeezing of Ref.[345].

C.1 Equation of motion for the Kicked top

We start by deriving the stroboscopic map for the classical limit of the kicked top [cf. Eq. (3.52)]. With reference to the setting and notations of Section 3.3, we adopt a convenient parametrization of the spin via spherical coordinates along the z axis via (2.73), so that the nonlinear part of the evolution — the kick $\hat{U}_\beta$ — looks simple. The discrete classical map that describes the stroboscopic evolution of the collective spin on the Bloch sphere is the composition of two maps, respectively generated by $\hat{U}_\alpha$ and $\hat{U}_\beta$. The classical map generated by $\hat{U}_\beta$ reads

$$\begin{cases} \theta'' = \theta' \\ \phi'' = \phi' + \beta \cos\theta' \end{cases} . \tag{C.1}$$

Due to the our choice of coordinates, obtaining the free precession described by $\hat{U}_\alpha$ is less straightforward. One strategy is to work it out in spherical coordinates with polar axis along x, and to transform into the original coordinates before and after the application of $\hat{U}_\alpha$. To this aim, we reparameterize the time-dependent collective spin direction as

$$\mathbf{Z} = \begin{pmatrix} \cos\eta \\ \sin\eta\cos\xi \\ \sin\eta\sin\xi \end{pmatrix} , \tag{C.2}$$

where η and ξ are respectively the polar and azimuthal angle in spherical coordinates with respect to the x axis. With this choice, the classical precession is described as

$$\begin{cases} \eta' = \eta \\ \xi' = \xi + \alpha \end{cases} . \tag{C.3}$$

The expression in the original coordinates is obtained by mapping (η, ξ) one-to-one to (θ, ϕ) by equating the two expressions of $\mathbf{Z}$ in Eqs. (2.73) and (C.2). This transformation yields Eqs.(3.52).

Let us now determine the evolution of quantum fluctuations. The transformation generated by $\hat{U}_\beta$ can be obtained straightforwardly following the procedure described in Section 3.1.2. One gets $\widetilde{H}_2 = \frac{1}{2}\beta \sin^2\theta \; \delta\hat{q}^2$ in Eq. (3.13), and hence

$$\begin{cases} \delta\hat{q}'' = \delta\hat{q}' \\ \delta\hat{p}'' = \delta\hat{p}' - \beta \, \sin^2\theta' \, \delta\hat{q}' \end{cases} . \tag{C.4}$$

To obtain the discrete transformation generated by $\hat{U}_\alpha$, we can again resort to the adapted coordinates (η, ξ). We define the rotated frame $(\bar{\mathbf{X}}, \bar{\mathbf{Y}}, \mathbf{Z})$ with the new spherical angles $\theta \to \eta$, $\phi \to \xi$, i.e.,

$$\bar{\mathbf{X}} \equiv \partial_\eta \mathbf{Z}/|\partial_\eta \mathbf{Z}| \, , \qquad \bar{\mathbf{Y}} \equiv \partial_\xi \mathbf{Z}/|\partial_\xi \mathbf{Z}| \, , \tag{C.5}$$

such that $(\bar{\mathbf{X}}, \bar{\mathbf{Y}}, \mathbf{Z})$ is an orthonormal frame adapted to the (η, ξ)-parameterization of the sphere. Along these lines, we define the corresponding transverse spin components and the associated bosonic variables via the truncated Holstein-Primakoff transformation,

$$\hat{S}^{\bar{X}} \equiv \bar{\mathbf{X}} \cdot \hat{\mathbf{S}} \simeq \sqrt{Ns} \, \delta\bar{q} \, , \qquad \hat{S}^{\bar{Y}} \equiv \bar{\mathbf{Y}} \cdot \hat{\mathbf{S}} \simeq \sqrt{Ns} \, \delta\bar{p} \, . \tag{C.6}$$

In this description, the free precession around x generated by $\hat{U}_\alpha$ is exactly canceled by the inertial term, and one obtains

$$\begin{cases} \delta\bar{q}' = \delta\bar{q} \\ \delta\bar{p}' = \delta\bar{p} \end{cases} . \tag{C.7}$$

Now, we only need to find the relation between $(\delta\bar{q}, \delta\bar{p})$ and $(\delta\hat{q}, \delta\hat{q})$. This can be obtained by noting that both $(\bar{\mathbf{X}}, \bar{\mathbf{Y}})$ and $(\mathbf{X}, \mathbf{Y})$ are orthonormal bases of the tangent plane to the unit sphere at the point $\mathbf{Z}$. Therefore, they must be related via a rotation, i.e.,

$$\begin{cases} \bar{\mathbf{X}} &= +\cos\psi \, \mathbf{X} + \sin\psi \, \mathbf{Y}, \\ \bar{\mathbf{Y}} &= -\sin\psi \, \mathbf{X} + \cos\psi \, \mathbf{Y} \end{cases} . \tag{C.8}$$

for some angle $\psi \in [0, 2\pi)$. This angle can be determined by noting that, by construction, $\bar{\mathbf{X}}$ belongs to the plane generated by $\mathbf{x}$ and $\mathbf{Z}$, and hence the equation

$$\bar{\mathbf{X}} \cdot (\mathbf{x} \times \mathbf{Z}) = 0 \tag{C.9}$$

holds. Substituting the first of Eqs. (C.8) as well as the third of Eqs. (2.73), we find

$$\psi = -\arctan\left(\frac{\tan\phi}{\cos\theta}\right) , \tag{C.10}$$

which determines ψ up to the ambiguity $\psi \leftrightarrow \psi + \pi$. Equation (C.8) immediately yields

$$\begin{cases} \delta\bar{q} &= +\cos\psi\,\delta\hat{q} + \sin\psi\,\delta\hat{p}, \\ \delta\bar{p} &= -\sin\psi\,\delta\hat{q} + \cos\psi\,\delta\hat{p}, \end{cases} . \tag{C.11}$$

hence one finds

$$\begin{cases} \delta\hat{q}' = +\cos(\psi-\psi')\,\delta\hat{q} + \sin(\psi-\psi')\,\delta\hat{p} \\ \delta\hat{p}' = -\sin(\psi-\psi')\,\delta\hat{q} + \cos(\psi-\psi')\,\delta\hat{p} \end{cases} . \tag{C.12}$$

Substituting the two maps in Eqs. (C.4) and (C.12) into the definition (3.16) of the correlation matrix $G(t)$, one directly obtains the desired, ambiguity-free, discrete-time evolution equations (3.53) for the quantum fluctuations.

C.2 Equation of motion for the Dicke model

Here, we derive the equations for the classical trajectory (3.58) and for the evolution of the quantum fluctuations around it (3.61) generated by the Dicke Hamiltonian (3.55) for large N.

Collective spin fluctuations can be described via a Holstein-Primakoff expansion around the time-dependent direction of the average orientation, as discussed in Section 3.1.3. Cavity mode fluctuations are represented by deviations away from its macroscopic expectation value. With reference to the setting and notations of Section 3.4, one has:

$$\hat{S}^\alpha \simeq X_\alpha(t)\sqrt{\frac{N}{2}}\,\delta\hat{q} + Y_\alpha(t)\sqrt{\frac{N}{2}}\,\delta\hat{p} + Z_\alpha(t)\left(\frac{N}{2} - \frac{\delta\hat{q}^2+\delta\hat{p}^2-1}{2}\right)$$

$$\hat{Q} = \sqrt{N}\mathcal{Q}(t) + \delta\hat{Q} \tag{C.13}$$

$$\hat{P} = \sqrt{N}\mathcal{P}(t) + \delta\hat{P} \tag{C.14}$$

with $\alpha = x, y, z$. The classical functions $\mathcal{Q}(t)$, $\mathcal{P}(t)$ and $\mathbf{Z}(t)$ are chosen in such a way that they account for the classical dynamics of the system. As a consequence, the quantum bosonic operators $(\delta\hat{q}, \delta\hat{p})$ and $(\delta\hat{Q}, \delta\hat{P})$ have vanishing expectation values and describe quantum fluctuations around the classical dynamics. The $\sqrt{N}$ scaling of classical variables may be understood as the occurrence that all terms in the Hamiltonian are extensive (and balance each other in equilibrium). Conversely, typical quantum fluctuations in equilibrium, quantified by the expectation values of quadratic bosonic operators, are of order $\mathcal{O}(1)$, i.e., subextensive. This corresponds to having an effective Planck constant $\hbar_{\text{eff}} = \hbar/N$.

The semiclassical time-evolution of the system can be obtained by substituting the time-dependent expansion above into the Hamiltonian and truncating to

quadratic order, cf. Eq.(3.13). We obtain

$$\hat{H} = N\,\mathcal{H}_{\rm cl} + \sqrt{N}\,\hat{H}_1 + \hat{H}_2 + \mathcal{O}\left(\frac{1}{\sqrt{N}}\right), \tag{C.15}$$

with $\mathcal{H}_{\rm cl}$ given by Eq.(3.56),

$$\hat{H}_1 = \sqrt{s}\big(\omega_0\,X_z + \gamma\mathcal{Q}\,X_x\big)\,\delta\hat{q} + \sqrt{s}\big(\omega_0\,Y_z + \gamma\mathcal{Q}\,Y_x\big)\,\delta\hat{p} + \big(\omega\mathcal{Q} + s\gamma\,Z_x\big)\,\delta\hat{Q} + (\omega\,\mathcal{P})\,\delta\hat{P} \tag{C.16}$$

and

$$\hat{H}_2 = -\big(\omega_0\,Z_x + \gamma\mathcal{Q}\,Z_x\big)\frac{\delta\hat{q}^2 + \delta\hat{p}^2 - 1}{2} + \omega\frac{\delta\hat{Q}^2 + \delta\hat{P}^2 - 1}{2} + \sqrt{s}\gamma\Big(X_x\,\delta\hat{q}\,\delta\hat{Q} + Y_x\,\delta\hat{p}\,\delta\hat{Q}\Big)\,. \tag{C.17}$$

The dynamics of quantum fluctuations are generated by the modified Hamiltonian $\widetilde{H} = \hat{H} - i\dot{\hat{V}}(t)\hat{V}^\dagger(t)$, which includes the inertial terms, due to the time-dependence of the transformation

$$\begin{aligned}\widetilde{H}_1 &= \hat{H}_1 - \Big(\sqrt{s}\,\dot{\mathbf{Y}}\cdot\mathbf{Z}\,\delta\hat{q} + \sqrt{s}\,\dot{\mathbf{Z}}\cdot\mathbf{X}\,\delta\hat{p} - \dot{\mathcal{P}}\,\delta\hat{Q} + \dot{\mathcal{Q}}\,\delta\hat{P}\Big)\\ \widetilde{H}_2 &= \hat{H}_2 + \dot{\mathbf{X}}\cdot\mathbf{Y}\,\frac{\delta\hat{q}^2 + \delta\hat{p}^2 - 1}{2}\,.\end{aligned} \tag{C.18}$$

In order for the quadratic approximation to be self-consistent, one must appropriately choose the classical functions $\mathcal{Q}(t)$, $\mathcal{P}(t)$ and $\mathbf{Z}(t)$ in such a way that linear terms in the bosonic variables vanish, i.e., $\widetilde{H}_1 \equiv 0$. This results in the classical dynamics of the collective spin and the radiation field

$$\begin{cases}\dot{\mathcal{Q}} = \omega\mathcal{P}\\ \dot{\mathcal{P}} = -\omega\mathcal{Q} - \dfrac{\gamma}{2}Z_x\\ \dot{\mathbf{Y}}\cdot\mathbf{Z} = \omega_0\,X_z + \gamma\mathcal{Q}\,X_x\\ \dot{\mathbf{Z}}\cdot\mathbf{X} = \omega_0\,Y_z + \gamma\mathcal{Q}\,Y_x\end{cases}. \tag{C.19}$$

The dynamics of quantum fluctuations is regulated by the equations of motion generated by the quadratic Hamiltonian $\widetilde{H}_2$

$$\begin{cases}\dot{\delta\hat{Q}} = +\omega\delta\hat{P}\\ \dot{\delta\hat{P}} = -\omega\delta\hat{Q} - \sqrt{s}\gamma(X_x\,\delta\hat{q} + Y_x\,\delta\hat{p})\\ \dot{\delta\hat{q}} = -(\omega_0\,Z_z + \gamma\mathcal{Q}\,Z_x - \dot{\mathbf{X}}\cdot\mathbf{Y})\delta\hat{p} + \sqrt{s}\gamma\,Y_x\,\delta\hat{Q}\\ \dot{\delta\hat{p}} = +(\omega_0\,Z_z + \gamma\mathcal{Q}\,Z_x - \dot{\mathbf{X}}\cdot\mathbf{Y})\delta\hat{q} - \sqrt{s}\gamma\,X_x\,\delta\hat{Q}\end{cases}. \tag{C.20}$$

With the usual choice of parameterization of the rotating frame (2.73) one has

$$\dot{\mathbf{Y}}\cdot\mathbf{Z} = -\sin\theta\dot{\phi}\,, \qquad \dot{\mathbf{Z}}\cdot\mathbf{X} = \dot{\theta}\,, \qquad \dot{\mathbf{X}}\cdot\mathbf{Y} = \cos\theta\dot{\phi}\,. \tag{C.21}$$

From these equations, by substituting explicitly the coordinates (2.73), one gets the classical equations of motion in Eq.(3.58) in the main text, and, for the fluctuations $\delta\hat{\boldsymbol{\xi}} = (\delta\hat{Q}, \delta\hat{P}, \delta\hat{q}, \delta\hat{p})$, Eq. (C.20) can be written as

$$\frac{d}{dt}\delta\hat{\boldsymbol{\xi}} = A(t)\,\delta\hat{\boldsymbol{\xi}}\ , \tag{C.22}$$

with the 4×4 matrix $A(t)$ expressed by Eq.(3.61) in the main text.

C.3 *Benettin* et al. algorithm for computing the Lyapunov spectrum

The by-now standard numerical algorithm for a robust computation of the Lyapunov spectrum has been proposed by Benettin, Galgani and Strelcyn in a series of papers around 1980, see Refs. [329–331]. Its central idea is based on the evolution of K tangent vectors $(\mathbf{w}^{(1)}, \dots \mathbf{w}^{(K)})$ and the use of the linearized equations of motion to compute the volumes $\mathrm{Vol}_K(t)$ and the resulting Lyapunov exponents $\{\lambda_k\}_{k=1}^K$. In chaotic systems, numerical errors grow exponentially fast in time and infinitesimal displacements $\mathbf{w}^{(k)}(t)$ might result in computer overflows at large t. To solve these issues, the method relies on the periodic orthonormalization of the evolved tangent-space basis, after a suitable time interval s. (This allows one to disregard the numerical instability due to the use of non-symplectic integrators.) In Ref.[331], the authors show that by choosing the Gram-Schmidt orthonormalization procedure, one can evaluate all the volumes $\{\mathrm{Vol}_k\}_{k=1}^K$ at once.

Fixing initial condition $\mathbf{x}(0) = \mathbf{x}_0$, the procedure goes as follows. Choose K independent tangent vectors at random at $t = 0$, i.e. $\{\mathbf{w}_0^{(k)}\}_{k=1}^K$. Then, for $1 \le i \le n$:

1. evolve the vectors $\{\mathbf{w}_{(i-1)s}^{(k)}\}$ for a time interval s via Eq.(3.2) and initial conditions $\mathbf{x}_{(i-1)s}$; this yields $\{\mathbf{w}_{is}^{(k)}\}$;

2. apply Gram-Schmidt procedure

$$\alpha_i^{(1)} = |\mathbf{w}_{is}^{(1)}|\ , \qquad \mathbf{w}_{is}^{\prime(1)} = \mathbf{w}_{is}^{(1)}/\alpha_i^{(1)} \tag{C.23}$$

   where $|\cdot|$ is the euclidean norm [1]. For $2 \le k \le K$

$$\alpha_i^{(k)} = \left| \mathbf{w}_{is}^{(k)} - \sum_{l=1}^{k-1} (\mathbf{w}_{is}^{\prime(l)} \cdot \mathbf{w}_{is}^{(k)})\, \mathbf{w}_{is}^{\prime(l)} \right|\ , \tag{C.24a}$$

$$\mathbf{w}_{is}^{\prime(k)} = \frac{1}{\alpha_i^{(k)}} \left(\mathbf{w}_{is}^{(k)} - \sum_{l=1}^{k-1} (\mathbf{w}_{is}^{\prime(l)} \cdot \mathbf{w}_{is}^{(k)})\, \mathbf{w}_{is}^{\prime(l)} \right)\ ; \tag{C.24b}$$

3. re-initialize the vectors $\mathbf{w}_{is}^{(k)} = \mathbf{w}_{is}^{\prime(k)}$ for $1 \le k \le K$.

[1] Note that the specific choice of the phase space metric is actually immaterial.

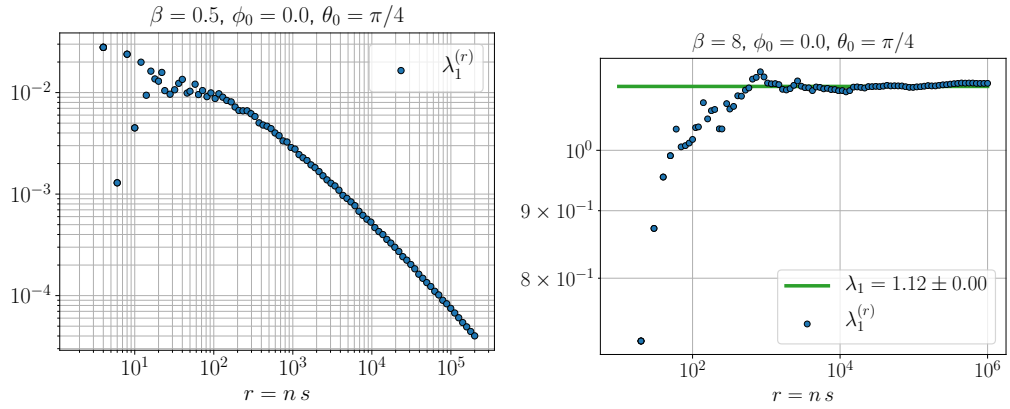

Figure C.1: Convergence of the maximum Lyapunov exponent (C.25) for the kicked top dynamics in the predominantly regular and chaotic regimes. The trajectories shown here correspond to those in Figure 3.5, with initial condition $\phi_0 = 0$ and $\theta_0 = \pi/4$: a regular one for $\beta = 0.5$, with $s = 2$ (left panel) and a chaotic one for $\beta = 8$, with $s = 10$ (right panel).

From this, the finite-time Lyapunov spectrum $\{\lambda_k(\mathbf{x}_0)\}$ is computed as

$$\lambda_k^{(n,s)}(\mathbf{x}_0) = \frac{1}{ns} \sum_{i=1}^{n} \ln \alpha_i^{(k)} \,, \tag{C.25}$$

for $k \leq 1 \leq K$. Convergence as $n \to \infty$ yields the proper, asymptotic Lyapunov spectrum. Notice that $\lambda_k^{(n,s)}(\mathbf{x}_0)$ should not depend on the time-interval s and on the number of iterations n independently, but rather via the product $r = s\,n$, i.e. $\lambda_k^{(r)}(\mathbf{x}_0)$. As r increases, $\lambda_k^{(r)}$ approaches a well defined limit, the k-th Lyapunov exponent $\lambda_k = \lim_{r\to\infty} \lambda_k^{(r)}$.

C.4 Lyapunov exponents for the kicked top and the Dicke model

We report the computation of the Lyapunov exponents of the kicked top (see Section 3.3) and of the Dicke model (see Section 3.4) obtained via the algorithm described in Appendix C.3.

We apply that procedure to the kicked top evolution at stroboscopic times (3.52), by evolving the linear displacements via the map in Eqs.(C.4-C.12). We fix a number s of kicks and we study the black trajectories in Figure 3.5-3.6. The results are shown in Figure C.1 and Figure C.2 respectively. We plot the finite-time maximum Lyapunov exponent $\lambda_1^{(r)}$ in Eq.(C.25) as a function of r. The maximum Lyapunov exponent λ_1 (green in the plots) is extracted numerically by averaging over the last two decades of the time window. For regular initial conditions, it approaches zero in the long-time limit $r \to \infty$, while for chaotic trajectories it clearly converges to a finite value, at very large times $r \gg 10^4$. As expected, the Lyapunov exponent for the chaotic trajectory in the intermediate regime with a mixed phase space is much

smaller than the one for the fully chaotic phase, and convergence to the asymptotic value is much slower.

The same procedure is applied to the classical dynamics of the Dicke model (3.58), fixing $s = 1$. The results for the regular and chaotic regimes are plotted in Figure C.3 and for the intermediate regime with a mixed phase space in Figure C.4. Because of the conservation of energy, the second Lyapunov exponent λ_2 always vanishes. As for λ_1, similar remarks to the case of the kicked top apply.

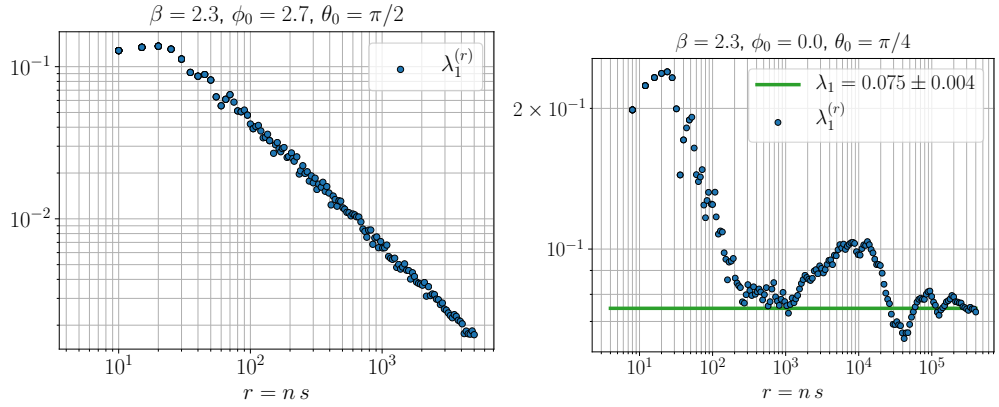

Figure C.2: Convergence of the maximum Lyapunov exponent (C.25) for the kicked top dynamics in the intermediate regime with a mixed phase space. The trajectories correspond to those in Figure 3.6, with $\beta = 2.3$: a regular one with $\theta_0 = \pi/2$ and $\phi_0 = 2.7$ (left panel), and a chaotic one with $\theta_0 = \pi/4$ and $\phi_0 = 0$ (right panel). Here we have fixed $s = 5$.

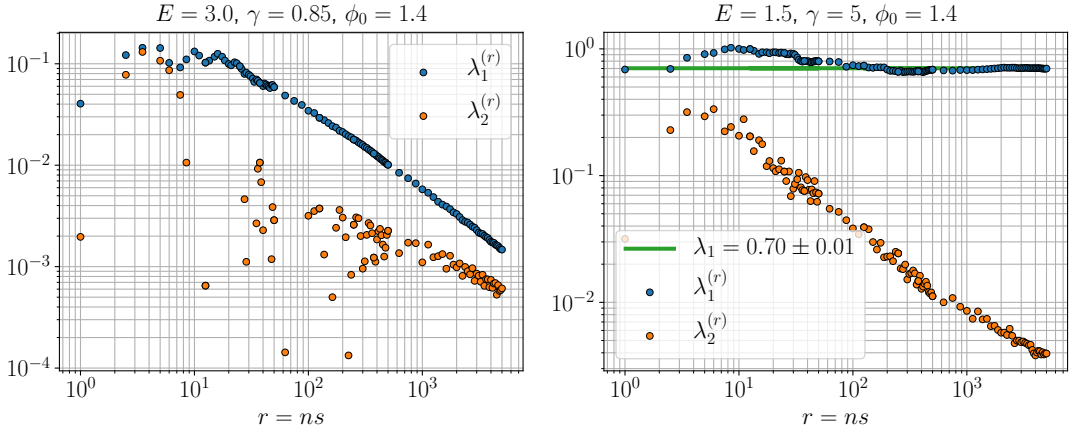

Figure C.3: Convergence of the maximum Lyapunov exponent (C.25) for the Dicke model dynamics in the predominantly regular and chaotic regimes. Left panel: regular trajectory with $E = 3$, $\gamma = 0.85$ Right panel: chaotic trajectory with $\beta = 1.5$, $\gamma = 5$. The common initial condition $\phi_0 = 1.4$ and $\cos\theta_0 = 0.1$ corresponds to the two trajectories in Figure 3.7. Here we have set $s = 0.5$.

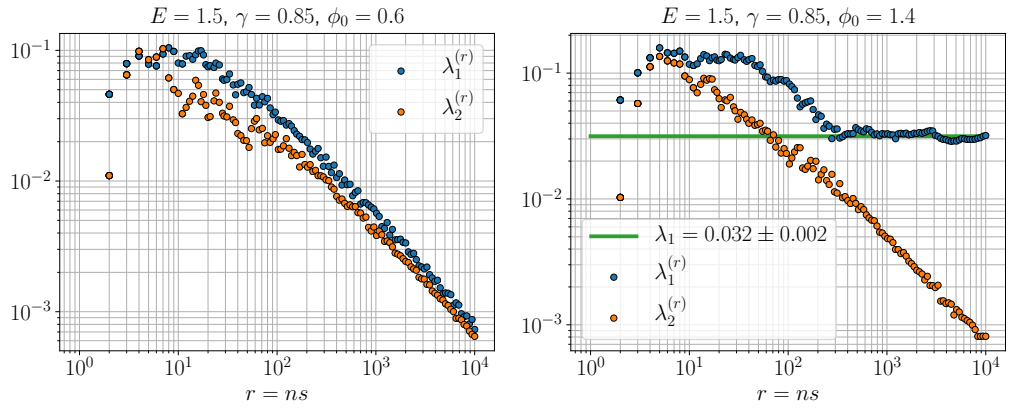

Figure C.4: Convergence of the maximum Lyapunov exponent (C.25) for the Dicke model dynamics in the intermediate regime with a mixed phase space. Here, $E = 1.5$, $\gamma = 0.5$. Left panel: Regular trajectory with initial condition $\cos\theta_0 = 0.1$ and $\phi_0 = 0.6$. Right panel: chaotic trajectory with initial condition $\cos\theta_0 = 0.1$ and $\phi_0 = 1.4$. The parameters and initial conditions chosen here correspond to the two highlighted trajectories in Figure 3.8. Here we have set $s = 1$.

C.5 Comparison with Sorelli et al. PRA (2019)

In Section 3.2.2, we have derived exact results for the entanglement dynamics starting from a polarized state in the z direction. Here, we compare the early time expansions of the QFI and spin squeezing with the results of Sorelli and collaborators in Ref.[345].

In order to derive the QFI f_Q and the spin squeezing ξ^2 we resort to Eqs. (3.25);

$$f_Q(t) = 1 + 2\langle \hat{n}_{\rm exc}(t)\rangle + 2\sqrt{\langle \hat{n}_{\rm exc}(t)\rangle(\langle \hat{n}_{\rm exc}(t)\rangle + 1)}\,, \tag{C.26a}$$

$$\xi^2(t) = 1 + 2\langle \hat{n}_{\rm exc}(t)\rangle - 2\sqrt{\langle \hat{n}_{\rm exc}(t)\rangle(\langle \hat{n}_{\rm exc}(t)\rangle + 1)}\,, \tag{C.26b}$$

where the number of collective excitations is

$$\langle \hat{n}_{\rm exc}\rangle = \frac{\langle \delta\hat{q}^2\rangle + \langle \delta\hat{p}^2\rangle - 1}{2}\,. \tag{C.27}$$

In Section 3.2.2 we have discussed the asymptotic behavior, when $\langle \hat{n}_{\rm exc}\rangle \gg 1$ and $f_Q \sim \langle \hat{n}_{\rm exc}\rangle$, $\xi^2 \sim 1/\langle \hat{n}_{\rm exc}\rangle$. On the other hand, at short times one needs to study the exact behavior and expand Eqs.(C.26) for $\langle \hat{n}_{\rm exc}\rangle \ll 1$.

In the case of one-axis twisting, one has (3.44)

$$\langle \hat{n}_{\rm exc}\rangle = \frac{J^2t^2}{4}\,. \tag{C.28}$$

By plugging this equation into Eq.(C.26), the Taylor expansion at short times leads to

$$f_Q(t)^{-1} = \xi^2(t) = 1 - Jt + \frac{(Jt)^2}{2} - \frac{(Jt)^3}{8} + \mathcal{O}((Jt)^5)\,, \tag{C.29}$$

which corresponds to Eq.(30) of Ref.[345] (remember that in their notation $\chi = J/N$). Notice, however, that at long times (but before the Ehrenfest time) one has $f_Q \sim 1/\xi^2 \sim t^2$.

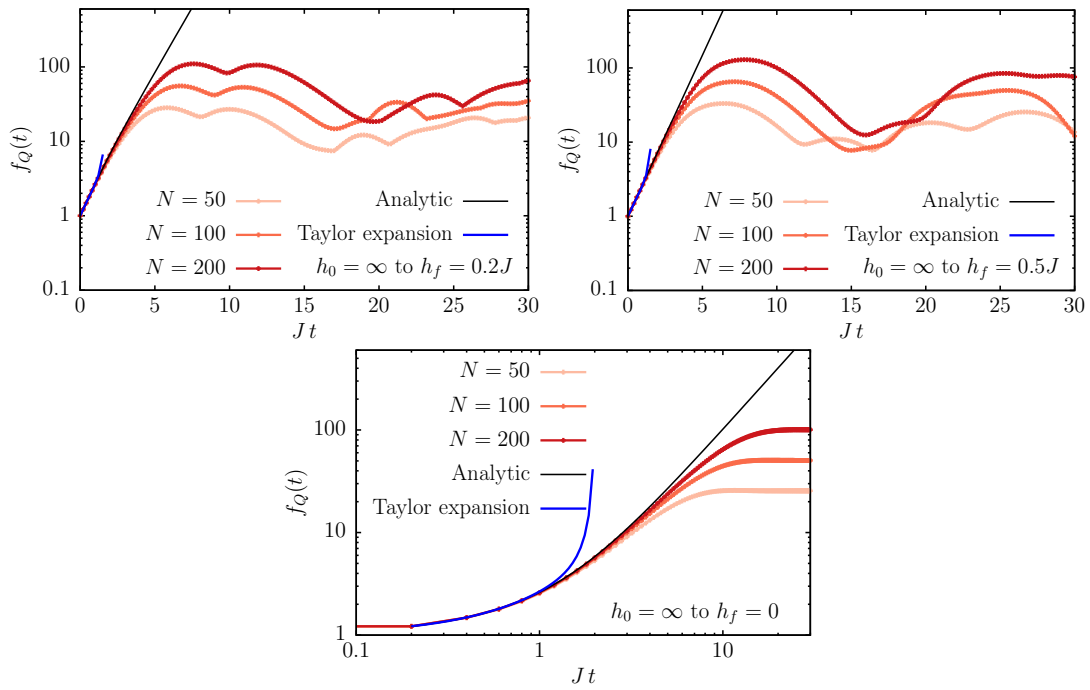

Figure C.5: Growth of the QFI initializing the system on the polarized state along z corresponding to $h_0 = \infty$. Exact numerics performed with ED for finite systems's sizes are compared with the analytical result in Eq.(C.26) and the Taylor expansions of Eq.(C.29) and (C.31) of this Appendix [or equivalently Eqs.(30) and (27) of Ref.[345]]. (Top) unstable trajectories with $h_f = 0.2J$ and $h_f = 0.5J$ respectively (bottom) one-axis twisting $h_f = 0$. Here we have fixed $J = 1$.

Let us now discuss the general case in which $h \neq 0$. As we have discussed, for $h > |J|$ entanglement oscillates in time, see e.g. Figure 3.4 (left). This has also been predicted by Ref.[345]. On the other hand, for $h < |J|$ one has (3.49)

$$\langle \hat{n}_{\rm exc} \rangle = \frac{1}{4}\left(\frac{\Omega}{\lambda_h} + \frac{\lambda_h}{\Omega}\right)^2 \sinh^2(\lambda_h t)\ , \tag{C.30}$$

with λ_h defined in Eq.(3.38). Hence, for large times (but before the Ehrenfest time) $f_Q = \xi^2 \sim \langle \hat{n}_{\rm exc} \rangle \sim e^{2\lambda_h t}$ as predicted by the semiclassical approach. However, by plugging the Taylor expansion of Eq.(C.30) into Eq.(C.26) at order $O(t^5)$ one finds

$$f_Q(t)^{-1} = \xi^2 = 1 - Jt + \frac{(Jt)^2}{2} - \frac{(Jt)^3}{8} - \frac{1}{6}J\lambda_h^2\, t^3 + \frac{1}{6}J^2\lambda_h^2 t^4 + \mathcal{O}((Jt)^5)\ , \tag{C.31}$$

which corresponds to Eq.(27) of Ref.[345].

Notice that we retrieve also the value of the parameters for which the generation of entanglement is the fastest. This is obtained finding the maximum of the instability eigenvalue λ_h, which is given by $h/J = 1/2$.

The analytical results obtained via Eqs.(C.26) and the Taylor expansions are compared with the numerical data for finite system sizes in Figure C.5, finding perfect agreement.

Chapter D

TWA as the saddle point of the path-integral formulation

In this appendix we recall how to derive the truncated Wigner approximation (Section 2.2.1) via the saddle point approximation of the path integral. Secondly, we show that quantum corrections are sub-leading for the Sherrington-Kirkpatrick model discussed in Chapter 6.

D.1 General derivation

In this section, we sketch the steps for the derivation of the TWA within the path integral formalism providing its formal justification in the large N limit. Feynman's path integral representation of the time evolution is well known to connect quantum and classical dynamics [527]. As such, it provides a convenient framework which allows to define classical evolution as an appropriate saddle point and to find the leading quantum corrections. If one is interested in kinetic type approaches, it is convenient to work in the Schrödinger representation where one can develop diagrammatic expansions within the Keldysh path integral [528]. However, if the dynamics are far from equilibrium and the effective $\hbar$ is the only small parameter then it is convenient to work in the Heisenberg picture, where the density matrix only enters through the initial conditions. As we discussed in the main text, formally one can exactly map dynamics of spins into the dynamics of Schwinger bosons using Eqs. (2.42).

For simplicity, we will focus here only on the expectation values of time-dependent observables. This analysis can be extended in a similar fashion to analyze various non-equal time correlation functions including OTOC [195, 280]. Let us assume that our observable of interest is represented by some operator $\hat{O}$. Then in the Heisenberg representation, its expectation value is given by

$$\langle \hat{O}(t) \rangle = \mathrm{Tr}\left[\hat{\rho}_0 \, T_K \, e^{\frac{i}{\hbar}\int_0^t \hat{H}(\tau) d\tau} \, \hat{O} e^{-i\int_0^t \hat{H}(\tau) d\tau} \right] , \tag{D.1}$$

where T_K denotes the time ordering along the Keldysh contour with later times appearing closer to the operator $\hat{O}$. For the sake of illustration, we consider phase-space representation in terms of coherent variable $(\boldsymbol{\alpha}, \boldsymbol{\alpha}^*)$ [cf. Eq.(2.39)]. The path

integral representation for this expectation value is obtained by Trotterization of the time evolution operators and inserting resolution of identity through coherent states between each Trotter step. Details of the derivation of such path integral can be found in Refs. [195, 280]; here we only quote the final result

$$\langle \hat{O}(t) \rangle = \int d\boldsymbol{\alpha}_0 d\boldsymbol{\alpha}_0^* \, W(\boldsymbol{\alpha}_0, \boldsymbol{\alpha}_0^*) \int \mathcal{D}\boldsymbol{\alpha}\mathcal{D}\boldsymbol{\alpha}^*\mathcal{D}\boldsymbol{\eta}\mathcal{D}\boldsymbol{\eta}^* \, O^{\mathrm{w}}(\boldsymbol{\alpha}(t), \boldsymbol{\alpha}(t)^*)$$
$$\exp\Big\{ \int_0^t d\tau \Big[\eta_j^*(\tau) \frac{\partial \alpha_j(\tau)}{\partial \tau} - \eta_j(\tau) \frac{\partial \alpha_j^*(\tau)}{\partial \tau} + i H^{\mathrm{w}}\Big(\boldsymbol{\alpha}(\tau) + \frac{\boldsymbol{\eta}(\tau)}{2}, \boldsymbol{\alpha}^*(\tau) + \frac{\boldsymbol{\eta}^*(\tau)}{2}, \tau\Big)$$
$$- i H^{\mathrm{w}}\Big(\boldsymbol{\alpha}(\tau) - \frac{\boldsymbol{\eta}(\tau)}{2}, \boldsymbol{\alpha}^*(\tau) - \frac{\boldsymbol{\eta}^*(\tau)}{2}, \tau\Big) \Big] \Big\} , \tag{D.2}$$

where $\boldsymbol{\alpha} \equiv \{\alpha_j\}$, $\boldsymbol{\alpha}^*$, $\boldsymbol{\eta}$, $\boldsymbol{\eta}^*$ are the classical (symmetric) and quantum (antisymmetric) bosonic fields with the index j running over both different sites and different Schwinger boson flavors. The vectors $\boldsymbol{\alpha}_0$ and $\boldsymbol{\alpha}_0^*$ represent initial "classical" fields, which are distributed according to the Wigner function. We highlight that in this form the path integral representation of the evolution is exact and both the Weyl symbols of the Hamiltonian and the observable and the Wigner function automatically emerge. The TWA emerges from the path integral by taking the saddle point approximation of the action (integrand) with respect to quantum variables $\eta_j(\tau)$ and $\eta_j^*(\tau)$. It is easy to see that this saddle point approximation is equivalent to linearizing the difference between Hamiltonians H^{w} on the forward and the backward path to the linear order in $\boldsymbol{\eta}$:

$$H^{\mathrm{w}}\Big(\boldsymbol{\alpha}(\tau) + \frac{\boldsymbol{\eta}(\tau)}{2}, \boldsymbol{\alpha}^*(\tau) + \frac{\boldsymbol{\eta}(\tau)^*}{2}\Big) - H^{\mathrm{w}}\Big(\boldsymbol{\alpha}(\tau) - \frac{\boldsymbol{\eta}(\tau)}{2}, \boldsymbol{\alpha}^*(\tau) - \frac{\boldsymbol{\eta}^*(\tau)}{2}\Big)$$
$$= \eta_j(\tau) \frac{\partial H^{\mathrm{w}}(\boldsymbol{\alpha}(\tau), \alpha^*(\tau))}{\partial \boldsymbol{\alpha}_j(\tau)} + \eta_j^*(\tau) \frac{\partial H^{\mathrm{w}}(\boldsymbol{\alpha}(\tau), \boldsymbol{\alpha}^*(\tau))}{\partial \alpha_j^*(\tau)} + \mathcal{O}(|\eta^3(\tau)|). \tag{D.3}$$

By integrating over quantum $\boldsymbol{\eta}(\tau)$ and $\boldsymbol{\eta}^*(\tau)$ variables, one enforces the deterministic evolution of the classical variables $\boldsymbol{\alpha}(\tau)$ and $\boldsymbol{\alpha}^*(\tau)$ according to the standard Hamiltonian equations of motion [cf. Eq.(2.45)]

$$i\frac{d\alpha_j}{dt} = \frac{\partial H^{\mathrm{w}}(\boldsymbol{\alpha}(\tau), \boldsymbol{\alpha}^*(\tau))}{d\alpha_j^*}(\tau) \equiv \{\alpha_j(\tau), H^{\mathrm{w}}(\boldsymbol{\alpha}(\tau), \boldsymbol{\alpha}^*(\tau))\} .$$

As discussed in the main text, these equations are equivalent to the Hamiltonian equations for spins (angular momentum) variables if one goes back from complex $\boldsymbol{\alpha}$ variables to standard classical angular momentum variables [195]. If one ignores fluctuations in the initial conditions setting $\boldsymbol{\alpha}_0$ to a fixed mean field value, and interprets the Schwinger boson components for each spin α_0 and α_1 as the components of the wave function, then TWA reduces to the Dirac's variational principle. Let us note, however, that one needs much stronger assumptions about the nature of initial state and absence of unstable chaotic dynamics in order to justify this variational principle. In most cases it leads to very poor predictions for the dynamics even if the effective $\hbar$ controlling the saddle point approximation is very small. Conversely, TWA is not relying on the assumptions about the initial state.

D.2 Validity of semiclassics for the SK model

To justify the TWA for the SK model, we need to show that $1/N$ plays the role of the effective Planck's constant. This can be readily seen by analyzing the effect of neglected cubic terms in η of Eq. (D.3) on the observable $\langle \hat{O}(t) \rangle$. Let us show that these terms indeed are suppressed by $1/N$. We compute the derivatives of the Weyl symbol of the Hamiltonian (6.17). Ignoring numerical prefactors of the order of unity, the neglected terms in the path integral are of the type

$$\frac{J}{\sqrt{N}} \sum_{ij} g_{ij}\, \alpha_i^*(\tau)\eta_i(\tau)\eta_j^*(\tau)\eta_j(\tau) + c.c.,$$

where g_{ij} are the Gaussian random variables with zero average and unit variance, appearing in the couplings (6.18). Here for simplicity, we suppress a spin Schwinger boson index in $\boldsymbol{\alpha}$, $\boldsymbol{\eta}$ variables since it is unimportant for the scaling and we only keep the site index. In Ref. [195] it was shown that these terms result in the cubic response of the observable O^{w} to the infinitesimal quantum jumps on the classical $\boldsymbol{\alpha}$ fields integrated over time:

$$\delta O(t) \sim \frac{J}{\sqrt{N}} \int_0^t d\tau W(\boldsymbol{\alpha}_0, \boldsymbol{\alpha}_0^*) \sum_{ij} g_{ij} \left(\alpha_i^*(\tau) \frac{\partial}{\partial \alpha_i^*(\tau)} \frac{\partial}{\partial \alpha_j^*(\tau)} \frac{\partial}{\partial \alpha_j(\tau)} + c.c. \right) O^{\mathrm{w}}(\boldsymbol{\alpha}(t), \boldsymbol{\alpha}^*(t)) \,. \tag{D.4}$$

To simplify the further discussion suppose that O^{w} is linear in spin variables, say it represents the magnetization as analyzed in the main text $O^{\mathrm{w}} = s_k^z \sim \alpha_k^* \alpha_k$. One can see that the deviation of the expectation value of the observable from its TWA value is suppressed by at least $1/N$ factor as

$$\delta O(t) \sim \frac{O^{TWA}}{N} \,. \tag{D.5}$$

The first $1/\sqrt{N}$ comes from the coupling's normalization in Eq.(D.4), and the other contributions come from the double summation. Anyhow, only terms with $ij \neq k$ should be accounted, for which it is easy to see that each derivative contributes with

$$\frac{\partial}{\partial \alpha_j} s_k \sim J \frac{g_{jk}}{\sqrt{N}} s_k \,.$$

This observation immediately follows from the structure of the classical equations of motion as this derivative represents the response of the k-th spin to an infinitesimal perturbation of the j-th spin, which is suppressed (at least at short times) by the coupling constant, which scales as $1/\sqrt{N}$. Combining all the factors of N and performing the disorder average we get immediately the estimate in Eq.(D.5).
We note that there is a standard issue of controllability of TWA (as well as of any other numerical method) at long times, which is very difficult to resolve analytically. In the present work, we show that for the echo or OTOC the TWA works until the Ehrenfest time, which scales as $\ln(N)$, while for standard forward observables the mistake remains suppressed at all times.

Chapter E

Details on the calculations in the Dyson hierarchical model

In this appendix, we report the explicit calculations of some results presented in the main text. In Appendix E.1 we derive the recursive structure of the reduced density matrix for the interval $\ell_k = 2^{n-k}$ (7.21) in partition (1). In Appendix E.2, we derive the asymptotic expansions of the entanglement entropy for $\ell = 2^m + 1$ in Eqs.(7.34) and (7.35). In Appendix E.3 we show the finiteness of the rank of the reduced density matrix (cf. Eq. (7.41)) by linear algebra methods.

E.1 Recurrence relations for the reduced density matrix in partition (1).

Here we derive explicitly the recurrence relations in Eqs. (7.21) and (7.22). We first compute the reduced density matrix of half-system in the ground state $|+\rangle\langle+|^{[n]}$ (cf. Eq. (7.10))

$$\hat{\rho}_{L/2} \equiv \mathrm{tr}_B\, |+\rangle\langle+|^{[n]} = \hat{\tau}_0^{[1]} = a_{n-1}^2\ |+\rangle\langle+|_1^{[n-1]} + b_{n-1}^2\ |-\rangle\langle-|_1^{[n-1]}\ , \tag{E.1}$$

where $\hat{\tau}_0^{[k]}$ is defined in Eq. (7.20) and $|\pm\rangle_1^{[n-1]}$ is the basis of the first effective spin at level $n-1$. The reduced density matrix for $\ell_2 = L/4$ is obtained first by rewriting $\hat{\tau}_0^{[1]}$ in terms of the effective spins at the level $n-2$ as

$$\begin{aligned}
\hat{\tau}_0^{[1]} &= c_1|+\rangle\langle+|_1^{[n-1]} + d_1|-\rangle\langle-|_1^{[n-1]} \\
&= c_1 \left(a_{n-2}|++\rangle_1^{[n-2]} + b_{n-1}|--\rangle_1^{[n-2]}\right)\left(a_{n-2}\langle++|_1^{[n-2]} + b_{n-2}\langle--|_1^{[n-2]}\right) \\
&\quad + \frac{1}{2}d_1 \left(|++\rangle_1^{[n-2]} + |--\rangle_1^{[n-2]}\right)\left(\langle++|_1^{[n-2]} + \langle--|_1^{[n-2]}\right)\ ,
\end{aligned}$$

and then tracing out the second spin at level $n-2$, obtaining

$$\hat{\rho}_{L/4} = \hat{\tau}_0^{[2]} = \left(c_1 a_{n-2}^2 + \frac{1}{2}d_1\right)|+\rangle\langle+|_1^{[n-2]} + \left(c_1 b_{n-2}^2 + \frac{1}{2}d_1\right)|-\rangle\langle-|_1^{[n-2]}\ , \tag{E.2}$$

which is Eq. (7.21) with $k=2$. Iterating this procedure, one easily gets the recurrence relation for $\hat{\rho}_{L/2^k}$. At the critical point the coefficients in Eq.(7.11) are constant for all k. All the recursion relations simplify and admit as solution Eq.(7.23).

E.2 Asymptotic expansions of the entanglement entropy for partition (2)

Here we work out the asymptotic expressions of the entanglement entropy for $\ell_m = 2^m + 1$ in Eqs. (7.34-7.35) in the limits $\sigma \gg 1$ and $\sigma \ll 1$. In this case the reduced density matrix (7.33) for $p = 1$, i.e.

$$\hat{\rho}_{\ell_m} = c_\nu^+ \hat{\rho}_0^{[1,m]} + d_\nu^+ \hat{\rho}_1^{[1,m]}, \tag{E.3}$$

is a 4×4 block-diagonal matrix in the basis $|\pm\rangle_1^{[m]} \otimes |\pm\rangle_{\ell_m}^{[0]}$, which makes all calculations straightforward. This equation can be solved using the recurrence relations (7.29) with the initial conditions (7.23), obtaining

$$\hat{\rho}_{\ell_m} = \begin{pmatrix} \hat{\rho}^s_{\nu,m} & 0 \\ 0 & \hat{\rho}^a_{\nu,m} \end{pmatrix} , \tag{E.4}$$

with $\hat{\rho}^{s/a}_{\nu,m}$ block matrices of the form

$$\hat{\rho}^{s/a}_{\nu,m} = \begin{pmatrix} A^{s/a}_{\nu,m} & C^{s/a}_{\nu,m} \\ C^{s/a}_{\nu,m} & B^{s/a}_{\nu,m} \end{pmatrix} = \begin{pmatrix} A^{s/a}_\nu + D^{s/a}_\nu e^{-\alpha m} & C^+_\nu e^{-\beta m} \pm C^-_\nu e^{-\gamma m} \\ C^+_\nu e^{-\beta m} \pm C^-_\nu e^{-\gamma m} & B^{s/a}_\nu + E^{s/a}_\nu e^{-\alpha m} \end{pmatrix} , \tag{E.5}$$

where $A^{s/a}_\nu, \cdots E^{s/a}_\nu$ are read from Eqs. (7.23) and (7.33). We take now the limit $n \to \infty$ and, since $\nu = n - p - m$, the elements c^+_ν, d^+_ν are constant and given by the limit for $k \to \infty$ of Eq. (7.23). Defining $\xi \equiv \sqrt{K^2 + 4}$, the coefficients in (E.5) are

$$A^s = \frac{\xi^2}{4(\xi-1)^2} , \qquad A^a = B^a = \frac{\xi^2(1+K^2) - 2\xi}{4(\xi^2-1)^2} , \qquad B^s = \frac{(\xi-2)^2}{4(\xi-1)^2} , \tag{E.6a}$$

$$D^s = E^s = \frac{K^2}{4(\xi^2(1+K^2) + 2\xi)} , \qquad D^a = E^a = -D^s , \tag{E.6b}$$

$$C^\pm = \frac{\sqrt{\xi^2 - 2\xi} \pm \sqrt{\xi^2 + 2\xi} \mp 2\sqrt{1+2\xi}}{8(\xi-1)} . \tag{E.6c}$$

The reduced density matrix can be diagonalised and from its four eigenvalues $\{\lambda_i\}$, the entanglement entropy $S_A = -\sum_{i=1}^4 \lambda_i \ln \lambda_i$ is obtained as a function of K. In the limits $\sigma \gg 1$ and $\sigma \ll 1$, we derive the asymptotic expression of S_{ℓ_m} in Eqs. (7.34-7.35).

Asymptotic result for $\sigma \ll 1$. We consider the limit $\sigma \ll 1$, equivalent to $K \to 0$, see Eq. (7.14). At order $\mathcal{O}(K^3)$ the matrix elements (E.5) read

$$A^s_m = 1 - \frac{K^2}{4} + \frac{K^2}{32}\frac{1}{2^m} + \mathcal{O}(K^3), \qquad B^s_m = \frac{K^2}{32}\frac{1}{2^m} + \mathcal{O}(K^4), \tag{E.7a}$$

$$C^s_m = \frac{K}{16\sqrt{2}}\frac{1}{2^{m/2}} + \mathcal{O}(K^3), \qquad C^a_m = \frac{K^2}{32\sqrt{2}}\frac{(m+2)}{2^{m/2}} + \mathcal{O}(K^3). \tag{E.7b}$$

$$A^a_m = B^a_m = \frac{K^2}{8} - \frac{K^2}{32}\frac{1}{2^m} + \mathcal{O}(K^3). \tag{E.7c}$$

With these elements, the eigenvalues of the symmetric and anti-symmetric matrices (E.5) are

$$\begin{aligned}\lambda_1 &= \mathcal{O}(K^3)\,, \\ \lambda_2 &= 1 - \frac{K^2}{4}\left(1 - 2^{-(m+2)}\right) + \mathcal{O}(K^3)\,, \\ \lambda_{3,4} &= \frac{K^2}{8}\left(1 - 2^{-(m+2)} \pm 2^{(m+3)/2}(m+2)\right) + \mathcal{O}(K^3),\end{aligned} \tag{E.8}$$

hence the asymptotic entanglement entropy as a function of m reads

$$S_{\ell_m} = \frac{K^2}{4}\Big(1 - \ln\frac{K^2}{8}\Big) + \frac{K^2}{16}\frac{1}{2^m}\Big(\ln\frac{K^2}{8} - \frac{(m+2)^2}{4}\Big) + \mathcal{O}(K^3)\,, \tag{E.9}$$

that, as function of $2^m = \ell_m - 1$, is the same as Eq. (7.34).

Asymptotic result for $\sigma \gg 1$. Here we consider the limit $\sigma \gg 1$, i.e. for $K \to \infty$, and we expand the matrix elements (E.5) at $\mathcal{O}(K^{-3})$. The saturation value is obtained for $\alpha\, m, \beta m, \gamma\, m \gg 1$, corresponding to have only diagonal terms in Eq. (E.5) given by

$$A^s = \frac{1}{4} + \frac{1}{2K} + \frac{3}{4K^2} + \mathcal{O}(K^{-3})\,, \tag{E.10a}$$

$$B^s = \frac{1}{4} - \frac{1}{2K} - \frac{1}{4K^2} + \mathcal{O}(K^{-3})\,, \tag{E.10b}$$

$$A^a = B^a = \frac{1}{4} - \frac{1}{4K^2} + \mathcal{O}(K^{-3})\,, \tag{E.10c}$$

leading to the following saturation entanglement entropy

$$S_{\text{sat}} = 2\ln 2 - \frac{1}{K^2} + \mathcal{O}(K^{-3})\,. \tag{E.11}$$

The pre-asymptotic regime is obtained by taking the limit $K \to \infty$ at fixed m. In this limit

$$\alpha = 2\ln K + \frac{4}{K^2} + \mathcal{O}(K^{-3}), \qquad \beta = \frac{1}{2K^2} + \mathcal{O}(K^{-3}), \qquad \gamma = \ln K + \frac{3}{2K^2} + \mathcal{O}(K^{-3}), \tag{E.12}$$

and the exponent $\beta \to 0$, so that we cannot neglect the non-diagonal parts of Eq. (E.5). Thus, there is another regime in which $m \gg \alpha^{-1}, \gamma^{-1}$ but with $\beta m \ll 1$, i.e., in terms of K, $(\ln K)^{-1} \ll m \ll 2K^2$. In this regime, the diagonal terms $A_m^{s/a}, B_m^{s/a}$ are the same as in Eqs. (E.10), but the non-diagonal ones become

$$C_m^s = C_m^a = \left(\frac{1}{4} - \frac{3+m}{8K^2}\right) + \mathcal{O}(K^{-3}, m^2K^{-4}). \tag{E.13}$$

The diagonalisation of the reduced density matrix (E.4) finally yields

$$S_A = \ln 2 + \frac{m}{4K^2}\Big(1 - \ln\frac{m}{4K^2}\Big) + \mathcal{O}\left(K^{-3}, m^2K^{-4}, K^{-m}\right), \tag{E.14}$$

that in terms of $2^m = \ell_m - 1$ is Eq. (7.35) in the main text.

E.3 Rank of reduced density matrices.

Here we show Eq. (7.41) of the main text. All the matrices $\hat{\rho}_i^{[n]}$ in Eq. (7.31) can be written in a compact form as

$$\hat{\rho}_i^{[n]} = \sum_{j,k=0}^{3} \gamma_{jk}^i \hat{P}_j \otimes \hat{\rho}_k^{[n]} \,, \tag{E.15}$$

where

$$\hat{P}_0 = \begin{pmatrix} 1 & 0 \\ 0 & 0 \end{pmatrix} \,, \quad \hat{P}_1 = \begin{pmatrix} 0 & 0 \\ 0 & 1 \end{pmatrix} \,, \quad \hat{P}_2 = \begin{pmatrix} 0 & 1 \\ 0 & 0 \end{pmatrix} \,, \quad \hat{P}_3 = \hat{P}_2^T \,, \tag{E.16}$$

while the real coefficients of the tensor γ_{jk}^i can be obtained from Eq. (7.31). For fixed i, j there is only one k_{ij} such that $\gamma_{jk_{ij}}^i \neq 0$ (e.g. $\gamma_{0k}^0 = a^2\, \delta_{k0}$). The coefficients $\gamma_{jk_{ij}}^i$ satisfy the following property

$$\gamma_{0,k_{0i}}^i \, \gamma_{1,k_{1i}}^i - \gamma_{2,k_{2i}}^i \, \gamma_{3,k_{3i}}^i = 0 \quad \forall i \,. \tag{E.17}$$

Eq. (E.15) is written in the basis of the spin blocks at level n, see Fig. 7.2 (e.g. $\hat{\rho}_i^{[n=0]}$ is written in terms of the physical spins). For generic n, $\hat{\rho}_i^{[n]}$ is a matrix of size $2^{n+1} \times 2^{n+1}$. By construction, up to a change of basis, the matrices $\rho_i^{[n]}$ are either diagonal or anti-diagonal

$$\rho_{0,1}^{[n]} = \begin{pmatrix} A_{0,1}^{[n]} & 0 \\ 0 & B_{0,1}^{[n]} \end{pmatrix} \,, \quad \rho_2^{[n]} = \begin{pmatrix} 0 & C_2^{[n]} \\ D_2^{[n]} & 0 \end{pmatrix} \quad \text{and} \quad \rho_3^{[n]} = \left(\rho_2^{[n]}\right)^T . \tag{E.18}$$

In order to prove Eq. (7.41), we show that $\forall n$ it holds

$$A_0^{[n]} \, B_1^{[n]} = C_2^{[n]} D_3^{[n]} \quad \text{and} \quad A_1^{[n]} \, B_0^{[n]} = \left(D_2^{[n]}\right)^2 \,, \tag{E.19a}$$

$$\text{Rank}\left[A_{0,1}^{[n]}\right] = \text{Rank}\left[B_{0,1}^{[n]}\right] = \text{Rank}\left[C_2^{[n]}\right] = \text{Rank}\left[D_2^{[n]}\right] = 1 \,, \quad \text{Rank}\left[\rho_i^{[n]}\right] = 2 \,. \tag{E.19b}$$

Proof. We will prove by induction. The step $n = 0$ is obvious. Let us first see what happens for $n = 1$ in order to start the induction. We construct the matrices $\hat{\rho}_i^{[1]}$ with γ_{jk}^i given by Eq. (7.31). Let us consider

$$\rho_0^{[1]} = \begin{pmatrix} \gamma_{0,k_{00}}^0 A_0^{[0]} & 0 & 0 & \gamma_{2,k_{02}}^0 C_2^{[0]} \\ 0 & \gamma_{0,k_{00}}^0 B_0^{[0]} & \gamma_{2,k_{02}}^0 D_2^{[0]} & 0 \\ 0 & \gamma_{3,k_{30}}^0 C_3^{[0]} & \gamma_{1,k_{01}}^0 A_1^{[0]} & 0 \\ \gamma_{3,k_{30}}^0 D_3^{[0]} & 0 & 0 & \gamma_{1,k_{01}}^0 B_1^{[0]} \end{pmatrix} \tag{E.20}$$

and analogously for the other $\rho_i^{[1]}$. After a change of basis, this defines the recurrence

for the matrices A, B, C, D as

$$A_0^{[1]} = \begin{pmatrix} \gamma^0_{0,k_{00}} A_0^{[0]} & \gamma^0_{2,k_{02}} C_2^{[0]} \\ \gamma^0_{3,k_{03}} D_3^{[0]} & \gamma^0_{1,k_{01}} B_1^{[0]} \end{pmatrix} \qquad B_0^{[1]} = \begin{pmatrix} \gamma^0_{1,k_{01}} A_1^{[0]} & \gamma^0_{3,k_{03}} C_3^{[0]} \\ \gamma^0_{2,k_{02}} D_2^{[0]} & \gamma^0_{0,k_{00}} B_0^{[0]} \end{pmatrix} \tag{E.21}$$

$$A_1^{[1]} = \begin{pmatrix} \gamma^1_{0,k_{10}} A_1^{[0]} & \gamma^1_{2,k_{12}} C_3^{[0]} \\ \gamma^1_{3,k_{13}} D_2^{[0]} & \gamma^1_{1,k_{11}} B_0^{[0]} \end{pmatrix} \qquad B_1^{[1]} = \begin{pmatrix} \gamma^1_{0,k_{11}} A_0^{[0]} & \gamma^1_{3,k_{13}} C_2^{[0]} \\ \gamma^1_{2,k_{12}} D_3^{[0]} & \gamma^1_{0,k_{10}} B_1^{[0]} \end{pmatrix}$$

$$C_2^{[1]} = \begin{pmatrix} \gamma^2_{0,k_{20}} A_0^{[0]} & \gamma^2_{2,k_{23}} C_2^{[0]} \\ \gamma^2_{3,k_{23}} D_3^{[0]} & \gamma^2_{1,k_{21}} B_1^{[0]} \end{pmatrix} \qquad D_2^{[1]} = \begin{pmatrix} \gamma^2_{1,k_{21}} A_1^{[0]} & \gamma^2_{3,k_{23}} C_3^{[0]} \\ \gamma^2_{2,k_{22}} D_2^{[0]} & \gamma^2_{0,k_{20}} B_0^{[0]} \end{pmatrix}$$

These matrices have rank one if the determinant is zero (since they are not zero, the rank is not null). For the matrix $A_0^{[1]}$ we have

$$\begin{aligned} \det A_0^{[1]} = \gamma^0_{1,k_{01}} \gamma^0_{1,k_{01}} A_1^{[0]} B_1^{[0]} - \gamma^0_{2,k_{02}} \gamma^0_{3,k_{03}} C_2^{[0]} D_3^{[0]} = \\ = A_1^{[0]} B_1^{[0]} \left(\gamma^0_{1,k_{01}} \gamma^0_{1,k_{01}} - \gamma^0_{2,k_{02}} \gamma^0_{3,k_{03}} \right) = 0 \, . \end{aligned} \tag{E.22}$$

Because of Eqs. (7.29-E.16-E.17), the same is true for all the matrices.

Let us now assume Eq. (E.19) to be true at $n-1$ and show that the same holds at level n. Eq. (E.21) holds at every step after a permutation of the basis elements. We now want to prove that they have rank one. Let us re-write the block matrices $A_0^{[n]}$ setting $\gamma^0_{0,k_{00}}/\gamma^0_{2,k_{02}} = \gamma^0_{3,k_{03}}/\gamma^0_{1,k_{01}} = w_0$. Up to a multiplication of the first and the second rows by a coefficient, we have

$$A_0^{[n]} = \begin{pmatrix} w_0 A_0^{[n-1]} & C_2^{[n-1]} \\ w_0 D_3^{[n-1]} & B_1^{[n-1]} \end{pmatrix} \to \begin{pmatrix} w_0 A_0^{[n-1]} B_1^{[n-1]} & B_1^{[n-1]} C_2^{[n-1]} \\ w_0 C_2^{[n-1]} D_3^{[n-1]} & C_2^{[n-1]} B_1^{[n-1]} \end{pmatrix} , \tag{E.23}$$

where we multiplied the first row by the block matrix $B_1^{[n-1]}$ on the right and of the second row by the block matrix $C_2^{[n-1]}$ on the left. Since we assumed $A_0^{[m]} B_1^{[m]} = C_2^{[m]} D_3^{[m]}$ to hold at $n-1$, this means that the second row is linearly dependent on the first, hence the rank is the one of the first rows $\text{Rank}[A_0^{[n]}] = \text{Rank}[\left(w_0 A_0^{[n-1]}, B_1^{[n-1]} \right)] = \min \left(\text{Rank}[A_0^{[n-1]}], \text{Rank}[B_1^{[n-1]} \right) = 1$. It is immediate to verify that $A_0^{[n]} B_1^{[n]} = C_2^{[n]} D_3^{[n]}$. □

Chapter F

Bounds on $\tilde{f}_{\alpha,\mathbf{k}}$ for long-range models

In this appendix we derive the bounds (5.6) on the couplings $\tilde{f}_{\alpha,\mathbf{k}}$, which dictate the dynamics in momentum space of long-range interacting models.

We consider the couplings $\tilde{f}_{\alpha,\mathbf{k}}$ defined in Eq.(5.3). Assuming long-range interactions with $\alpha \leq d$, we can safely approximate sums with integrals in their defining expression (5.3), which captures the leading order exactly. Hence, we can switch to spherical coordinates and integrate over all the angles, obtaining

$$\widetilde{f}_{\alpha,\mathbf{k}\neq\mathbf{0}} \sim \frac{1}{L^{d-\alpha}} \int_1^L d\rho\, \rho^{d-1-\alpha}\, \frac{\mathcal{J}_{d/2-1}(|\mathbf{k}|\rho)}{(|\mathbf{k}|\rho)^{d/2-1}}, \tag{F.1}$$

where $\mathcal{J}_\nu(x)$ is the standard Bessel function of order ν. While for small ρ the integral is never singular (due to the assumption of long-range interactions, $\alpha \leq d$), for large ρ the integrand is asymptotically oscillating with period $2\pi/|\mathbf{k}|$ and amplitude decaying as $\rho^{(d-1)/2-\alpha}$, which yields convergence only for $\alpha > (d-1)/2$. In this case, by rescaling $|\mathbf{k}|\rho = \eta$ to obtain a dimensionless integrand and denoting by $F(\eta)$ its primitive which satisfies $F(\infty) = 0$ and is uniformly bounded, one obtains the asymptotic estimate

$$\widetilde{f}_{\alpha,\mathbf{k}\neq\mathbf{0}} \underset{L\to\infty}{\sim} -\frac{F(|\mathbf{k}|)}{(|\mathbf{k}|L)^{d-\alpha}}. \tag{F.2}$$

In the limiting case $\alpha = d$, one can similarly compute

$$\widetilde{f}_{\alpha,\mathbf{k}\neq\mathbf{0}} \underset{L\to\infty}{\sim} -\frac{\ln|\mathbf{k}| + \tilde{F}(|\mathbf{k}|)}{\ln L}, \tag{F.3}$$

where $\tilde{F}$ is the non-singular (bounded) part of the primitive F. On the other hand, for $\alpha \leq (d-1)/2$, by isolating the purely oscillatory terms and repeatedly integrating by parts, we can obtain an expansion of the primitive of the form

$$\widetilde{f}_{\alpha,\mathbf{k}\neq\mathbf{0}} \sim \frac{1}{(|\mathbf{k}|L)^{d-\alpha}} \left(c_1 (|\mathbf{k}|L)^{\frac{d-1}{2}-\alpha} + c_2 (|\mathbf{k}|L)^{\frac{d-1}{2}-\alpha-1} + \dots \right), \tag{F.4}$$

with $c_{1,2,\ldots}$ numerical constants. To sum up, the following estimates have been established

$$\left|\widetilde{f}_{\alpha,\mathbf{k}\neq\mathbf{0}}\right| \leq \begin{cases} \text{const} \times \dfrac{1}{(|\mathbf{k}|L)^{\frac{d+1}{2}}} & \text{for } \alpha \leq \dfrac{d-1}{2}, \\ \text{const} \times \dfrac{1}{(|\mathbf{k}|L)^{d-\alpha}} & \text{for } \dfrac{d-1}{2} < \alpha < d, \\ \text{const} \times \dfrac{\left|\ln|\mathbf{k}| + \tilde{F}(|\mathbf{k}|)\right|}{\ln L} & \text{for } \alpha = d. \end{cases} \tag{F.5}$$